

**Compact State-Space Models for Complex
Superconducting Radio-Frequency Structures
Based on Model Order Reduction and
Concatenation Methods**

Dissertation

zur

Erlangung des akademischen Grades

Doktor-Ingenieur (Dr.-Ing.)

der Fakultät für Informatik und Elektrotechnik

der Universität Rostock

vorgelegt von

Thomas Flisgen, geboren am 08.05.1983 in Mönchengladbach
aus Bad Doberan

Rostock, 7. April 2015

Tag der Einreichung: 07.04.2015
Tag der Verteidigung: 15.07.2015

Gutachter

Prof. Dr. Ursula van Rienen, Universität Rostock
Prof. Dr. Herbert De Gersen, Technische Universität Darmstadt
Prof. Dr. Rolf Schuhmann, Technische Universität Berlin

Abstract

The modeling of large chains of superconducting cavities with couplers is a challenging task in computational electrical engineering. The direct numerical treatment of these structures can easily lead to problems with more than ten million degrees of freedom. Problems of this complexity are typically solved with the help of parallel programs running on supercomputing infrastructures. However, these infrastructures are expensive to purchase, to operate, and to maintain. The aim of this thesis is to introduce and to validate an approach which allows for modeling large structures on a standard workstation. The novel technique is called *State-Space Concatenations* and is based on the decomposition of the complete structure into individual segments. The radio-frequency properties of the generated segments are described by a set of state-space equations which either emerge from analytical considerations or from numerical discretization schemes. The model order of these equations is reduced using dedicated model order reduction techniques. In a final step, the reduced-order state-space models of the segments are concatenated in accordance with the topology of the complete structure. The concatenation is based on algebraic continuity constraints of electric and magnetic fields on the decomposition planes and results in a compact state-space system of the complete radio-frequency structure. Compared to the original problem, the number of degrees of freedom is drastically reduced, i.e. a problem with more than ten million degrees of freedom can be reduced on a standard workstation to a problem with less than one thousand degrees of freedom. The final state-space system allows for determining frequency-domain transfer functions, field distributions, resonances, and quality factors of the complete structure in a convenient manner. This thesis presents the theory of the state-space concatenation approach and discusses several validation and application examples. The examples show that the resulting compact state-space models accurately describe the radio-frequency properties of the full structure and that the error introduced by the model order reduction and the concatenation of the segments is smaller than the error arising from the numerical treatment of the segments. In conclusion, the state-space concatenation scheme enables the investigation of radio-frequency properties of large structures without the application of supercomputers.

Zusammenfassung

Die Modellierung von Ketten supraleitender Hohlraumresonatoren mit Kopplern ist eine anspruchsvolle Aufgabe der rechnergestützten Elektrotechnik. Die direkte numerische Behandlung solcher Strukturen führt zu Problemen mit mehr als zehn Millionen Freiheitsgraden. Probleme dieser Komplexität lassen sich typischerweise nur mit Hilfe paralleler Programme lösen, die auf modernen Hochleistungsrechnern ausgeführt werden. Hochleistungsrechner sind allerdings teuer in der Anschaffung, im Betrieb und in der Wartung. Das Ziel der vorliegenden Arbeit ist die Einführung und die Validierung eines neuartigen Verfahrens, das die Modellierung von großen und komplexen Hochfrequenzstrukturen auf einem Arbeitsplatzrechner ermöglicht. Das neuartige Verfahren trägt den englischen Namen *State-Space Concatenations* und basiert auf der Zerlegung der Gesamtstruktur in einzelne Segmente. Die Hochfrequenzeigenschaften der Einzelsegmente werden dabei durch einen Satz von Zustandsmodellen beschrieben. Je nach Geometrie der Segmente werden deren Zustandsmodelle entweder durch kontinuierliche oder diskrete Verfahren erstellt. In einem folgenden Schritt wird die Modellordnung der Zustandsmodelle mit Hilfe von entsprechenden Techniken reduziert. Abschließend werden die reduzierten Zustandsmodelle der Segmente gemäß der Topologie der Gesamtstruktur zu einem Zustandsmodell verküpft. Diese Verkettung basiert auf algebraisch formulierten Kontinuitätsbedingungen für das elektrische und das magnetische Feld an den Schnittflächen und liefert ein kompaktes Zustandsmodell der Gesamtstruktur. Im Vergleich zum Ursprungsproblem ist die Anzahl der Freiheitsgrade dieses Zustandsmodells erheblich reduziert. Ein Problem mit zehn Millionen Freiheitsgraden kann auf einem Arbeitsplatzrechner zu einem Problem mit weniger als tausend Freiheitsgraden zurückgeführt werden. Das erstellte Zustandsmodell ermöglicht die schnelle Berechnung von Hochfrequenzeigenschaften der Gesamtstruktur, zum Beispiel Übertragungsfunktionen im Frequenzbereich, Feldverteilungen, Resonanzen und Güten. Die vorliegende Arbeit beschreibt die Theorie der Methode der Verkopplung von Zustandsmodellen und diskutiert Validierungs- und Anwendungsbeispiele. Die Beispiele zeigen, dass die erzeugten kompakten Zustandsmodelle die Hochfrequenzeigenschaften der Gesamtstruktur präzise widerspiegeln. Der Fehler durch die Modellordnungsreduktion und die Verknüpfung ist geringer als der durch die Diskretisierung der Einzelsegmente entstandene Fehler. Abschließend lässt sich feststellen, dass die Methode der Verkopplung von Zustandsmodellen die Untersuchung von Hochfrequenzeigenschaften komplexer Strukturen ohne den Einsatz von Hochleistungsrechnern erlaubt.

Danksagungen

Die vorliegende Arbeit wäre nicht ohne die Unterstützung meiner lieben Mitmenschen entstanden. Ich möchte mich deshalb bei den Personen bedanken, die mich bei der Erstellung der Arbeit unterstützt haben:

- Prof. Dr. U. van Rienen für die Möglichkeit ein Teil ihrer Arbeitsgruppe zu sein, für die jahrelange gute Zusammenarbeit und das in mich gesetzte Vertrauen,
- Prof. Dr.-Ing. R. Schuhmann und Prof. Dr.-Ing. H. De Gersem für die Übernahme der externen Gutachten,
- meinen (Ex)Kollegen aus der Arbeitsgruppe Theoretische Elektrotechnik, insbesondere Christian Bahls, Korinna Brackebusch, Dr. Tomasz Galek, Petra Gefken, Dr. Anne Grünbaum, Dr. Dirk Hecht, Dr. Aleks Markovic, Dr. Carsten Potratz, Dr. Gisela Pöplau, Dr. Christian Schmidt und Ulf Zimmermann für viele Diskussionen und für Dienstreisen mit Klassenfahrtsfeeling,
- Dr. Hans-Walter Glock für die intensive Unterstützung in der ersten Phase der Promotionszeit und für seine gründlichen und konstruktiven Kritiken an meinen Arbeiten,
- meinem ehemaligen Hiwi, Bachelorand, Masterrand und mittlerweile Arbeitskollegen Johann Heller für motivierende Worte und viele Beiträge, wie die Erstellung der Automatisierung von SSC und die Erstellung von dreidimensionalen Feldplots,
- Maja Gudat, Dr. Bernhard Himmel, Kathrin Krebs, Jörg Romahn, Toralf Thiel und Tina Zorn für die Unterstützung bei Papierkram, Netzwerk- und Druckerproblemen und die Bereitstellung des Institutsgrills,
- meinen (Ex)Kollegen aus dem EuCard Projekt Dr. Nicoleta Baboi, Prof. Dr. Roger Jones, Dr. Ian Shinton und Dr. Pei Zhang für die Zusammenarbeit z.B. bei den Streuparametermessungen beim DESY in Hamburg,
- meinen Professoren und Studienkollegen von der Hochschule Niederrhein, insbesondere meinem ehemaligen Laborpartner Philipp Kampermann,
- Michael Brindle für viele Verbesserungsvorschläge und das Korrekturlesen bezüglich der englischen Sprache,
- meinen Freunden aus Viersen, Mönchengladbach und Bad Doberan, besonders Katharina Müller, für viele schöne Erlebnisse,
- meiner Familie für die uneingeschränkte Unterstützung 24/7 über 31 Jahre.

Thesis Statements

of the dissertation

Compact State-Space Models for Complex Superconducting Radio-Frequency Structures based on Model Order Reduction and Concatenation Methods

by Thomas Flisgen

1. The investigation of radio-frequency properties of superconducting cavity chains is a challenging task in computational electrical engineering. Typically, the cavities in the chain are separately treated and the flanges at their beam pipes are equipped with perfect electric, perfect magnetic, or absorbing boundary conditions.
2. The restriction to a single cavity does not cover the mutual coupling of the cavities in the chain. Electromagnetic energy, which is not trapped in the cavity, is either reflected completely by the perfect conducting boundaries or is dissipated at the open boundaries.
3. The treatment of the cavity chain is computationally demanding: The chain has a length in the order of meter and typically contains structures with fine features in the order of millimeter, such as the HOM coupler parts. The direct discretization of the complete cavity chain can result in a problem with more than ten million degrees of freedom.
4. In addition to the number of degrees of freedom, the consideration of the entire cavity chain increases the complexity of field patterns. The radio-frequency bands of the chains are more densely populated with resonances when compared to single cavities.
5. The straightforward computation of radio-frequency properties of the complete chain requires parallel solvers running on supercomputers. However, supercomputers are expensive to buy, to maintain, and to operate. Moreover, the straightforward formulation of the problem can lead to ill-conditioned system matrices.
6. Alternatively to straightforward computations, the cavity chain can be decomposed into individual segments. State-space models can be generated to describe the radio-frequency properties of the arising segments in a rigorous sense.

7. The model order of the state-space models can be drastically reduced using dedicated model order reduction techniques so that compact state-space models of the respective segments emerge.
8. These compact state-space models can be concatenated by algebraic formulated continuity constraints of electric and magnetic fields on the decomposition planes.
9. The concatenation delivers a state-space model which is further reduced so that a compact state-space model of the full structure arises. This model allows for the computation of relevant radio-frequency properties of the full structure such as frequency-domain transfer functions, field distributions, resonant frequencies, and quality factors.
10. The described technique allows for determining radio-frequency properties of superconducting cavity chains on standard workstations. In other words, the application of expensive supercomputers can be avoided.
11. In contrast to other segmentation techniques, the segments are described by reduced order models. The state-space models enable the construction of field distributions inside the segments and are free of redundant information.

Contents

List of Acronyms	v
List of Symbols	vii
1 Introduction and Objectives	1
1.1 Structure and Novel Scientific Contributions of the Thesis	3
1.2 Particle Accelerators and Superconducting RF Structures	4
1.3 Problem Statement	7
1.4 State of the Art Approaches to Solutions	9
1.5 State-Space Concatenations Compared to Existing Methods	12
2 Foundations of Electromagnetic Field Theory	15
2.1 Maxwell's Equations	15
2.1.1 Charge Conservation	17
2.1.2 Energy Conservation or Poynting's Theorem	18
2.1.3 Wave Equations	19
2.2 Discrete Formulation of Maxwell's Equations	20
2.3 Electromagnetic Fields in Longitudinally Uniform Waveguides	24
2.3.1 Generation of Transverse Modal Field Patterns	26
2.3.2 Frequency-Domain Solutions of Klein-Gordon Equation	28
2.3.3 Wave and Line Impedances	29
2.3.4 Normalized Wave Amplitudes	31
2.4 Electromagnetic Fields in Closed Structures	32
2.4.1 Energy Dissipation and Quality Factors	34
2.4.2 Normalized Longitudinal Voltage and Shunt Impedance	35
3 System Theory and Model Order Reduction	37
3.1 Waveguide Ports	37
3.2 State-Space Systems of RF Structures	41
3.2.1 State Matrices Arising from Continuous Case	44
3.2.2 State Matrices Arising from Discrete Case	49
3.3 Important Properties of State-Space Systems	51
3.3.1 Lumped and Distributed Systems	52
3.3.2 Causality of Systems	52
3.3.3 Stability of Systems	52

3.3.4	Frequency-Domain Transfer Functions	55
3.4	Model Order Reduction of State-Space Systems	58
3.4.1	Model Order Reduction by Projection	59
4	Compact State-Space Models for Complex Structures	61
4.1	Decomposition of RF Structure and Description of Segments	61
4.2	Generation of Compact Models	66
4.3	Concatenation of Segments	68
4.4	Model Order Reduction for the Linked State-Space Model	73
4.5	Further Representations of the Compact State-Space System	73
4.5.1	Transfer into First-Order Impedance Formulation	73
4.5.2	Transfer into First-Order Scattering Formulation	74
4.6	Computation of Relevant RF Quantities	75
4.6.1	Field Distributions in 3D by Means of State Vectors	76
4.6.2	Frequency-Domain and Time-Domain Excitations	77
4.6.3	Impedance and Scattering Parameters	78
4.6.4	Eigenmodes	78
4.6.5	Accounting for Losses and Computation of Quality Factors	80
5	Application Examples	87
5.1	Rectangular Waveguide	87
5.1.1	Generation of State-Space Systems for Segments	88
5.1.2	Concatenation of Waveguide Segments	91
5.1.3	Validation	92
5.2	Excitation of the Waveguide by Means of Coupling Probes	95
5.2.1	Generation of Compact State-Space Model by Means of SSC	96
5.2.2	Validation	97
5.3	Waveguide Power Splitter	99
5.3.1	Generation of State-Space Model by Means of SSC	99
5.3.2	Validation	100
5.4	Rotationally Symmetric Chains of Third-Harmonic Cavities	102
5.4.1	Generation of State-Space Models for Chains	103
5.4.2	Validation Using Chain with Two Nine-Cell Resonators	105
5.4.3	Longitudinal Voltages Depending on Number of Cavities	107
5.5	Third-Harmonic TESLA Cavities with HOM and Power Couplers	108
5.5.1	Generation of Compact State-Space Models	110
5.5.2	Validation	111
5.5.3	RF Properties of the Cavity Strings with Couplers	114
6	Discussion, Summary, and Outlook	119

A	Commonly Used Waveguides Modes or Port Modes	123
A.1	Modal Field Patterns in Rectangular Waveguides	123
A.2	Modal Field Patterns in Circular Waveguides	124
A.3	Modal Field Pattern in Coaxial Waveguides	127
B	Analytical Derivations Related to Rectangular Waveguides	129
B.1	Frequency-Domain Field Distributions	129
B.2	Impedance Parameters of Rectangular Waveguide	131
B.3	Eigenmodes in a Rectangular Waveguide	131
B.4	State-Space System for Rectangular Waveguide	133
C	Miscellaneous	135
C.1	Accuracy and Convergence of Eigenmode Expansions	135
C.1.1	Order of Approximation of Electric Fields	135
C.1.2	A Practical Convergence Consideration of Electric Fields . . .	137
C.1.3	Impedance Parameters based on Eigenmode Expansions . . .	138
C.2	Kirchhoff's Circuit Laws Emerging from Continuity Constraints . . .	140
C.3	Symmetric Negative-Semidefinite Matrices	143
C.3.1	Generation of Negative-Semidefinite Matrices	143
C.3.2	Eigenvalues of Symmetric Negative-Semidefinite Matrices . . .	144
D	Mesh Refinement Studies	147
	Bibliography	159

List of Acronyms

ACE3P	Advanced Computational Electromagnetic 3D Parallel
BEM	boundary element method
BIBO	bounded-input bounded-output
CAE	computer aided engineering
CSC	Coupled S-Parameter Calculation
CST MWS	CST MICROWAVE STUDIO®
DESY	Deutsches Elektronen Synchrotron
EuCARD	European Coordination for Accelerator Research and Development
FEL	free-electron laser
FEM	finite element methods
FLASH	Free-Electron Laser Hamburg
HOM	higher order modes
HOMC	higher order mode couplers
LEP	Large Electron-Positron Collider
LHC	Large Hadron Collider
LOM	lower order modes
MOR	model order reduction
PBA	perfect boundary approximation
PC	power couplers
PEC	perfect electric conducting
PETSc	Portable, Extensible Toolkit for Scientific Computation
PMC	perfect magnetic conducting
RF	radio-frequency
SSC	State-Space Concatenations
SSM	state-space models
SIBC	surface impedance boundary condition
SPICE	Simulation Program with Integrated Circuit Emphasis
TESLA	TeV-Energy Superconducting Linear Accelerator
TE	transverse electric
TEM	transverse electric and magnetic
TM	transverse magnetic

List of Symbols

Symbol	Unit	Description
a	m	width of rectangular waveguide
$\underline{\mathbf{a}}$	\sqrt{VA}	complex vector with ampl. of incident waves
$\underline{\mathbf{a}}_{\text{ext}}$	\sqrt{VA}	complex vector with ampl. of external incident waves
$\underline{a}_m(z)$	\sqrt{VA}	complex ampl. (pos. direction) of m th mode
$\underline{a}_{p,m}$	\sqrt{VA}	complex ampl. (pos. direction) of m th mode at p th port
A^{TE}	1	scaling constant for TE waveguide modes
A^{TEM}	1	scaling constant for TEM waveguide modes
A^{TM}	1	scaling constant for TM waveguide modes
\mathbf{A}_f	1/s	first-order state matrix
\mathbf{A}_{fc}	1/s	first-order state matrix (cont. case)
\mathbf{A}_{fd}	1/s	first-order state matrix (discrete case)
\mathbf{A}_{flr}	1/s	reduced first-order state matrix of linked system
\mathbf{A}_s	1/s ²	second-order state matrix
\mathbf{A}_{sb}	1/s ²	second-order block state matrix
\mathbf{A}_{sc}	1/s ²	second-order state matrix (cont. case)
\mathbf{A}_{sd}	1/s ²	second-order state matrix (discrete case)
$\mathbf{A}_{s,r}$	1/s ²	second-order state matrix of r th segment
\mathbf{A}_{sr}	1/s ²	reduced second-order state matrix
$\mathbf{A}_{sr,r}$	1/s ²	reduced second-order state matrix of r th segment
\mathbf{A}_{sl}	1/s ²	second-order state matrix of linked system
\mathbf{A}_{slr}	1/s ²	reduced second-order state matrix of linked system
b	m	height of rectangular waveguide
$\underline{\mathbf{b}}$	\sqrt{VA}	complex vector with ampl. of scattered waves
$\underline{\mathbf{b}}_{\text{ext}}$	\sqrt{VA}	complex vector with ampl. of external scattered waves
$\underline{b}_m(z)$	\sqrt{VA}	complex ampl. (neg. direction) of m th mode
$\underline{b}_{p,m}$	\sqrt{VA}	complex ampl. (neg. direction) of m th mode at p th port
$\mathbf{B}(\mathbf{r}, t)$	Vs/m ²	magnetic flux density
$\mathbf{b}_{sc,n}$	\sqrt{V}/\sqrt{As}	n th row of the matrix \mathbf{B}_{sc}
$\mathbf{b}_{slr,n}$	\sqrt{V}/\sqrt{As}	n th row of the matrix \mathbf{B}_{slr}

Symbol	Unit	Description
$\widehat{\mathbf{b}}$	Vs	vector holding magnetic grid fluxes
\mathbf{b}	Vs/m ²	vector holding magnetic flux densities
\mathbf{B}_f	\sqrt{V}/\sqrt{As}	first-order input matrix
\mathbf{B}_{fc}	\sqrt{V}/\sqrt{As}	first-order input matrix (cont. case)
\mathbf{B}_{fd}	\sqrt{V}/\sqrt{As}	first-order input matrix (discrete case)
\mathbf{B}_{flr}	\sqrt{V}/\sqrt{As}	reduced first-order input matrix of linked system
\mathbf{B}_s	\sqrt{V}/\sqrt{As}	second-order input matrix
\mathbf{B}_{sb}	\sqrt{V}/\sqrt{As}	second-order block input matrix
$\bar{\mathbf{B}}_{sb}$	\sqrt{V}/\sqrt{As}	permuted second-order block input matrix
\mathbf{B}_{sc}	\sqrt{V}/\sqrt{As}	second-order input matrix (cont. case)
\mathbf{B}_{sd}	\sqrt{V}/\sqrt{As}	second-order input matrix (discrete case)
$\mathbf{B}_{s,r}$	\sqrt{V}/\sqrt{As}	second-order input matrix of r th segment
\mathbf{B}_{sr}	\sqrt{V}/\sqrt{As}	reduced second-order input matrix
$\mathbf{B}_{sr,r}$	\sqrt{V}/\sqrt{As}	reduced second-order input matrix of r th segment
\mathbf{B}_{sl}	\sqrt{V}/\sqrt{As}	second-order input matrix of linked system
\mathbf{B}_{slr}	\sqrt{V}/\sqrt{As}	reduced second-order input matrix of linked system
C_n	As/V	model capacity of n th eigenmode
c	m/s	speed of light
\mathbf{C}_f	\sqrt{V}/\sqrt{As}	first-order output matrix
\mathbf{C}_{fc}	\sqrt{V}/\sqrt{As}	first-order output matrix (cont. case)
\mathbf{C}_{fd}	\sqrt{V}/\sqrt{As}	first-order output matrix (discrete case)
\mathbf{C}_s	\sqrt{V}/\sqrt{As}	second-order output matrix
\mathbf{C}_{sc}	\sqrt{V}/\sqrt{As}	second-order output matrix (cont. case)
\mathbf{C}_{sd}	\sqrt{V}/\sqrt{As}	second-order output matrix (discrete case)
\mathcal{C}	1	discrete curl operator for primary grid
$\tilde{\mathcal{C}}$	1	discrete curl operator for dual grid
d	m	length of the cavity
$\mathbf{D}(\mathbf{r}, t)$	As/m ²	electric flux density
$\widehat{\mathbf{d}}$	As	vector holding electric grid fluxes
\mathbf{d}	As/m ²	vector holding electric flux densities
\mathbf{D}_f	V/A	first-order input matrix
\mathbf{D}_s	Vs/A	second-order input matrix
$\underline{\mathbf{D}}_Z(j\omega)$	V/A	complex diagonal matrix with wave impedances
\mathbf{D}_Z	V/A	real diagonal matrix with wave impedances
\mathcal{D}_β	1	diagonal matrix for grid dispersion correction
\mathcal{D}_s	m	diagonal matrix with lengths of primary grid edges
$\tilde{\mathcal{D}}_s$	m	diagonal matrix with lengths of dual grid edges

Symbol	Unit	Description
\mathcal{D}_A	m^2	diagonal matrix with areas of primary grid facets
$\tilde{\mathcal{D}}_A$	m^2	diagonal matrix with areas of dual grid facets
$\tilde{\mathcal{D}}_V$	m^3	diagonal matrix with volumes of dual grid
\mathcal{D}_ε	$\text{As}/(\text{Vm})$	diagonal matrix with mean permittivities
\mathcal{D}_μ	$\text{Vs}/(\text{Am})$	diagonal matrix with mean permeabilities
\mathcal{D}_σ	$\text{A}/(\text{Vm})$	diagonal matrix with mean conductivities
$\mathbf{E}(\mathbf{r}, t)$	V/m	electric field
$\mathbf{E}_r(\mathbf{r}, t)$	V/m	electric field in r th segment
$\tilde{\mathbf{E}}_{r,n}(\mathbf{r})$	V/m	electric field of n th eigenmode in r th segment
$\underline{\mathbf{E}}_{\text{res}}(\mathbf{r})$	V/m	complex residual term of eigenmode expansion
$\mathbf{E}^{\text{TEM}}(\mathbf{r}_t, z, t)$	V/m	electric field of TEM waveguide mode
$\underline{\mathbf{E}}^{\text{TM},+}(\mathbf{r})$	V/m	electric field of TM mode prop. in pos. direction
$\underline{E}_z^{\text{TM},+}(\mathbf{r})$	V/m	long. electric field of TM mode prop. in pos. direction
$\mathbf{E}_m^{\text{wg}}(\mathbf{r}, t)$	V/m	electric field of m th waveguide mode
$E_{z,m}^{\text{wg}}(\mathbf{r}, t)$	V/m	longitudinal electric field of m th waveguide mode
$\tilde{\mathbf{E}}_\ell(\mathbf{r})$	V/m	electric field of ℓ th eigenmode
$\tilde{\mathbf{E}}_n(\mathbf{r})$	V/m	electric field of n th eigenmode
$\mathbf{E}_n(\mathbf{r}, t)$	V/m	transient electric field of n th eigenmode
$\tilde{E}_{n,z}(x, y, z)$	V/m	longitudinal component of E-field of n th eigenmode
$\mathbf{E}_t(\mathbf{r}_t, t)$	V/m	transient transversal electric fields on the port plane
$\mathbf{E}_{t,m}(\mathbf{r}_t, t)$	V/m	transient transversal E-field of m th port mode on plane
$\bar{\mathbf{e}}$	V	vector holding electric grid voltages
\mathbf{e}	V/m	vector holding electric field strengths
$\bar{\mathbf{e}}'$	$\sqrt{\text{VAs}}$	similarity transformed of $\bar{\mathbf{e}}$
$\bar{\mathbf{e}}_r$	V	vector holding electric grid voltages of r th segment
$\bar{\mathbf{e}}'_r$	$\sqrt{\text{VAs}}$	similarity transformed of $\bar{\mathbf{e}}_r$
f	Hz	frequency
$f_{\text{co},m}$	Hz	cutoff frequency of m th waveguide mode
f_{max}	Hz	maximal frequency
f_{min}	Hz	minimal frequency
\tilde{f}_n	Hz	resonant frequency of n th eigenmode
$\tilde{f}_{\text{ref},n}$	Hz	reference resonant frequencies
$\tilde{f}_{\text{CST},n}$	Hz	resonant freq. of n th eigenmode computed with CST
$\tilde{f}_{\text{SSC},n}$	Hz	resonant freq. of n th eigenmode computed with SSC
\mathbf{F}	1	matrix accounting for Kirchhoff's laws
\mathbf{F}_L	kg m/s^2	Lorentz force
$h_{n,p,m}$	$\sqrt{\text{V}}/\sqrt{\text{As}}$	interaction integral

Symbol	Unit	Description
$\mathbf{H}(\mathbf{r}, t)$	A/m	magnetic field strength
$\mathbf{H}^{\text{TEM}}(\mathbf{r}_t, z, t)$	A/m	magnetic field of TEM waveguide mode
$\underline{\mathbf{H}}^{\text{TE},+}(\mathbf{r})$	A/m	magnetic field of TE mode prop. in pos. direction
$\underline{H}_z^{\text{TE},+}(\mathbf{r})$	A/m	long. magnetic field of TE mode prop. in pos. direction
$\mathbf{H}_m^{\text{wg}}(\mathbf{r}, t)$	A/m	magnetic field of m th waveguide mode
$H_{z,m}^{\text{wg}}(\mathbf{r}, t)$	A/m	longitudinal magnetic field of m th waveguide mode
$\tilde{\mathbf{H}}_\ell(\mathbf{r})$	A/m	magnetic field of ℓ th eigenmode
$\tilde{\mathbf{H}}_n(\mathbf{r})$	A/m	magnetic field of n th eigenmode
$\mathbf{H}_n(\mathbf{r}, t)$	A/m	transient magnetic field of n th eigenmode
$\mathbf{H}_t(\mathbf{r}_t, t)$	A/m	transient transversal magnetic fields on the port plane
$\mathbf{H}_{t,m}(\mathbf{r}_t, t)$	A/m	transient transversal H-field of m th port mode on plane
$\hat{\mathbf{h}}$	A	vector holding magnetic grid currents
\mathbf{h}	A/m	vector holding sampled magnetic field strengths
$\hat{\mathbf{h}}'$	$\sqrt{\text{VAs}}$	similarity transformed of $\hat{\mathbf{h}}$
$i_m(z, t)$	A	modal current of m th waveguide mode
$i_m(t)$	A	modal current of m th mode
$i_{p,m}(t)$	A	modal current of m th mode at p th port
$i_{r,p,m}(t)$	A	modal current of m th mode at p th port at r th segment
$\underline{I}_{p,m}$	A	complex modal current of m th mode at p th port
$\underline{I}_m(z)$	A	complex modal current of m th waveguide mode
$\underline{I}_m^+(z)$	A	complex currents of waves prop. in pos. direct.
$\underline{I}_m^-(z)$	A	complex currents of waves prop. in neg. direct.
$\underline{I}^{\text{TE},+}(z)$	A	long. depend. of current of TE wave prop. in pos. direct.
$\underline{I}^{\text{TM},+}$	A	current of TM wave prop. in pos. direction
$\underline{I}^{\text{TM},+}(z)$	A	long. depend. of current of TM wave prop. in pos. direct.
$\underline{I}^{\text{TEM},+}(z)$	A	long. depend. of curr. of TEM wave prop. in pos. direct.
I_p	1	number of grid nodes in x -direction
$\mathbf{i}(t)$	A	vector holding modal currents
$\underline{\mathbf{i}}$	A	complex vector holding currents
$\mathbf{i}_r(t)$	A	vector with modal currents of r th segment
$\mathbf{i}_{r,p}(t)$	A	vector with modal currents of p th port of r th segment
$\mathbf{i}_{\text{can}}(t)$	A	vector with currents in canonical order
$\mathbf{i}_{\text{sort}}(t)$	A	vector with currents in sorted order
$\mathbf{i}_{\text{int}}(t)$	A	vector holding internal currents
$\mathbf{i}_{\text{ext}}(t)$	A	vector holding external currents
$\hat{\mathbf{i}}_{\text{int}}(t)$	A	vector with linearly independent currents
$\underline{\mathbf{i}}_{\text{ext}}$	A	complex vector holding external currents

Symbol	Unit	Description
\mathbf{I}		identity matrix
$\Im \{ \}$		imaginary part
j	1	complex unit
J_p	1	number of grid nodes in y -direction
$\mathbf{J}(\mathbf{r}, t)$	A/m ²	electric current density
$\mathbf{J}_{ic}(\mathbf{r}, t)$	A/m ²	impressed electric current density
$\mathbf{J}_{cc}(\mathbf{r}, t)$	A/m ²	convection electric current density
$\mathbf{J}_{\sigma}(\mathbf{r}, t)$	A/m ²	Ohmic electric current density
$\mathbf{J}_{prt,m}(\mathbf{r}, t)$	A/m ²	electric current density of m th port mode
$\mathbf{J}_{prt,m}(\mathbf{r})$	1/m ²	current pattern of m th port mode
$\mathbf{J}_{prt,p,m}(\mathbf{r}, t)$	A/m ²	electric current density of m th mode at p th port
$\mathbf{J}_{prt,p,m}(\mathbf{r})$	1/m ²	current pattern of m th mode at p th port
$\hat{\mathbf{j}}$	A	vector holding electric grid currents
$\hat{\mathbf{j}}$	A/m ²	vector holding electric grid current densities
$\hat{\mathbf{j}}_{ic}$	A	vector holding impressed grid currents
$\hat{\mathbf{j}}_{ic}$	A/m ²	vector holding impressed grid current densities
$\hat{\mathbf{j}}_{cc}$	A	vector holding convection grid currents
$\hat{\mathbf{j}}_{cc}$	A/m ²	vector holding convection grid current densities
$\hat{\mathbf{j}}_{\sigma}$	A	vector holding Ohmic grid currents
$\hat{\mathbf{j}}_{\sigma}$	A/m ²	vector holding Ohmic grid current densities
\tilde{k}_n	1/m	wavenumber of n th eigenmode
k_t	1/m	separation constant of waveguide mode
k_t^{TE}	1/m	separation constant of TE waveguide modes
k_t^{TM}	1/m	separation constant of TM waveguide modes
$k_{t,m}$	1/m	separation constant of m th waveguide mode
K_p	1	number of grid nodes in z -direction
\mathbf{K}	1	concatenation operator
ℓ	1	index
L	m	length
L_r	m	length of r th waveguide segment
L_{tot}	m	total length waveguide
L_n	Vs/A	model inductance of n th mode
$\mathbf{L}_{t,m}(\mathbf{r}_t)$	1/m	transverse field of m th port mode
$\mathbf{L}_{t,p,m}(\mathbf{r}_t)$	1/m	transverse field of of m th mode at p th port
$\mathbf{L}_{t,m}^{wg}(\mathbf{r}_t)$	1/m	transverse field of m th waveguide mode
$\mathbf{L}_t^{TE}(\mathbf{r}_t)$	1/m	transverse field of TE waveguide modes
$\mathbf{L}_t^{TE10}(\mathbf{r}_t)$	1/m	transverse field of TE ₁₀ waveguide mode

List of Symbols

Symbol	Unit	Description
$\mathbf{L}_t^{\text{TEM}}(\mathbf{r}_t)$	1/m	transverse field of TEM waveguide modes
$\mathbf{L}_t^{\text{TM}}(\mathbf{r}_t)$	1/m	transverse field of TM waveguide modes
m	1	port mode index
m_x	1	index
m_y	1	index
m_φ	1	index
m_r	1	index
M_p	1	number of port modes at p th port
$M_{r,p}$	1	number of port modes at p th port of r th segment
\mathbf{M}	1	orthogonal matrix
\mathcal{M}_ε	As/V	mapping from grid voltages to fluxes
$\mathcal{M}_{\varepsilon,r}$	As/V	mapping from grid voltages to fluxes for r th segment
\mathcal{M}_σ	A/V	mapping from grid electric voltages to grid currents
\mathcal{M}_μ	Vs/A	mapping from magnetic grid voltages to fluxes
n	1	index
n_p	1	lexicographic index
N_e	1	number of eigenmodes for series expansion
$N_{e,r}$	1	number of eigenmodes for expansion in r th segment
N_{ext}	1	number of external terminals
N_f	1	number of states of first-order system
N_t	1	number of terminals
N_p	1	total number of primary grid nodes
N_s	1	number of states of second-order system
N_{sr}	1	number of states of reduced second-order model
N_{int}	1	number of internal terminals
\mathbf{n}	1	unit vector
$\mathcal{O}()$		asymptotic notation
p	1	port index
P	1	total number of ports
P_r	1	total number of ports of r th segment
$p_{\text{int}}(\mathbf{r}, t)$	VA/m ³	internal energy loss per volume element
$P(t)$	VA	instantaneous power
$P_{\text{int}}(t)$	VA	intrinsic loss of energy
$P_{\text{int},n}(t)$	VA	intrinsic loss of energy of n th mode
$P_{\text{ext}}(t)$	VA	external loss of energy
$P_{\text{ext},n}(t)$	VA	external loss of energy of n th mode
$P_{\text{tot}}(t)$	VA	total loss of energy

Symbol	Unit	Description
$P_{\text{tot},n}(t)$	VA	total loss of energy of n th mode
\mathbf{P}	1	permutation matrix
q	As	electric charge
$Q_{\text{tot},n}$	1	quality factor of n th mode
$Q_{\text{ext},n}$	1	external quality factor of n th mode
$Q_{\text{int},n}$	1	intrinsic quality factor of n th mode
\mathbf{Q}_f	1	orthogonal matrix
$\mathbf{Q}_{s,\text{inc}}$	1	orthogonal matrix with inc. set of eigenvectors
\mathbf{Q}_s	1	orthogonal matrix
r	1	index of segments
R	1	total number of segments
R_o	m	outer radius
R_i	m	inner radius
R_n	Ω	model shunt impedance n th eigenmode
R_n/Q_n	Ω	normalized longitudinal voltage of n th eigenmode
\mathbf{r}	m	position vector
\mathbf{r}_t	m	transverse position vector
\mathbf{R}	1	real quadratic matrix
\mathcal{R}	1	FIT matrix storing port modes
$\Re\{\}$		real part
$\underline{s}_{p,m,\eta,\nu}(j\omega)$	1	complex coefficients of scattering matrix
$\underline{s}_{\text{tr},m}(j\omega)$	1	complex trans. coefficient of m th waveguide mode
$\mathbf{S}(\mathbf{r}, t)$	VA/m ²	Poynting vector or energy flow per unit area
$\underline{\mathbf{S}}(j\omega)$	1	complex scattering matrix
\mathcal{S}	1	discrete divergence operator for primary grid
$\tilde{\mathcal{S}}$	1	discrete divergence operator for dual grid
t	s	time
$T_{\text{lsy},n}$	s	basic period of lossy n th mode
T_{rd}	s	computation time required for reduction
$\mathbf{u}_{\text{slr},n}^{\text{PEC}}$	$\sqrt{\text{VAs}}$	n th eigenvector of $\mathbf{\Theta}^T \mathbf{A}_{\text{slr}} \mathbf{\Theta}$
$\mathbf{u}_{\text{slr},n}^{\text{PMC}}$	$\sqrt{\text{VAs}}$	n th eigenvector of \mathbf{A}_{slr}
\mathbf{U}	1	real quadratic matrix
$v_m(z, t)$	V	modal voltage of m th waveguide mode
$v_m(t)$	V	modal voltage of m th mode
$v_{p,m}(t)$	V	modal voltage of m th mode at p th port
$v_{r,p,m}(t)$	V	modal voltage of m th mode at p th port at r th segment
$V_{\text{acc},n}(x, y)$	V	accelerating voltage of n th mode

Symbol	Unit	Description
$\tilde{V}_n(z)$	V	voltage along the waveguide of TE ₁₀ eigenmode
$\underline{V}(z)$	V	complex voltage along the waveguide of TE ₁₀ mode
$\underline{V}_m(z)$	V	complex modal voltage of m th waveguide mode
$\underline{V}_m^+(z)$	V	complex voltages of waves prop. in pos. direct.
$\underline{V}_m^-(z)$	V	complex voltages of waves prop. in neg. direct.
$\underline{V}_{p,m}$	V	complex modal voltage of m th mode at p th port
$\underline{V}^{\text{TE},+}$	V	voltage of TE wave prop. in pos. direct.
$\underline{V}^{\text{TE},+}(z)$	V	long. depend. of volt. of TE wave prop. in pos. direct.
$\underline{V}^{\text{TEM},+}(z)$	V	long. depend. of volt. of TEM wave prop. in pos. direct.
$\mathbf{v}(t)$	V	vector holding modal voltages
$\underline{\mathbf{v}}$	V	complex vector holding modal voltages
$\mathbf{v}_r(t)$	V	vector with modal voltages of r th segment
$\mathbf{v}_{r,p}(t)$	V	vector with modal voltages of p th port at r th segment
$\mathbf{v}_{\text{can}}(t)$	V	vector with voltages in canonical order
$\mathbf{v}_{\text{sort}}(t)$	V	vector with voltages in sorted order
$\mathbf{v}_{\text{int}}(t)$	V	vector holding internal voltages
$\mathbf{v}_{\text{ext}}(t)$	V	vector holding external voltages
$\underline{\mathbf{v}}_{\text{ext}}$	V	complex vector holding external voltages
\mathbf{V}_{slr}	1	reduction matrix of concatenated system
\mathbf{V}_{sr}	1	reduction matrix
$\mathbf{V}_{\text{sr},r}$	1	reduction matrix of the r th segment
$w_e(\mathbf{r}, t)$	VAs/m ³	energy per volume element stored in electric fields
$w_m(\mathbf{r}, t)$	VAs/m ³	energy per volume element stored in magnetic fields
$W_e(t)$	VAs	time-dependent energy stored in electric fields
$W_m(t)$	VAs	time-dependent energy stored in magnetic fields
W_ℓ	VAs	energy stored in ℓ th eigenmode
W_n	VAs	energy stored in n th eigenmode
$W_{r,n}$	VAs	energy stored in n th eigenmode of r th segment
$W_{\text{sto},n}(t)$	VAs	time-dependent energy in the n th mode
\mathbf{W}_{sr}	1	reduction matrix
$x_n(t)$	$\sqrt{\text{VAs}}$	transient weighting factors for electric field
$x_{r,n}(t)$	$\sqrt{\text{VAs}}$	transient weighting factors for electric field in r th segment
$x_{\text{slr},n}(t)$	$\sqrt{\text{VAs}}$	n th coefficient of vector $\mathbf{x}_{\text{slr}}(t)$
$\mathbf{x}_f(t)$	$\sqrt{\text{VAs}}$	first-order state vector
$\mathbf{x}_{\text{fc}}(t)$	$\sqrt{\text{VAs}}$	first-order state vector (cont. case)
$\mathbf{x}_{\text{fd}}(t)$	$\sqrt{\text{VAs}}$	first-order state vector (discrete case)
$\mathbf{x}_{\text{flr}}(t)$	$\sqrt{\text{VAs}}$	reduced first-order state vector of linked system

Symbol	Unit	Description
$\mathbf{x}_s(t)$	$\sqrt{\text{VAs}}$	second-order state vector
$\underline{\mathbf{x}}_s$	$\sqrt{\text{VAs}}$	complex second-order state vector
$\mathbf{x}_{sb}(t)$	$\sqrt{\text{VAs}}$	second-order block state vector
$\mathbf{x}_{sc}(t)$	$\sqrt{\text{VAs}}$	second-order state vector (cont. case)
$\mathbf{x}_{sc,r}(t)$	$\sqrt{\text{VAs}}$	second-order state vector (cont. case) of r th segment
$\mathbf{x}_{sd}(t)$	$\sqrt{\text{VAs}}$	second-order state vector (discrete case)
$\mathbf{x}_{sd,r}(t)$	$\sqrt{\text{VAs}}$	second-order state vector (discrete case) of r th segment
$\mathbf{x}_{s,r}(t)$	$\sqrt{\text{VAs}}$	second-order state vector of r th segment
$\mathbf{x}_{sr}(t)$	$\sqrt{\text{VAs}}$	reduced second-order state vector
$\mathbf{x}_{sr,r}(t)$	$\sqrt{\text{VAs}}$	reduced second-order state vector of r th segment
$\mathbf{x}_{sl}(t)$	$\sqrt{\text{VAs}}$	second-order state vector of linked system
$\mathbf{x}_{slr}(t)$	$\sqrt{\text{VAs}}$	reduced second-order state vector of linked system
$\mathbf{X}_{s,\text{sp}}$	1	snapshot matrix with field information
$\mathbf{y}_f(t)$	$\sqrt{\text{VAs}}$	transformed first-order state vector
$\mathbf{y}_s(t)$	$\sqrt{\text{VAs}}$	transformed second-order state vector
z_{const}	m	length of constant cross section
$\underline{z}_{p,m,\eta,\nu}(j\omega)$	V/A	complex coefficients of impedance matrix
$\underline{Z}_{p,m}(j\omega_{\text{lsy}})$	V/A	complex termination of m th mode at p th port
Z_{fs}	V/A	free space impedance
$\underline{Z}_m(j\omega)$	V/A	normalization impedance for m th waveguide port
$\underline{Z}_w^{\text{TE}}(j\omega)$	V/A	wave impedance of TE modes
$\underline{Z}_w^{\text{TM}}(j\omega)$	V/A	wave impedance of TM modes
$Z_w^{\text{TEM}}(j\omega)$	V/A	wave impedance of TEM modes
$Z_{\text{line}}^{\text{TEM}}$	V/A	line impedance of TEM modes
$\underline{\mathbf{Z}}(j\omega)$	V/A	complex impedance matrix
$\alpha_{\text{lsy},n}$	1/s	real part of angular resonant freq. of n th mode
β_v	1	scaling constant for modal voltages
β_i	1	scaling constant for modal currents
$\underline{\gamma}_m(j\omega)$	1/m	propagation constant of m th waveguide mode
$\delta(z)$	1/m	Dirac distribution
Δ	1/m ²	Laplace operator
Δ_t	1/m ²	transverse Laplace operator
Δf	Hz	bandwidth
Δx	m	transverse offset in x -direction
Δy	m	transverse offset in y -direction
ε	As/(Vm)	permittivity
ε_0	As/(Vm)	permittivity of free space

Symbol	Unit	Description
ε_r	1	relative permittivity
$\epsilon_{\text{err}}(N_e)$	1	relative error in electric fields
ϵ_{FIT}	1	relative accuracy criterion for mesh refinement studies
ϵ_{rd}	1	accuracy criterion for model order reduction
$\lambda_{\text{slr},n}^{\text{PEC}}$	1/s ²	n th eigenvalue of $\Theta^T \mathbf{A}_{\text{slr}} \Theta$
$\lambda_{\text{slr},n}^{\text{PMC}}$	1/s ²	n th eigenvalue of \mathbf{A}_{slr}
$\underline{\lambda}_n^{\text{sct}}$	1/s	complex eigenvalues of the matrix $(\mathbf{A}_{\text{flr}} - \mathbf{B}_{\text{flr}} \mathbf{D}_Z^{-1} \mathbf{B}_{\text{flr}}^T)$
$\mathbf{\Lambda}_f$	1/s	skew-symmetric block matrix
$\mathbf{\Lambda}_s$	1/s ²	symmetric block matrix
μ	Vs/(Am)	permeability
μ_0	Vs/(Am)	permeability of free space
μ_r	1	relative permeability
$\rho(\mathbf{r}, t)$	As/m ³	electric charge density
$\hat{\hat{\hat{\mathbf{q}}}}$	As	vector holding electrical grid charges
\mathbf{q}	As/m ³	vector holding sampled charge densities
σ	A/(Vm)	conductivity
Σ	1	diagonal matrix with positive real numbers
ξ	1	index
Π_n	$\sqrt{\text{VAs}}$	constant
φ_0	rad	constant angle
Ψ_n	$\sqrt{\text{VAs}}$	constant
Ψ_n^{TE}	V	constant for TE _{10n} eigenmodes in rect. waveguides
Θ	1	orthogonal matrix
ω	1/s	angular frequency
$\omega_{\text{co},m}$	1/s	angular cutoff frequency of m th waveguide mode
$\omega_{\text{lsy},n}$	1/s	imag. part of angular resonant freq. of n th mode
ω_{max}	1/s	maximal angular frequency
ω_{min}	1/s	minimal angular frequency
$\underline{\omega}_{\text{lsy},n}$	1/s	angular resonant frequency of n th lossy mode
$\underline{\omega}_{\text{lsy}}$	1/s	complex angular frequency
$\tilde{\omega}_n$	1/s	resonant angular freq. of n th eigenmode
$\tilde{\omega}_{\text{slr},n}$	1/s	resonant angular freq. of n th mode in linked system
$\tilde{\omega}_{\text{slr},n}^{\text{PEC}}$	1/s	resonant angular freq. of n th mode in linked system
$\tilde{\omega}_{\text{slr},n}^{\text{PMC}}$	1/s	resonant angular freq. of n th mode in linked system
$\bar{\omega}_n$	1	normalized angular frequency
$\nabla \cdot$	1/m	divergence operator
$\nabla_{\text{t}} \cdot$	1/m	transverse divergence operator

Symbol	Unit	Description
∇	1/m	gradient operator
$\nabla \times$	1/m	curl operator

1 Introduction and Objectives

Broadband modeling of linear and time-invariant waveguide devices with ports, further referred to as radio-frequency (RF) structures, is a demanding task in computational electrical engineering. The modeling of very large and complex structures, such as chains of superconducting cavities with couplers, typically requires supercomputers. This thesis proposes a new approach which allows for the generation of compact wideband models of complex, linear, passive, and time-invariant RF structures without the usage of supercomputers. To create these models, the complex structure is decomposed into several individual segments. In a subsequent step, the segments are described by state-space models (SSM). These state-space models include a huge number of degrees of freedom and arise from analytical considerations for segments of simple geometry or from discretization approaches for segments of more sophisticated shape. The state-space models of the individual segments are reduced by a suitable model order reduction (MOR) technique and are combined to a state-space model of the full structure. Finally, this relatively small system is further reduced by means of MOR. The resulting compact state-space model is a time-domain formulation which describes the RF quantities of the full structure in a finite frequency interval. It allows for the fast computation of 3D field distributions in time and in frequency domain. In addition, resonant frequencies, resonant field distributions, and secondary quantities such as transfer functions or external quality factors are readily available. The workflow of the new scheme, which is referred to as State-Space Concatenations (SSC), is visualized in Figure 1.1 on page 2 in form of a block diagram. The SSC scheme is generally applicable to model waveguide structures, occurring for example in radar applications, satellites or microwave radio links. However, as the development of the approach is mainly motivated by the modeling of superconducting RF structures in the context of particle accelerator applications, the treatment of losses due to finite surface conductivities is not a focus of this work. Nonetheless, already lossless models of RF structures with finite surface conductivities enable a sophisticated comprehension of the emerging electromagnetic effects, in particular during the phase of design and development. The objectives of this thesis are the derivation of the scheme sketched in Figure 1.1 and the presentation of validation and application examples. The application examples aim at showing that the scheme delivers reasonable results and that it can significantly reduce computational demands for determining RF properties of very large and complex structures.

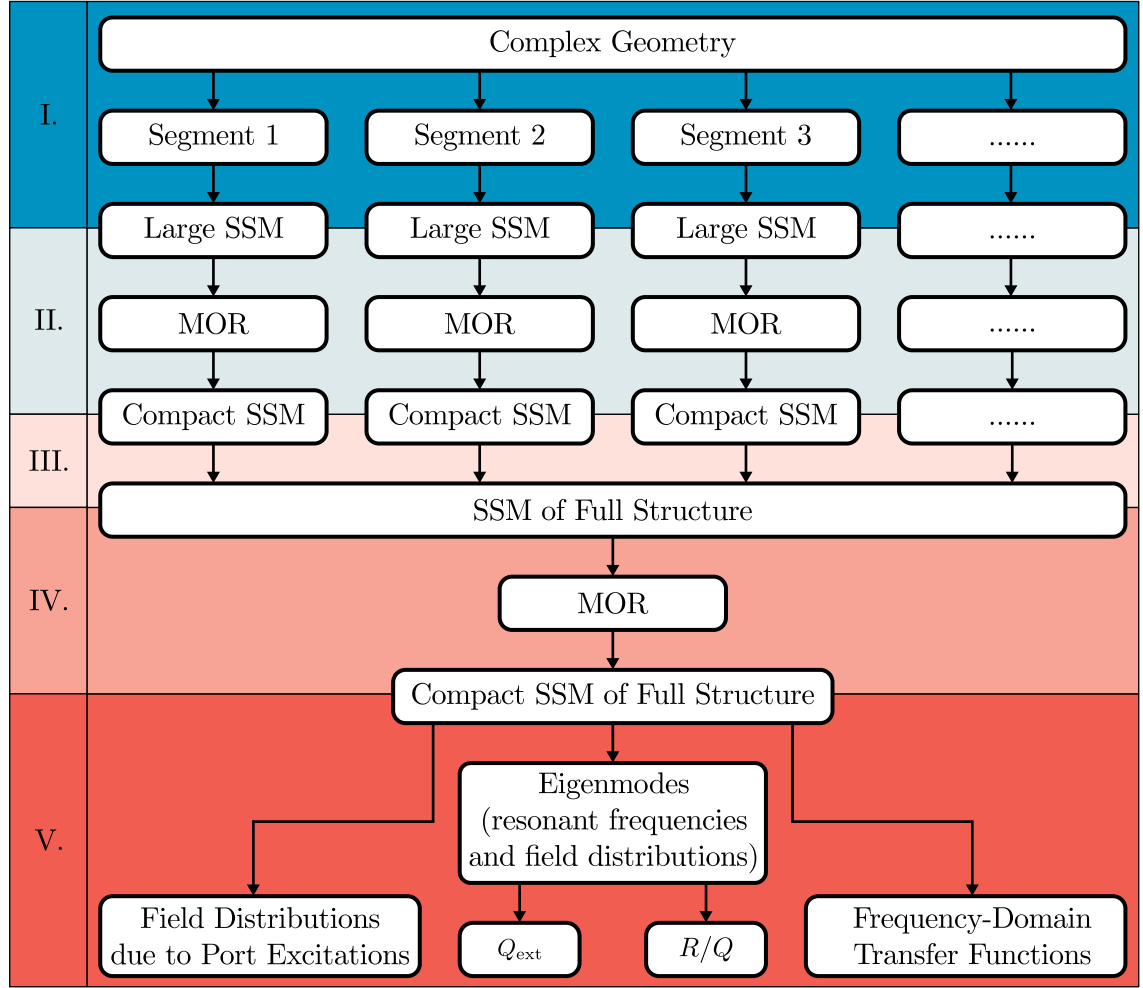


Figure 1.1: Block diagram of the workflow of the entire SSC approach. In Step I the complex RF structure is decomposed into segments and large state-space models (SSM) describing the RF properties of the segments which have been generated by means of analytical or numerical techniques. The size of these models is reduced in Step II by model order reduction (MOR) to obtain compact models for the respective segments. The compact models are combined in Step III using the State-Space Concatenation (SSC) formalism. The arising state-space model of the full structure is again reduced in Step IV so that a compact state-space model of the full structure is delivered. Step V indicates that the compact state-space model rigorously describes the RF properties of the full structure in a finite frequency range. It allows for the convenient computation of field distributions due to frequency- or time-domain excitations, of transfer functions such as scattering or impedance parameters, of resonant frequencies and resonant field patterns of eigenmodes, and of quantities deduced from eigenmodes.

1.1 Structure and Novel Scientific Contributions of the Thesis

This thesis is organized as follows: The following section of the introduction covers fundamental facts related to superconducting RF structures in the framework of particle accelerators. The detailedness of the section is required so that the problem statement, which is basically the main motivation for the development of the SSC scheme, is understandable. Subsequently, Section 1.3 describes the problem statement and Section 1.4 presents state of the art solution approaches. Particularly, an overview of existing segmentation approaches is provided. Furthermore, the individual advantages and disadvantages of the introduced segmentation techniques are discussed and the benefits of the SSC scheme are highlighted. Chapter 2 summarizes relevant textbook knowledge about electromagnetic fields so that a consistent nomenclature for further considerations is provided. Chapter 3 is focused on system theory in the context of RF structures. After the treatment of waveguide ports, two different approaches for the generation of state-space models are discussed. One approach describes the creation of state-space models based on analytical techniques whereas the other is based on a discrete formulation of the governing partial differential equations. In addition, Chapter 3 discusses properties, such as stability or frequency-domain transfer functions, of the generated state-space models and presents fundamental facts related to model order reduction techniques. Chapter 4 is dedicated to the generation of state-space models for complex structures by means of the segmentation approach. The decomposition of the structure into segments as well as the stability conserving model order reduction and concatenation of the state-space models is discussed. Moreover, the determination of 3D field distributions due to port excitations in frequency and time domain, frequency-domain transfer functions, and eigenmodes of the full structure is described. The treatment of energy losses via waveguide ports, which is the dominant loss mechanism at superconducting cavities [1], is discussed as well. Chapter 5 presents several application examples of SSC and Chapter 6 concludes the present thesis.

To the authors' best knowledge, this thesis contains two new scientific contributions. These contributions were previously published in [2] in preparation of this thesis.

- The concatenation of reduced-order state-space models of segments of complex RF structures by means of 2D port modes so that a reduced-order state-space model of the RF structure is generated. This model describes the RF properties of the complex structure in a rigorous manner.
- The formal derivation of state-space models for (segments of) RF structures of unspecified shape with an arbitrary number of waveguide ports and 2D port modes using analytical techniques. Despite the fact that [3] describes a related

approach, it does not explicitly derive state-space equations and the (time-domain) excitation of RF structures by an arbitrary number of waveguide ports with an arbitrary number of port modes is not considered. Another formulation which is very similar to the one introduced in Subsection 3.2.1 is available in [4]. The derivations presented therein result in a state-space model for the structure under concern as well. However, the excitation of electromagnetic fields in the structure is due to a bunch of charged particles. The excitation of fields by means of waveguide ports is also not discussed in [4].

1.2 Particle Accelerators and Superconducting RF Structures

Devices to accelerate charged particles by means of electromagnetic fields are widely employed nowadays. They are, for instance, used in the semiconductor industry for manufacturing transistors, integrated circuits, and photovoltaic materials. Furthermore, accelerators are being used for medical treatment such as proton and ion beam therapy to cure cancer. Apart from industrial and medical applications, particle accelerators play a vital role in fundamental research. This field has advanced the development of accelerators in a significant manner. In experiments, bunches of charged particles are accelerated to high energies and brought to collision in so-called interaction points. The subatomic particles arising from the collision provide information on the inner structure of matter. For instance, the Tevatron [5], the Large Electron-Positron Collider (LEP) [6] or the Large Hadron Collider (LHC) [7] enabled the discovery of several subatomic particles which were predicted by theoretical particle physics. Apart from colliders, accelerators are used as synchrotron light sources, for instance BESSY II or PETRA III [8], to perform experiments related to material sciences or biology, for instance. The latest generation of light sources are free-electron lasers (FELs) such as the Free-Electron Laser Hamburg (FLASH) [9] or the European X-Ray Free-Electron Laser (European XFEL) [10] at the Deutsches Elektronen Synchrotron (DESY) in Hamburg. FELs allow for the observation of physical, chemical and biochemical processes at atomic resolutions in the femtosecond regime.

For particle acceleration it is desirable to have a large energy gain of the charged particles per length of the accelerating device. Therefore, high accelerating electric fields strengths are required. Choosing static electric fields limits the achievable energy gain due to field emission effects. In consequence, the particle acceleration is mainly accomplished in the mentioned facilities by RF fields resonating in metal cavities. The accelerating field strengths of standing waves in copper cavities, operated in continuous wave mode¹, is limited due to losses on the conducting surface.

¹or operated in a mode with a higher duty factor

The surface losses can be significantly reduced by employing superconducting cavities. These cavities are made of niobium or niobium alloys which are cooled down to 2 K by dedicated cryogenic infrastructure. The microwave surface resistivity of superconducting niobium is approximately 10 n Ω at 2 K [11] which is five orders of magnitude lower than the surface resistivity of copper. The small intrinsic losses lead to large intrinsic quality factors in the order of $10^9 \dots 10^{11}$, which are some of the highest quality factors observed in nature [12]. Quality factors (see Subsection 2.4.1 for a formal definition) are in fact a universal measure for the number of oscillations needed to dissipate the energy stored in a resonant structure. Despite the fact that the required cryogenic infrastructure lowers the overall efficiency of the facility, the usage of superconducting cavities results in a significant reduction of primary electric energy requirements.

Figure 1.2 depicts a third-harmonic TESLA cavity [13, 14, 15, 16] with nine cells as an example for a superconducting cavity. The geometry of this cavity is constructed by means of lines and ellipses. The third-harmonic cavity is a special type of superconducting cavity as it is designed to linearize the longitudinal dependence of the accelerating fields at FLASH or the European XFEL. The linearized longitudinal dependence of the accelerating fields enables an increase of peak current after the bunch compression [17]. The third-harmonic TESLA cavity is equipped with a power coupler (PC) to excite a dedicated electromagnetic resonance which is commonly known as the $\text{TM}_{01}\text{-}\pi$ -mode. The mode is referred to as π -mode due to the phase shift from cell to cell of π . The third-harmonic cavity is designed such that its $\text{TM}_{01}\text{-}\pi$ -mode resonates at 3.9 GHz which is in fact three times the frequency of the $\text{TM}_{01}\text{-}\pi$ -mode of the TESLA cavity [11]. The corresponding field distribution is indicated in Figure 1.2. The $\text{TM}_{01}\text{-}\pi$ -mode is used to accelerate or decelerate the charged particles. In addition to this mode, an infinite number of resonances exists in the cavity (refer to Section 2.4 for a formal description of fields in cavities). These resonances are characterized by their respective resonant frequencies and field distributions. Modes with resonant frequencies below the resonant frequency of the $\text{TM}_{01}\text{-}\pi$ -mode are referred to as lower order modes (LOMs), whereas modes with resonant frequencies above the resonant frequency of the $\text{TM}_{01}\text{-}\pi$ -mode are called higher order modes (HOMs). If bunches of charged particles traverse the structure, they excite electromagnetic fields. These so-called wakefields can be interpreted as a weighted, time-dependent superposition of the cavity modes. LOMs and HOMs, once excited by the bunch of charged particles, decay very slowly due to the small losses of the superconducting structure. Therefore, these modes need to be actively dampend to reduce the unwanted interactions of the modes with following bunches or additional loads of the cryogenic system due to surface losses, for example. To dampen the unwanted modes outside the superconducting cryostat, each cavity is equipped with two so-called HOM couplers. Dedicated notch filters of the HOM couplers prevent their coupling to the $\text{TM}_{01}\text{-}\pi$ -mode. As a consequence of the excitation of unwanted modes by the bunches of charged particles, it is required to define

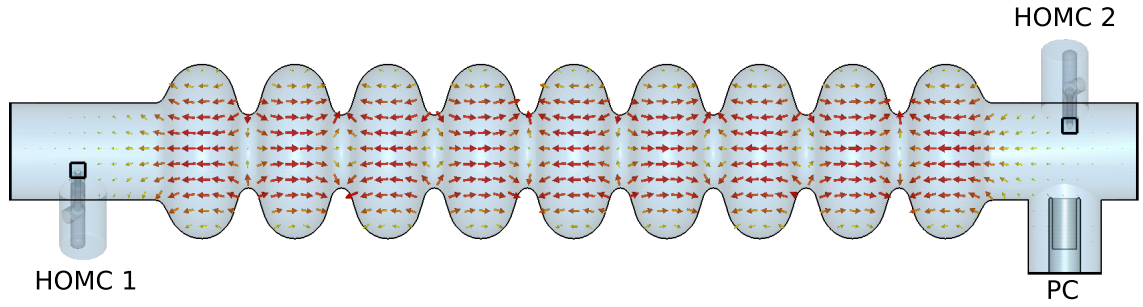


Figure 1.2: Third-harmonic cavity with nine cells. The structure is equipped with two higher order mode couplers (HOMC) and one power coupler (PC). The power coupler is used to excite the $TM_{01}-\pi$ -mode whose field distribution is depicted in the figure. The sketch is generated with CST MICROWAVE STUDIO® [18].

criteria which determine whether a particular mode is problematic for the operation of the accelerator (see Subsection 2.4.1 and Subsection 2.4.2). Therefore, detailed knowledge of the RF properties of the structure, specifically its electromagnetic resonances, is needed.

In addition to their dedicated purpose of HOM damping, HOM couplers can be used in a “parasitical” manner for diagnostics as demonstrated in [19] for the 1.3 GHz TESLA cavity and in [20, 21] for the 3.9 GHz TESLA cavity. The excitation of monopole modes² is marginally dependent on the transversal offset of the bunch, but on its total charge. The excitation of dipole modes³ is approximately linearly dependent on the transversal offset. Both statements require the offset to be sufficiently small. Each resonant mode has its individual resonant frequency and couples in a distinct manner⁴ to the HOM couplers. Therefore, monitoring of HOM port signals allows for the deduction of data on transversal offset and total charge of the bunch. In addition, machine parameters, such as misalignment of the cavities, is available by evaluating the HOM signals. Since the HOM couplers are anyhow attached to most superconducting cavities for damping purposes, no additional RF hardware is needed in the beamline to acquire additional information regarding e.g. transversal offset or total charge of the bunch. The challenge in using HOM coupler signals for diagnostics lies in understanding the excitation of modes by the bunch of charged particles and their coupling to the HOM couplers.

²resonances whose field distribution does not show an azimuthal dependence

³resonances whose field distribution shows a $\sin(\phi)$ dependence, where ϕ is the azimuthal angle

⁴the coupling is determined by the field distribution of the resonance

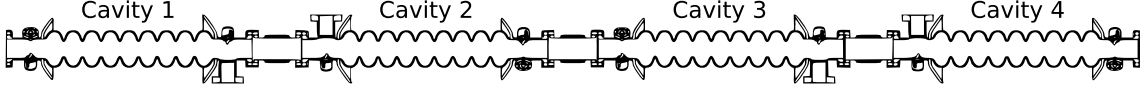


Figure 1.3: Arrangement of four third-harmonic cavities in the cryomodule ACC39, mounted in the FLASH beamline. Each cavity is equipped with two HOM couplers and one power coupler. Bellows are located in-between the cavities. Picture courtesy of Elmar Vogel [24].

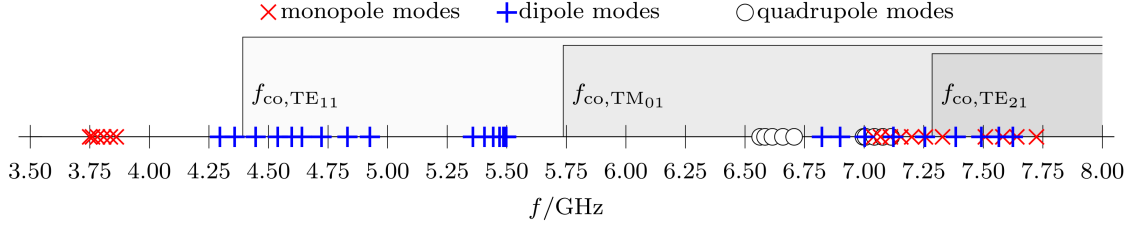


Figure 1.4: Resonant frequencies of individual third-harmonic cavities without couplers and electric boundary conditions enforced at the end of the beam pipes. Monopole modes are depicted as red crosses, dipole modes as blue plusses, and quadrupole modes as black circles. The regions where the TE_{11} , the TM_{01} and the TE_{21} waveguide modes can propagate through the beam pipe are depicted in terms of grey shaded rectangular frames. The depicted cutoff frequencies are listed in Table A.2 and the resonant frequencies are given in [22]. The diagram is taken from [1].

1.3 Problem Statement

Superconducting cavities are accommodated in cryomodules providing the cryogenic infrastructure to cool the cavities to 2 K. Typically, several cavities are housed in a single the cryomodule. For instance, each of the cryomodules at the European XFEL accommodates eight superconducting cavities. At FLASH each of the cryomodules comprising the 1.3 GHz TESLA resonators contains eight cavities as well, whereas FLASH's third-harmonic module ACC39 houses four third-harmonic cavities (see Figure 1.3). Literature provides a large variety of studies determining the RF properties of superconducting cavities by means of numerical modeling and simulation (see [13, 15, 22, 23] and many more). Most of the numerical models solely consider single cavities, whose beam pipe flanges are equipped with perfect electric conducting, perfect magnetic conducting, periodic, or open boundary conditions. Therefore, field distributions, which are not localized in the cavity due to the high-pass characteristic of its beam pipes, are assumed to be reflected at the perfect conducting boundaries or to be dissipated via the open boundaries.

Figure 1.4 depicts the resonant frequencies of the third-harmonic cavity arising from a single cavity model without couplers and perfect electric conducting bound-

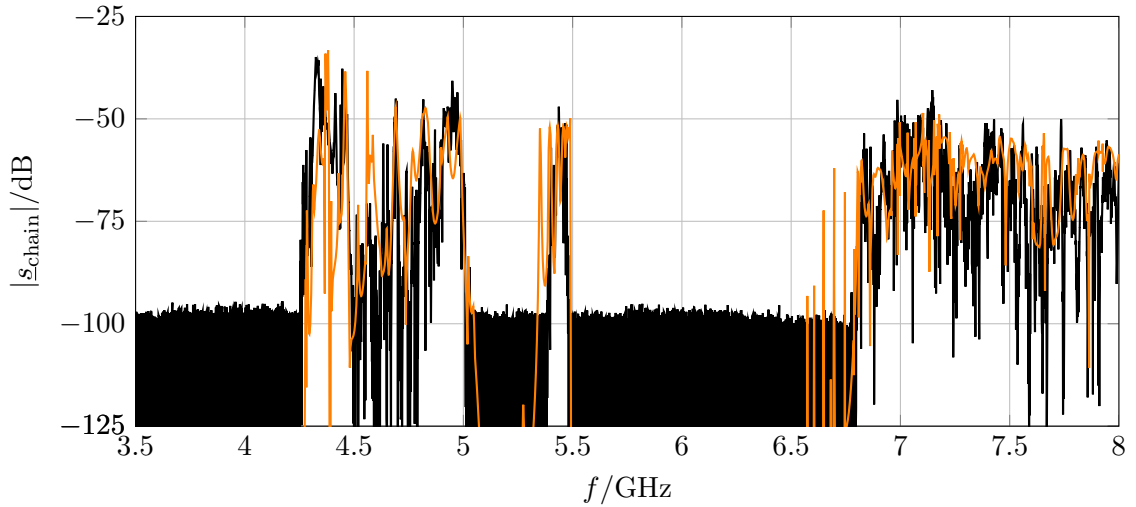


Figure 1.5: Measured (black) and simulated (orange) transmission from left HOM coupler of Cavity 1 to right HOM coupler of Cavity 4 at FLASH’s cryomodule ACC39 (refer to Figure 1.3). In contrast to the simulated data, the measured data shows a noise floor at -100 dB. The plot depicts that transmission via the entire chain takes place. According to Figure 1.4, the first two bands are assumed to belong to resonances with a dipole character whereas the narrow peaks in the interval 6.5 GHz to 6.75 GHz are attributed to quadrupole-like field distributions. The diagram is taken from [1].

any conditions at the end of the beam pipes [22]. In addition, the cutoff frequencies of the first three waveguide modes (refer to Table A.2) are shown. The fundamental monopole band, located in the frequency interval 3.74 GHz to 3.9 GHz is trapped in the nine-cell cavity as the frequencies of the resonant modes are smaller than the fundamental cutoff frequency of the circular waveguide-like beam pipe. In contrast, the resonances starting from the third resonance of the first dipole band (blue plusses) have resonant frequencies larger than the cutoff frequency of the fundamental waveguide mode. Thus, these modes are not required to be confined in the individual cavity. In other words, HOMs may be distributed along the entire cavity chain as they can couple via the beam pipes to the adjacent cavities. The described behavior is also expressed in the measured transmission from the left HOM coupler of Cavity 1 to the right HOM coupler of Cavity 4 as depicted in terms of the black line in Figure 1.5. This transmission measurement has been conducted in the framework of the European Coordination for Accelerator Research and Development (EuCARD) project⁵ at the cryomodule ACC39, mounted in the FLASH beamline at DESY in Hamburg. Amongst others, one aim of the study was the characterization of HOMs in the structure. Figure 1.5 shows that a strong inter-cavity coupling for

⁵Workpackage 10.5 HOM Diagnostics in Superconducting Accelerator Cavities. Work funded by EU FP7 Research Infrastructure Grant No. 227579

frequencies larger than 4.39246 GHz (cutoff frequency of the fundamental mode of the beam pipes) takes place. According to [22], the first two bands in the transmission are attributed to resonances with dipole character whereas the narrow peaks in the interval 6.5 GHz to 6.75 GHz are assumed to have quadrupole character. The fundamental band, which is located in the interval 3.72 GHz to 3.90 GHz, is not visible in the transmission spectrum, as the resonant frequencies are smaller than the cutoff frequency of the fundamental waveguide mode in the beam pipe. Moreover, the notch filters of the HOM couplers prevent their coupling to the $\text{TM}_{01}-\pi$ -mode. A comprehensive description of the measurements is available in [1].

As a consequence of the mutual coupling of the cavities, the consideration of the entire cavity chain is necessary for a reasonable characterization of HOMs. Considering the entire cavity chain, rather than restricting to individual cavities, results in drastically increased computational effort. The cavity chain has a total length of 2.3296 m and comprises tiny elements in the order of mm such as the elliptically shaped cavity cells or the fine parts belonging to the notch filters of the HOM couplers. In addition to this large aspect ratio, the consideration of the entire cavity string raises the complexity of possible field patterns: RF bands of the structure are more densely populated with modes, since resonances in one cavity can couple to appropriate resonances in neighboring cavities of the string (multi-cavity modes).

1.4 State of the Art Approaches to Solutions

Direct approaches⁶ to compute the RF properties of the complex superconducting cavity string require its complete discretization. For instance, the direct hexahedral discretization of the complete four-cavity string including HOM and power couplers in Figure 5.15(b) with CST MICROWAVE STUDIO® (CST MWS) results in approximately $2.6 \cdot 10^7$ degrees of freedom⁷. Numerical problems of this complexity typically demand high performance computers in combination with dedicated software. Amongst others, [25] presents straightforward scattering parameter computations for the four-cavity string depicted in Figure 5.15(b). The computations are performed by the ACE3P (Advanced Computational Electromagnetic 3D Parallel) suite on high performance computing infrastructures with more than 38,640 cores and 77 TBytes memory [26]. Unfortunately, [25] does not discuss computation times. Another example for computations with many degrees of freedom is [27]: The computation of twenty eigenvectors of a generalized eigenvalue problem with $6 \cdot 10^6$ degrees of freedom approximately requires 1.6 h on a cluster computer with 344 Intel Xeon X5650 processors. Despite fact that the problems in [27] do not directly correspond to the aforementioned problem statement, they give an idea about the

⁶often also referred to as brute-force approaches

⁷The RF properties are investigated in the interval 1 GHz to 6 GHz based on a discretization with 15 lines per wavelength.

computing infrastructure and the computational time required to determine the RF properties of the four-cavity string.

In addition to the need of expensive computing infrastructures, the results delivered by brute-force methods can be unsatisfying due to round-off errors or numerical instabilities arising from ill-conditioned system matrices. Therefore, it is advantageous to carry out analytical calculations as far as possible and by this to reduce the numerical complexity of the underlying problem. Moreover, the usage of analytical calculations enhances the understanding of the physical phenomena involved. Diakoptics⁸ or decomposition approaches [23, 28, 29, 30, 31, 32] provide an opportunity to avoid brute-force methods. These approaches are based on splitting the complex structure into segments, followed by the individual treatment of the segments. Subsequently, the properties of the segments are combined to the properties of the full structure by means of suitable concatenation algorithms. The concatenation algorithms enforce the continuity of fields on the decomposition planes via algebraic expressions. In this sense, these methods can be considered as hybrid approaches, because they combine numerical schemes with analytically expressed continuity constraints. The decomposition of the structure is motivated by the following advantages [2, 30]:

- The numerical treatment of the individual sections is less computationally demanding and can be performed in parallel on standard workstation computers.
- Identical segments have to be treated only once.
- In case of segments, whose field distributions are available analytically⁹, the numerical treatment of the segments is not required.
- If complex structures can be decomposed such that the arising segments show rotational symmetry, the respective sections can be treated by a 2D instead of a 3D solver.
- The effect of geometric modifications of a segment on the RF properties of the entire structure can be computed in an efficient manner e.g. for optimization procedures by the determination of the RF properties of the modified segment, followed by a fast concatenation.

The methods proposed in literature mainly differ in the way the segments are described and in the RF quantity of the full structure which is finally delivered by the respective approach. For instance, the finite-difference time-domain diakoptics

⁸greek *dia*-through and *kopto*-cut,tear

⁹Typically this is the case for structures (e.g. circular or rectangular waveguides) whose boundaries are parallel to the axis of appropriate coordinate systems, so that a separation of variables can be performed (see e.g. [33, Section 4.5]).

method [28] describes the dynamical properties of the segments by means of an impulse response matrix holding finite impulse responses which are sampled in time. In combination with a dedicated concatenation approach this enables the computation of transient responses of the full structure. However, the restriction to a finite response and the sampling of this response in time can lead to an improper dynamical description of the segments, in particular for structures with large quality factors. Moreover, the information of field distributions is lost in this formulation and the computational complexity of the required numerical convolution scales quadratically with the number of time samples.

In addition to time-domain segmentation approaches, frequency-domain methods are widely distributed. One of the most prominent representatives is the mode matching technique [34, 35, 36, 37, 38] which provides field distributions and has been applied successfully during the last decades. The mode matching technique is very efficient if the segments of the decomposed structure are of simple geometry so that the electromagnetic field distributions are available analytically. For sophisticated segments such as elliptical cavities, the application of this semi-analytical approach is difficult. Combining the basic idea of modal field matching with numerical scattering parameter (refer to Subsection 3.3.4 for a formal definition) simulations for segments of sophisticated geometry results in the Coupled S-Parameter Calculation (CSC) formalism [23, 29, 30]. CSC or equivalent implementations of the approach in e.g. CST DESIGN STUDIO™ [18, 31] deliver the scattering matrix of a complex structure on discrete frequency samples based on the scattering matrices of its segments, sampled on discrete frequencies in combination with topology information. CSC is neither restricted to waveguide port or mode numbers nor to the topology of the structure under concern. The method is successfully applied to determine the scattering parameters of the entire ACC39 string [1]. Figure 1.5 shows the simulated transmission via the entire cavity string in orange as a part of the results presented in [1]. Unfortunately, CSC does not account for field distributions in the structures directly, as this information is not captured in the scattering matrices of the segments. Nonetheless, fields can be reconstructed with some effort by the complex amplitudes of the incident signals of each segment and additional 3D field computations for each segment as demonstrated in [29, 39].

The computation of scattering matrices of resonant segments such as cavities is a problem in itself as discussed in [1]: The application of time-domain methods fails due to large time constants arising from large quality factors. Alternatively, frequency-domain approaches are based on a formulation in which the system is a priori in a steady state. Frequency-domain evaluations of the scattering matrices comprise the solution of a large, complex, and linear system of equations for each discrete frequency sample. Large quality factors manifest in narrow peaks in the scattering spectra. Therefore, a huge number of scattering matrices and solutions of the complex linear systems of equations have to be computed in order to sample the peaks in an accurate and reasonable manner in the frequency interval of interest.

The problem of computing scattering spectra of resonant structures¹⁰ can be tackled by means of MOR techniques as proposed in examples [40, 41, 42]. Once the model order reduction is performed, the scattering matrices are readily computable on a huge number of discrete frequency samples so that narrow peaks are captured in an adequate way. Nonetheless, the description of the segments by a large number of sampled scattering matrices is inconvenient, as the concatenation with CSC has to be performed frequency sample by frequency sample. In this context it is worth highlighting that network matrices in general or scattering matrices in particular are integral properties arising from a field problem. They can be expressed in terms of a relatively small number of poles and zeros, when restricting to a finite frequency interval [40, 41, 43]. In this sense, the description of the segments by a large collection of sampled scattering matrices leads to redundancy of information.

In [32], the segments are directly described by means of pole expansions of the admittance matrix and the concatenation delivers the admittance matrix of the entire structure in the form of pole expansions. Thus, the method avoids the redundant handling of multi-frequency data by making use of inherent properties of the network (in this case the admittance) matrices. However, [32] does not account for field distributions either and the concatenation of structures with arbitrary topology by the proposed approach is inconvenient and difficult to automate by computer codes.

In contrast to this, [40, 41] propose the employment of a Simulation Program with Integrated Circuit Emphasis (SPICE) for the concatenation, because of its topological flexibility and its availability. Here, the individual segments are described by equivalent circuits with controlled current sources. These circuits arise from reduced-order models of the segments of the complex structure. Similar to [32], the combination of MOR with SPICE circumvents the hard work of dealing with large collections of network matrices, which are computed on discrete frequencies. The method allows for time-domain and frequency-domain considerations, but does not account for field distributions.

1.5 State-Space Concatenations Compared to Existing Methods

The development of the novel SSC scheme is in fact triggered by the application of CSC in combination with MOR to characterize the RF properties of a string of superconducting cavities [1]. Rather than evaluating the transfer functions of the

¹⁰Another approach to solve this problem is to decompose the resonant structures into non-resonating segments and to interpolate the comparatively smooth scattering spectra of the generated segments. Subsequently, the matrices of the segments are combined with CSC to obtain densely sampled spectra of the resonant structure. While the application of this approach can be advantageous for certain geometries, it is not advisable for elliptically shaped cavities due to the number of port modes required at the decomposition planes (see Section 4.1).

segments on frequency samples and combining them frequency sample by frequency sample to the transfer functions of the entire structure, it is more natural and elegant to directly use the state-space models arising from the MOR for the concatenation. The state-space systems inherently account for the nature of electromagnetic fields in the segments in a rigorous sense and describe the RF properties on a wide band with a comparatively small number of degrees of freedom. The SSC scheme unifies the advantages of the previously introduced existing concatenation methods:

- It directly allows for the computation of field distributions of the complex structure on a wide band, based on a comparatively small set of field ansatz functions for the respective segments.
- It is conveniently usable in time and in frequency domain to ensure full flexibility. In addition to frequency-domain characterizations of RF structures, which are standard, the investigation of broadband, transient processes related to waveguide structures is of growing interest [44, 45, 46, 47, 48, 49].
- It avoids the redundant handling of RF quantities, such as frequency-domain transfer functions or time-domain system responses, on discrete samples.
- It conveniently allows for the handling of arbitrary topologies of RF structures.
- It supports an arbitrary number of 2D port modes, which are i.a. used to ensure the continuity of fields on the decomposition planes (refer to Section 4.1 for a description of 2D port modes assigned on the decomposition planes).
- It is suitable for automation.
- It readily delivers integral quantities arising from field distributions based on the compact model of the full structure.

2 Foundations of Electromagnetic Field Theory

This chapter introduces the fundamental partial differential equations which describe the properties of RF structures. In addition, a discrete formulation of the partial differential equations is presented which is required to determine the RF behavior of structures of sophisticated shape. Subsequently, properties of electromagnetic fields in longitudinally uniform waveguides or in closed resonating structures are defined.

2.1 Maxwell's Equations

In the 19th century, James Clerk Maxwell recapitulated and improved important laws on electric and magnetic phenomena [50]. These laws had been previously established by other scientists over several decades based on experimental observations. In the following decades, Oliver Heaviside and Josiah Willard Gibbs independently reformulated the equations into the nowadays commonly known form. These so-called Maxwell's equations are the basis of classical electrodynamics. Their integral representation is given by

$$\oiint_{\partial\Omega} \mathbf{D}(\mathbf{r}, t) \cdot d\mathbf{A} = \iiint_{\Omega} \rho(\mathbf{r}, t) dV, \quad (2.1)$$

$$\oiint_{\partial\Omega} \mathbf{B}(\mathbf{r}, t) \cdot d\mathbf{A} = 0, \quad (2.2)$$

$$\oint_{\partial\Gamma} \mathbf{E}(\mathbf{r}, t) \cdot d\mathbf{s} = - \iint_{\Gamma} \frac{\partial}{\partial t} \mathbf{B}(\mathbf{r}, t) \cdot d\mathbf{A}, \quad (2.3)$$

$$\oint_{\partial\Gamma} \mathbf{H}(\mathbf{r}, t) \cdot d\mathbf{s} = \iint_{\Gamma} \left(\frac{\partial}{\partial t} \mathbf{D}(\mathbf{r}, t) + \mathbf{J}(\mathbf{r}, t) \right) \cdot d\mathbf{A}, \quad (2.4)$$

where $\mathbf{D}(\mathbf{r}, t)$ denotes the *electric flux density*, $\rho(\mathbf{r}, t)$ the *electric charge density*, $\mathbf{B}(\mathbf{r}, t)$ the *magnetic flux density*, $\mathbf{E}(\mathbf{r}, t)$ the *electric field strength*, $\mathbf{H}(\mathbf{r}, t)$ the *magnetic field strength*, and $\mathbf{J}(\mathbf{r}, t)$ the *electric current density*. The spatial dependence of the introduced quantities is expressed by \mathbf{r} , whereas the time dependence is indicated by t . *Gauss' law* (2.1) enforces that the total electric flux through the

closed boundary $\partial\Omega$ of a domain Ω is equal to the total charge contained in the domain. *Gauss' law for magnetism* (2.2) demands the total magnetic flux through the closed boundary $\partial\Omega$ of a domain Ω to be equal to zero. This means that the field lines of the magnetic flux density are closed due to the absence of magnetic charges. *Faraday's law of induction* (2.3) states that the negative time derivative of the total magnetic flux through a surface Γ is equal to the integration of the electric field along the closed boundary $\partial\Gamma$ of the surface. In close analogy, *Ampère's law with Maxwell's extension* (2.4) expresses that the total current through a surface Γ is equal to the integration of the magnetic field along the closed boundary $\partial\Gamma$ of the surface. One strength of Maxwell's equations is their flexibility as they hold for arbitrary surfaces Γ or volumes Ω , e.g. the choice of Γ and Ω is independent on material boundaries.

The total electric current density $\mathbf{J}(\mathbf{r}, t)$ in (2.4) is in fact a superposition of three constituents:

$$\mathbf{J}(\mathbf{r}, t) = \mathbf{J}_{\text{ic}}(\mathbf{r}, t) + \underbrace{\mathbf{v}(\mathbf{r}, t) \rho(\mathbf{r}, t)}_{\mathbf{J}_{\text{cc}}(\mathbf{r}, t)} + \underbrace{\sigma \mathbf{E}(\mathbf{r}, t)}_{\mathbf{J}_{\sigma}(\mathbf{r}, t)}. \quad (2.5)$$

The impressed current density $\mathbf{J}_{\text{ic}}(\mathbf{r}, t)$ does not depend on field strengths in the domain and reflects the influence of external excitations. The convection current density $\mathbf{J}_{\text{cc}}(\mathbf{r}, t)$ embraces effects of moving charges, e.g. in electron tubes, particle accelerators or semiconductor devices. Here, $\mathbf{v}(\mathbf{r}, t)$ is the velocity field corresponding to the charge density $\rho(\mathbf{r}, t)$. The Ohmic current density $\mathbf{J}_{\sigma}(\mathbf{r}, t)$ is proportional to the electric field strength with the proportionality constant, called conductivity σ . The conductivity is a property of matter. In addition, two further characteristics are required to describe the interaction of electric and magnetic fields with matter. The *permittivity* ε relates the electric flux density with the electric field strength:

$$\mathbf{D}(\mathbf{r}, t) = \underbrace{\varepsilon_0 \varepsilon_r}_{\varepsilon} \mathbf{E}(\mathbf{r}, t). \quad (2.6)$$

The permittivity is the product of the vacuum permittivity $\varepsilon_0 = 8.85418782 \cdot 10^{-12} \text{ F/m}$ and a material-dependent relative permittivity ε_r . Analogously, the *permeability* μ relates the magnetic flux density with the magnetic field:

$$\mathbf{B}(\mathbf{r}, t) = \underbrace{\mu_0 \mu_r}_{\mu} \mathbf{H}(\mathbf{r}, t). \quad (2.7)$$

The permeability is the product of the vacuum permeability $\mu_0 = 4\pi \cdot 10^{-7} \text{ H/m}$ and a material-dependent relative permeability μ_r . The introduced material parameters, also referred to as *constitutive parameters*, are in general tensors to account for the anisotropy of matter. In addition, the parameters depend on space and time. In case of nonlinear materials, the parameters also depend on the field strengths themselves. This thesis is restricted to linear, lossless, isotropic, reciprocal, spatial- and time-independent materials, because RF cavities, beam-pipes or waveguide systems are

assumed to be evacuated or filled with air. For the sake of completeness it has to be pointed out, that for example, RF cavities with ferrite materials or beam-pipes with absorbing materials are also in use in accelerator physics [51, 52, 53]. Moreover, nonlinear, anisotropic or nonreciprocal materials are used in RF engineering for mixers, gyrators or circulators [54, 55].

Despite the fact that the introduced equations are conveniently interpretable and describe classical electrodynamics in a rigorous and complete manner, the integral form of Maxwell's equations (2.1) - (2.4) is often not suitable for analytical considerations. Therefore, the integral form is transferred to the differential form of Maxwell's equations

$$\nabla \cdot \mathbf{D}(\mathbf{r}, t) = \rho(\mathbf{r}, t), \quad (2.8)$$

$$\nabla \cdot \mathbf{B}(\mathbf{r}, t) = 0, \quad (2.9)$$

$$\nabla \times \mathbf{E}(\mathbf{r}, t) = -\frac{\partial}{\partial t} \mathbf{B}(\mathbf{r}, t), \quad (2.10)$$

$$\nabla \times \mathbf{H}(\mathbf{r}, t) = \frac{\partial}{\partial t} \mathbf{D}(\mathbf{r}, t) + \mathbf{J}(\mathbf{r}, t) \quad (2.11)$$

by employing the *divergence* theorem [56, p. 879, (I. 33)] and *Stoke's* theorem [56, p. 879, (I. 36)] from vector analysis. The *curl operator* $\nabla \times$ on the left-hand side of (2.10) and (2.11) measures the circulation of the electric and magnetic field in an infinitely small test area. The *divergence operator* $\nabla \cdot$ on the left-hand side of (2.8) and (2.9) measures the total outward electric and magnetic flux from an infinitely small test volume. It is remarked that Maxwell's equations in differential form are restricted to continuous media. In case of discontinuous material continuity constraints are required in addition to (2.8) - (2.11). These constraints can be derived from the integral form of Maxwell's equations (2.1) - (2.4). Note that these continuity constraints are not needed in the scope of this thesis, because constitutive parameters are assumed to be independent on spatial coordinates anyhow.

Particularly in the context of particle accelerators, it is important to note that electric fields and magnetic flux densities can be verified by the Lorentz force \mathbf{F}_L acting on a particle moving with the velocity \mathbf{v} and carrying the charge q :

$$\mathbf{F}_L = q (\mathbf{E}(\mathbf{r}, t) + \mathbf{v} \times \mathbf{B}(\mathbf{r}, t)). \quad (2.12)$$

2.1.1 Charge Conservation

An important property of Maxwell's equations is their inherent conservation of charges. This can be shown by taking the divergence of Ampère's law (2.11) in differential representation:

$$\underbrace{\nabla \cdot (\nabla \times \mathbf{H}(\mathbf{r}, t))}_0 = \nabla \cdot \frac{\partial}{\partial t} \mathbf{D}(\mathbf{r}, t) + \nabla \cdot \mathbf{J}(\mathbf{r}, t). \quad (2.13)$$

It is commonly known from vector analysis that the divergence of a curl operation equals zero. Changing the order of spatial and time derivatives on the right-hand side of (2.13) using *Schwarz's* theorem [57, p. 282] and employing (2.8) delivers

$$0 = \frac{\partial}{\partial t} \rho(\mathbf{r}, t) + \nabla \cdot \mathbf{J}(\mathbf{r}, t). \quad (2.14)$$

Integrating this equation over the domain Ω and employing the divergence theorem [56, p. 879, (I. 33)] results in

$$0 = \frac{\partial}{\partial t} \iiint_{\Omega} \rho(\mathbf{r}, t) dV + \oint_{\partial\Omega} \mathbf{J}(\mathbf{r}, t) \cdot d\mathbf{A}. \quad (2.15)$$

The equation reveals that the negative change of the total charge within the domain Ω has to be equal to the total outward electric current through the boundary $\partial\Omega$ of the domain. Qualitatively speaking, (2.15) claims that the movement of a charged particle leaving a volume leads to a reduction of total charge contained in the volume and to a current flowing through the boundaries of the volume.

2.1.2 Energy Conservation or Poynting's Theorem

Apart from charge conservation, Maxwell's equations are energy conserving as well. This arises from multiplying (2.10) with the magnetic field, (2.11) with the electric field and the subtraction of both equations:

$$\begin{aligned} \mathbf{H}(\mathbf{r}, t) \cdot (\nabla \times \mathbf{E}(\mathbf{r}, t)) - \mathbf{E}(\mathbf{r}, t) \cdot (\nabla \times \mathbf{H}(\mathbf{r}, t)) = \\ - \underbrace{\mathbf{H}(\mathbf{r}, t) \cdot \frac{\partial}{\partial t} \mathbf{B}(\mathbf{r}, t)}_{\partial_t w_m(\mathbf{r}, t)} - \underbrace{\mathbf{E}(\mathbf{r}, t) \cdot \frac{\partial}{\partial t} \mathbf{D}(\mathbf{r}, t)}_{\partial_t w_e(\mathbf{r}, t)} - \underbrace{\mathbf{E}(\mathbf{r}, t) \cdot \mathbf{J}(\mathbf{r}, t)}_{p_{\text{int}}(\mathbf{r}, t)}. \end{aligned} \quad (2.16)$$

Here, $\partial_t w_e(\mathbf{r}, t)$ and $\partial_t w_m(\mathbf{r}, t)$ denote the change of energy stored in the electric and magnetic fields in an infinitely small volume element and $p_{\text{int}}(\mathbf{r}, t)$ the loss of energy per volume element. Employing the vector calculus identity $\nabla \cdot (\mathbf{E}(\mathbf{r}, t) \times \mathbf{H}(\mathbf{r}, t)) = \mathbf{H}(\mathbf{r}, t) \cdot (\nabla \times \mathbf{E}(\mathbf{r}, t)) - \mathbf{E}(\mathbf{r}, t) \cdot (\nabla \times \mathbf{H}(\mathbf{r}, t))$ (see e.g. [56, p. 879, (I. 24)]) to simplify the left-hand side of (2.16) and shifting $p_{\text{int}}(\mathbf{r}, t)$ from the right-hand side to the left-hand side of the equation delivers

$$p_{\text{int}}(\mathbf{r}, t) + \nabla \cdot \underbrace{(\mathbf{E}(\mathbf{r}, t) \times \mathbf{H}(\mathbf{r}, t))}_{\mathbf{S}(\mathbf{r}, t)} = -\frac{\partial}{\partial t} w_e(\mathbf{r}, t) - \frac{\partial}{\partial t} w_m(\mathbf{r}, t). \quad (2.17)$$

The cross product between the electric and magnetic field is commonly known as *Poynting vector* $\mathbf{S}(\mathbf{r}, t)$ and defines the flow of energy per unit area due to electromagnetic fields. Integrating (2.17) over the volume Ω of interest and applying the

divergence theorem yields

$$\underbrace{\iiint_{\Omega} p_{\text{int}}(\mathbf{r}, t) dV}_{P_{\text{int}}(t)} + \underbrace{\oint_{\partial\Omega} \mathbf{S}(\mathbf{r}, t) \cdot d\mathbf{A}}_{P_{\text{ext}}(t)} = \underbrace{-\frac{\partial}{\partial t} \iiint_{\Omega} w_e(\mathbf{r}, t) dV}_{W_e(t)} - \underbrace{\frac{\partial}{\partial t} \iiint_{\Omega} w_m(\mathbf{r}, t) dV}_{W_m(t)}. \quad (2.18)$$

This statement balances the *internal or intrinsic energy losses* $P_{\text{int}}(t)$ in Ω and the energy flowing through the boundary $\partial\Omega$, further referred to as *external energy losses* $P_{\text{ext}}(t)$, to the change of total energy stored in electric $W_e(t)$ and magnetic $W_m(t)$ fields. The internal losses $P_{\text{int}}(t)$ can be attributed to Ohmic dissipation effects as a consequence of finite resistivities and dielectric and magnetic losses, for example. Furthermore, the transfer of energy to charged particles residing in Ω is accounted for in $P_{\text{int}}(t)$. In contrast, the external losses $P_{\text{ext}}(t)$ cover the propagation of energy through waveguide ports. Depending on the definition of the domain Ω and its boundary $\partial\Omega$, losses due to finite surface conductivities of the walls of the RF structure can either contribute to $P_{\text{int}}(t)$ or to $P_{\text{ext}}(t)$. Hereinafter, the domain Ω (and thus its boundary $\partial\Omega$) is chosen such that surface losses are covered by $P_{\text{int}}(t)$. It should be emphasized that $P_{\text{int}}(t)$ and $P_{\text{ext}}(t)$ can become negative if for example, charged particles are decelerated in Ω or energy propagates into the structure through $\partial\Omega$ due to an external excitation of the waveguide ports. In these cases $P_{\text{int}}(t)$ and $P_{\text{ext}}(t)$ are related to energy gains rather than to energy losses.

2.1.3 Wave Equations

Faraday's law of induction (2.10) and Ampère's law with Maxwell's extension (2.11) are first-order differential vector equations which are mutually coupled by the electrical quantities $\mathbf{E}(\mathbf{r}, t)$, $\mathbf{D}(\mathbf{r}, t)$ and the magnetic quantities $\mathbf{B}(\mathbf{r}, t)$ and $\mathbf{H}(\mathbf{r}, t)$. To solve these equations, it might be more convenient to combine them in such a way that either only the electric quantities or only the magnetic quantities occur in one equation. This can be achieved for example for the electric field by taking the curl of (2.10) and replacing the magnetic flux density on the right-hand side with the magnetic field strength using (2.7). In a following step, the order of spatial and time differentiation is changed. For homogeneous materials, the permeability μ is constant and thus can be placed outside the curl operator. The curl of the magnetic field remains on the right-hand side and is replaced by (2.11). Substituting the electric flux in the resulting equation with (2.6) gives the so-called *curl curl equation*

$$\nabla \times \nabla \times \mathbf{E}(\mathbf{r}, t) = -\varepsilon\mu \frac{\partial^2}{\partial t^2} \mathbf{E}(\mathbf{r}, t) - \mu \frac{\partial}{\partial t} \mathbf{J}(\mathbf{r}, t) \quad (2.19)$$

for electric fields. Using the vector identity $\nabla \times \nabla \times \mathbf{E}(\mathbf{r}, t) = \nabla(\nabla \cdot \mathbf{E}(\mathbf{r}, t)) - \Delta \mathbf{E}(\mathbf{r}, t)$ (see e.g. [54, p. 879, (I. 24)]) the equation can be modified to the *wave equation for electric fields*:

$$\Delta \mathbf{E}(\mathbf{r}, t) = \varepsilon \mu \frac{\partial^2}{\partial t^2} \mathbf{E}(\mathbf{r}, t) + \nabla \left(\underbrace{\nabla \cdot \mathbf{E}(\mathbf{r}, t)}_{\rho(\mathbf{r}, t)/\varepsilon} \right) + \mu \frac{\partial}{\partial t} \mathbf{J}(\mathbf{r}, t). \quad (2.20)$$

Based on the assumption of homogeneous material properties, the divergence of the electric field can be replaced by the charge density divided by the permittivity using (2.6) and (2.8). In a similar fashion, the *wave equation for magnetic fields*

$$\Delta \mathbf{H}(\mathbf{r}, t) = \varepsilon \mu \frac{\partial^2}{\partial t^2} \mathbf{H}(\mathbf{r}, t) - \nabla \times \mathbf{J}(\mathbf{r}, t) \quad (2.21)$$

can be derived for homogeneous media from the differential form of Maxwell's equations. The wave equations are hyperbolic partial differential vector equations and explain the wave nature of time-dependent electromagnetic fields. They describe propagation phenomena in free space and in waveguides or standing waves in closed cavities (see Section 2.4 for more details on standing waves in closed cavities).

2.2 Discrete Formulation of Maxwell's Equations

Analytical solutions for Maxwell's equations or for the corresponding wave equations (2.20) or (2.21) are solely available for very simple geometries. As mentioned previously, partial differential equations can be typically solved by means of analytical approaches if a coordinate system can be found whose axes are parallel to the boundaries of the geometry under concern. For arbitrary geometries analytical methods to solve field problems often fail and numerical methods are applied. Over the last six decades, a large variety of different numerical methods for tackling electromagnetic problems has been developed. Most of these methods rely on a mesh which enables a discrete formulation of the continuous partial differential equations. The discretization introduces an error which is reducible by choosing a finer mesh. Unfortunately, a finer mesh imposes higher requirements on the computing infrastructure and the computational time needed for the field computation. A reasonable trade-off between accuracy and computational demands is identified by means of a *mesh refinement study*. In [58] several numerical state of the art methods to solve Maxwell's equations are presented in a hands-on manner. Boundary element methods (BEM) for instance solely discretize surfaces whereas finite element methods (FEM) discretize finite volumes. The inevitable restriction to a finite domain, the so-called *computational domain*, enforces the specification of suitable field conditions on the boundary of the computational domain.

The numerical field computations presented in the thesis are performed by means of the finite integration technique (FIT). Therefore, the method is briefly outlined hereinafter in order to have a consistent nomenclature in the framework of the thesis. A rigorous introduction to FIT is available in [38], for example. Initially, the FIT scheme was introduced in 1977 in [59]. From then on, a vast number of improvements and modifications were developed, see examples [60, 61, 62]. Similar to FEM approaches, the FIT scheme discretizes volumes. FIT allows for an intuitive understanding because it directly results from the integral form of Maxwell's equations. The commercial implementation CST MWS [18] of FIT¹ is used in the scope of this thesis to export a discrete formulation of Maxwell's equations arising from 3D computer aided engineering (CAE) models of RF structures.

To convert the integral form of Maxwell's equations into a discrete form, FIT allocates its field quantities on two staggered grids as shown in Figure 2.1. The black grid is the *primary grid* G whereas the grey grid is the *dual grid* \tilde{G} . Every edge of the dual grid intersects one facet of the primary grid and vice versa. The primary grid nodes (black dots) in Figure 2.1 are labeled with their *lexicographic index* $1 \leq n_p \leq N_p$. The complete grid has I_p nodes in x -direction, J_p nodes in y -direction, and K_p nodes in z -direction. The total number of nodes in the primary grid is denoted by $N_p = I_p J_p K_p$. Despite the fact that FIT is applicable on different mesh types [60, 61], the following outline is restricted to hexahedral meshes for the sake of simplicity. Furthermore, the numerical computations presented in Chapter 5 are performed by CST MWS based on hexahedral meshes. Primary and dual grid allow for the transfer of the integral form of Maxwell's equations (2.1) - (2.4) to the *integral-state representation of Maxwell's grid equations*:

$$\tilde{\mathcal{S}} \hat{\hat{\mathbf{d}}} = \hat{\hat{\mathbf{q}}}, \quad (2.22)$$

$$\mathcal{S} \hat{\mathbf{b}} = \mathbf{0}, \quad (2.23)$$

$$\mathcal{C} \hat{\mathbf{e}} = -\frac{d}{dt} \hat{\hat{\mathbf{b}}}, \quad (2.24)$$

$$\tilde{\mathcal{C}} \hat{\mathbf{h}} = \frac{d}{dt} \hat{\hat{\mathbf{d}}} + \hat{\hat{\mathbf{j}}}. \quad (2.25)$$

Maxwell's grid equations are in fact a set of matrix equations which can be stored and processed by digital computers. The matrices $\tilde{\mathcal{S}} \in \mathbb{R}^{N_p \times 3N_p}$ and $\mathcal{S} \in \mathbb{R}^{N_p \times 3N_p}$ are the discrete FIT counterpart of the divergence operator acting on dual and primary grid quantities respectively. These matrices are sparse and contain six bands with the coefficients $\{-1, 0, 1\}$. The matrices $\mathcal{C} \in \mathbb{R}^{3N_p \times 3N_p}$ and $\tilde{\mathcal{C}} = \mathcal{C}^T \in \mathbb{R}^{3N_p \times 3N_p}$ are the FIT counterparts of the curl operator acting on primary grid and dual grid quantities, respectively. These matrices are sparse as well and contain twelve off-diagonal bands with the coefficients $\{-1, 0, 1\}$. The vector $\hat{\hat{\mathbf{d}}}$ collects all *electric grid fluxes* in the computational domain. These fluxes flow through the

¹CST MICROWAVE STUDIO[®] supports FEM and BEM approaches as well.

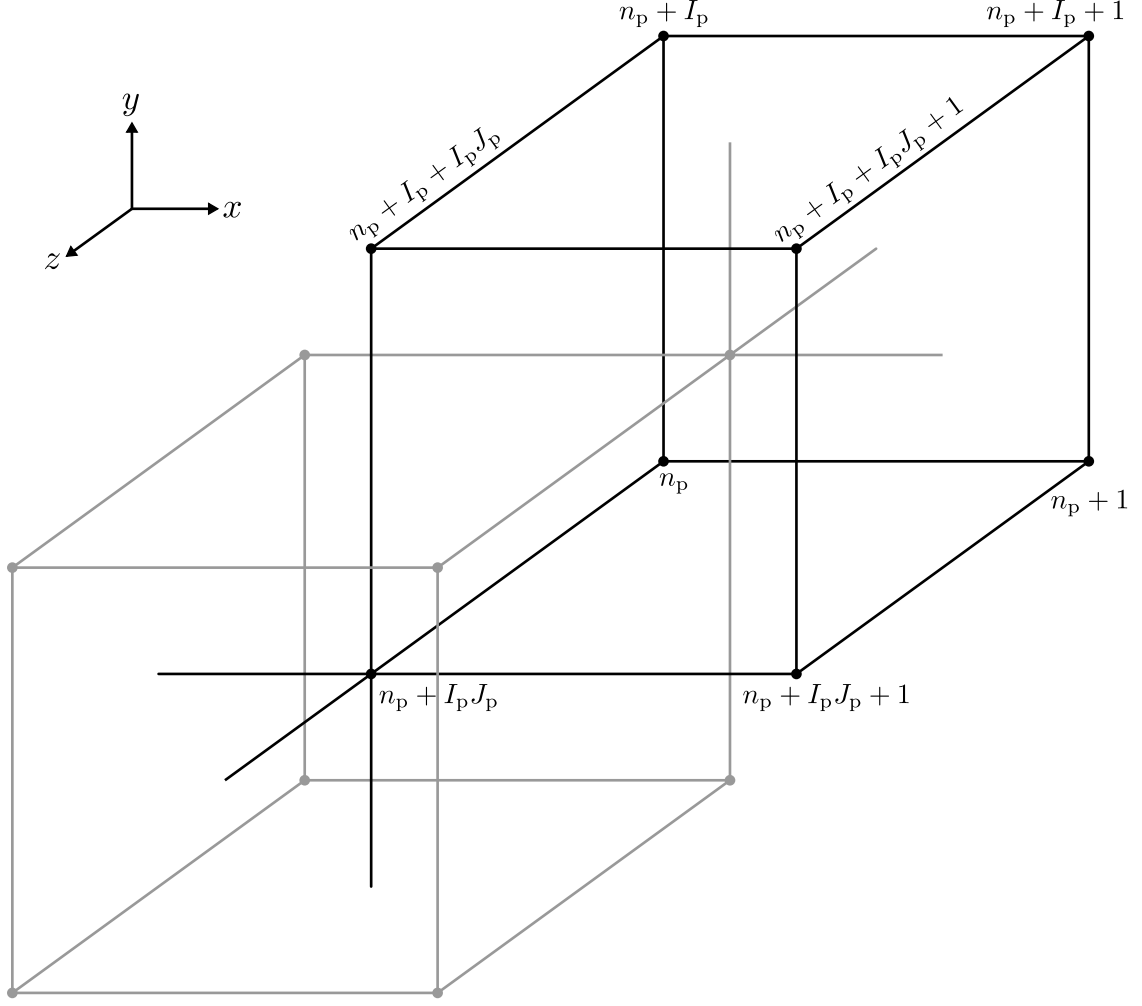


Figure 2.1: Unit cell of primary grid G (black lines) and dual grid \tilde{G} (grey lines) for the spatial discretization of the computational domain. The nodes of the primary grid (black dots) are equipped with their lexicographic indices. It is assumed that the entire grid has I_p nodes in x -direction, J_p nodes in y -direction, and K_p nodes in z -direction.

facets of the dual grid. The vector $\hat{\hat{\mathbf{q}}}$ comprises *electric grid charges* distributed in the computational domain. FIT allocates electric grid charges in the volumes of the dual grid. The *magnetic grid fluxes* are stored in the vector $\hat{\mathbf{b}}$. Magnetic grid fluxes flow through facets of the primary grid. The vector $\hat{\mathbf{e}}$ comprises the so-called *electric grid voltages*. These voltages are defined across nodes of the primary grid. In close analogy, the so-called *magnetic grid voltages* are collected in $\hat{\mathbf{h}}$. The magnetic grid voltages are defined between nodes of the dual grid. The *electric grid currents* are gathered in $\hat{\mathbf{j}}$. They flow through facets of the dual grid just as the electric fluxes $\hat{\mathbf{d}}$. Analogously to the continuous case, the grid currents $\hat{\mathbf{j}}$ are superpositions of

impressed currents $\widehat{\mathbf{j}}_{ic}$, convection currents $\widehat{\mathbf{j}}_{cc}$, and Ohmic currents $\widehat{\mathbf{j}}_{\sigma}$. It should be stressed that the introduced integral-state representation of Maxwell's grid equations is free of approximation, because the integral-state variables are directly defined in terms of path (one bow), surface (two bows), and volume (three bows) integrals. Approximations are introduced by expressing the integral-state quantities in terms of sample-state quantities:

$$\widehat{\mathbf{d}} \approx \tilde{\mathcal{D}}_A \mathbf{d}, \quad (2.26)$$

$$\widehat{\widehat{\mathbf{q}}} \approx \tilde{\mathcal{D}}_V \mathbf{q}, \quad (2.27)$$

$$\widehat{\mathbf{b}} \approx \mathcal{D}_A \mathbf{b}, \quad (2.28)$$

$$\widehat{\mathbf{e}} \approx \mathcal{D}_s \mathbf{e}, \quad (2.29)$$

$$\widehat{\mathbf{h}} \approx \tilde{\mathcal{D}}_s \mathbf{h}, \quad (2.30)$$

$$\widehat{\mathbf{j}} \approx \tilde{\mathcal{D}}_A \mathbf{j}. \quad (2.31)$$

The diagonal matrices \mathcal{D}_s and $\tilde{\mathcal{D}}_s$ contain edge lengths, the diagonal matrices \mathcal{D}_A and $\tilde{\mathcal{D}}_A$ surface areas, and the diagonal matrix $\tilde{\mathcal{D}}_V$ volume sizes. Matrices without tilde refer to grid properties of the primary grid whereas matrices with tilde comprise properties of the dual grid. The vectors on the right-hand side of (2.26) - (2.31) collect the sample-state quantities, namely *electric grid flux densities* \mathbf{d} , *electric grid charge densities* \mathbf{q} , *electric grid field strengths* \mathbf{e} , *magnetic grid field strengths* \mathbf{h} , and *electric grid current densities* \mathbf{j} . The sample-state quantities are allocated in the center of edges, facets, and volumes of primary and dual grid cells. As a result of the sophisticated allocation of field quantities in the computational domain, the sampled-state quantities are approximated with second-order accuracy by means of the midpoint rule for path, surface, and volume integrals. The error arising from the approximation of the integrals is referred to as *discretization error*. Replacing the integral-state quantities in (2.22) - (2.25) by their sample-state counterparts using (2.26) - (2.31) delivers Maxwell's grid equations in *sample-state representation*

$$\tilde{\mathcal{S}} \tilde{\mathcal{D}}_A \mathbf{d} \approx \tilde{\mathcal{D}}_V \mathbf{q}, \quad (2.32)$$

$$\mathcal{S} \mathcal{D}_A \mathbf{b} \approx \mathbf{0}, \quad (2.33)$$

$$\mathcal{C} \mathcal{D}_s \mathbf{e} \approx -\frac{d}{dt} \mathcal{D}_A \mathbf{b}, \quad (2.34)$$

$$\tilde{\mathcal{C}} \tilde{\mathcal{D}}_s \mathbf{h} \approx \tilde{\mathcal{D}}_A \left(\frac{d}{dt} \mathbf{d} + \mathbf{j} \right). \quad (2.35)$$

The sample-state quantities are mutually connected by the FIT equivalents of the constitutive equations:

$$\mathbf{d} \approx \mathcal{D}_\varepsilon \mathbf{e}, \quad (2.36)$$

$$\mathbf{j}_\sigma \approx \mathcal{D}_\sigma \mathbf{e}, \quad (2.37)$$

$$\mathbf{b} \approx \mathcal{D}_\mu \mathbf{h}. \quad (2.38)$$

The diagonal matrices \mathcal{D}_ε , \mathcal{D}_σ , and \mathcal{D}_μ comprise averaged permittivities, conductivities, and permeabilities. The averaging of material properties introduces an additional error which contributes to the aforementioned discretization error. Based on the FIT equivalents of the constitutive equations and the relations between integral- and sample-state quantities, the grid fluxes can be expressed in terms of the grid voltages:

$$\hat{\mathbf{d}} \approx \mathcal{M}_\varepsilon \hat{\mathbf{e}} \text{ where } \mathcal{M}_\varepsilon \approx \tilde{\mathcal{D}}_A \mathcal{D}_\varepsilon \mathcal{D}_s^{-1}, \quad (2.39)$$

$$\hat{\mathbf{j}}_\sigma \approx \mathcal{M}_\sigma \hat{\mathbf{e}} \text{ where } \mathcal{M}_\sigma = \tilde{\mathcal{D}}_A \mathcal{D}_\sigma \mathcal{D}_s^{-1}, \quad (2.40)$$

$$\hat{\mathbf{b}} \approx \mathcal{M}_\mu \hat{\mathbf{h}} \text{ where } \mathcal{M}_\mu = \mathcal{D}_A \mathcal{D}_\mu \tilde{\mathcal{D}}_s^{-1}. \quad (2.41)$$

In addition to the discretization error, the FIT scheme with hexahedral grid introduces a *geometry error* if the boundary of the geometry under concern does not coincide with the grid. In such situations, partially filled cells² are used to reduce the geometry error. Another error source in numerical schemes in general is the *round-off error* which arises from the finite machine precision of digital computers. Despite the fact that (2.26) - (2.41) are only approximately equal, the subsequent part of the thesis uses equality signs in the context of FIT to avoid confusion. Nonetheless, it should be kept in mind that the FIT scheme introduces errors.

A crucial characteristic³ of FIT is the conservation of the properties of continuous vectors operators in the discrete case, e.g. curl fields are free of sources:

$$\nabla \cdot \nabla \times \dots = 0 \Leftrightarrow \mathcal{SC} = \mathbf{0} \text{ and } \tilde{\mathcal{S}}\tilde{\mathcal{C}} = \mathbf{0}. \quad (2.42)$$

Amongst others, this property allows for proving that the FIT formulation is charge and energy conserving just as Maxwell's equations are [38]. This property is a key benefit of FIT, because numerical solutions can be checked for physical consistency.

2.3 Electromagnetic Fields in Longitudinally Uniform Waveguides

Apart from electromagnetic wave propagation in unbounded media, waves confined by material boundaries can propagate as *guided waves* as well. Figure 2.2 presents an incomplete selection of such structures. These structures are referred to as *waveguides*. Their cross section $\mathbf{\Gamma}_{\text{wg}}$ is assumed to be constant along the direction z of wave propagation⁴. All depicted waveguides are made of a perfect electric enclosure (conductivity $\sigma \rightarrow \infty$) filled with a homogeneous isotropic insulating material with

²This technique is commonly known as perfect boundary approximation (PBA) in CST MWS.

³often referred to as *consistency*

⁴further referred to as *longitudinal direction*

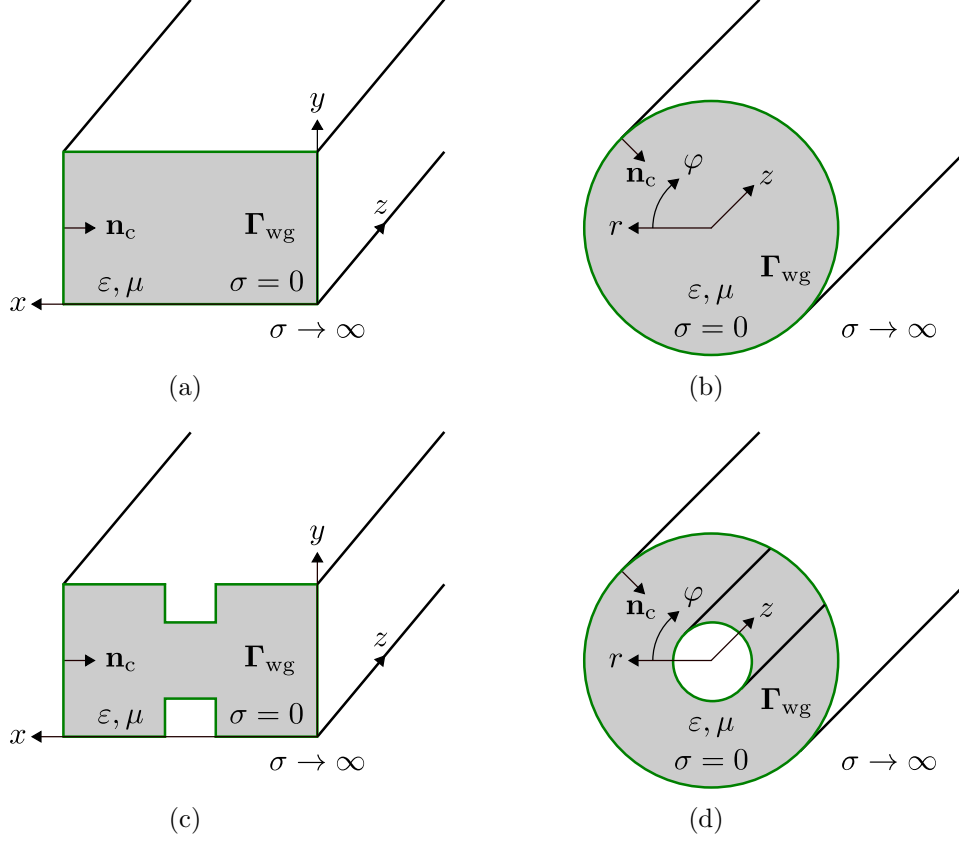


Figure 2.2: Selection of longitudinally uniform waveguides with different cross sections Γ_{wg} (marked in grey): (a) rectangular waveguide, (b) circular waveguide, (c) ridge waveguide, and (d) coaxial waveguide. The waveguides are made of a perfect electric enclosure which is filled with an isotropic homogeneous insulating material with the permittivity ε and the permeability μ . The vector \mathbf{n}_c is normal to the boundary $\partial\Gamma_{\text{wg}}$ (marked in green) of the uniform cross section Γ_{wg} . The quantities x , y , and z are spatial coordinates of a Cartesian system whereas r , φ , and z are the coordinates of a cylindrical system. In contrast to the hollow waveguides (a) - (c), the coaxial waveguide is multiply connected, due to the existence of the inner conductor.

the constitutive parameters ε , μ and $\sigma = 0$. The rectangular waveguide in Figure 2.3, the circular waveguide in Figure 2.3 and the ridge waveguide in Figure 2.3 are hollow waveguides, because they only have an outer conductor. In contrast to those waveguides, the coaxial waveguide depicted in Figure 2.3 is equipped with an additional inner conductor.

The electromagnetic field distributions in the waveguide have to obey (2.20) and (2.21) with $\rho(\mathbf{r}, t) = 0$, $\mathbf{J}(\mathbf{r}, t) = \mathbf{0}$ in Γ_{wg} , and vanishing tangential electric fields on the waveguide boundaries, i.e. $\mathbf{n}_c \times \mathbf{E}(\mathbf{r}, t) = \mathbf{0}$ on $\partial\Gamma_{\text{wg}}$. Moreover, electric and magnetic fields are mutually coupled by means of Faraday's law and Ampère's

law. Following for example [63], all fields in longitudinally invariant structures with arbitrarily shaped perfect electric conducting cross sections are expressible in terms of a superposition of an infinite number of so-called *waveguide modes*:

$$\mathbf{E}(\mathbf{r}, t) = \sum_{m=1}^{\infty} \underbrace{\left(\mathbf{L}_{t,m}^{\text{wg}}(\mathbf{r}_t) v_m(z, t) + \mathbf{n}_z E_{z,m}^{\text{wg}}(\mathbf{r}, t) \right)}_{\mathbf{E}_m^{\text{wg}}(\mathbf{r}, t)}, \quad (2.43)$$

$$\mathbf{H}(\mathbf{r}, t) = \sum_{m=1}^{\infty} \underbrace{\left(\mathbf{n}_z \times \mathbf{L}_{t,m}^{\text{wg}}(\mathbf{r}_t) i_m(z, t) + \mathbf{n}_z H_{z,m}^{\text{wg}}(\mathbf{r}, t) \right)}_{\mathbf{H}_m^{\text{wg}}(\mathbf{r}, t)}. \quad (2.44)$$

Here, $\mathbf{E}_m^{\text{wg}}(\mathbf{r}, t)$ is the electric field and $\mathbf{H}_m^{\text{wg}}(\mathbf{r}, t)$ the magnetic field of the m th waveguide mode. The field distributions of all waveguide modes are expressible by means of a separation between transversal and longitudinal dependencies. The field patterns $\mathbf{L}_{t,m}^{\text{wg}}(\mathbf{r}_t)$ solely depend on the transverse spatial coordinates $\mathbf{r}_t \in \mathbf{\Gamma}_{\text{wg}}$ and describe the transverse dependencies of the electric and magnetic fields of the individual waveguide modes. The corresponding weighting coefficients $v_m(z, t)$ and $i_m(z, t)$ are referred to as *modal voltages* and *modal currents*⁵ of the waveguide modes. These quantities are of formal nature as direct measurements of voltages and currents⁶ are not feasible in the RF regime. Nonetheless, the introduction of modal voltages and currents has several benefits as discussed in Section 3.1. The scalar quantities $E_{z,m}^{\text{wg}}(\mathbf{r}, t)$ and $H_{z,m}^{\text{wg}}(\mathbf{r}, t)$ in (2.43) and (2.44) account for the longitudinal electric and magnetic fields where \mathbf{n}_z is the unit vector in longitudinal direction. Poynting's theorem (2.17) states that the transverse field patterns are responsible for the longitudinal power flow in the waveguide. Therefore, the transverse fields are of special interest in the subsequent considerations. However, for the sake of completeness it should be noted that the longitudinal field components $E_{z,m}^{\text{wg}}(\mathbf{r}, t)$ and $H_{z,m}^{\text{wg}}(\mathbf{r}, t)$ are uniquely determined by the transverse field patterns in combination with Faraday's law (2.10) and Ampère's law with Maxwell's extension (2.11).

2.3.1 Generation of Transverse Modal Field Patterns

Substituting the electric fields in the wave equation (2.20) by the ansatz for $\mathbf{E}_m^{\text{wg}}(\mathbf{r}, t)$ given in (2.43) and substituting the magnetic fields in the wave equation (2.21) by the ansatz for $\mathbf{H}_m^{\text{wg}}(\mathbf{r}, t)$ given in (2.44) leads to the *Klein-Gordon equation* (KGE) for modal voltages and currents [46, 47, 48]:

$$\frac{\partial^2}{\partial z^2} \begin{Bmatrix} v_m(z, t) \\ i_m(z, t) \end{Bmatrix} = \varepsilon \mu \frac{\partial^2}{\partial t^2} \begin{Bmatrix} v_m(z, t) \\ i_m(z, t) \end{Bmatrix} - k_{t,m}^2 \begin{Bmatrix} v_m(z, t) \\ i_m(z, t) \end{Bmatrix} \quad (2.45)$$

⁵often they are also referred to as generalized modal voltages and currents

⁶in particular direct measurements of modal voltages and currents

with the separation constants $k_{t,m}$. The vector functions $\mathbf{L}_{t,m}^{\text{wg}}(\mathbf{r}_t)$ are in fact eigenfunctions of the 2D vector Laplace operator Δ_t on the cross section Γ_{wg} of the waveguide, whereas the separation constants $k_{t,m}$ are the corresponding eigenvalues:

$$\Delta_t \mathbf{L}_{t,m}^{\text{wg}}(\mathbf{r}_t) + k_{t,m}^2 \mathbf{L}_{t,m}^{\text{wg}}(\mathbf{r}_t) = \mathbf{0} \text{ in } \Gamma_{\text{wg}}. \quad (2.46)$$

The equation is also referred to as 2D Helmholtz equation. As the inner domain of the waveguide is free of charges

$$\nabla_t \cdot \mathbf{L}_{t,m}^{\text{wg}}(\mathbf{r}_t) = 0 \text{ in } \Gamma_{\text{wg}} \quad (2.47)$$

holds. Here, $\nabla_t \cdot$ represents the transverse divergence operator. As a consequence of the perfect electric conducting walls, the tangential electric fields are required to vanish on the boundary. Therefore, the transverse modal field patterns have to satisfy

$$\mathbf{n}_c \times \mathbf{L}_{t,m}^{\text{wg}}(\mathbf{r}_t) = \mathbf{0} \text{ on } \partial\Gamma_{\text{wg}}. \quad (2.48)$$

It should be stressed that field patterns $\mathbf{L}_{t,m}^{\text{wg}}(\mathbf{r}_t)$ neither depend on frequency nor on time but on the cross section of the waveguide. In consequence, the patterns can be employed to expand the transverse electric and magnetic fields in the waveguide in frequency as well as in time domain.

Theory states that the partial differential equation (2.46) with the boundary condition (2.48) has an infinite number of solutions which constitute an orthogonal set of basis functions for Γ_{wg} [56, Section 5.2]. In this thesis, all transverse patterns are chosen such that they are mutually orthonormal:

$$\iint_{\Gamma_{\text{wg}}} \mathbf{L}_{t,\xi}^{\text{wg}}(\mathbf{r}_t) \cdot \mathbf{L}_{t,m}^{\text{wg}}(\mathbf{r}_t) dA = \begin{cases} 1 & \text{if } \xi = m, \\ 0 & \text{if } \xi \neq m. \end{cases} \quad (2.49)$$

All transverse field patterns in a waveguide are sorted in ascending order by their separation constant, so that $k_{t,1} \leq k_{t,2} \leq k_{t,3} \leq \dots$ holds. As a matter of fact, only the waveguide modes with the smallest eigenvalues (or separation constants) are of technical relevance. Modes having different field patterns but the same eigenvalues are called *degenerated modes* [55].

In fact, three different classes of waveguide modes arise from the 2D Helmholtz equation on the cross section of the waveguide. They are distinguished as follows: The longitudinal component of the electric field of *transverse electric waves* (TE) equals zero, i.e. $E_{z,m}^{\text{wg}}(\mathbf{r}, t) = 0$. TE waves are also known as *H waves* or *waves of magnetic type*. In contrast, the longitudinal component of the magnetic field of *transverse magnetic waves* (TM), also referred to as *E waves* or *waves of electric type* is zero, i.e. $H_{z,m}^{\text{wg}}(\mathbf{r}, t) = 0$. *Transverse electric and magnetic waves* (TEM) neither have longitudinal electric nor longitudinal magnetic fields, i.e. $E_{z,m}^{\text{wg}}(\mathbf{r}, t) = 0$ and $H_{z,m}^{\text{wg}}(\mathbf{r}, t) = 0$. An infinite number of TE and TM waveguide modes exists

in hollow waveguides as well as in waveguides which are connected multiply. Their separation constants are larger than zero. In contrast, TEM waveguide modes solely exist in waveguides whose cross section is bounded multiply. The number of TEM waveguide modes is equal to the number of inner conductors in the waveguide, i.e. no TEM modes in the rectangular, circular and ridge waveguide and one TEM mode in the coaxial cable (refer to Figure 2.2). The separation constant of TEM waveguide modes is equal to zero.

2.3.2 Frequency-Domain Solutions of Klein-Gordon Equation

The solutions of the Klein-Gordon equation are given for the frequency f by

$$v_m(z, t) = \Re \{ \underline{V}_m(z) e^{j\omega t + \varphi_0} \}, \quad (2.50)$$

$$i_m(z, t) = \Re \{ \underline{I}_m(z) e^{j\omega t + \varphi_0} \} \quad (2.51)$$

with the complex-valued voltages along the waveguide

$$\underline{V}_m(z) = \underbrace{\underline{V}_m^+ e^{-\gamma_m(j\omega)z}}_{\underline{V}_m^+(z)} + \underbrace{\underline{V}_m^- e^{\gamma_m(j\omega)z}}_{\underline{V}_m^-(z)} \quad (2.52)$$

and the complex-valued currents along the waveguide

$$\underline{I}_m(z) = \underbrace{\underline{I}_m^+ e^{-\gamma_m(j\omega)z}}_{\underline{I}_m^+(z)} + \underbrace{\underline{I}_m^- e^{\gamma_m(j\omega)z}}_{\underline{I}_m^-(z)}. \quad (2.53)$$

Here, $\omega = 2\pi f$ denotes the angular frequency, φ_0 a constant phase, and

$$\gamma_m(j\omega) = \sqrt{\varepsilon\mu} \sqrt{(j\omega)^2 + \omega_{co,m}^2} \quad (2.54)$$

the so-called *propagation constants*. These constants characterize the longitudinal change of the field amplitudes in the waveguide. For frequencies above the *cutoff angular frequencies*

$$\omega_{co,m} = 2\pi f_{co,m} = \frac{k_{t,m}}{\sqrt{\varepsilon\mu}} \quad (2.55)$$

the propagation constants become complex-valued numbers. In these cases propagation of fields (*propagating modes*) takes places. According to (2.52) and (2.53), waves can propagate in the positive and negative z -direction. The complex-valued amplitudes \underline{V}_m^+ and \underline{I}_m^+ refer to transverse electric and magnetic fields of waves traveling in the positive z -direction whereas the complex-valued amplitudes \underline{V}_m^- and \underline{I}_m^- refer to waves traveling in the negative z -direction. These constants are determined by excitation and termination conditions of the waveguide. For excitations

below the cutoff angular frequency $\omega_{\text{co},m}$ of the m th waveguide mode, the propagation constant $\underline{\gamma}_m(j\omega)$ is a real-valued number such that the corresponding fields exponentially decay in longitudinal direction (*evanescent modes*). TEM waveguide modes cannot be evanescent, because their separation constant and therefore their cutoff angular frequency equals zero.

2.3.3 Wave and Line Impedances

The relationship between modal voltages and currents of a waveguide mode which is propagating (or decaying) in either the positive or the negative longitudinal direction is described by means of the *wave impedances*.

To compute the wave impedance of TE waveguide modes, a TE wave propagating in the positive z -direction is considered. The modal current arising from the modal voltage of a TE wave is obtained by the magnetic field. This field is determined by using (2.7) and (2.10) with the ansatz for the electric field of a TE mode propagating (or decaying) in the positive z -direction:

$$\begin{aligned}\underline{\mathbf{H}}^{\text{TE},+}(\mathbf{r}) &= -\frac{1}{j\omega\mu}\nabla \times \left(\mathbf{L}_t^{\text{TE}}(\mathbf{r}_t) \underbrace{V^{\text{TE},+} e^{-\underline{\gamma}(j\omega)z}}_{\underline{V}^{\text{TE},+}(z)} \right) \\ &= \mathbf{n}_z \times \mathbf{L}_t^{\text{TE}}(\mathbf{r}_t) \underbrace{\underline{V}^{\text{TE},+} \frac{\underline{\gamma}(j\omega)}{j\omega\mu} e^{-\underline{\gamma}(j\omega)z}}_{\underline{I}^{\text{TE},+}(z)} + \mathbf{n}_z \underline{H}_z^{\text{TE},+}(\mathbf{r}).\end{aligned}\quad (2.56)$$

Here, $\underline{\mathbf{H}}^{\text{TE},+}(\mathbf{r})$ denotes the magnetic field of the TE waveguide mode propagating in the positive z -direction, $\mathbf{L}_t^{\text{TE}}(\mathbf{r}_t)$ accounts for its transverse field pattern, and $\underline{H}_z^{\text{TE},+}(\mathbf{r})$ for its longitudinal magnetic field. The wave impedance of TE modes is delivered by dividing the modal voltage $\underline{V}^{\text{TE},+}(z)$ by the modal current $\underline{I}^{\text{TE},+}(z)$ of the wave propagating in the positive z -direction:

$$\underline{Z}_w^{\text{TE}}(j\omega) = \frac{\underline{V}^{\text{TE},+}(z)}{\underline{I}^{\text{TE},+}(z)} = \frac{j\omega\mu}{\underline{\gamma}(j\omega)} = Z_{\text{fs}} \frac{j\omega}{\sqrt{(j\omega)^2 + \omega_{\text{co}}^2}}. \quad (2.57)$$

Here, $Z_{\text{fs}} = \sqrt{\mu/\varepsilon} \approx 377 \Omega \sqrt{\mu_r/\varepsilon_r}$ is the free space wave impedance of the insulating material.

To compute the wave impedance of TM waveguide modes, a TM wave propagating (or decaying) in the positive z -direction is considered. The modal voltage is determined by the transverse electric field of the TM mode. This field is determined

by using (2.11) and (2.6) with the ansatz for the magnetic field:

$$\begin{aligned}\underline{\mathbf{E}}^{\text{TM},+}(\mathbf{r}) &= \frac{1}{j\omega\varepsilon} \nabla \times \left(\mathbf{n}_z \times \mathbf{L}_t^{\text{TM}}(\mathbf{r}_t) \underbrace{\underline{I}^{\text{TM},+} e^{-\gamma(j\omega)z}}_{\underline{I}^{\text{TM},+}(z)} \right) \\ &= \mathbf{L}_t^{\text{TM}}(\mathbf{r}_t) \underbrace{\underline{I}^{\text{TM},+} \frac{\gamma(j\omega)}{j\omega\varepsilon} e^{-\gamma(j\omega)z}}_{\underline{V}^{\text{TM},+}(z)} + \mathbf{n}_z \underline{E}_z^{\text{TM},+}(\mathbf{r}),\end{aligned}\quad (2.58)$$

where $\underline{\mathbf{E}}^{\text{TM},+}(\mathbf{r})$ is the electric field of the TM waveguide mode propagating in the positive z -direction, $\mathbf{L}_t^{\text{TM}}(\mathbf{r}_t)$ accounts for its transverse field patterns, and $\underline{E}_z^{\text{TM},+}(\mathbf{r})$ for its longitudinal electric field. The wave impedance for TM modes is determined by dividing the modal voltage $\underline{V}^{\text{TM},+}(z)$ by the modal current $\underline{I}^{\text{TM},+}(z)$ of the wave propagating in the positive z -direction:

$$\underline{Z}_w^{\text{TM}}(j\omega) = \frac{\underline{V}^{\text{TM},+}(z)}{\underline{I}^{\text{TM},+}(z)} = \frac{\gamma(j\omega)}{j\omega\varepsilon} = Z_{\text{fs}} \frac{\sqrt{(j\omega)^2 + \omega_{\text{co}}^2}}{j\omega}. \quad (2.59)$$

The real parts of the TE and TM wave impedances (2.57) and (2.59) are zero below the cutoff frequencies whereas the imaginary parts are zero above the cutoff frequencies. For frequencies much larger than the cutoff frequency, the wave impedances tend to the impedance of free space Z_{fs} .

The wave impedance for TEM modes arises in accordance with (2.57) and (2.59) and a cutoff frequency being equal to zero:

$$\underline{Z}_w^{\text{TEM}}(j\omega) = \frac{\underline{V}^{\text{TEM},+}(z)}{\underline{I}^{\text{TEM},+}(z)} = \frac{\gamma(j\omega)}{j\omega\varepsilon} \Big|_{\omega_{\text{co}}=0} = \frac{j\omega\mu}{\gamma(j\omega)} \Big|_{\omega_{\text{co}}=0} = Z_{\text{fs}}. \quad (2.60)$$

A further quantity of interest for TEM waveguide modes is the *line impedance*. In close analogy to the wave impedance of the TEM mode, the line impedance is determined by the ratio between the voltage and the current of a wave solely propagating in one direction. In contrast to the wave impedance, the line impedance is not directly referred to the previously defined modal voltages and currents but to a voltage and current definition arising from line integrals [33, 55]:

$$v^{\text{TEM,li}}(z, t) = \int_{\partial\Gamma_{\text{wg},i}}^{\partial\Gamma_{\text{wg},o}} \mathbf{E}^{\text{TEM}}(\mathbf{r}_t, z, t) \cdot d\mathbf{s} = \underbrace{\int_{\partial\Gamma_{\text{wg},i}}^{\partial\Gamma_{\text{wg},o}} \mathbf{L}_t^{\text{TEM}}(\mathbf{r}_t) \cdot d\mathbf{s}}_{\beta_v} v^{\text{TEM}}(z, t) \quad (2.61)$$

and

$$i^{\text{TEM,li}}(z, t) = \oint_{\partial\Gamma_{\text{wg},o}} \mathbf{H}^{\text{TEM}}(\mathbf{r}_t, z, t) \cdot d\mathbf{s} = \underbrace{\oint_{\partial\Gamma_{\text{wg},o}} \mathbf{n}_z \times \mathbf{L}_t^{\text{TEM}}(\mathbf{r}_t) \cdot d\mathbf{s}}_{\beta_i} i^{\text{TEM}}(z, t). \quad (2.62)$$

Here, $v^{\text{TEM,li}}(z, t)$ and $i^{\text{TEM,li}}(z, t)$ denote the voltages and currents of the TEM waveguide modes, which are specified by the line integrals. The transverse field patterns of the TEM waveguide modes are specified by $\mathbf{L}_t^{\text{TEM}}(\mathbf{r}_t)$. The modal voltages and currents of TEM waveguide modes are given by $v^{\text{TEM}}(z, t)$ and $i^{\text{TEM}}(z, t)$. The inner conducting boundaries of the waveguide are denoted by $\partial\Gamma_{\text{wg,i}}$ and the outer conducting boundary by $\partial\Gamma_{\text{wg,o}}$. According to (2.61) and (2.62), the modal voltages and currents are connected to line integral voltages and currents by the constants β_v and β_i . These constants solely depend on the cross section of the waveguide. Based on these considerations, the line impedance for TEM waveguide modes is given by

$$\underline{Z}_{\text{line}}^{\text{TEM}} = \frac{V^{\text{TEM,li},+}(z)}{\underline{I}^{\text{TEM,li},+}(z)} = \frac{\beta_v}{\beta_i} \frac{V^{\text{TEM},+}(z)}{\underline{I}^{\text{TEM},+}(z)} = \frac{\beta_v}{\beta_i} Z_{\text{fs}}. \quad (2.63)$$

It is worth highlighting that line impedances and wave impedances above cutoff are finite and real numbers, despite the fact that the waveguide is assumed to be lossless. The real and finite nature of the wave and line impedances accounts for active energy propagating along the waveguide.

2.3.4 Normalized Wave Amplitudes

In the RF regime amplitudes of waves traveling (or decaying) in positive or negative longitudinal direction are often normalized with respect to the square root of the wave impedance in case of TE and TM modes or the square root of the line impedance in case of TEM modes. For waves propagating (or decaying) in positive longitudinal direction this yields

$$\begin{aligned} \underline{a}_m(z) &= \frac{V_m^+(z)}{\sqrt{\underline{Z}_m(j\omega)}} = \underline{I}_m^+(z) \sqrt{\underline{Z}_m(j\omega)} \\ &= \frac{1}{2} \left(\frac{V_m(z)}{\sqrt{\underline{Z}_m(j\omega)}} + \underline{I}_m(z) \sqrt{\underline{Z}_m(j\omega)} \right) \end{aligned} \quad (2.64)$$

whereas for waves propagating (or decaying) in negative longitudinal direction this gives

$$\begin{aligned} \underline{b}_m(z) &= \frac{V_m^-(z)}{\sqrt{\underline{Z}_m(j\omega)}} = \underline{I}_m^-(z) \sqrt{\underline{Z}_m(j\omega)} \\ &= \frac{1}{2} \left(\frac{V_m(z)}{\sqrt{\underline{Z}_m(j\omega)}} - \underline{I}_m(z) \sqrt{\underline{Z}_m(j\omega)} \right). \end{aligned} \quad (2.65)$$

Depending on the type of the m th waveguide mode, $\underline{Z}_m(j\omega)$ either accounts for the wave impedances (2.57) and (2.59) or for the line impedance (2.63).

2.4 Electromagnetic Fields in Closed Structures

In addition to waves in partially open structures such as waveguides, the analysis of superconducting RF structures requires the determination of fields in closed structures. Hereinafter, resonant field distributions in closed, non-excited, lossless and source-free structures, so-called *eigenmodes*, are in the focus of interest. On account of these side constraints, the concept of eigenmodes appears to be theoretical and not of practical relevance: Lossless structures do not exist and closed structures cannot be excited by external devices such as microwave generators. Nonetheless, the eigenmode concept is extremely useful, because losses or field excitations via waveguide ports can be considered by perturbation approaches based on eigenmodes.

Figure 2.3 sketches the cutaway view of a superconducting RF resonator with five cells as an example for a closed structure. The shape of the cells is constructed with the help of lines and ellipses. The inner domain Ω of the resonator is made of perfect insulating materials with the properties ε , μ and $\sigma = 0$ (typically vacuum) whereas the wall boundaries $\partial\Omega_{\text{wall}}$ (black lines) of the structure are assumed to be perfect electric conducting. Depending on the problem statement, the beam pipe boundaries $\partial\Omega_{\text{pipe}}$ (green lines) are either perfect electric or perfect magnetic conducting. Eigenmodes in the described arrangement can solely oscillate on discrete real-valued angular resonant frequencies $\tilde{\omega}_n$ due to the conservation of energy. Therefore, the time-dependent electric and magnetic field distributions of the n th eigenmode are expressible by

$$\mathbf{E}_n(\mathbf{r}, t) = \Re \left\{ \tilde{\mathbf{E}}_n(\mathbf{r}) e^{j(\tilde{\omega}_n t + \varphi_0)} \right\}, \quad (2.66)$$

$$\mathbf{H}_n(\mathbf{r}, t) = \Re \left\{ \tilde{\mathbf{H}}_n(\mathbf{r}) e^{j(\tilde{\omega}_n t - \frac{\pi}{2} + \varphi_0)} \right\}, \quad (2.67)$$

where $\tilde{\mathbf{E}}_n(\mathbf{r})$ and $\tilde{\mathbf{H}}_n(\mathbf{r})$ denote the real-valued spatial dependencies of the electric and the magnetic field of the n th eigenmode. Substituting these statements in the wave equations (2.20) and (2.21) for non-excited ($\mathbf{J}(\mathbf{r}, t) = \mathbf{0}$) and source-free ($\rho(\mathbf{r}, t) = 0$) domains yields the *Helmholtz equation* for electric and magnetic fields in three dimensions:

$$\Delta \begin{Bmatrix} \tilde{\mathbf{E}}_n(\mathbf{r}) \\ \tilde{\mathbf{H}}_n(\mathbf{r}) \end{Bmatrix} + \tilde{k}_n^2 \begin{Bmatrix} \tilde{\mathbf{E}}_n(\mathbf{r}) \\ \tilde{\mathbf{H}}_n(\mathbf{r}) \end{Bmatrix} = \mathbf{0} \text{ in } \Omega, \quad (2.68)$$

where $\tilde{k}_n = \tilde{\omega}_n \sqrt{\varepsilon \mu}$. As the domain is free of charges, the additional constraint

$$\nabla \cdot \begin{Bmatrix} \tilde{\mathbf{E}}_n(\mathbf{r}) \\ \tilde{\mathbf{H}}_n(\mathbf{r}) \end{Bmatrix} = 0 \text{ in } \Omega \quad (2.69)$$

is required. The boundary condition for the perfect electric conducting wall is specified by means of

$$\mathbf{n} \times \tilde{\mathbf{E}}_n(\mathbf{r}) = \mathbf{0} \text{ and } \mathbf{n} \cdot \tilde{\mathbf{H}}_n(\mathbf{r}) = 0 \text{ on } \partial\Omega_{\text{wall}}, \quad (2.70)$$

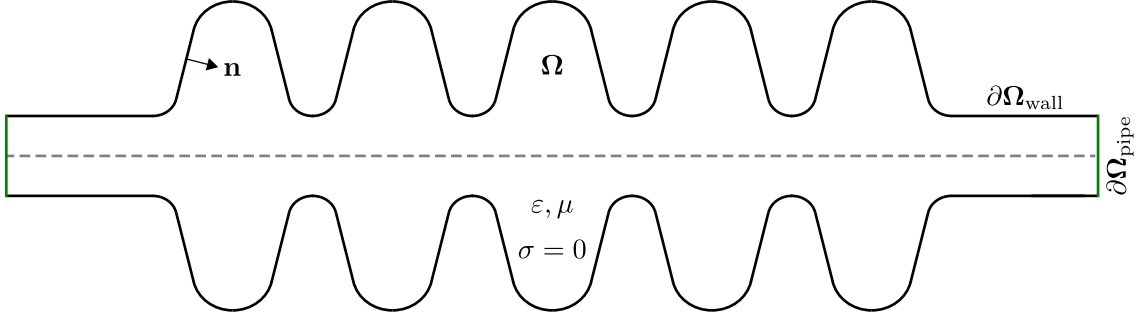


Figure 2.3: Cutaway view of a rotationally symmetric superconducting cavity resonator which is constructed by a set of ellipses. The structure is made of a perfect insulating material (typically vacuum) and enclosed by the boundary $\partial\Omega = \partial\Omega_{\text{wall}} \cup \partial\Omega_{\text{pipe}}$. The normal component of $\partial\Omega$ is denoted by \mathbf{n} . Perfect electric boundary conditions are assigned on $\partial\Omega_{\text{wall}}$ (black lines). Depending on the problem formulation either perfect electric or perfect magnetic boundary conditions are enforced on $\partial\Omega_{\text{pipe}}$ (green lines). The dashed grey line indicates the rotational symmetry axis.

where \mathbf{n} is normal on the boundary $\partial\Omega$. If perfect electric conducting boundary conditions are assigned at the ends of the beam pipes, (2.70) holds for $\partial\Omega_{\text{pipe}}$ as well. In case of perfect magnetic conducting boundary conditions

$$\mathbf{n} \cdot \tilde{\mathbf{E}}_n(\mathbf{r}) = 0 \text{ and } \mathbf{n} \times \tilde{\mathbf{H}}_n(\mathbf{r}) = \mathbf{0} \text{ on } \partial\Omega_{\text{pipe}} \quad (2.71)$$

is specified. In fact, (2.70) claims that the tangential components of the electric field and the normal components of the magnetic field vanish on the boundaries whereas (2.71) enforces normal components of the electric field and tangential components of the magnetic field to be zero on the respective boundaries. Despite the fact that (2.68) is a partial differential equation exclusively dealing either with the electric field or with the magnetic field, both fields always occur simultaneously for $\tilde{\omega}_n \neq 0$, because both fields are mutually coupled by means of Maxwell's equations:

$$\nabla \times \tilde{\mathbf{E}}_n(\mathbf{r}) = -j\tilde{\omega}_n\mu\tilde{\mathbf{H}}_n(\mathbf{r})e^{-j\frac{\pi}{2}}, \quad (2.72)$$

$$\nabla \times \tilde{\mathbf{H}}_n(\mathbf{r}) = j\tilde{\omega}_n\varepsilon\tilde{\mathbf{E}}_n(\mathbf{r})e^{j\frac{\pi}{2}}. \quad (2.73)$$

The equations show that the electric and magnetic fields of the 3D eigenmodes are mutually phase-shifted by $\pm\pi/2$ in the lossless case.

The eigenvalue problem (2.68) with the constraints (2.69), (2.70), and (2.71) has an infinite number of solutions which can be split into two sets: A solenoidal set with a divergence of zero and a non-zero curl and an irrotational set with a non-zero divergence and a curl of zero. The latter set exclusively arises if the closed structure is bounded multiply. The eigenvalues \tilde{k}_n of these irrotational eigenmodes are equal to zero, so that $\tilde{\omega}_n = 0$ (static eigenmodes). The electric field of irrotational eigenmodes

is expressible in terms of a scalar potential and the corresponding magnetic fields are equal to zero. The source of the electric field of static modes are charges residing on the surfaces of the multiply bounded structure.

Analogously to the 2D waveguide modes, theory shows that also the 3D eigenmodes are mutually orthogonal [54, pp. 529 - 532] and form a complete set⁷ of basis functions. The orthogonality condition for 3D eigenmodes is given for the electric fields by

$$\iiint_{\Omega} \tilde{\mathbf{E}}_{\ell}(\mathbf{r}) \cdot \tilde{\mathbf{E}}_n(\mathbf{r}) dV = \begin{cases} 2 W_n/\varepsilon, & \text{if } \ell = n, \\ 0, & \text{if } \ell \neq n, \end{cases} \quad (2.74)$$

and for the magnetic fields by

$$\iiint_{\Omega} \tilde{\mathbf{H}}_{\ell}(\mathbf{r}) \cdot \tilde{\mathbf{H}}_n(\mathbf{r}) dV = \begin{cases} 2 W_n/\mu, & \text{if } \ell = n, \\ 0, & \text{if } \ell \neq n. \end{cases} \quad (2.75)$$

Following Poynting's theorem (see Subsection 2.1.2) W_n denotes the electric, respectively magnetic, energy stored in the n th eigenmode.

It should be emphasized that the eigenmodes of very simple geometries are available by means of analytical techniques (see Appendix B.3 for the eigenmodes of a closed rectangular waveguide, i.e. for a brick resonator). For more sophisticated geometries a discrete eigenvalue formulation is established with the help of FIT [38, 42, 59] for example, and solved by numerical schemes.

2.4.1 Energy Dissipation and Quality Factors

So far, losses in the cavity are neglected. However, in real world applications energy, which is stored in the electric and magnetic fields of the cavity modes, is steadily lost due to different loss mechanisms. In accordance with Poynting's theorem (2.18) energy losses are separated into internal losses $P_{\text{int},n}(t)$ and external losses $P_{\text{ext},n}(t)$ of the n th mode. Modes resonating in lossy structures have complex-valued resonant frequencies:

$$\underline{\omega}_{\text{lsy},n} = \omega_{\text{lsy},n} + j\alpha_{\text{lsy},n}, \quad (2.76)$$

where

$$\alpha_{\text{lsy},n} = \frac{1}{2T_{\text{lsy},n}} \underbrace{\int_0^{T_{\text{lsy},n}} \frac{P_{\text{tot},n}(t)}{W_{\text{sto},n}(t)} dt}_{2\pi/Q_{\text{tot},n}}. \quad (2.77)$$

The total energy loss of the n th mode is denoted by $P_{\text{tot},n}(t) = P_{\text{int},n}(t) + P_{\text{ext},n}(t)$, the total energy stored in the mode by $W_{\text{sto},n}(t)$, and the periodicity of the mode

⁷Electric fields arising from charges in the domain Ω require an additional set of basis functions.

by $T_{\text{lsy},n} = 2\pi/\omega_{\text{lsy},n}$. The imaginary part of the complex angular frequency $\omega_{\text{lsy},n}$ describes the exponential decay of fields. Note that $\Re(\omega_{\text{lsy},n}) = \omega_{\text{lsy},n}$ is different to the resonant angular frequencies $\tilde{\omega}_n$ of eigenmodes of lossless structures. The statement (2.77) introduces the so-called *quality factor* $Q_{\text{tot},n}$. In contrast to the presented definition of the quality factor, the definition

$$Q_{\text{tot},n} = \omega_{\text{lsy},n} \frac{W_{\text{sto},n}}{P_{\text{tot},n}} \quad (2.78)$$

is much more popular in textbooks [12, 38, 55, 63]. Unfortunately, most of the textbooks refrain from specifying the relationship between instantaneous total energy $W_{\text{sto},n}(t)$ and energy loss $P_{\text{tot},n}(t)$ and the constants $W_{\text{sto},n}$ and $P_{\text{tot},n}$. The commonly known quality factor definition can be transferred into the definition given in (2.76) by averaging the time-dependent quantities over one period $T_{\text{lsy},n}$ as follows:

$$Q_{\text{tot},n} = \omega_{\text{lsy},n} \frac{T_{\text{lsy},n}}{\int_0^{T_{\text{lsy},n}} P_{\text{tot},n}(t)/W_{\text{sto},n}(t) dt} = \frac{2\pi}{\int_0^{T_{\text{lsy},n}} P_{\text{tot},n}(t)/W_{\text{sto},n}(t) dt}. \quad (2.79)$$

The quality factors are a measure for the energy loss of the individual resonances. Small losses lead to large quality factors and large time constants for the exponential decay. Indeed, $Q_{\text{tot},n}/\pi$ periods of the oscillation are needed for the amplitude of the electric or magnetic field of a resonance to decrease by a factor of $1/e$ whereas $Q_{\text{tot},n}/2/\pi$ periods are required for the energy to decrease by a factor of $1/e$. In addition to the total quality factor $Q_{\text{tot},n}$, two further quality factors are defined: the external quality factor $Q_{\text{ext},n}$ solely refers to external losses $P_{\text{ext},n}$, whereas the intrinsic quality factor $Q_{\text{int},n}$ solely accounts for internal losses $P_{\text{int},n}$.

2.4.2 Normalized Longitudinal Voltage and Shunt Impedance

The quantification of the interaction between charged particles traversing the resonator with approximately the speed of light $v \rightarrow c$ and the resonator eigenmodes is crucial for particle accelerators. Depending on the phase relation between charged particles and 3D modes, energy is transferred from the particle to the field or from the field to the particle. To quantify this mutual interaction, an accelerating voltage is defined [12]:

$$\underline{V}_{\text{acc},n}(x, y) = \int_0^d \tilde{E}_{n,z}(x, y, z) e^{j\tilde{\omega}_n z/c} dz, \quad (2.80)$$

where z is the longitudinal direction, $\tilde{E}_{n,z}(x, y, z)$ is the longitudinal component of the electric field of the n th 3D eigenmode, and d the length of the cavity. The voltages $\underline{V}_{\text{acc},n}(x = 0, y = 0)$ for particles on the design trajectory (indicated in

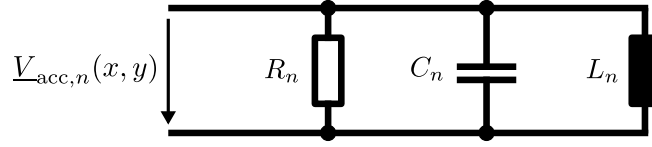


Figure 2.4: Simple equivalent circuit of the n th cavity resonance. The longitudinal voltage is denoted by $V_{\text{acc},n}(x, y)$. The losses due to the acceleration of charged particles is regarded in R_n , the energy stored in the electric field in C_n , and the energy stored in the magnetic field in L_n .

Figure 2.3 by the dashed grey line) are of special relevance. Nonetheless, the trajectories of the charged particles can have transversal offsets Δx and Δy from the design trajectories. It follows from (2.80) that the accelerating voltage depends on the integrated electric field strength along the symmetry axis of the cavity. According to (2.74), this field strength depends on the total energy stored in the 3D eigenmode. Therefore, it is desired to find a measure of the particle-beam (or beam-particle) interaction which is normalized with respect to the energy stored in the 3D eigenmode. To derive such a normalized quantity, a parallel circuit of an inductance, a capacitance, and an impedance is considered in Figure 2.4 as a simple equivalent circuit for a cavity resonance. The shunt impedance R_n models energy losses of the mode. The capacitance C_n and the inductance L_n model energy stored in electric and magnetic fields, respectively. Following circuit theory, the energy loss of the n th mode is given by

$$P_n = \frac{|V_{\text{acc},n}(x, y)|^2}{R_n} = \frac{\tilde{\omega}_n W_n}{Q_n}, \quad (2.81)$$

where Q_n is the respective quality factor. Reordering this statement delivers the accelerating voltage normalized with respect to the energy stored in the n th eigenmode:

$$\frac{R_n}{Q_n}(x, y) = \frac{|V_{\text{acc},n}(x, y)|^2}{\tilde{\omega}_n W_n}. \quad (2.82)$$

This normalized quantity is often referred to as the characteristic R/Q value of the n th resonance. It is a quantity which solely depends on the geometry of the cavity. For the sake of completeness, it should be noted that different definitions of the characteristic R/Q value are used in the accelerator physics community. For instance, the definition presented in [64, p. 589, (16.48)] differs from (2.82) by a factor of two.

3 System Theory and Model Order Reduction

This chapter introduces system theory and model order reduction. For this reason, the handling of waveguide ports of RF structures is shown first. Subsequently, the creation of state-space systems for RF structures is described. Both considerations are based on the previously described foundations of electromagnetic field theory. In the next step, essential properties of the generated state-space equations are discussed. Finally, the chapter ends with the description of an approach to reduce the order of the constructed state-space systems.

3.1 Waveguide Ports

This section discusses the formal treatment of waveguide ports and follows [2, Section II-A]. In fact, waveguide ports are central elements of the present thesis. By assumption, the RF structures under consideration solely exchange energy with the periphery by means of the ports. In addition, quantities related to the waveguide ports are used to combine the RF segments in such a way that a state-space representation of the entire structure is generated.

As mentioned in Chapter 2, amplitudes of incident and scattered waves are port quantities of practical relevance in RF regimes as they can be directly measured by the employment of network analyzers, for example. Nonetheless, this section focusses on modal voltages and currents for the following two reasons:

1. The employment of modal voltages and currents directly leads to a lossless impedance formulation, i.e. energy is inherently not lost via waveguide ports. In consequence, the numerical demand of the entire scheme is significantly reduced. For instance, complex algebra is avoided and solely real-valued eigenvectors and field vectors are required for the generation of reduced-order state-space models.
2. The commonly known Kirchhoff's circuit laws can be used to concatenate the individual segments. It should be stressed that these circuits are applicable in the context of this thesis, because these laws enforce the tangential electric and magnetic fields on the cut planes to be continuous.

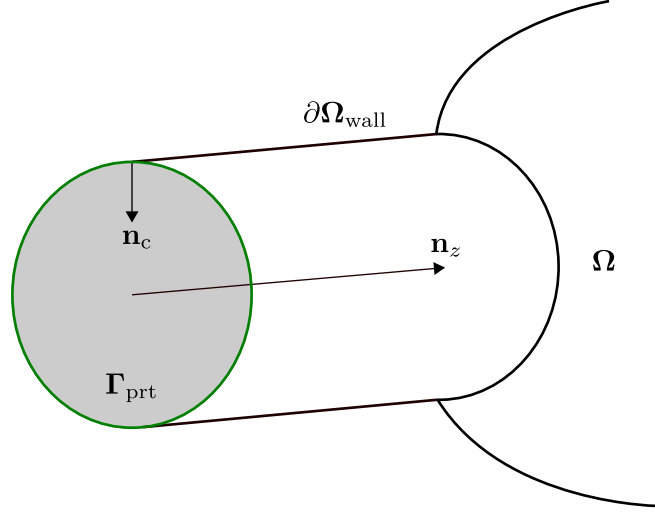


Figure 3.1: Waveguide port plane $\partial\Omega_{\text{prt}} = \Gamma_{\text{prt}}$ (grey facet) connected to an RF structure. The inner region Ω of the structure is made of an insulator with permittivity ε and permeability μ whereas the boundary $\partial\Omega_{\text{wall}}$ is assumed to be a perfect electric conductor. The vector \mathbf{n}_z is normal to the port plane and the vector $\mathbf{n}_c \in \Gamma_{\text{prt}}$ is normal to the contour of the waveguide boundary $\partial\Gamma_{\text{prt}}$ (indicated as green circle).

Figure 3.1 depicts a waveguide port of an RF structure. In contrast to Figure 2.2, the sketched structure is not longitudinally uniform. Without loss of generality the coordinate system is defined such that the port plane $\partial\Omega_{\text{prt}} = \Gamma_{\text{prt}}$ (indicated as grey facet) is allocated at $z = 0$ and that the normal component \mathbf{n}_z of the port plane is directed into the structure. The entire boundary $\partial\Omega_{\text{wall}}$ of the structure is assumed to be perfect electric conducting. Therefore, the tangential components of the electric field on the contour $\partial\Gamma_{\text{prt}} = \Gamma_{\text{prt}} \cap \partial\Omega_{\text{wall}}$ (marked in green) of the port plane vanish:

$$\mathbf{n}_c \times \mathbf{E}(\mathbf{r}, t) = \mathbf{0} \text{ on } \partial\Gamma_{\text{prt}}, \quad (3.1)$$

where $\mathbf{n}_c \in \Gamma_{\text{prt}}$ is a unit vector normal to the contour $\partial\Gamma_{\text{prt}}$. Deduced from Poynting's theorem (2.17), the components of the electric and magnetic fields tangential to Γ_{prt} are responsible for the longitudinal energy flow through the port plane Γ_{prt} . Consequently, the total instantaneous energy propagating (i.e. power) through the depicted port plane Γ_{prt} is determined by

$$P(t) = \iint_{\Gamma_{\text{prt}}} \mathbf{S}(\mathbf{r}_t, t) \cdot \mathbf{n}_z \, dA = \iint_{\Gamma_{\text{prt}}} \mathbf{E}_t(\mathbf{r}_t, t) \times \mathbf{H}_t(\mathbf{r}_t, t) \cdot \mathbf{n}_z \, dA, \quad (3.2)$$

where $\mathbf{S}(\mathbf{r}_t, t)$, $\mathbf{E}_t(\mathbf{r}_t, t)$, and $\mathbf{H}_t(\mathbf{r}_t, t)$ denote the transient Poynting vector, the transient transversal electric, and the transient transversal magnetic fields on the port

plane, respectively. They depend on the time t and on the transversal spatial coordinates $\mathbf{r}_t \in \Gamma_{\text{prt}}$.

As discussed in Section 2.3, transverse transient electric and magnetic fields in a plane with a perfect conducting enclosure are expressible as a summation of a complete set $\mathbf{L}_{t,m}(\mathbf{r}_t)$ of spatial dependent field patterns (refer to (2.43), (2.44) in general and to Appendix A.2 for the first eight 2D port modes of circular waveguide ports in particular). Thus, electric and magnetic fields in the port plane (grey facet in Figure 3.1) are expandable in terms of

$$\mathbf{E}_t(\mathbf{r}_t, t) = \sum_{m=1}^{\infty} \underbrace{\mathbf{L}_{t,m}(\mathbf{r}_t) v_m(t)}_{\mathbf{E}_{t,m}(\mathbf{r}_t, t)}, \quad (3.3)$$

$$\mathbf{H}_t(\mathbf{r}_t, t) = \sum_{m=1}^{\infty} \underbrace{\mathbf{n}_z \times \mathbf{L}_{t,m}(\mathbf{r}_t) i_m(t)}_{\mathbf{H}_{t,m}(\mathbf{r}_t, t)}. \quad (3.4)$$

If the transversal electric and magnetic fields (3.3) and (3.4) are substituted in (3.2) and the orthonormality (2.49) of the field patterns is employed, a formula for the total instantaneous power as a function of modal voltages and currents is obtained:

$$P(t) = \sum_{m=1}^{\infty} v_m(t) i_m(t). \quad (3.5)$$

The equation conveys that the total power transmitted through the port boundary Γ_{prt} is the summation of the power contribution of each individual waveguide port mode. Also on account of the orthonormality (2.49) of the modal field patterns, the modal port voltages and currents are directly computable from the transverse electric and magnetic fields in the port plane by means of

$$v_m(t) = \iint_{\Gamma_{\text{prt}}} \mathbf{L}_{t,m}(\mathbf{r}_t) \cdot \mathbf{E}_t(\mathbf{r}_t, t) dA, \quad (3.6)$$

and

$$i_m(t) = \iint_{\Gamma_{\text{prt}}} \mathbf{n}_z \times \mathbf{L}_{t,m}(\mathbf{r}_t) \cdot \mathbf{H}_t(\mathbf{r}_t, t) dA. \quad (3.7)$$

In an intermediate step, it is assumed that the tangential magnetic fields on the port plane Γ_{prt} vanish by assigning perfect magnetic conducting boundary conditions:

$$\mathbf{n}_z \times \mathbf{H}(\mathbf{r}_t, t) = \mathbf{H}_t(\mathbf{r}_t, t) = \mathbf{0} \text{ on } \Gamma_{\text{prt}}. \quad (3.8)$$

As the tangential components of the magnetic fields are zero, no energy propagates through the port plane. Moreover, according to (3.7), the perfect magnetic boundary

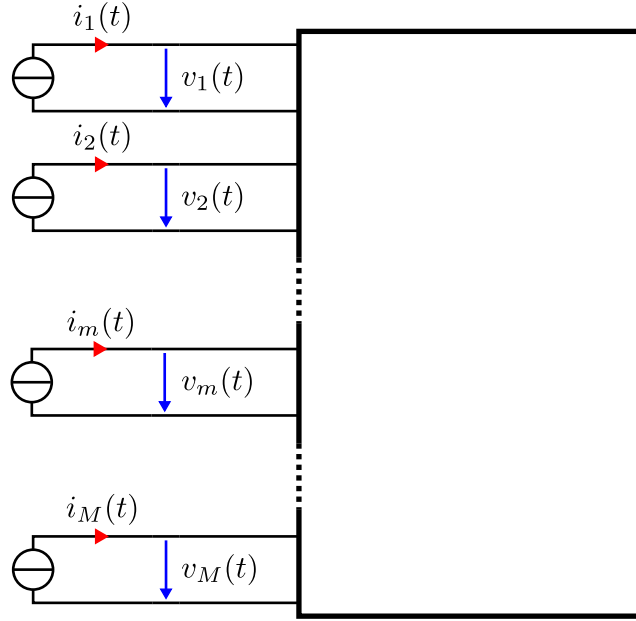


Figure 3.2: Abstract counterpart of the waveguide port plane depicted in Figure 3.1. Here only M (of an infinite number of) port modes are indicated by terminals. Each terminal is equipped with voltages $v_m(t)$, indicated by blue arrows, and currents $i_m(t)$, indicated by red arrows. The current sources connected to the M terminals are assumed to be ideal (their inner resistivity is infinite).

enforces the modal port currents to be zero. Based on the described assumptions, the waveguide port plane can be considered in terms of the abstract network equivalent depicted in Figure 3.2 where all modal port currents are equal to zero, i.e. $i_m(t) = 0$. It should be emphasized, that for a single waveguide port of an RF structure an infinite number of port modes $\mathbf{L}_{t,m}(\mathbf{r}_t)$ exists and therefore an infinite number of terminals with modal port voltages and currents arises. However, only a finite number of port modes is of practical relevance: Following Subsection 2.3.2, only a finite number of waveguide modes can propagate in the frequency interval $f_{\min} < f < f_{\max}$, i.e. the waveguide modes with $f_{\text{co},m} < f$. The remaining modes are evanescent waveguide modes with $f_{\text{co},m} > f_{\max}$. Their field distributions exponentially decay along regions of uniform cross section. Note that waveguide ports of RF structures are typically designed in such a way that only one port mode propagates in the operational frequency range in order to have distinct propagation properties.

The waveguide modes at the ports can be excited by transient modal port currents $i_m(t) \neq 0$. According to (3.4), non-zero modal port currents are connected to tangential magnetic fields on $\mathbf{\Gamma}_{\text{prt}}$. These tangential magnetic fields are generated based on electric current densities which are imposed on the port plane $\mathbf{\Gamma}_{\text{prt}}$. Following *Schelkunoff's* surface equivalence theorem [56, Section 1.8, pp. 37 - 39], the

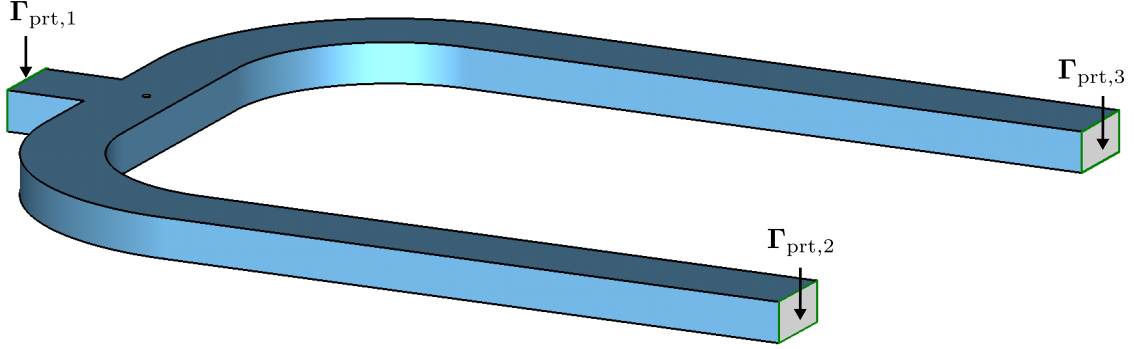


Figure 3.3: Rectangular waveguide power splitter as an example for an RF structure. The grey facets with the green enclosure represent waveguide ports.

electric excitation current density exciting the m th port mode is chosen based on the transverse modal magnetic field $\mathbf{H}_{t,m}(\mathbf{r}_t, t)$:

$$\mathbf{J}_{\text{prt},m}(\mathbf{r}, t) = \mathbf{n}_z \times \mathbf{H}_{t,m}(\mathbf{r}_t, t) \delta(z), \quad (3.9)$$

where $\delta(z)$ is the Dirac delta function. Substituting $\mathbf{H}_{t,m}(\mathbf{r}_t, t)$ with its corresponding modal port pattern and its modal current (see e.g. (2.44) or (3.4)) yields

$$\mathbf{J}_{\text{prt},m}(\mathbf{r}, t) = \mathbf{J}_{\text{prt},m}(\mathbf{r}) i_m(t). \quad (3.10)$$

Here, $\mathbf{J}_{\text{prt},m}(\mathbf{r}) = -\mathbf{L}_{t,m}(\mathbf{r}_t) \delta(z)$ are the spatially dependent current density patterns which correspond to the m th 2D port mode. The patterns are solely unequal to zero in the port plane Γ_{prt} .

3.2 State-Space Systems of RF Structures

State-space equations are a common and powerful formalism to model the dynamic properties of a wide range of applications arising from different scientific disciplines. State-space equations are used in engineering to model for instance: electrical circuits, electrical motors, chemical reactors, satellites in earth orbits, and airplanes [65]. In biology they are employed to express, for example, the dynamics of two populations, where one population acts as a predator and the other as prey [66].

Figure 3.3 depicts a waveguide power splitter. This splitter is used in the following as an example for an RF structure. The waveguide ports of the power splitter are indicated by grey facets with a green enclosure. The ports are treated according to Section 3.1. Figure 3.4 shows the abstract counterpart of the waveguide power splitter as a white box model. The modal voltages and currents are denoted by $v_{p,m}(t)$ and $i_{p,m}(t)$ where p is the port index and m the index of the mode at port

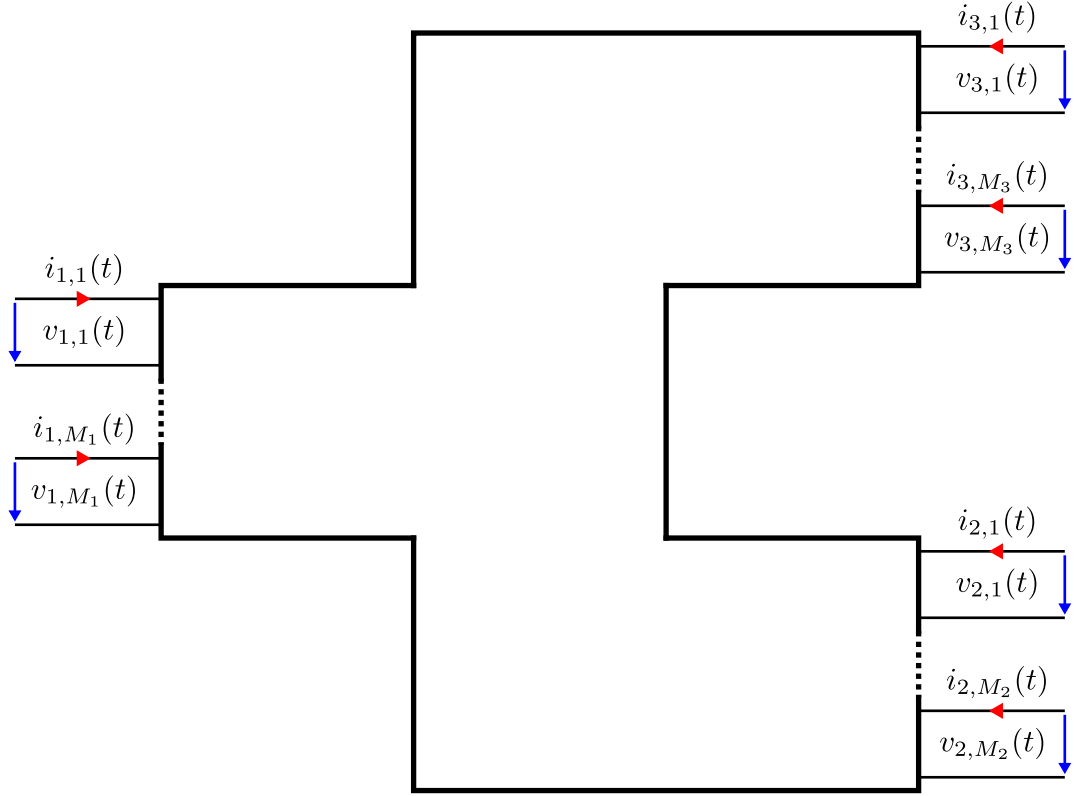


Figure 3.4: Abstract counterpart of the RF structure depicted in Figure 3.3. The ports and the respective 2D port modes are indicated by terminals. At the terminals the voltages $v_{p,m}(t)$ and currents $i_{p,m}(t)$ are assigned. Here, p is the port index, and m the considered 2D mode at the port. At the p th port M_p modes are regarded. In contrast to Figure 3.2, the current sources are not explicitly sketched in order to save place.

p . The example structure is equipped with $P = 3$ ports in total, whereas M_p modes are considered at the p th port. Consequently,

$$N_t = \sum_{p=1}^P M_p \quad (3.11)$$

terminals belong to the white box shown in Figure 3.4. If only one 2D port mode is considered at the p th port (typically this is the 2D port mode with the smallest cutoff frequency), the second index of the modal voltages and currents is omitted for the sake of simplicity, i.e. $v_p(t)$ and $i_p(t)$.

The term white box is chosen as the relationship between port voltages and currents is determined by Maxwell's equations. Formally, the relationship between the

port quantities is expressible by

$$\frac{d}{dt}\mathbf{x}_f(t) = \mathbf{A}_f \mathbf{x}_f(t) + \mathbf{B}_f \mathbf{i}(t), \quad (3.12)$$

$$\mathbf{v}(t) = \mathbf{C}_f \mathbf{x}_f(t) + \mathbf{D}_f \mathbf{i}(t), \quad (3.13)$$

because the RF structures of interest are linear and time-invariant (LTI). The state-space system (3.12) - (3.13) is constituted by the *state matrix* $\mathbf{A}_f \in \mathbb{R}^{N_f \times N_f}$, the *input matrix* $\mathbf{B}_f \in \mathbb{R}^{N_f \times N_t}$, the *control matrix* or *output matrix* $\mathbf{C}_f \in \mathbb{R}^{N_t \times N_f}$, and the *direct input-output link* $\mathbf{D}_f \in \mathbb{R}^{N_t \times N_t}$. The vector $\mathbf{x}_f(t) \in \mathbb{R}^{N_f}$ is referred to as *state vector* and exists in the state space \mathbb{R}^{N_f} [65]. The number of states N_f is also often referred to as the number of degrees of freedom. The matrices and vectors in (3.12) and (3.13) are equipped with the subscript “f” to indicate that they correspond to a linear first-order¹ coupled system of ordinary differential equations. This system is continuous in time. The *input vector* or *vector of control inputs* $\mathbf{i}(t)$ acts as excitation term for the system and holds the currents of all N_t terminals:

$$\mathbf{i}(t) = (i_{1,1}(t), \dots, i_{1,M_1}(t), i_{2,1}(t), \dots, i_{2,M_2}(t), \dots, \\ i_{P,1}(t), \dots, i_{P,M_P}(t))^T \in \mathbb{R}^{N_t}. \quad (3.14)$$

The *output vector* or *vector of observations*

$$\mathbf{v}(t) = (v_{1,1}(t), \dots, v_{1,M_1}(t), v_{2,1}(t), \dots, v_{2,M_2}(t), \dots, \\ v_{P,1}(t), \dots, v_{P,M_P}(t))^T \in \mathbb{R}^{N_t} \quad (3.15)$$

comprises the port voltages at the terminals. The state-space system allows for the computation of transient port voltages $\mathbf{v}(t)$ by means of standard ordinary differential equation solvers based on an initial condition $\mathbf{x}_f(t_0) = \mathbf{x}_{f,0}$ and the transient current stimulus $\mathbf{i}(t)$.

In the following subsections, the generation of state-space systems for lossless linear RF structures is described. Subsection 3.2.1 presents an approach based on analytical derivations and Subsection 3.2.2 depicts a derivation based on the FIT formalism using the nomenclature introduced in Section 2.2. In the framework of this thesis, two sets of state-space systems are discussed. The first set corresponds to a first-order state-space system in the form (3.12) - (3.13) and the second set to a second-order² state-space system given by

$$\frac{d^2}{dt^2}\mathbf{x}_s(t) = \mathbf{A}_s \mathbf{x}_s(t) + \mathbf{B}_s \frac{d}{dt}\mathbf{i}(t), \quad (3.16)$$

$$\mathbf{v}(t) = \mathbf{C}_s \mathbf{x}_s(t) + \mathbf{D}_s \frac{d}{dt}\mathbf{i}(t). \quad (3.17)$$

¹First-order because (3.12) solely contains first-order derivatives.

²Second-order because (3.16) solely contains a second-order derivatives.

In close analogy to the first-order state-space system, the second-order state-space system is constituted by the state matrix $\mathbf{A}_s \in \mathbb{R}^{N_s \times N_s}$, the input matrix $\mathbf{B}_s \in \mathbb{R}^{N_s \times N_t}$, the control matrix or output matrix $\mathbf{C}_s \in \mathbb{R}^{N_t \times N_s}$, and the direct input-output link $\mathbf{D}_s \in \mathbb{R}^{N_t \times N_t}$. The vector $\mathbf{x}_s(t) \in \mathbb{R}^{N_s}$ denotes the state vector. The involved matrices are equipped with the subscript “s” to stress that they correspond to a second-order system. This system is continuous in time as well.

The first-order and the second-order representation are equivalently usable to describe the electromagnetic properties of the RF structures which are relevant to this thesis. Compared to the first-order state-space representation, the corresponding second-order state-space representation has only half the number of degrees of freedom, i.e. $N_s = N_f/2$. Therefore, the second-order representation is the preferred formalism for model order reduction, concatenation of state-space models, the computation of eigenmodes, and frequency-domain transfer functions. The first-order representation is appropriate when losses are accounted for by perturbation approaches, because losses require a first order differentiation term. Additionally, the first-order representation is used when transient system responses have to be computed by means of ordinary differential equation solvers, because these solvers typically require first-order equations rather than second-order equations.

3.2.1 State Matrices Arising from Continuous Case

To generate state-space systems for lossless RF structures with an analytical approach [2, Section II-C], the concepts published in [3, 4] are generalized so that waveguide ports are accounted for. To the best knowledge of the author this generalization is one of the original contributions of the current thesis. The proposed method requires 2D port modes (see Section 3.1) and 3D eigenmodes (see Section 2.4) of the RF structure.

As an initial step, the transient electric fields in the structure are expressed in terms of a weighted summation of normalized 3D eigenmodes:

$$\mathbf{E}(\mathbf{r}, t) := \sum_{n=1}^{N_e} \frac{\tilde{\mathbf{E}}_n(\mathbf{r})}{\sqrt{2W_n}} x_n(t). \quad (3.18)$$

Here, $x_n(t)$ are the transient weighting factors for the electric fields $\tilde{\mathbf{E}}_n(\mathbf{r})$ of the n th eigenmode of the RF structure. For a complete eigenmode expansion an infinite number of 3D eigenmodes has to be taken into account, i.e. $N_e \rightarrow \infty$. Apart from the fact that in most cases these modes are not available, dealing with an infinite number of modes is virtually impossible. Therefore, the modal expansion (3.18) has to cease after a finite number of terms and is an approximation³.

³The consideration in Appendix C.1 reveals that the error in the electric field of the eigenmode expansion scales in the limit linear with the number of 3D eigenmodes, i.e. doubling the number of 3D eigenmodes, leads to a reduction of the error by a factor of two.

As discussed in Section 2.4, the eigenmodes satisfy the 3D Helmholtz equation (2.68). On account of the perfect electric conductivity of the boundaries,

$$\mathbf{n} \times \tilde{\mathbf{E}}_n(\mathbf{r}) = \mathbf{0} \text{ on } \partial\Omega_{\text{wall}} \quad (3.19)$$

holds for the 3D eigenmodes. Following Section 3.1, perfect magnetic conducting boundary conditions

$$\mathbf{n} \cdot \tilde{\mathbf{E}}_n(\mathbf{r}) = 0 \text{ on } \partial\Omega_{\text{prts}} \quad (3.20)$$

are enforced for the 3D eigenmodes on the port planes. The latter boundary condition directly corresponds to (3.8). Similar to port modes satisfying the 2D Helmholtz equation (2.46), the eigenmodes satisfying the 3D Helmholtz equation neither depend on frequency nor on time, but on the shape of the RF structure. Therefore, they can be employed for field expansions in frequency and in time domain.

The substitution of electric fields in the wave equation (2.20) for a charge-free domain ($\rho(\mathbf{r}, t) = 0$) by the approach (3.18) delivers

$$\sum_{n=1}^{N_e} \frac{1}{\sqrt{2W_n}} \left(\Delta \tilde{\mathbf{E}}_n(\mathbf{r}) x_n(t) - \varepsilon \mu \tilde{\mathbf{E}}_n(\mathbf{r}) \frac{\partial^2}{\partial t^2} x_n(t) \right) = \mu \frac{\partial}{\partial t} \mathbf{J}_{\text{ic}}(\mathbf{r}, t) \quad (3.21)$$

assuming convection and Ohmic current densities to be equal to zero. As the eigenmodes $\tilde{\mathbf{E}}_n(\mathbf{r})$ satisfy the 3D Helmholtz equation, $\Delta \tilde{\mathbf{E}}_n(\mathbf{r})$ can be replaced in (3.21) by $-\tilde{\omega}_n^2 \varepsilon \mu \tilde{\mathbf{E}}_n(\mathbf{r})$:

$$\sum_{n=1}^{N_e} \frac{\tilde{\mathbf{E}}_n(\mathbf{r})}{\sqrt{2W_n}} \left(\tilde{\omega}_n^2 x_n(t) + \frac{\partial^2}{\partial t^2} x_n(t) \right) = -\frac{1}{\varepsilon} \frac{\partial}{\partial t} \mathbf{J}_{\text{ic}}(\mathbf{r}, t). \quad (3.22)$$

Due to this step the spatial derivatives are excluded and an ordinary differential equation arises. Next, (3.22) is multiplied with the ℓ th normalized eigenmode $\tilde{\mathbf{E}}_\ell(\mathbf{r})/\sqrt{2W_\ell}$ and integrated over the entire volume Ω :

$$\begin{aligned} \sum_{n=1}^{N_e} \frac{1}{2\sqrt{W_n W_\ell}} \iiint_{\Omega} \tilde{\mathbf{E}}_\ell(\mathbf{r}) \cdot \tilde{\mathbf{E}}_n(\mathbf{r}) \, dV \left(\tilde{\omega}_n^2 x_n(t) + \frac{\partial^2}{\partial t^2} x_n(t) \right) \\ = -\frac{1}{\varepsilon} \frac{\partial}{\partial t} \iiint_{\Omega} \frac{\tilde{\mathbf{E}}_\ell(\mathbf{r}) \cdot \mathbf{J}_{\text{ic}}(\mathbf{r}, t)}{\sqrt{2W_\ell}} \, dV. \end{aligned} \quad (3.23)$$

On account of the orthogonality of the 3D eigenmodes (2.74), the volume integral is equal to zero for $n \neq \ell$ and equal to $2W_n/\varepsilon$ for $n = \ell$. Therefore, only the n th term is left from the summation on the left-hand side of (3.23) and

$$\left(\tilde{\omega}_n^2 x_n(t) + \frac{\partial^2}{\partial t^2} x_n(t) \right) = -\frac{\partial}{\partial t} \iiint_{\Omega} \frac{\tilde{\mathbf{E}}_n(\mathbf{r}) \cdot \mathbf{J}_{\text{ic}}(\mathbf{r}, t)}{\sqrt{2W_n}} \, dV \quad (3.24)$$

is obtained. The excitation current density $\mathbf{J}_{\text{ic}}(\mathbf{r}, t)$ is a superposition of the impressed current densities (refer to (3.10)). At the p th port M_p modal currents are assigned, so that the total excitation current density is given by:

$$\mathbf{J}_{\text{ic}}(\mathbf{r}, t) = \sum_{p=1}^P \sum_{m=1}^{M_p} \mathbf{J}_{\text{prt},p,m}(\mathbf{r}) i_{p,m}(t). \quad (3.25)$$

These currents generate the required tangential magnetic fields⁴ on $\Gamma_{\text{prt},p}$ which are not covered by the 3D eigenmodes due to the PMC boundary condition (3.20). As mentioned in Section 3.1, the spatial-dependent current patterns $\mathbf{J}_{\text{prt},p,m}(\mathbf{r})$ are only non-zero in the port planes $\Gamma_{\text{prt},p}$. Therefore, the volume integral on the right-hand side of (3.24) can be reduced to integrals over port surfaces:

$$\begin{aligned} \iiint_{\Omega} \frac{\tilde{\mathbf{E}}_n(\mathbf{r}) \cdot \mathbf{J}_{\text{ic}}(\mathbf{r}, t)}{\sqrt{2W_n}} dV = \\ - \sum_{p=1}^P \sum_{m=1}^{M_p} \underbrace{\frac{1}{\sqrt{2W_n}} \iint_{\Gamma_{\text{prt},p}} \tilde{\mathbf{E}}_n(\mathbf{r}_t) \cdot \mathbf{L}_{t,p,m}(\mathbf{r}_t) dA}_{h_{n,p,m}} i_{p,m}(t). \end{aligned} \quad (3.26)$$

The scalar constants $h_{n,p,m}$ quantify the interaction between the m th 2D port mode at port p and the n th 3D eigenmode. Replacing the integral in (3.24) by (3.26) and employing the definition of the scalar constants yields

$$\left(\tilde{\omega}_n^2 x_n(t) + \frac{d^2}{dt^2} x_n(t) \right) = \sum_{p=1}^P \sum_{m=1}^{M_p} h_{n,p,m} \frac{d}{dt} i_{p,m}(t). \quad (3.27)$$

This equation describes the evolution of the transient weighting factors $x_n(t)$ of the 3D eigenmodes due to modal current excitations at the waveguide ports.

To establish the relationship between the transient weighting factors $x_n(t)$ and the voltages at the waveguide ports, (3.6) is recalled and modified so that the voltage of the m th mode at the p th port can be determined. Subsequently, the electric fields

⁴Computing the magnetic fields in the RF structure by means of Faraday's law of induction and the ansatz (3.18) does not deliver correct results for the tangential magnetic field on the surfaces of the waveguide ports, because the eigenmodes are chosen such that their tangential magnetic field is zero on $\Gamma_{\text{prt},p}$. The missing tangential magnetic fields on $\Gamma_{\text{prt},p}$ need to be constructed based on the surface currents $\mathbf{J}_{\text{ic}}(\mathbf{r}, t)$.

are replaced by the ansatz (3.18):

$$\begin{aligned}
 v_{p,m}(t) &= \iint_{\Gamma_{\text{prt},p}} \mathbf{E}(\mathbf{r}_t, t) \cdot \mathbf{L}_{t,p,m}(\mathbf{r}_t) dA \\
 &= \sum_{n=1}^{N_e} \underbrace{\frac{1}{\sqrt{2W_n}} \iint_{\Gamma_{\text{prt},p}} \tilde{\mathbf{E}}_n(\mathbf{r}_t) \cdot \mathbf{L}_{t,p,m}(\mathbf{r}_t) dA}_{h_{n,p,m}} x_n(t)
 \end{aligned} \tag{3.28}$$

First-Order State-Space System

To generate a first-order state-space system, (3.27) is integrated with respect to time:

$$\left(\tilde{\omega}_n \hat{x}_n(t) + \frac{d}{dt} x_n(t) \right) = \sum_{p=1}^P \sum_{m=1}^{M_p} h_{n,p,m} i_{p,m}(t), \tag{3.29}$$

where

$$\frac{d}{dt} \hat{x}_n(t) = \tilde{\omega}_n x_n(t). \tag{3.30}$$

The integration constants are set to zero as it is assumed that the excitation currents are equal to zero before the initial time t_0 . Collecting (3.29) and (3.30) for N_e considered 3D eigenmodes delivers the state equation

$$\begin{aligned}
 \frac{d}{dt} \underbrace{\begin{pmatrix} \hat{x}_1(t) \\ x_1(t) \\ \hat{x}_2(t) \\ x_2(t) \\ \vdots \\ \hat{x}_{N_e}(t) \\ x_{N_e}(t) \end{pmatrix}}_{\mathbf{x}_{\text{fc}}(t)} &= \underbrace{\begin{pmatrix} 0 & \tilde{\omega}_1 & 0 & 0 & \dots & 0 & 0 \\ -\tilde{\omega}_1 & 0 & 0 & 0 & \dots & 0 & 0 \\ 0 & 0 & 0 & \tilde{\omega}_2 & \dots & 0 & 0 \\ 0 & 0 & -\tilde{\omega}_2 & 0 & \dots & 0 & 0 \\ \vdots & \vdots & \vdots & \vdots & \ddots & \vdots & \vdots \\ 0 & 0 & 0 & 0 & & 0 & \tilde{\omega}_{N_e} \\ 0 & 0 & 0 & 0 & \dots & -\tilde{\omega}_{N_e} & 0 \end{pmatrix}}_{\mathbf{A}_{\text{fc}}} \underbrace{\begin{pmatrix} \hat{x}_1(t) \\ x_1(t) \\ \hat{x}_2(t) \\ x_2(t) \\ \vdots \\ \hat{x}_{N_e}(t) \\ x_{N_e}(t) \end{pmatrix}}_{\mathbf{x}_{\text{fc}}(t)} \\
 &+ \underbrace{\begin{pmatrix} 0 & \dots & 0 & \dots & 0 & \dots & 0 \\ h_{1,1,1} & \dots & h_{1,1,M_1} & \dots & h_{1,P,1} & \dots & h_{1,P,M_P} \\ 0 & \dots & 0 & \dots & 0 & \dots & 0 \\ h_{2,1,1} & \dots & h_{2,1,M_1} & \dots & h_{2,P,1} & \dots & h_{2,P,M_P} \\ \vdots & & \vdots & \vdots & \vdots & \vdots & \vdots \\ 0 & \dots & 0 & \dots & 0 & \dots & 0 \\ h_{N_e,1,1} & \dots & h_{N_e,1,M_1} & \dots & h_{N_e,P,1} & \dots & h_{N_e,P,M_P} \end{pmatrix}}_{\mathbf{B}_{\text{fc}}} \underbrace{\begin{pmatrix} i_{1,1}(t) \\ \vdots \\ i_{1,M_1}(t) \\ \vdots \\ i_{P,1}(t) \\ \vdots \\ i_{P,M_P}(t) \end{pmatrix}}_{\mathbf{i}(t)}.
 \end{aligned} \tag{3.31}$$

To derive the corresponding output equation, (3.28) is collected for all modal voltages and all 3D eigenmodes by

$$\underbrace{\begin{pmatrix} v_{1,1}(t) \\ \vdots \\ v_{1,M_1}(t) \\ \vdots \\ v_{P,1}(t) \\ \vdots \\ v_{P,M_P}(t) \end{pmatrix}}_{\mathbf{v}(t)} = \underbrace{\begin{pmatrix} 0 & h_{1,1,1} & 0 & h_{2,1,1} & \dots & 0 & h_{N_e,1,1} \\ \vdots & \vdots & \vdots & \vdots & & \vdots & \vdots \\ 0 & h_{1,1,M_1} & 0 & h_{2,1,M_1} & \dots & 0 & h_{N_e,1,M_1} \\ \vdots & \vdots & \vdots & \vdots & & \vdots & \vdots \\ 0 & h_{1,P,1} & 0 & h_{2,P,1} & \dots & 0 & h_{N_e,P,1} \\ \vdots & \vdots & \vdots & \vdots & & \vdots & \vdots \\ 0 & h_{1,P,M_P} & 0 & h_{2,P,M_P} & \dots & 0 & h_{N_e,P,M_P} \end{pmatrix}}_{\mathbf{C}_{\text{fc}}} \underbrace{\begin{pmatrix} \hat{x}_1(t) \\ x_1(t) \\ \hat{x}_2(t) \\ x_2(t) \\ \vdots \\ \hat{x}_{N_e}(t) \\ x_{N_e}(t) \end{pmatrix}}_{\mathbf{x}_{\text{fc}}(t)}. \quad (3.32)$$

The statements (3.31) and (3.32) are referred to as the first-order state-space equation of a lossless RF structure arising from the continuous case. The subscript “fc” of the respective matrices and vectors highlights that these quantities belong to the first-order system received from the continuous case. The state-space system has $N_f = 2N_e$ degrees of freedom ($\mathbf{x}_{\text{fc}} \in \mathbb{R}^{2N_e}$), the output matrix is the transposed of the input matrix ($\mathbf{C}_{\text{fc}} = \mathbf{B}_{\text{fc}}^T \in \mathbb{R}^{N_t \times 2N_e}$), the sparse system matrix is skew-symmetric ($\mathbf{A}_{\text{fc}} = -\mathbf{A}_{\text{fc}}^T \in \mathbb{R}^{2N_e \times 2N_e}$), and the direct input-output link equals zero ($\mathbf{D}_{\text{fc}} = \mathbf{0} \in \mathbb{R}^{N_t \times N_t}$).

Second-Order State-Space System

The statement (3.27) is directly expressible for N_e considered 3D eigenmodes as the second-order system

$$\underbrace{\frac{d^2}{dt^2} \begin{pmatrix} x_1(t) \\ x_2(t) \\ \vdots \\ x_{N_e}(t) \end{pmatrix}}_{\mathbf{x}_{\text{sc}}(t)} = \underbrace{\begin{pmatrix} -\tilde{\omega}_1^2 & 0 & \dots & 0 \\ 0 & -\tilde{\omega}_2^2 & \dots & 0 \\ \vdots & \vdots & \ddots & \vdots \\ 0 & 0 & \dots & -\tilde{\omega}_{N_e}^2 \end{pmatrix}}_{\mathbf{A}_{\text{sc}}} \underbrace{\begin{pmatrix} x_1(t) \\ x_2(t) \\ \vdots \\ x_{N_e}(t) \end{pmatrix}}_{\mathbf{x}_{\text{sc}}(t)} + \underbrace{\begin{pmatrix} h_{1,1,1} & \dots & h_{1,1,M_1} & \dots & h_{1,P,1} & \dots & h_{1,P,M_P} \\ h_{2,1,1} & \dots & h_{2,1,M_1} & \dots & h_{2,P,1} & \dots & h_{2,P,M_P} \\ \vdots & & \vdots & & \vdots & & \vdots \\ h_{N_e,1,1} & \dots & h_{N_e,1,M_1} & \dots & h_{N_e,P,1} & \dots & h_{N_e,P,M_P} \end{pmatrix}}_{\mathbf{B}_{\text{sc}}} \frac{d}{dt} \underbrace{\begin{pmatrix} i_{1,1}(t) \\ \vdots \\ i_{1,M_1}(t) \\ \vdots \\ i_{P,1}(t) \\ \vdots \\ i_{P,M_P}(t) \end{pmatrix}}_{\mathbf{i}(t)}. \quad (3.33)$$

Based on (3.28) and the state-vector $\mathbf{x}_{\text{sc}}(t)$, the corresponding output equation reads as

$$\underbrace{\begin{pmatrix} v_{1,1}(t) \\ \vdots \\ v_{1,M_1}(t) \\ \vdots \\ v_{P,1}(t) \\ \vdots \\ v_{P,M_P}(t) \end{pmatrix}}_{\mathbf{v}(t)} = \underbrace{\begin{pmatrix} h_{1,1,1} & h_{2,1,1} & \dots & h_{N_e,1,1} \\ \vdots & \vdots & & \vdots \\ h_{1,1,M_1} & h_{2,1,M_1} & \dots & h_{N_e,1,M_1} \\ \vdots & \vdots & & \vdots \\ h_{1,P,1} & h_{2,P,1} & \dots & h_{N_e,P,1} \\ \vdots & \vdots & & \vdots \\ h_{1,P,M_P} & h_{2,P,M_P} & \dots & h_{N_e,P,M_P} \end{pmatrix}}_{\mathbf{C}_{\text{sc}}} \underbrace{\begin{pmatrix} x_1(t) \\ x_2(t) \\ \vdots \\ x_{N_e}(t) \end{pmatrix}}_{\mathbf{x}_{\text{sc}}(t)}. \quad (3.34)$$

The subscript “sc” denotes that the matrices and vectors belong to the second-order system arising from the continuous case. This second-order system has N_e degrees of freedom ($\mathbf{x}_{\text{sc}} \in \mathbb{R}^{N_e}$). The output matrix is the transpose of the input matrix ($\mathbf{C}_{\text{sc}} = \mathbf{B}_{\text{sc}}^T \in \mathbb{R}^{N_t \times N_e}$). The state matrix \mathbf{A}_{sc} is a diagonal matrix and therefore it is symmetric ($\mathbf{A}_{\text{sc}} = \mathbf{A}_{\text{sc}}^T \in \mathbb{R}^{N_e \times N_e}$). Moreover, \mathbf{A}_{sc} is negative semidefinite ($\mathbf{x}_{\text{sc}}^T \mathbf{A}_{\text{sc}} \mathbf{x}_{\text{sc}} \leq 0 \forall \mathbf{x}_{\text{sc}}$) (see Appendix C.3) and the direct input-output link equals zero ($\mathbf{D}_{\text{sc}} = \mathbf{0} \in \mathbb{R}^{N_t \times N_t}$).

3.2.2 State Matrices Arising from Discrete Case

This subsection follows [40, 41] and discusses the generation of state-space systems for lossless RF structures directly arising from the FIT approach (refer to Chapter 2.2). Constructing the state-space systems from the discrete case requires the FIT matrices which are obtained from the discretization of the geometry under concern.

First-Order State-Space System

To formulate the FIT equations in terms of a state-space model, the magnetic fluxes in the discrete induction law (2.24) are replaced by the magnetic grid voltages using (2.41). In addition, the electric fluxes in the discrete form of Ampère’s law (2.25) are replaced by the electric grid voltages employing (2.39). Both equations can be combined to

$$\frac{d}{dt} \begin{pmatrix} \widehat{\mathbf{e}}(t) \\ \widehat{\mathbf{h}}(t) \end{pmatrix} = \begin{pmatrix} \mathbf{0} & \mathcal{M}_{\epsilon}^{-1} \mathbf{C}^T \\ -\mathcal{M}_{\mu}^{-1} \mathbf{C} & \mathbf{0} \end{pmatrix} \begin{pmatrix} \widehat{\mathbf{e}}(t) \\ \widehat{\mathbf{h}}(t) \end{pmatrix} - \begin{pmatrix} \mathcal{M}_{\epsilon}^{-1} \widehat{\mathbf{j}}_{\text{ic}}(t) \\ \mathbf{0} \end{pmatrix} \quad (3.35)$$

assuming the convection grid currents $\widehat{\mathbf{j}}_{\text{cc}}(t)$ to be equal to zero. Moreover, on account of the absence of losses, the Ohmic grid currents $\widehat{\mathbf{j}}_{\sigma}(t)$ are zero as well. In contrast to Section 2.2, time-dependent quantities are highlighted accordingly

in (3.35). The matrices \mathcal{M}_ε and \mathcal{M}_μ are diagonal and therefore they are easily invertible. The excitation current densities are determined by means of the mapping

$$-\hat{\mathbf{j}}_{\text{ic}}(t) = \mathcal{R} \mathcal{D}_\beta \mathbf{i}(t). \quad (3.36)$$

The vector $\mathbf{i}(t)$ comprises the modal excitation currents. Similar to the continuous case (3.10), the statement (3.36) impresses currents on the surfaces of the waveguide ports according to the considered 2D port modes. The output equation corresponding to (3.35) is given by

$$\mathbf{v}(t) = (\mathcal{R}^T \quad \mathbf{0}) \begin{pmatrix} \hat{\mathbf{e}}(t) \\ \hat{\mathbf{h}}(t) \end{pmatrix}. \quad (3.37)$$

The matrix $\mathcal{R} \in \mathbb{R}^{3N_p \times N_t}$ contains the field patterns of the 2D port modes which arise from the FIT analogon of the 2D Helmholtz equation (2.46) on the cross sections of the ports. A rigorous discussion about determining the 2D port modes by means of FIT can be found in [42, 60] whereas the generation of \mathcal{R} is specified in detail in [41, 42]. The diagonal matrix $\mathcal{D}_\beta \in \mathbb{R}^{N_t \times N_t}$ contains coefficients for a grid dispersion correction [41, 42, 60]. This dispersion correction is necessary because excitation currents and grid voltages are not defined at the same place in the discretized space: Electric grid voltages are defined along edges of the primary grid G and excitation currents flow through facets of the dual grid \tilde{G} . Thus, modal voltages and modal currents are not allocated in the same plane. However, for sufficiently small edge lengths of the grid, the grid dispersion matrix tends to the identity matrix, i.e. $\mathcal{D}_\beta \rightarrow \mathbf{I}$. Assuming the dispersion correction matrix to be equal to the identity matrix and introducing the state

$$\begin{pmatrix} \hat{\mathbf{e}}'(t) \\ \hat{\mathbf{h}}'(t) \end{pmatrix} = \begin{pmatrix} \mathcal{M}_\varepsilon^{1/2} & \mathbf{0} \\ \mathbf{0} & \mathcal{M}_\mu^{1/2} \end{pmatrix} \begin{pmatrix} \hat{\mathbf{e}}(t) \\ \hat{\mathbf{h}}(t) \end{pmatrix} \quad (3.38)$$

in (3.35) and (3.37) results in

$$\begin{aligned} \underbrace{\frac{d}{dt} \begin{pmatrix} \hat{\mathbf{e}}'(t) \\ \hat{\mathbf{h}}'(t) \end{pmatrix}}_{\mathbf{x}_{\text{fd}}(t)} &= \underbrace{\begin{pmatrix} \mathbf{0} & \mathcal{M}_\varepsilon^{-1/2} \mathcal{C}^T \mathcal{M}_\mu^{-1/2} \\ -\mathcal{M}_\mu^{-1/2} \mathcal{C} \mathcal{M}_\varepsilon^{-1/2} & \mathbf{0} \end{pmatrix}}_{\mathbf{A}_{\text{fd}}} \underbrace{\begin{pmatrix} \hat{\mathbf{e}}'(t) \\ \hat{\mathbf{h}}'(t) \end{pmatrix}}_{\mathbf{x}_{\text{fd}}(t)} \\ &+ \underbrace{\begin{pmatrix} \mathcal{M}_\varepsilon^{-1/2} \mathcal{R} \\ \mathbf{0} \end{pmatrix}}_{\mathbf{B}_{\text{fd}}} \mathbf{i}(t) \end{aligned} \quad (3.39)$$

with

$$\mathbf{v}(t) = \underbrace{(\mathcal{R}^T \mathcal{M}_\varepsilon^{-1/2} \quad \mathbf{0})}_{\mathbf{C}_{\text{fd}}} \underbrace{\begin{pmatrix} \hat{\mathbf{e}}'(t) \\ \hat{\mathbf{h}}'(t) \end{pmatrix}}_{\mathbf{x}_{\text{fd}}(t)}. \quad (3.40)$$

The state-space system is a first-order system, which is obtained from the discrete case. It has $N_t = 6N_p$ degrees of freedom ($\mathbf{x}_{fd}(t) \in \mathbb{R}^{6N_p}$). The output matrix is the input matrix transposed ($\mathbf{C}_{fd} = \mathbf{B}_{fd}^T \in \mathbb{R}^{N_t \times 6N_p}$), the sparse state matrix is skew-symmetric⁵ ($\mathbf{A}_{fd} = -\mathbf{A}_{fd}^T \in \mathbb{R}^{6N_p \times 6N_p}$), and the direct input-output link is equal to zero ($\mathbf{D}_{fd} = \mathbf{0} \in \mathbb{R}^{N_t \times N_t}$).

Second-Order State-Space System

To derive the second-order state-space system from the discrete case, the first row of the block equation (3.39) is derived with respect to time:

$$\frac{d^2}{dt^2} \hat{\mathbf{e}}'(t) = \mathcal{M}_\varepsilon^{-1/2} \mathcal{C}^T \mathcal{M}_\mu^{-1/2} \frac{d}{dt} \hat{\mathbf{h}}'(t) + \mathcal{M}_\varepsilon^{-1/2} \mathcal{R} \frac{d}{dt} \mathbf{i}(t). \quad (3.41)$$

Subsequently, the second row of (3.39)

$$\frac{d}{dt} \hat{\mathbf{h}}'(t) = -\mathcal{M}_\mu^{-1/2} \mathcal{C} \mathcal{M}_\varepsilon^{-1/2} \hat{\mathbf{e}}'(t) \quad (3.42)$$

is employed to replace the time derivative of $\hat{\mathbf{h}}'(t)$ in (3.41). This results in the second-order state equation of the system which is obtained from the discrete case:

$$\frac{d^2}{dt^2} \underbrace{\hat{\mathbf{e}}'(t)}_{\mathbf{x}_{sd}(t)} = -\underbrace{\mathcal{M}_\varepsilon^{-1/2} \mathcal{C}^T \mathcal{M}_\mu^{-1} \mathcal{C} \mathcal{M}_\varepsilon^{-1/2}}_{\mathbf{A}_{sd}} \underbrace{\hat{\mathbf{e}}'(t)}_{\mathbf{x}_{sd}(t)} + \underbrace{\mathcal{M}_\varepsilon^{-1/2} \mathcal{R}}_{\mathbf{B}_{sd}} \frac{d}{dt} \mathbf{i}(t). \quad (3.43)$$

The corresponding output equation arises from (3.40) and is given by

$$\mathbf{v}(t) = \underbrace{\mathcal{R}^T \mathcal{M}_\varepsilon^{-1/2}}_{\mathbf{C}_{sd}} \underbrace{\hat{\mathbf{e}}'(t)}_{\mathbf{x}_{sd}(t)}. \quad (3.44)$$

This system is equipped with $N_s = 3N_p$ degrees of freedom ($\mathbf{x}_{sd}(t) \in \mathbb{R}^{3N_p}$). The output matrix is the transpose of the input matrix ($\mathbf{C}_{fd} = \mathbf{B}_{fd}^T \in \mathbb{R}^{N_t \times 3N_p}$) just as in all previous cases. The sparse state matrix is symmetric ($\mathbf{A}_{sd} = \mathbf{A}_{sd}^T \in \mathbb{R}^{3N_p \times 3N_p}$) and negative semidefinite ($\mathbf{x}_{sd}^T \mathbf{A}_{sd} \mathbf{x}_{sd} \leq 0 \forall \mathbf{x}_{sd}$) (see Appendix C.3). The direct input-output link is equal to zero ($\mathbf{D}_{fd} = \mathbf{0} \in \mathbb{R}^{N_t \times N_t}$).

3.3 Important Properties of State-Space Systems

After the introduction of state-space systems and the derivation of state matrices dedicated to RF structures, some general concepts are discussed for the sake of completeness. The subsection follows [65, 67].

⁵It should be stressed that the symmetrization is straightforward in FIT due to the diagonality of \mathcal{M}_ε and \mathcal{M}_μ . However, this symmetrization is computationally demanding for other discretization approaches such as the FEM.

3.3.1 Lumped and Distributed Systems

A system with an infinite number of states or degrees of freedom is called *distributed* system. Typically, the modeling of processes which are governed by partial differential equations, results in distributed systems. The state-space equations (3.31) - (3.32) and (3.33) - (3.34) resulting from Maxwell's equations are distributed systems because the number of states tends to infinity for a complete 3D eigenmode expansion. Distributed systems are difficult to handle and therefore they are typically approximated by systems with a finite number of states. These so-called *lumped* systems are obtained from distributed systems by, for example, the simple restriction to a finite number of 3D eigenmodes in the expansions (3.18) or the discretization of the continuous space as it is sketched in Section 2.2.

3.3.2 Causality of Systems

A dynamical system is said to be *causal* or *nonanticipatory* if the present output $\mathbf{v}(t)$ solely depends on previous inputs⁶ and present inputs $\mathbf{i}(t)$ and not on future inputs $\mathbf{i}(t + T)$, with $T > 0$ s. A non-causal system has the ability to predict future inputs. All physical processes however do not have this property and are inherently causal. A system is said to be *strictly causal* if the present output $\mathbf{v}(t)$ depends solely on previous inputs. The state-space systems for RF structures derived in Section 3.2 are strictly causal as their direct input-output link equals zero ($\mathbf{D}_f = \mathbf{0}$) so that their output $\mathbf{v}(t)$ exclusively depends on the state $\mathbf{x}(t)$.

Despite the fact that causality is a crucial constraint for time-domain formulations, frequency-domain approaches do not rely on the principle of causality. In [39], the concept of inverse lengths is introduced to de-embed the properties of waveguides with constant cross section in scattering parameters. Inverse lengths however violate causality principles. Nonetheless, the concept of inverse lengths is successful for frequency-domain computations as demonstrated in e.g. [1].

3.3.3 Stability of Systems

Stability is a key property for state-space models. However, there is no unique definition of stability in the theory of linear systems. A system is, for example, *bounded-input bounded-output* (BIBO) stable if every bounded excitation $\|\mathbf{i}(t)\|$ results in a bounded response $\|\mathbf{v}(t)\|$. In contrast, *internal stability* is focussed on the non-excited system, i.e. $\mathbf{i}(t) = \mathbf{0}$. The zero-input response of first- or second-order state-space equations is said to be *marginally stable* if every finite initial state $\|\mathbf{x}(t = 0)\| = \|\mathbf{x}_0\|$ results in a bounded response. It is said to be *asymptotically stable* if every finite initial state $\|\mathbf{x}_0\|$ results in a bounded response which tends to zero as time tends to infinity, i.e. $\lim_{t \rightarrow \infty} \mathbf{x}(t) = \mathbf{0}$. The internal stability is a more

⁶Previous inputs are reflected in the states $\mathbf{x}_f(t)$ and $\mathbf{x}_s(t)$.

profound demand, because instabilities, which are not excited by the input signal, are detectable. However, BIBO stability does not follow from internal stability.

Internal Stability Consideration for First-Order State-Space Systems

The derived state matrices \mathbf{A}_f of first-order state-space systems for lossless RF structures are real-valued, skew-symmetric and the number of rows and columns is even. Following a spectral theorem [57, pp. 661 - 662], these matrices can be decomposed⁷ in the form $\mathbf{A}_f = \mathbf{Q}_f \mathbf{\Lambda}_f \mathbf{Q}_f^T$. The matrix \mathbf{Q}_f is real-valued and orthogonal and

$$\mathbf{A}_f = \text{diag} \left(\begin{pmatrix} 0 & \tilde{\omega}_1 \\ -\tilde{\omega}_1 & 0 \end{pmatrix}, \begin{pmatrix} 0 & \tilde{\omega}_2 \\ -\tilde{\omega}_2 & 0 \end{pmatrix}, \dots \right) \quad (3.45)$$

is a block diagonal matrix holding the real-valued resonant frequencies $\tilde{\omega}_n$ of the 3D eigenmodes of the (continuous or discretized) RF structure. Employing this matrix decomposition to replace \mathbf{A}_f in the first-order state equation without excitation and multiplying \mathbf{Q}_f^T from left-hand side delivers

$$\frac{d}{dt} \underbrace{\mathbf{Q}_f^T \mathbf{x}_f(t)}_{\mathbf{y}_f(t)} = \underbrace{\mathbf{Q}_f^T \mathbf{Q}_f}_{\mathbf{I}} \mathbf{\Lambda}_f \underbrace{\mathbf{Q}_f^T \mathbf{x}_f(t)}_{\mathbf{y}_f(t)} \quad (3.46)$$

with the new state vector

$$\mathbf{y}_f(t) = \mathbf{Q}_f^T \mathbf{x}_f(t) = (\hat{y}_{f,1}(t), y_{f,1}(t), \hat{y}_{f,2}(t), y_{f,2}(t), \dots)^T. \quad (3.47)$$

Due to the block diagonal form of the matrix $\mathbf{\Lambda}_f$, the new states are only coupled pairwise:

$$\frac{d}{dt} \hat{y}_{f,n}(t) = \tilde{\omega}_n y_{f,n}(t), \quad (3.48)$$

$$\frac{d}{dt} y_{f,n}(t) = -\tilde{\omega}_n \hat{y}_{f,n}(t). \quad (3.49)$$

This coupled system of differential equations is a second-order representation of the commonly known *harmonic oscillator*. The real-valued solution of the coupled system is given by

$$\hat{y}_{f,n}(t) = \Pi_n \sin(\tilde{\omega}_n t) - \Psi_n \cos(\tilde{\omega}_n t), \quad (3.50)$$

$$y_{f,n}(t) = \Pi_n \cos(\tilde{\omega}_n t) + \Psi_n \sin(\tilde{\omega}_n t). \quad (3.51)$$

⁷For the first-order state matrix \mathbf{A}_{fc} from the continuous consideration the decomposition is trivial, because the matrix is already in the form of (3.45), so that $\mathbf{Q}_{fc} = \mathbf{I}$ and $\mathbf{\Lambda}_{fc} = \mathbf{A}_{fc}$. In contrast, the discussion is of theoretical nature for \mathbf{A}_{fd} due to the numerical effort to compute the described decomposition for large skew-symmetric matrices of general form.

Here, Π_n and Ψ_n are constants which are determined by the initial conditions. Based on the skew symmetry of the state matrix \mathbf{A}_f , the consideration shows that the states $\mathbf{y}_f(t)$ remain bounded (but do not tend to zero for $t \rightarrow \infty$), if the initial constants Π_n and Ψ_n are finite. In this case, the original states $\mathbf{x}_f(t) = \mathbf{Q}_f \mathbf{y}_f(t)$ are bounded as well. Therefore, first-order state-space systems with skew-symmetric state matrices are internally marginally stable.

Internal Stability Consideration for Second-Order State-Space Systems

The state matrix of the second-order state-space systems for lossless RF structures is real-valued, symmetric, and negative semidefinite. Thus, its eigendecomposition⁸ is given by $\mathbf{A}_s = \mathbf{Q}_s \mathbf{\Lambda}_s \mathbf{Q}_s^T$. The orthogonal matrix \mathbf{Q}_s holds the real-valued eigenvectors and the diagonal matrix $\mathbf{\Lambda}_s$ the real-valued eigenvalues on the main diagonal. Due to the symmetry and the negative semidefiniteness of \mathbf{A}_s its eigenvalues are real-valued and smaller than or equal to zero (refer to Appendix C.3.2). As a matter of fact, the negative squares of the resonant frequencies of the 3D eigenmodes of the (continuous or discretized) RF structure are contained on the main diagonal: $\mathbf{\Lambda}_s = \text{diag}(-\tilde{\omega}_1^2, -\tilde{\omega}_2^2, \dots)$. Using the eigendecomposition to replace \mathbf{A}_s in the second-order state equation without excitation and multiplying \mathbf{Q}_s^T from left-hand side, yields

$$\frac{d^2}{dt^2} \underbrace{\mathbf{Q}_s^T \mathbf{x}_s(t)}_{\mathbf{y}_s(t)} = \underbrace{\mathbf{Q}_s^T \mathbf{Q}_s}_{\mathbf{I}} \mathbf{\Lambda}_s \underbrace{\mathbf{Q}_s^T \mathbf{x}_s(t)}_{\mathbf{y}_s(t)}, \quad (3.52)$$

where $\mathbf{y}_s(t)$ is the new state vector determined by $\mathbf{y}_s(t) = \mathbf{Q}_s^T \mathbf{x}_s(t)$. On account of the diagonality of the new state matrix, the states $\mathbf{y}_s(t)$ are not mutually coupled. Writing (3.52) for the n th state gives

$$\frac{d^2}{dt^2} y_{s,n}(t) + \tilde{\omega}_n^2 y_{s,n}(t) = 0. \quad (3.53)$$

This equation is a second-order representation of the harmonic oscillator. The general real-valued solution of this differential equation is given by

$$y_{s,n}(t) = \Pi_n \cos(\tilde{\omega}_n t) + \Psi_n \sin(\tilde{\omega}_n t). \quad (3.54)$$

The constants Π_n and Ψ_n are determined by the initial conditions. The solution conveys that the states $y_{s,n}(t)$ are bounded, if the coefficients Π_n and Ψ_n are finite. In this case the original states $\mathbf{x}_s(t) = \mathbf{Q}_s \mathbf{y}_s(t)$ remain bounded as well. Therefore, second-order state-space systems with a symmetric and negative-semidefinite state matrix are internally marginally stable.

⁸For the state matrix \mathbf{A}_{sc} from the continuous consideration the eigendecomposition is straightforward, because the matrix is already diagonal, so that $\mathbf{Q}_{sc} = \mathbf{I}$ and $\mathbf{\Lambda}_{sc} = \mathbf{A}_{sc}$. In contrast, the consideration is of formal nature for \mathbf{A}_{sd} , because it is not practical to compute complete eigendecompositions of large matrices.

3.3.4 Frequency-Domain Transfer Functions

Frequency-domain transfer functions of multiport networks as depicted in Figure 3.4 are important to characterize the relationship between the scalar quantities assigned to the individual port modes at the different ports. These relations are expressed by frequency-dependent matrices which are commonly known as *network matrices*. Aside from computing network matrices with analytical or numerical methods, they can be recorded by means of vector network analyzers. The current thesis is restricted to *impedance* and *scattering parameters* despite the fact that literature [33, 54, 55] defines a set of further network matrices. As a matter of fact, the network matrices can be transferred from one into the other.

Impedance Parameters

Impedance parameters relate modal voltages $\underline{\mathbf{v}}$ to modal currents $\underline{\mathbf{i}}$ at the ports of the device under test. To determine the impedance matrix, the second-order state equation⁹ is transformed to frequency domain:

$$\underbrace{(j\omega)^2}_{-\omega^2} \underline{\mathbf{x}}_s = \mathbf{A}_s \underline{\mathbf{x}}_s + \mathbf{B}_s j\omega \underline{\mathbf{i}}, \quad (3.55)$$

where $j\omega$ is the complex angular frequency. Subsequently, this equation is sorted for the complex-valued state vector:

$$\underline{\mathbf{x}}_s = \left(\underbrace{(j\omega)^2}_{-\omega^2} \mathbf{I} - \mathbf{A}_s \right)^{-1} \mathbf{B}_s j\omega \underline{\mathbf{i}}. \quad (3.56)$$

The complex state $\underline{\mathbf{x}}_s$ is replaced in the frequency-domain transform of the second-order output equation, so that

$$\underline{\mathbf{v}} = \underbrace{\mathbf{B}_s^T \left((j\omega)^2 \mathbf{I} - \mathbf{A}_s \right)^{-1} \mathbf{B}_s j\omega}_{=: \underline{\mathbf{Z}}(j\omega)} \underline{\mathbf{i}} \quad (3.57)$$

is obtained. The arising *impedance matrix*

$$\underline{\mathbf{Z}}(j\omega) = \begin{pmatrix} \underline{z}_{1,1,1,1}(j\omega) & \cdots & \underline{z}_{1,1,1,M_1}(j\omega) & \cdots & \underline{z}_{1,1,P,M_P}(j\omega) \\ \vdots & \ddots & \vdots & & \vdots \\ \underline{z}_{1,M_1,1,1}(j\omega) & \cdots & \underline{z}_{1,M_1,1,M_1}(j\omega) & \cdots & \underline{z}_{1,M_1,P,M_P}(j\omega) \\ \vdots & & \vdots & \ddots & \vdots \\ \underline{z}_{P,M_P,1,1}(j\omega) & \cdots & \underline{z}_{P,M_P,1,M_1}(j\omega) & \cdots & \underline{z}_{P,M_P,P,M_P}(j\omega) \end{pmatrix} \quad (3.58)$$

⁹The derivation employing the first-order system delivers the same impedance matrix $\underline{\mathbf{Z}}(j\omega)$. However, in such cases a linear system of equations with complex coefficients and twice as many degrees of freedom has to be solved in general for each complex angular frequency $j\omega$.

is continuous in the complex angular frequency $j\omega$ and allows for the determination of the terminal voltages based on current excitations. According to (3.57), the evaluation of $\underline{\mathbf{Z}}(j\omega) \in \mathbb{C}^{N_t \times N_t}$ for a specific complex angular frequency $j\omega$ requires the solution of a linear system of equations with real-valued coefficients.

Due to the linearity of Maxwell's equations, the voltage at each terminal is a linear superposition of the inflowing currents at all ports multiplied with the corresponding impedance coefficients $\underline{z}_{p,m,\eta,\nu}(j\omega)$. Each coefficient is determined by the voltage $\underline{V}_{p,m}$ of the m th mode at the p th port normalized to the current $\underline{I}_{\eta,\nu}$ of the ν th mode at the η th port if all other currents are equal to zero:

$$\underline{z}_{p,m,\eta,\nu}(j\omega) = \left. \frac{V_{p,m}}{I_{\eta,\nu}} \right|_{\underline{I}_{k,g}(j\omega)=0 \forall (k,g) \neq (\eta,\nu)}. \quad (3.59)$$

If the waveguide ports are only equipped with one 2D port mode each, the indices addressing the port modes are omitted in order to have a compact notation, e.g. $\underline{z}_{p,\eta}(j\omega)$ is the modal voltage \underline{V}_p at the 2D port mode at port p normalized with respect to the excitation current \underline{I}_η at the 2D port mode at port η .

The formula (3.57) defining the frequency-dependent impedance matrix can be modified by means of the eigendecomposition $\mathbf{A}_s = \mathbf{Q}_s \mathbf{\Lambda}_s \mathbf{Q}_s^T$ (refer to Subsection 3.3.3) as follows:

$$\begin{aligned} \underline{\mathbf{Z}}(j\omega) &= \mathbf{B}_s^T ((j\omega)^2 \mathbf{I} - \mathbf{Q}_s \mathbf{\Lambda}_s \mathbf{Q}_s^T)^{-1} \mathbf{B}_s j\omega \\ &= \underbrace{\mathbf{B}_s^T \mathbf{Q}_s}_{\mathbf{G}^T} ((j\omega)^2 \mathbf{I} - \mathbf{\Lambda}_s)^{-1} \underbrace{\mathbf{Q}_s^T \mathbf{B}_s}_{\mathbf{G}} j\omega = \sum_{n=1}^N \frac{j\omega}{(j\omega)^2 + \tilde{\omega}_n^2} \mathbf{g}_{r,n}^T \mathbf{g}_{r,n}. \end{aligned} \quad (3.60)$$

The vector $\mathbf{g}_{r,n}$ is the n th row of the matrix \mathbf{G} . The representation (3.60) reveals that the impedance matrix is a summation of rational fractions. The resonant frequencies $\tilde{\omega}_n$ of each eigenmode of the structure correspond to a pole in the impedance matrix. For the second-order state-space system arising from the continuous consideration ($N_s = N_e \rightarrow \infty$) the matrix $(\mathbf{g}_{r,n}^T \mathbf{g}_{r,n}) \in \mathbb{R}^{N_t \times N_t}$ is explicitly given by

$$\mathbf{g}_{r,n}^T \mathbf{g}_{r,n} = \begin{pmatrix} h_{n,1,1}^2 & \cdots & h_{n,1,M_1} h_{n,1,1} & \cdots & h_{n,P,M_P} h_{n,1,1} \\ \vdots & \ddots & \vdots & & \vdots \\ h_{n,1,1} h_{1,1,M_1} & \cdots & h_{n,1,M_1}^2 & \cdots & h_{n,P,M_P} h_{1,1,M_1} \\ \vdots & & \vdots & \ddots & \vdots \\ h_{n,1,1} h_{n,P,M_P} & \cdots & h_{n,1,M_1} h_{n,P,M_P} & \cdots & h_{n,P,M_P}^2 \end{pmatrix} \quad (3.61)$$

with the constants specifying the interaction integrals (3.26) between the 3D eigenmodes and the 2D port modes. Note that representations of the frequency-dependent impedance matrix similar to (3.60) are available in [40, 41, 42, 43] as well.

Another property of the impedance matrix is its symmetry $\underline{\mathbf{Z}}(j\omega) = \underline{\mathbf{Z}}^T(j\omega)$ which is a consequence of the reciprocity of Maxwell's equations [54, pp. 235 - 236]. Moreover, the real part of the impedance matrix equals zero for lossless structures [54, pp. 236 - 237], i.e. $\Re(\underline{\mathbf{Z}}(j\omega)) = \mathbf{0}$.

Scattering Parameters

As mentioned in Section 2.3, voltages and currents are difficult to measure directly in the microwave regime. Consequently, impedance parameters are not the preferred formalism to describe the frequency-domain transfer properties of structures under test. Scattering parameters are of broader practical relevance as they relate incident and scattered wave amplitudes which can be measured. The definitions of normalized wave amplitudes in Subsection 2.3.4 can be employed to express incident and scattered waves in terms of voltages and currents. Writing (2.64) and (2.65) for all N_t terminals of the RF structure yields

$$\underline{\mathbf{a}} = \frac{1}{2} \left(\underline{\mathbf{D}}_Z^{-\frac{1}{2}}(j\omega) \underline{\mathbf{v}} + \underline{\mathbf{D}}_Z^{\frac{1}{2}}(j\omega) \underline{\mathbf{i}} \right), \quad (3.62)$$

$$\underline{\mathbf{b}} = \frac{1}{2} \left(\underline{\mathbf{D}}_Z^{-\frac{1}{2}}(j\omega) \underline{\mathbf{v}} - \underline{\mathbf{D}}_Z^{\frac{1}{2}}(j\omega) \underline{\mathbf{i}} \right). \quad (3.63)$$

The vector

$$\underline{\mathbf{a}} = (\underline{a}_{1,1}, \dots, \underline{a}_{1,M_1}, \dots, \underline{a}_{P,1}, \dots, \underline{a}_{P,M_P})^T \quad (3.64)$$

collects the amplitudes of incident waves, whereas the vector

$$\underline{\mathbf{b}} = (\underline{b}_{1,1}, \dots, \underline{b}_{1,M_1}, \dots, \underline{b}_{P,1}, \dots, \underline{b}_{P,M_P})^T \quad (3.65)$$

holds the amplitudes of scattered waves. The matrix

$$\underline{\mathbf{D}}_Z(j\omega) = \text{diag}(\underline{Z}_{1,1}(j\omega), \dots, \underline{Z}_{1,M_1}(j\omega), \dots, \underline{Z}_{P,1}(j\omega), \dots, \underline{Z}_{P,M_P}(j\omega)) \quad (3.66)$$

contains the wave (for TE or TM modes) or the line impedances (for TEM modes) of the respective 2D port modes on the main diagonal.

The impedance matrix formulation (3.57) can be transferred to the *scattering matrix* formulation

$$\underline{\mathbf{b}} = \underbrace{\left[\left(\underline{\mathbf{D}}_Z^{-\frac{1}{2}}(j\omega) \underline{\mathbf{Z}}(j\omega) \underline{\mathbf{D}}_Z^{-\frac{1}{2}}(j\omega) + \mathbf{I} \right)^{-1} \left(\underline{\mathbf{D}}_Z^{-\frac{1}{2}}(j\omega) \underline{\mathbf{Z}}(j\omega) \underline{\mathbf{D}}_Z^{-\frac{1}{2}}(j\omega) - \mathbf{I} \right) \right]}_{\underline{\mathbf{S}}(j\omega)} \underline{\mathbf{a}} \quad (3.67)$$

based on (3.62) and (3.63). Similar to the impedance matrix, the arising complex

scattering matrix

$$\underline{\mathbf{S}}(j\omega) = \begin{pmatrix} \underline{s}_{1,1,1,1}(j\omega) & \cdots & \underline{s}_{1,1,1,M_1}(j\omega) & \cdots & \underline{s}_{1,1,P,M_P}(j\omega) \\ \vdots & \ddots & \vdots & & \vdots \\ \underline{s}_{1,M_1,1,1}(j\omega) & \cdots & \underline{s}_{1,M_1,1,M_1}(j\omega) & \cdots & \underline{s}_{1,M_1,P,M_P}(j\omega) \\ \vdots & & \vdots & \ddots & \vdots \\ \underline{s}_{P,M_P,1,1}(j\omega) & \cdots & \underline{s}_{P,M_P,1,M_1}(j\omega) & \cdots & \underline{s}_{P,M_P,P,M_P}(j\omega) \end{pmatrix} \quad (3.68)$$

is a function in the complex angular frequency $j\omega$. The entries on the main diagonal of $\underline{\mathbf{S}}(j\omega) \in \mathbb{C}^{N_t \times N_t}$ are referred to as reflection coefficients. The scattering matrix formulation (3.67) states that the scattered wave amplitudes are superpositions of the incident wave amplitudes multiplied with the respective scattering coefficients. Every scattering coefficient is determined by the scattered wave amplitude $\underline{b}_{p,m}$ of the m th 2D mode at the p th port normalized to the incident wave amplitude $\underline{a}_{\eta,\nu}$ at the ν th mode at the η th port if all other incident wave amplitudes equal zero, i.e.

$$\underline{s}_{p,m,\eta,\nu}(j\omega) = \left. \frac{\underline{b}_{p,m}}{\underline{a}_{\eta,\nu}} \right|_{\underline{a}_{k,g}=0 \forall (k,g) \neq (\eta,\nu)}. \quad (3.69)$$

In close analogy to the impedance parameters, the scattering parameter notation is shortened, if the waveguide ports are solely equipped with one 2D port mode. In that case $\underline{s}_{p,\eta}(j\omega)$ is the amplitude \underline{b}_p of the wave scattered in the 2D port mode at port p normalized with respect to the amplitude \underline{a}_η of the incident wave at port η .

3.4 Model Order Reduction of State-Space Systems

As previously mentioned, state-space equations arising from partial differential equations have many degrees of freedom, on account of the distributedness of the underlying physical phenomena. Even for very simple RF structures, such as waveguides with constant cross section, a large number of 3D eigenmodes (and therefore a large number of degrees of freedom) is required to ensure that the truncation error of the series expansion (3.18) is small¹⁰. For more sophisticated geometries such as elliptical shaped RF cavities with couplers, no closed analytical formula for the eigenmodes is available. In these cases, the state-space equations are generated using discretization approaches which lead to state-space equations with several million unknowns. Dealing with these large state-space models is demanding. For instance, the computation of field distributions (3.56) and secondary quantities such as impedance parameters (3.57) requires the solution of a large system of equations

¹⁰Refer to Appendix C.1 for convergence properties of 3D eigenmode expansions.

for every complex angular frequency $j\omega$. Moreover, the determination of transient system responses based on large state-space models is expensive because matrix vector multiplications with large matrices and vectors have to be performed for each discrete time step.

Fortunately, the behavior of the state-space model is only of interest in a certain frequency interval. This restriction allows for an approximation of the full state-space models by state-space models with a drastically reduced number of degrees of freedom or states. The smaller models are often referred to as *reduced-order models*. Model order reduction algorithms are an active field of research and enable the automatic generation of reduced-order models which still approximate the main features of the full model in a restricted frequency interval. These algorithms require as input: The full model to be approximated, the frequency interval of interest, and a suitable stopping criterion for specifying the quality of the approximation. It is obvious that the demand for a reduced-order model with a better accuracy leads to more degrees of freedom. In the actual thesis, the following requirements are set to the model order reduction approach.

1. The approximation error should be small, although the number of degrees of freedom of the reduced-order model should be small as well.
2. The internal stability of the reduced-order model has to be preserved.
3. The reduced-order model should allow for reconstructing the field distribution inside the structure.¹¹
4. The model order reduction approach should be reliable and computationally efficient.

3.4.1 Model Order Reduction by Projection

Following [68], reduction methods are based on a projection of the full state-space into a reduced space. The fundamental idea of this projection is explained with a second-order state-space system such as (3.33) - (3.34) or (3.43) - (3.44). The second-order systems are the preferred representation for the model order reduction, because the reduction can be performed by means of solving linear systems of equations with real-valued coefficients and half the number of degrees of freedom when comparing with the first-order representation. The projection methods are described by the rectangular matrices $\mathbf{V}_{\text{sr}} \in \mathbb{R}^{N_s \times N_{\text{sr}}}$ and $\mathbf{W}_{\text{sr}} \in \mathbb{R}^{N_{\text{sr}} \times N_s}$ with $\mathbf{W}_{\text{sr}}^T \mathbf{V}_{\text{sr}} = \mathbf{I} \in \mathbb{R}^{N_{\text{sr}} \times N_{\text{sr}}}$. The subscript “sr” indicates that the matrices refer to a second-order system and they are reduction matrices. From the previous considerations it is obvious that the number of states N_{sr} of the reduced model should be much smaller than the

¹¹Some model order reduction approaches solely aim at the determination of secondary quantities such as frequency-domain transfer functions.

number of states N_s of the full model, i.e. $N_s \gg N_{sr}$. The model order reduction is accomplished by expressing the full state in terms of the mapping

$$\mathbf{x}_s(t) = \mathbf{V}_{sr} \mathbf{x}_{sr}(t), \quad (3.70)$$

where $\mathbf{x}_s(t)$ denotes the full state vector of the second-order system and $\mathbf{x}_{sr}(t)$ the reduced state vector accordingly. In a subsequent step, (3.70) is used to substitute the state vector in the second-order system. Then, the resulting state equation is multiplied from the left-hand side with \mathbf{W}_s^T . This delivers the reduced state-space system

$$\underbrace{\mathbf{W}_s^T \mathbf{V}_s}_{\mathbf{I}} \frac{d^2}{dt^2} \mathbf{x}_{sr}(t) = \underbrace{\mathbf{W}_s^T \mathbf{A}_s \mathbf{V}_s}_{\mathbf{A}_{sr}} \mathbf{x}_{sr}(t) + \underbrace{\mathbf{W}_s^T \mathbf{B}_s}_{\mathbf{B}_{sr}} \frac{d}{dt} \mathbf{i}(t), \quad (3.71)$$

$$\mathbf{v}(t) = \underbrace{\mathbf{B}_s^T \mathbf{V}_s}_{\mathbf{B}_{sr}^T} \mathbf{x}_{sr}(t). \quad (3.72)$$

Literature proposes a large number of ways to generate the matrices \mathbf{W}_{sr} and \mathbf{V}_{sr} based on the characteristics of the full system [68].

Despite the fact that the introduced reduction approach with the matrices \mathbf{V}_{sr} and \mathbf{W}_{sr} is very flexible, it does not guarantee the stability of the reduced-order model. The choice $\mathbf{V}_{sr} = \mathbf{W}_{sr}$ enforces the system matrix of the reduced second-order system to be symmetric ($\mathbf{A}_{sr} = \mathbf{A}_{sr}^T$), because of $\mathbf{A}_s = \mathbf{A}_s^T$. Moreover, on account of the negative semidefiniteness of \mathbf{A}_s , \mathbf{A}_{sr} is negative semidefinite as well (refer to Appendix C.1). Therefore, the reduced model inherits the internal marginal stability (refer to Subsection 3.3.3) from the full model for $\mathbf{V}_{sr} = \mathbf{W}_{sr}$.

4 Compact State-Space Models for Complex Structures

Model order reduction is often not suitable right away for state-space models arising from very large and complex RF structures (e.g. the third-harmonic cavity strings of FLASH or of the European XFEL), due to the size of the resulting state-space systems (refer to the discussions in Section 1.3 and Section 1.4). This chapter introduces the State-Space Concatenation approach (SSC) which overcomes the problem of high computational demands for generating compact (reduced-order) state-space systems for large and complex structures. To the author's best knowledge, the SSC approach is one of the original contributions of the thesis. Section 4.1 describes the decomposition of the large structure into segments and Section 4.2 the model order reduction technique used to determine a compact model for each segment. Subsequently, Section 4.3 discusses the concatenation of the individual reduced-order state-space models in such a way that a reduced-order model of the entire structure arises. Section 4.4 illustrates the further reduction of this model and Section 4.5 introduces different representations of this final state-space model. Section 4.6 depicts how this final reduced-order model is used to determine RF properties of the full structure, such as field distributions, impedance parameters, and external quality factors.

It should be mentioned that for simple RF structures, whose state-space systems allow for a direct reduction of model order, Section 4.1, Section 4.3, and Section 4.5 can be skipped. The methods depicted in Section 4.6 are applicable to compact models which directly arise from MOR as well.

4.1 Decomposition of RF Structure and Description of Segments

This section corresponds to Step I in the high-level chart presented in Figure 1.1. For reasons of clarity, the decomposition of an RF structure is discussed with the help of the example shown in Figure 3.3. Figure 4.1 shows the decomposition of the example structure into segments, namely a 3 dB power splitter ($r = 1$), waveguide bendings ($r = 2$ and $r = 3$), and rectangular waveguides with uniform cross section ($r = 4$ and $r = 5$). Here, r denotes the index of the segments. The

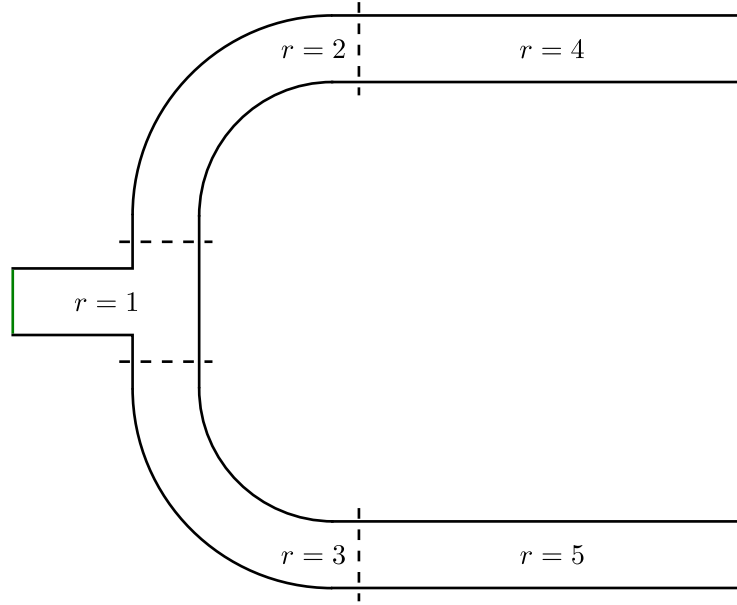


Figure 4.1: Rectangular waveguide structure serving as a decomposition example (refer to Figure 3.3). The decomposition planes are indicated by dashed lines. Waveguide ports employed to excite the structure are indicated in terms of green lines. The index r is assigned to every segment. The segment $r = 1$ is a 3dB power splitter, $r = 2$ and $r = 3$ are waveguide bendings, and $r = 4$ and $r = 5$ are rectangular waveguides with uniform cross section.

dashed lines show the cut planes. At each cut plane waveguide ports are assigned. In addition, waveguide ports to excite the entire structure are located at the green lines. All respective 2D port modes $\mathbf{L}_{t,m}(\mathbf{r}_t)$ are determined by the cross section of the cut planes. Figure 4.2 shows the abstract counterpart of the decomposed RF structure. Every segment is indicated as a white box with terminals accounting for the 2D port modes. The corresponding port voltages and currents are labeled by $v_{r,p,m}(t)$ and $i_{r,p,m}(t)$ whereas the index r denotes the segment, p the port, and m the port mode. At the p th waveguide port of the r th segment $M_{r,p}$ port modes are regarded. Ports generated by the decomposition are referred to as internal ports (located at the dashed lines in Figure 4.1) whereas ports used to excite the entire structure (located at the green lines in Figure 4.1) are referred to as external ports. At internal ports the same number of 2D port modes is assigned on both sides of the cut planes, i.e. $M_{1,2} = M_{3,1}$, $M_{1,3} = M_{2,1}$, $M_{3,2} = M_{5,2}$, and $M_{2,2} = M_{4,1}$ in Figure 4.2. The choice of cut plane locations and the total number of cut planes is a crucial issue for a reasonable decomposition. As a matter of fact, many cut planes lead to small segments so that their numerical treatment is convenient. However, cut planes should be located at regions of uniform cross section to reduce the number of port modes needed for the 2D field expansion on the cut planes.

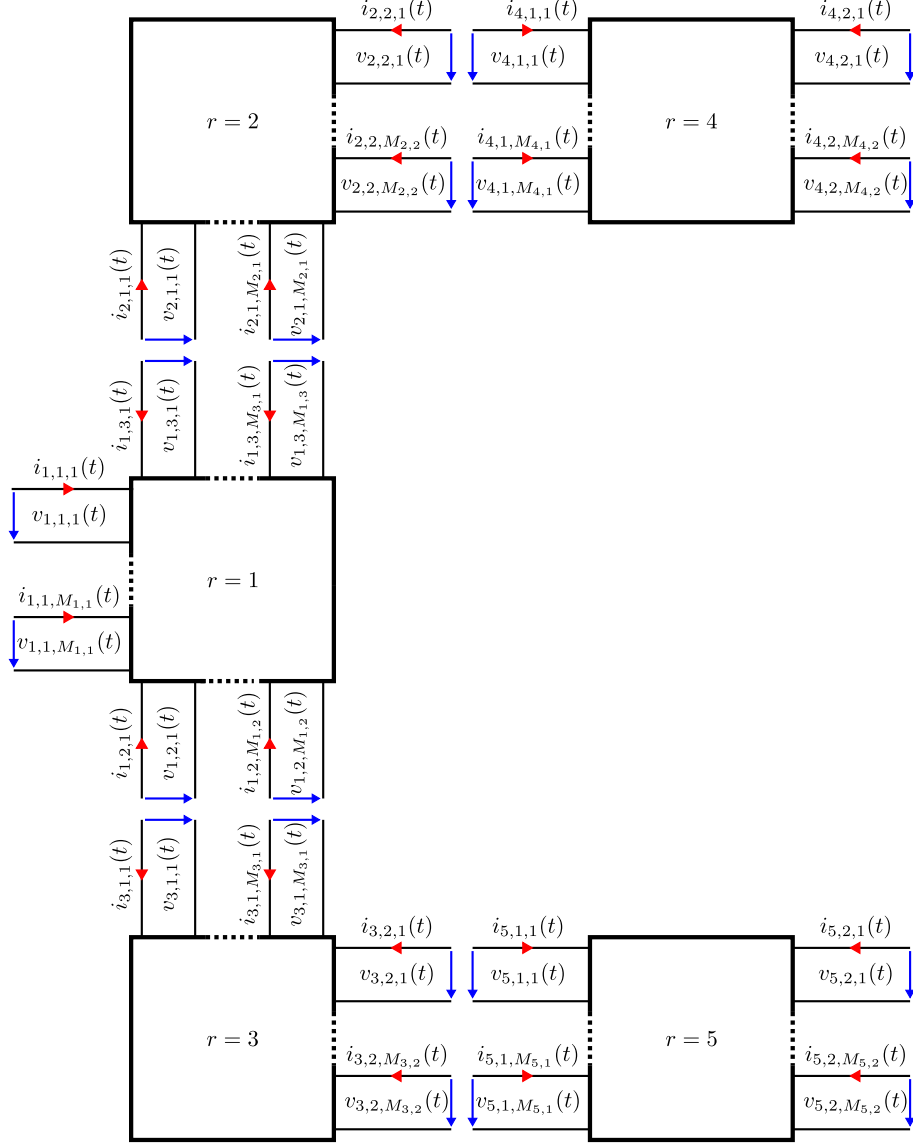


Figure 4.2: Abstract counterpart of the decomposed RF structure depicted in Figure 4.1. Each segment is indicated by a white box with terminals.

The choice of the decomposition plane locations distinguishes the proposed method from classical mode matching techniques [34, 38] and is subsequently discussed in a closer manner: Figure 4.3 shows two segments which are connected by a rectangular waveguide with constant cross section ($a = 22.86$ mm and $b = 10.16$ mm) as an example. Following (2.43) and (2.44), the electromagnetic fields in the region of constant cross section can be expressed by a superposition of an infinite number of waveguide modes with corresponding modal voltages and currents. If the char-

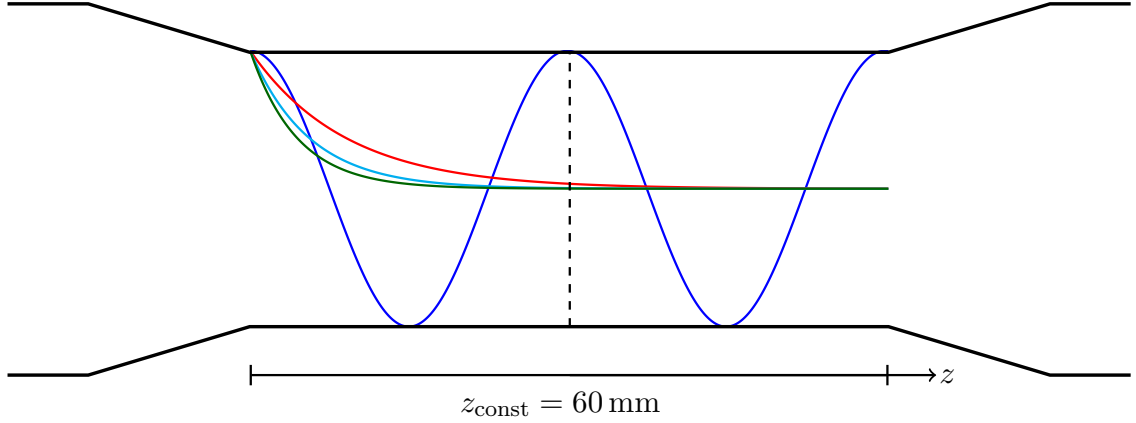


Figure 4.3: Close-up of two segments which are connected by a rectangular waveguide with constant cross section ($a = 22.86$ mm and $b = 10.16$ mm). The cut plane (dashed line) is located at the region of uniform cross section. The electromagnetic fields in the region of constant cross section can be expressed by a superposition of waveguide modes. The longitudinal dependences of the modal voltages of the first four waveguide modes (refer to Table A.1) are sketched by the solid lines: blue TE_{10} , red TE_{20} , cyan TE_{01} , and green line TE_{11} . The excitation takes place in the left segment with the frequency 12 GHz.

acterization of the RF structure is of interest in the frequency range f_{\min} to f_{\max} , two sets of modes exist: one set whose cutoff frequency $f_{co,m}$ is smaller than f_{\max} (propagating waveguide modes) and one set whose cutoff frequency $f_{co,m}$ is larger than f_{\max} (evanescent waveguide modes). The solid lines in Figure 4.3 correspond to the real parts of the frequency-domain modal voltages $\underline{V}_m^+(z)$ of the first four waveguide modes in the rectangular waveguide (cf. Table A.1), i.e. the solid lines are proportional to $\Re \left\{ \exp \left(-\underline{\gamma}_m(j\omega)z \right) \right\}$. The frequency-domain voltages of the waveguide modes emerge from a harmonic field excitation in the left segment with $f = f_{\max} = 12$ GHz. According to Table A.1, the TE_{10} mode (blue line) exclusively belongs to the set of propagating modes. The TE_{20} mode (red line), the TE_{01} mode (cyan line), and the TE_{11} mode (green line) belong to the set of evanescent modes. Propagating waveguide modes have propagation constants with $\Re \left\{ \underline{\gamma}_m(j\omega) \right\} = 0$ and do not experience an exponential decay along the region of constant cross section. Thus, all 2D port modes which correspond to propagating waveguide modes have to be regarded on the decomposition planes in general. In other words, all 2D port modes with a cutoff frequency smaller than the largest considered frequency are basically required for the field expansions on the cut planes. In addition, a finite set of evanescent 2D waveguide modes is also required in general. In contrast to propagating waveguide modes, evanescent modes have propagation constants with

$\Im \left\{ \gamma_m(j\omega) \right\} = 0$ which results in an exponential decay of the field patterns along the uniform cross section. The larger the cutoff frequency of the evanescent modes, the faster the decay as depicted in Figure 4.3: the red curve refers to a mode with $f_{\text{co},2} = 13.1174$ GHz, the cyan to a mode with $f_{\text{co},3} = 14.7571$ GHz, and the green to a mode with $f_{\text{co},4} = 16.1489$ GHz. The number of evanescent waveguide modes necessary at the cut planes typically depends on the length of constant cross section backward and forward of the cut planes. Qualitatively speaking, large lengths of uniform cross section lead to a small number of evanescent modes needed on the decomposition planes, because of the exponential decay. The influence of evanescent port modes can be estimated for concrete geometries by the help of the transmission coefficient

$$\underline{s}_{\text{tr},m}(j\omega) = e^{-\gamma_m(j\omega_{\text{max}})z_{\text{const}}} \quad (4.1)$$

deduced from (2.52). Here, z_{const} is the length of constant cross section backward and forward of the cut planes and $\omega_{\text{max}} = 2\pi f_{\text{max}}$. As there is no closed formula for the number of 2D port modes to consider at the decomposition planes to reach a certain accuracy, a convergence study has to be performed in practice. Alternatively, simple validation structures which allow for a direct computation of the RF properties can be used to estimate the number of 2D port modes required (see Chapter 6).

In contrast to internal waveguide ports, it is often sufficient to regard only one port mode at each external waveguide port. As already discussed in Section 3.1, RF structures are normally designed in such a way that only one mode propagates in the frequency range of interest to have distinct propagation properties.

The RF properties of every segment of the decomposed structure are described by means of the second-order state-space system

$$\frac{d^2}{dt^2} \mathbf{x}_{s,r}(t) = \mathbf{A}_{s,r} \mathbf{x}_{s,r}(t) + \mathbf{B}_{s,r} \frac{d}{dt} \mathbf{i}_r(t), \quad (4.2)$$

$$\mathbf{v}_r(t) = \mathbf{B}_{s,r}^T \mathbf{x}_{s,r}(t) \quad (4.3)$$

arising either from analytical (see Subsection 3.2.1) or from discrete techniques (see Subsection 3.2.2). The vectors $\mathbf{i}_r(t)$ and $\mathbf{v}_r(t)$ collect the transient modal currents and voltages of the r th segment, i.e.

$$\mathbf{i}_r(t) = (\mathbf{i}_{r,1}(t), \mathbf{i}_{r,2}(t), \dots, \mathbf{i}_{r,p}(t), \dots, \mathbf{i}_{r,P_r}(t))^T, \quad (4.4)$$

$$\mathbf{v}_r(t) = (\mathbf{v}_{r,1}(t), \mathbf{v}_{r,2}(t), \dots, \mathbf{v}_{r,p}(t), \dots, \mathbf{v}_{r,P_r}(t))^T, \quad (4.5)$$

where P_r is the total number of ports at segment r . The vectors $\mathbf{i}_{r,p}(t) \in \mathbb{R}^{M_{r,p}}$ and $\mathbf{v}_{r,p}(t) \in \mathbb{R}^{M_{r,p}}$ contain the quantities related to the p th waveguide port of the r th segment:

$$\mathbf{i}_{r,p}(t) = (i_{r,p,1}(t), i_{r,p,2}(t), \dots, i_{r,p,m}(t), \dots, i_{r,p,M_{r,p}}(t)), \quad (4.6)$$

$$\mathbf{v}_{r,p}(t) = (v_{r,p,1}(t), v_{r,p,2}(t), \dots, v_{r,p,m}(t), \dots, v_{r,p,M_{r,p}}(t)). \quad (4.7)$$

4.2 Generation of Compact Models

In the frame of the current thesis, a model order reduction approach based on an incomplete eigenmode decomposition is used [40, 41, 42, 43]. The section corresponds to the Step II and the Step IV in the top-level chart in Figure 1.1. Note that the subscripts r , which denote that the state-space matrices in (4.2) - (4.3) referring to the r th segment, are missing in this section. On the one hand, this ensures the compactness of the notation. On the other hand, the presented reduction approach is later on applied to reduce the state-space model which results from the concatenation, i.e. Step IV in Figure 1.1.

It follows from (3.60) that each eigenvalue of \mathbf{A}_s corresponds to a pole in the impedance spectrum. Thus, all eigenvectors of \mathbf{A}_s whose corresponding eigenvalues $\lambda_n = -\tilde{\omega}_n^2$ satisfy $\omega_{\min} \leq \tilde{\omega}_n \leq \omega_{\max}$ are computed by means of iterative algorithms such as Arnoldi or Jacobi-Davidson methods. The incomplete set of computed eigenvectors is listed as columns of the orthogonal matrix $\mathbf{Q}_{s,\text{inc}}$. Unfortunately, it is not sufficient to restrict the algorithm to these eigenvalues and eigenvectors, because the dynamical properties of the structure are still influenced by resonances whose resonant frequencies are not in the interval of interest. This error induces a smooth and bounded deviation of the transfer function of the reduced-order model, when comparing with the nonreduced model (see Figure C.2 or [42, p. 94, Figure 6.4]). To model the influence of the not considered eigenvectors, frequency-domain field distributions in the segment are computed on equidistant angular frequency samples ω_i in the interval of interest by

$$\underline{\mathbf{x}}_{s,i} = \left(\underbrace{(j\omega_i)^2}_{-\omega_i^2} \mathbf{I} - \mathbf{A}_s \right)^{-1} \mathbf{B}_s j\omega_i. \quad (4.8)$$

The involved matrix inversion is straightforward for state-space systems arising from analytical techniques, because the matrices $\mathbf{A}_s = \mathbf{A}_{sc} \in \mathbb{R}^{N_e \times N_e}$ are diagonal. The matrix inversion is not feasible for state-space systems generated by the FIT scheme in general, because the symmetric matrices $\mathbf{A}_s = \mathbf{A}_{sd} \in \mathbb{R}^{3N_p \times 3N_p}$ have off-diagonal bands and N_p is typically larger than 5,000. In the case where the matrix inversion is not feasible, (4.8) is determined by iterative solvers for linear real-valued systems of equations. In order to reduce the number of required iteration steps, the previously computed incomplete set of eigenvalues and eigenvectors is used beforehand to construct a reasonable initial guess. As a matter of fact, the computed states can be considered as snapshots of the state-space model in frequency domain. These snapshots are collected in a matrix as follows

$$\mathbf{X}_{s,\text{sp}} = \Im \left[\left(\frac{\underline{\mathbf{x}}_{s,1}}{\|\underline{\mathbf{x}}_{s,1}\|}, \frac{\underline{\mathbf{x}}_{s,2}}{\|\underline{\mathbf{x}}_{s,2}\|}, \dots, \frac{\underline{\mathbf{x}}_{s,i}}{\|\underline{\mathbf{x}}_{s,i}\|}, \dots \right) \right]. \quad (4.9)$$

The operator $\Im(\dots)$ delivers the imaginary parts of the coefficients of a matrix. The real parts are not of interest, because they are equal to zero according to (4.8), i.e.

$\Re(\mathbf{X}_{s,sp}) = \mathbf{0}$. After assembling the snapshot matrix, the *economy size singular value decomposition* [69] of the block matrix $[\mathbf{Q}_{s,inc}, \mathbf{X}_{s,sp}]$ is performed:

$$\mathbf{U}\mathbf{\Sigma}\mathbf{R}^T = [\mathbf{Q}_{s,inc}, \mathbf{X}_{s,sp}]. \quad (4.10)$$

Here, \mathbf{U} is a real orthogonal matrix, $\mathbf{\Sigma}$ a rectangular diagonal matrix with non-negative real numbers (the so-called *singular values*) on the diagonal, and \mathbf{R} a real quadratic matrix. The sampling frequencies and the total number of snapshots used for the model order reduction is determined in a while-loop based on the accuracy criterion ϵ_{rd} . Initially, two sampling angular frequencies are chosen for the snapshots matrix $\mathbf{X}_{s,sp}$ such that $\omega_1 = \omega_{min}$ and $\omega_2 = \omega_{max}$. If now the smallest singular value¹ is larger than ϵ_{rd} , new snapshots are computed on frequencies in between the old sampling frequencies. The new snapshots are attached to $\mathbf{X}_{s,sp}$ and the singular value decomposition of the new matrix $[\mathbf{Q}_{s,inc}, \mathbf{X}_{s,sp}]$ is performed. This procedure is iteratively repeated until the smallest singular value is smaller than or equal to ϵ_{rd} or the maximal number of field computations is reached. The maximal number of field computation is specified by the user when starting the model order reduction script. In the case that the smallest singular value does not fall below the specified accuracy criterion ϵ_{rd} and the maximal number of field computations is reached, the iteration is stopped and the reduction script throws an error warning.

Based on the resulting matrix \mathbf{U} the interims reduced-order model

$$\frac{d^2}{dt^2} \mathbf{x}_{sir}(t) = \underbrace{\mathbf{U}^T \mathbf{A}_s \mathbf{U}}_{\mathbf{A}_{sir}} \mathbf{x}_{sir}(t) + \underbrace{\mathbf{U}^T \mathbf{B}_s}_{\mathbf{B}_{sir}} \frac{d}{dt} \mathbf{i}(t), \quad (4.11)$$

$$\mathbf{v}(t) = \underbrace{\mathbf{B}_s^T \mathbf{U}}_{\mathbf{B}_{sir}^T} \mathbf{x}_{sir}(t) \quad (4.12)$$

is generated. In order to diagonalize the state matrix of the reduced-order model, the eigendecomposition $\mathbf{A}_{sir} = \mathbf{Q}_{sir} \mathbf{\Lambda}_{sir} \mathbf{Q}_{sir}^T$ is computed, where $\mathbf{\Lambda}_{sir}$ is a diagonal negative-semidefinite matrix and \mathbf{Q}_{sir} is orthonormal. Note that the computation of this decomposition is not very demanding due to the comparatively small number of rows (or columns) of \mathbf{A}_{sir} . In a next step, the state $\mathbf{x}_{sir}(t)$ is substituted by $\mathbf{Q}_{sir} \mathbf{x}_{sr}(t)$ to finally obtain the reduced-order model

$$\frac{d^2}{dt^2} \mathbf{x}_{sr}(t) = \underbrace{\mathbf{\Lambda}_{sir}}_{\mathbf{A}_{sr}} \mathbf{x}_{sr}(t) + \underbrace{\mathbf{Q}_{sir}^T \mathbf{B}_{sir}}_{\mathbf{B}_{sr}} \frac{d}{dt} \mathbf{i}(t), \quad (4.13)$$

$$\mathbf{v}(t) = \underbrace{\mathbf{B}_{sir}^T \mathbf{Q}_{sir}}_{\mathbf{B}_{sr}^T} \mathbf{x}_{sr}(t). \quad (4.14)$$

¹i.e. the smallest coefficient on the diagonal of $\mathbf{\Sigma}$

Based on these considerations, the projection to reduce the full model according to (3.71) - (3.72) is given by

$$\mathbf{x}_s(t) = \mathbf{V}_{sr} \mathbf{x}_{sr}(t) = \mathbf{W}_{sr} \mathbf{x}_{sr}(t) = \mathbf{U} \mathbf{Q}_{sr} \mathbf{x}_{sr}(t). \quad (4.15)$$

4.3 Concatenation of Segments

This section corresponds to Step III in the chart in Figure 1.1 and closely follows [2, Section II-D] where the concatenation of segments described by a first-order system of coupled differential equations is derived. Before starting with the concatenation, it is assumed that all segments are described by their respective reduced-order state-space models

$$\frac{d^2}{dt^2} \mathbf{x}_{sr,r}(t) = \mathbf{A}_{sr,r} \mathbf{x}_{sr,r}(t) + \mathbf{B}_{sr,r} \frac{d}{dt} \mathbf{i}_r(t), \quad (4.16)$$

$$\mathbf{v}_r(t) = \mathbf{B}_{sr,r}^T \mathbf{x}_{sr,r}(t). \quad (4.17)$$

The involved matrices are given by $\mathbf{A}_{sr,r} = \mathbf{V}_{sr,r}^T \mathbf{A}_{s,r} \mathbf{V}_{sr,r}$ and $\mathbf{B}_{sr,r} = \mathbf{V}_{sr,r}^T \mathbf{B}_{s,r}$, where $\mathbf{V}_{sr,r}$ is the reduction matrix of the r th segment. To combine the individual segments to the entire structure, the reduced-order state equations (4.16) of all segments are collected in the diagonal block system

$$\begin{aligned} \frac{d^2}{dt^2} \underbrace{\begin{pmatrix} \mathbf{x}_{sr,1}(t) \\ \mathbf{x}_{sr,2}(t) \\ \vdots \\ \mathbf{x}_{sr,r}(t) \\ \vdots \\ \mathbf{x}_{sr,R}(t) \end{pmatrix}}_{\mathbf{x}_{sb}(t)} &= \underbrace{\begin{pmatrix} \mathbf{A}_{sr,1} & \mathbf{0} & \dots & \mathbf{0} & \dots & \mathbf{0} \\ \mathbf{0} & \mathbf{A}_{sr,2} & \dots & \mathbf{0} & \dots & \mathbf{0} \\ \vdots & \vdots & \ddots & \vdots & \ddots & \vdots \\ \mathbf{0} & \mathbf{0} & \dots & \mathbf{A}_{sr,r} & \dots & \mathbf{0} \\ \vdots & \vdots & \ddots & \vdots & \ddots & \vdots \\ \mathbf{0} & \mathbf{0} & \dots & \mathbf{0} & \dots & \mathbf{A}_{sr,R} \end{pmatrix}}_{\mathbf{A}_{sb}} \underbrace{\begin{pmatrix} \mathbf{x}_{sr,1}(t) \\ \mathbf{x}_{sr,2}(t) \\ \vdots \\ \mathbf{x}_{sr,r}(t) \\ \vdots \\ \mathbf{x}_{sr,R}(t) \end{pmatrix}}_{\mathbf{x}_{sb}(t)} \\ &+ \underbrace{\begin{pmatrix} \mathbf{B}_{sr,1} & \mathbf{0} & \dots & \mathbf{0} & \dots & \mathbf{0} \\ \mathbf{0} & \mathbf{B}_{sr,2} & \dots & \mathbf{0} & \dots & \mathbf{0} \\ \vdots & \vdots & \ddots & \vdots & \ddots & \vdots \\ \mathbf{0} & \mathbf{0} & \dots & \mathbf{B}_{sr,r} & \dots & \mathbf{0} \\ \vdots & \vdots & \ddots & \vdots & \ddots & \vdots \\ \mathbf{0} & \mathbf{0} & \dots & \mathbf{0} & \dots & \mathbf{B}_{sr,R} \end{pmatrix}}_{\mathbf{B}_{sb}} \frac{d}{dt} \underbrace{\begin{pmatrix} \mathbf{i}_1(t) \\ \mathbf{i}_2(t) \\ \vdots \\ \mathbf{i}_r(t) \\ \vdots \\ \mathbf{i}_R(t) \end{pmatrix}}_{\mathbf{i}_{can}(t)}, \end{aligned} \quad (4.18)$$

where R is the total number of segments. In similar fashion, the output equations (4.17) of the reduced-order models are embraced for all R segments by the block

system:

$$\underbrace{\begin{pmatrix} \mathbf{v}_1(t) \\ \mathbf{v}_2(t) \\ \vdots \\ \mathbf{v}_r(t) \\ \vdots \\ \mathbf{v}_R(t) \end{pmatrix}}_{\mathbf{v}_{\text{can}}(t)} = \underbrace{\begin{pmatrix} \mathbf{B}_{\text{sr},1}^T & \mathbf{0} & \cdots & \mathbf{0} & \cdots & \mathbf{0} \\ \mathbf{0} & \mathbf{B}_{\text{sr},2}^T & \cdots & \mathbf{0} & \cdots & \mathbf{0} \\ \vdots & \vdots & \ddots & \vdots & \ddots & \vdots \\ \mathbf{0} & \mathbf{0} & \cdots & \mathbf{B}_{\text{sr},r}^T & \cdots & \mathbf{0} \\ \vdots & \vdots & \ddots & \vdots & \ddots & \vdots \\ \mathbf{0} & \mathbf{0} & \cdots & \mathbf{0} & \cdots & \mathbf{B}_{\text{sr},R}^T \end{pmatrix}}_{\mathbf{B}_{\text{sb}}^T} \underbrace{\begin{pmatrix} \mathbf{x}_1(t) \\ \mathbf{x}_2(t) \\ \vdots \\ \mathbf{x}_r(t) \\ \vdots \\ \mathbf{x}_R(t) \end{pmatrix}}_{\mathbf{x}_{\text{sb}}(t)}. \quad (4.19)$$

It is remarked that the block diagonal matrix \mathbf{A}_{sb} is symmetric negative semidefinite because the matrices $\mathbf{A}_{\text{sc},r}$ are symmetric negative semidefinite. The subscripts “sb” denote that the corresponding matrices and vectors refer to the second-order block system.

Following [30], the order of the currents in $\mathbf{i}_{\text{can}}(t)$ and the order of the voltages in $\mathbf{v}_{\text{can}}(t)$ is referred to as canonical order. The currents and voltages are reorganized to the so-called sorted order by means of the permutation matrix \mathbf{P}^T so that

$$\mathbf{i}_{\text{sort}}(t) = \begin{pmatrix} \mathbf{i}_{\text{int}}(t) \\ \mathbf{i}_{\text{ext}}(t) \end{pmatrix} = \mathbf{P}^T \mathbf{i}_{\text{can}}(t), \quad (4.20)$$

$$\mathbf{v}_{\text{sort}}(t) = \begin{pmatrix} \mathbf{v}_{\text{int}}(t) \\ \mathbf{v}_{\text{ext}}(t) \end{pmatrix} = \mathbf{P}^T \mathbf{v}_{\text{can}}(t). \quad (4.21)$$

Each row and each column of permutation matrices contain one coefficient which is equal to one whereas the remaining coefficients are equal to zero. The vectors $\mathbf{i}_{\text{int}}(t) \in \mathbb{R}^{N_{\text{int}}}$ and $\mathbf{v}_{\text{int}}(t) \in \mathbb{R}^{N_{\text{int}}}$ hold the terminal quantities related to internal ports. The vectors $\mathbf{i}_{\text{ext}}(t) \in \mathbb{R}^{N_{\text{ext}}}$ and $\mathbf{v}_{\text{ext}}(t) \in \mathbb{R}^{N_{\text{ext}}}$ store terminal quantities belonging to external ports. The total number of external terminals is denoted by N_{ext} whereas the total number of internal terminals is labeled as N_{int} . Recall from Section 4.1 that external ports (and terminals) are used to excite the entire structure and internal ports (and terminals) are generated by the decomposition.

For the following derivation, it is of crucial significance that the vectors storing the internal port quantities are ordered by the permutation matrix such that quantities of ports and terminals to be connected are listed below each other. By way of example, the internal port quantities of the structure shown in Figure 4.2 can be arranged as follows:

$$\begin{aligned} \mathbf{i}_{\text{int}}(t) = & (i_{1,2,1}(t), i_{3,1,1}(t), \dots, i_{1,2,M_{1,2}}(t), i_{3,1,M_{3,1}}(t), \\ & i_{1,3,1}(t), i_{2,1,1}(t), \dots, i_{1,3,M_{3,1}}(t), i_{2,1,M_{2,1}}(t), \\ & i_{2,2,1}(t), i_{4,1,1}(t), \dots, i_{2,2,M_{2,2}}(t), i_{4,1,M_{4,1}}(t), \\ & i_{3,2,1}(t), i_{5,1,1}(t), \dots, i_{3,2,M_{3,2}}(t), i_{5,1,M_{5,1}}(t))^T \in \mathbb{R}^{N_{\text{int}}} \end{aligned} \quad (4.22)$$

and

$$\begin{aligned} \mathbf{v}_{\text{int}}(t) = & (v_{1,2,1}(t), v_{3,1,1}(t), \dots, v_{1,2,M_{1,2}}(t), v_{3,1,M_{3,1}}(t), \\ & v_{1,3,1}(t), v_{2,1,1}(t), \dots, v_{1,3,M_{3,1}}(t), v_{2,1,M_{2,1}}(t), \\ & v_{2,2,1}(t), v_{4,1,1}(t), \dots, v_{2,2,M_{2,2}}(t), v_{4,1,M_{4,1}}(t), \\ & v_{3,2,1}(t), v_{5,1,1}(t), \dots, v_{3,2,M_{3,2}}(t), v_{5,1,M_{5,1}}(t))^T \in \mathbb{R}^{N_{\text{int}}}. \end{aligned} \quad (4.23)$$

The external port quantities are ordered according to

$$\begin{aligned} \mathbf{i}_{\text{ext}}(t) = & (i_{1,1,1}(t), \dots, i_{1,1,M_{1,1}}(t), i_{4,2,1}(t), \dots, i_{4,2,M_{4,2}}(t), \\ & i_{5,2,1}(t), \dots, i_{5,2,M_{5,2}}(t))^T \in \mathbb{R}^{N_{\text{ext}}} \end{aligned} \quad (4.24)$$

and

$$\begin{aligned} \mathbf{v}_{\text{ext}}(t) = & (v_{1,1,1}(t), \dots, v_{1,1,M_{1,1}}(t), v_{4,2,1}(t), \dots, v_{4,2,M_{4,2}}(t), \\ & v_{5,2,1}(t), \dots, v_{5,2,M_{5,2}}(t))^T \in \mathbb{R}^{N_{\text{ext}}}. \end{aligned} \quad (4.25)$$

In a next step, the orthogonality $\mathbf{P}^T = \mathbf{P}^{-1}$ of the permutation matrix is employed to solve (4.20) and (4.21) for the canonical quantities. Subsequently, the canonical quantities in (4.18) and (4.19) are replaced by the sorted quantities. This delivers

$$\frac{d^2}{dt^2} \mathbf{x}_{\text{sb}}(t) = \mathbf{A}_{\text{sb}} \mathbf{x}_{\text{sb}}(t) + \underbrace{\mathbf{B}_{\text{sb}} \mathbf{P}}_{\mathbf{B}_{\text{sb}}} \frac{d}{dt} \mathbf{i}_{\text{sort}}(t), \quad (4.26)$$

$$\mathbf{v}_{\text{sort}}(t) = \underbrace{\mathbf{P}^T \mathbf{B}_{\text{sb}}^T}_{\bar{\mathbf{B}}_{\text{sb}}^T} \mathbf{x}_{\text{sb}}(t). \quad (4.27)$$

These equations are separated by the segmentation

$$\bar{\mathbf{B}}_{\text{sb}} = (\bar{\mathbf{B}}_{\text{sb},1} \quad \bar{\mathbf{B}}_{\text{sb},2}). \quad (4.28)$$

The block $\bar{\mathbf{B}}_{\text{sb},1}$ is chosen to have N_{int} columns and the block $\bar{\mathbf{B}}_{\text{sb},2}$ is selected to have N_{ext} columns. The matrix segmentation is utilized to separate internal and external quantities in (4.26) and (4.27):

$$\frac{d^2}{dt^2} \mathbf{x}_{\text{sb}}(t) = \mathbf{A}_{\text{sb}} \mathbf{x}_{\text{sb}}(t) + \bar{\mathbf{B}}_{\text{sb},1} \frac{d}{dt} \mathbf{i}_{\text{int}}(t) + \bar{\mathbf{B}}_{\text{sb},2} \frac{d}{dt} \mathbf{i}_{\text{ext}}(t), \quad (4.29)$$

$$\mathbf{v}_{\text{int}}(t) = \bar{\mathbf{B}}_{\text{sb},1}^T \mathbf{x}_{\text{sb}}(t), \quad (4.30)$$

$$\mathbf{v}_{\text{ext}}(t) = \bar{\mathbf{B}}_{\text{sb},2}^T \mathbf{x}_{\text{sb}}(t). \quad (4.31)$$

The currents $\mathbf{i}_{\text{int}}(t)$ of the internal terminals are linearly dependent for concatenated segments. Following *Kirchhoff's current law* (or nodal rule), the currents flowing into a node are equal to the currents out of that node, for instance for the

connection between segment $r = 1$ and segment $r = 5$ in Figure 4.2 this reads as $i_{1,2,1}(t) = -i_{3,1,1}(t), \dots, i_{1,2,M_{1,2}}(t) = -i_{3,1,M_{3,1}}(t)$. The current law expresses the tangential magnetic fields on the decomposition planes to be continuous as discussed in Appendix C.2 in detail. According to (4.22), internal currents of terminals to be concatenated are ordered below each other in $\mathbf{i}_{\text{int}}(t)$ and therefore the linear dependent currents are listed below each other as well. Kirchhoff's current law is expressed for all internal currents by

$$\mathbf{i}_{\text{int}}(t) = \mathbf{F} \hat{\mathbf{i}}_{\text{int}}(t), \quad (4.32)$$

where

$$\mathbf{F} = \text{diag}\left(\begin{pmatrix} 1 \\ -1 \end{pmatrix}, \dots, \begin{pmatrix} 1 \\ -1 \end{pmatrix}\right) \in \mathbb{R}^{N_{\text{int}} \times N_{\text{int}}/2}. \quad (4.33)$$

The vector $\hat{\mathbf{i}}_{\text{int}}(t) \in \mathbb{R}^{N_{\text{int}}/2}$ contains the linearly independent currents flowing through the coupled terminals. Replacing this vector in (4.29) delivers

$$\frac{d^2}{dt^2} \mathbf{x}_{\text{sb}}(t) = \mathbf{A}_{\text{sb}} \mathbf{x}_{\text{sb}}(t) + \bar{\mathbf{B}}_{\text{sb},1} \mathbf{F} \frac{d}{dt} \hat{\mathbf{i}}_{\text{int}}(t) + \bar{\mathbf{B}}_{\text{sb},2} \frac{d}{dt} \mathbf{i}_{\text{ext}}(t). \quad (4.34)$$

Kirchhoff's voltage law states that the directed sum of the voltage around a closed circuit is zero. This results in $v_{1,2,1}(t) = v_{3,1,1}(t), \dots, v_{1,2,M_{1,2}}(t) = v_{3,1,M_{3,1}}(t)$ for the connection between segment $r = 1$ and segment $r = 5$ in Figure 4.2. Following Appendix C.2, Kirchhoff's voltage law enforces the tangential electric fields to be continuous on the decomposition planes. Applying Kirchhoff's voltage law for all internal port voltages gives

$$\mathbf{F}^T \mathbf{v}_{\text{int}}(t) = \mathbf{F}^T \bar{\mathbf{B}}_{\text{sb},1}^T \mathbf{x}_{\text{sb}}(t) = \mathbf{0}, \quad (4.35)$$

because voltages of terminals to be linked are listed below each other in $\mathbf{v}_{\text{int}}(t)$ as well. Multiplying (4.34) from the left-hand side with $\mathbf{F}^T \bar{\mathbf{B}}_{\text{sb},1}^T$ delivers

$$\begin{aligned} \frac{d^2}{dt^2} \underbrace{\mathbf{F}^T \bar{\mathbf{B}}_{\text{sb},1}^T \mathbf{x}_{\text{sb}}(t)}_{\mathbf{0}} &= \mathbf{F}^T \bar{\mathbf{B}}_{\text{sb},1}^T \mathbf{A}_{\text{sb}} \mathbf{x}_{\text{sb}}(t) \\ &+ \mathbf{F}^T \bar{\mathbf{B}}_{\text{sb},1}^T \bar{\mathbf{B}}_{\text{sb},1} \mathbf{F} \frac{d}{dt} \hat{\mathbf{i}}_{\text{int}}(t) + \mathbf{F}^T \bar{\mathbf{B}}_{\text{sb},1}^T \bar{\mathbf{B}}_{\text{sb},2} \frac{d}{dt} \mathbf{i}_{\text{ext}}(t). \end{aligned} \quad (4.36)$$

The left-hand side equals zero, because the second-order derivative of zero remains zero. Sorting for the time derivative of the internal currents yields

$$\begin{aligned} \frac{d}{dt} \hat{\mathbf{i}}_{\text{int}}(t) &= -[\mathbf{F}^T \bar{\mathbf{B}}_{\text{sb},1}^T \bar{\mathbf{B}}_{\text{sb},1} \mathbf{F}]^{-1} \mathbf{F}^T \bar{\mathbf{B}}_{\text{sb},1}^T \mathbf{A}_{\text{sb}} \mathbf{x}_{\text{sb}}(t) \\ &- [\mathbf{F}^T \bar{\mathbf{B}}_{\text{sb},1}^T \bar{\mathbf{B}}_{\text{sb},1} \mathbf{F}]^{-1} \mathbf{F}^T \bar{\mathbf{B}}_{\text{sb},1}^T \bar{\mathbf{B}}_{\text{sb},2} \frac{d}{dt} \mathbf{i}_{\text{ext}}(t). \end{aligned} \quad (4.37)$$

Replacing the internal currents in (4.34) results in the state equation

$$\frac{d^2}{dt^2} \mathbf{x}_{\text{sb}}(t) = \mathbf{K} \left[\mathbf{A}_{\text{sb}} \mathbf{x}_{\text{sb}}(t) + \bar{\mathbf{B}}_{\text{sb},2} \frac{d}{dt} \mathbf{i}_{\text{ext}}(t) \right] \quad (4.38)$$

with the idempotent ($\mathbf{K}^2 = \mathbf{K}$) and symmetric ($\mathbf{K}^T = \mathbf{K}$) matrix

$$\mathbf{K} = \left[\mathbf{I} - \bar{\mathbf{B}}_{\text{sb},1} \mathbf{F} [\mathbf{F}^T \bar{\mathbf{B}}_{\text{sb},1}^T \bar{\mathbf{B}}_{\text{sb},1} \mathbf{F}]^{-1} \mathbf{F}^T \bar{\mathbf{B}}_{\text{sb},1}^T \right]. \quad (4.39)$$

The statement (4.38) constitutes an orthogonal projection of the expression in the brackets in the null space of $\mathbf{F}^T \bar{\mathbf{B}}_{\text{sb},1}^T$. Qualitatively speaking, the orthogonal projection (4.38) ensures the system to evolve on a subspace of $\mathbf{x}_{\text{sb}}(t)$ so that the algebraic constraint (4.35) arising from Kirchhoff's voltage law is satisfied. The orthonormal basis of the null space of $\mathbf{F}^T \bar{\mathbf{B}}_{\text{sb},1}^T$ is determined by

$$\mathbf{M} = \text{Null}(\mathbf{F}^T \bar{\mathbf{B}}_{\text{sb},1}^T) \quad (4.40)$$

with $\mathbf{M}^T \mathbf{M} = \mathbf{I}$. This orthonormal basis is used to remove $N_{\text{int}}/2$ redundant states in $\mathbf{x}_{\text{sb}}(t) \in \mathbb{R}^{N_{\text{sb}}}$ by means of the mapping

$$\mathbf{x}_{\text{sb}}(t) = \mathbf{M} \mathbf{x}_{\text{sl}}(t) = \mathbf{K} \mathbf{M} \mathbf{x}_{\text{sl}}(t). \quad (4.41)$$

Here, $\mathbf{x}_{\text{sl}}(t) \in \mathbb{R}^{N_{\text{sl}}}$ is the reduced state vector with $N_{\text{sb}} = N_{\text{sl}} + N_{\text{int}}/2$. It should be stressed that every vector $\mathbf{M} \mathbf{x}_{\text{sl}}(t)$ is in the null space of $\mathbf{F}^T \bar{\mathbf{B}}_{\text{sb},1}^T$. Formally speaking this means that $\mathbf{F}^T \bar{\mathbf{B}}_{\text{sb},1}^T \mathbf{M} \mathbf{x}_{\text{sl}}(t) = \mathbf{0} \forall \mathbf{x}_{\text{sl}}(t)$ holds. Therefore, the vector remains unchanged when projecting it into this null space by multiplying from the left-hand side with the projection matrix \mathbf{K} (see right-hand side of (4.41)). Substituting (4.41) in (4.38) and (4.31) yields the second-order state-space system

$$\frac{d^2}{dt^2} \mathbf{x}_{\text{sl}}(t) = \underbrace{\mathbf{M}^T \mathbf{K} \mathbf{A}_{\text{sb}} \mathbf{K} \mathbf{M}}_{\mathbf{A}_{\text{sl}}} \mathbf{x}_{\text{sl}}(t) + \underbrace{\mathbf{M}^T \mathbf{K} \bar{\mathbf{B}}_{\text{sb},2}}_{\mathbf{B}_{\text{sl}}} \frac{d}{dt} \mathbf{i}_{\text{ext}}(t), \quad (4.42)$$

$$\mathbf{v}_{\text{ext}}(t) = \underbrace{\bar{\mathbf{B}}_{\text{sb},2}^T \mathbf{K} \mathbf{M}}_{\mathbf{B}_{\text{sl}}^T} \mathbf{x}_{\text{sl}}(t) \quad (4.43)$$

describing the dynamical properties of the concatenated RF structure. The subscript “sl” highlights that the matrices and vectors correspond to the second-order system which is generated from linking the state-space models of all segments. In accordance with the derivations for second-order systems in Section 3.2, the output matrix is the transposed of the input matrix. Moreover, on account of the symmetry of \mathbf{K} and the symmetric negative definiteness of \mathbf{A}_{sb} , \mathbf{A}_{sl} is symmetric negative semidefinite as well (cf. discussion in Appendix C.3). Following Subsection 3.3.3, state-space models with symmetric negative-semidefinite state matrices are internally marginally stable. In other other words, the internal marginal stability of the concatenated state-space system is preserved, if the state-space models of the segments are internally marginally stable.

4.4 Model Order Reduction for the Linked State-Space Model

This section corresponds to Step IV in the chart presented in Figure 1.1. Detailed investigations [70] have shown that the state-space system (4.42) - (4.43) still contains states which are not required in the frequency interval of interest. Therefore, it is advantageous to perform the model order reduction (refer to Section 4.2) for this system in order to have an even more compact model of the full structure. The state-space system (4.42) - (4.43) after a final model order reduction is denoted by

$$\frac{d^2}{dt^2} \mathbf{x}_{\text{slr}}(t) = \mathbf{A}_{\text{slr}} \mathbf{x}_{\text{slr}}(t) + \mathbf{B}_{\text{slr}} \frac{d}{dt} \mathbf{i}_{\text{ext}}(t), \quad (4.44)$$

$$\mathbf{v}_{\text{ext}}(t) = \mathbf{B}_{\text{slr}}^T \mathbf{x}_{\text{slr}}(t). \quad (4.45)$$

The subscript “slr” is introduced to highlight that the quantities refer to a second-order system of the linked structure. The system is reduced by means of model order reduction. The matrix which relates the system (4.42) - (4.43) with the reduced system (4.44) - (4.45) is denoted by \mathbf{V}_{slr} , i.e.

$$\mathbf{x}_{\text{sl}}(t) = \mathbf{V}_{\text{slr}} \mathbf{x}_{\text{slr}}(t). \quad (4.46)$$

4.5 Further Representations of the Compact State-Space System

The second-order state-space system (4.44) - (4.45), which describes the complete structure in an impedance formulation, is representable in terms of first-order state-space systems in an impedance and in a scattering formulation as well. Subsequently, the transfer of the second-order system to these first-order systems is discussed.

4.5.1 Transfer into First-Order Impedance Formulation

In order to obtain a first-order state-space system of the concatenated structure in an impedance formulation, the diagonality of the state matrix \mathbf{A}_{slr} is used and (4.44) is expressed line by line:

$$\frac{d^2}{dt^2} x_{\text{slr},n}(t) = -\tilde{\omega}_{\text{slr},n}^2 x_{\text{slr},n}(t) + \mathbf{b}_{\text{slr},n} \frac{d}{dt} \mathbf{i}_{\text{ext}}(t), \quad (4.47)$$

where $x_{\text{slr},n}(t)$ is the n th coefficient of the vector $\mathbf{x}_{\text{slr}}(t)$, $\mathbf{b}_{\text{slr},n} \in \mathbb{R}^{1 \times N_t}$ is the n th row of the matrix \mathbf{B}_{slr} , and $-\tilde{\omega}_{\text{slr},n}^2$ are the diagonal coefficients of \mathbf{A}_{slr} , so that

$\mathbf{A}_{\text{slr}} = \text{diag}(-\tilde{\omega}_{\text{slr},1}^2, -\tilde{\omega}_{\text{slr},2}^2, -\tilde{\omega}_{\text{slr},3}^2, \dots)$. Integrating (4.47) with respect to time yields

$$\frac{d}{dt}x_{\text{slr},n}(t) = -\tilde{\omega}_{\text{slr},n}^2 \hat{x}_{\text{slr},n}(t) + \mathbf{b}_{\text{slr},n} \mathbf{i}_{\text{ext}}(t), \quad (4.48)$$

where

$$\frac{d}{dt}\hat{x}_{\text{slr},n}(t) = x_{\text{slr},n}(t). \quad (4.49)$$

Introducing the state

$$y_{\text{slr},n}(t) = \tilde{\omega}_{\text{slr},n} \hat{x}_{\text{slr},n}(t) \quad (4.50)$$

and collecting (4.48) and (4.49) for all elements delivers the state equation with first-order derivatives and twice as many degrees of freedom in comparison with the second-order system:

$$\underbrace{\frac{d}{dt} \begin{pmatrix} y_{\text{slr},1}(t) \\ x_{\text{slr},1}(t) \\ y_{\text{slr},2}(t) \\ x_{\text{slr},2}(t) \\ \vdots \end{pmatrix}}_{\mathbf{x}_{\text{flr}}(t)} = \underbrace{\begin{pmatrix} 0 & \tilde{\omega}_{\text{slr},1} & 0 & 0 & \dots \\ -\tilde{\omega}_{\text{slr},1} & 0 & 0 & 0 & \dots \\ 0 & 0 & 0 & \tilde{\omega}_{\text{slr},2} & \dots \\ 0 & 0 & -\tilde{\omega}_{\text{slr},2} & 0 & \dots \\ \vdots & \vdots & \vdots & \vdots & \ddots \end{pmatrix}}_{\mathbf{A}_{\text{flr}}} \underbrace{\begin{pmatrix} y_{\text{slr},1}(t) \\ x_{\text{slr},1}(t) \\ y_{\text{slr},2}(t) \\ x_{\text{slr},2}(t) \\ \vdots \end{pmatrix}}_{\mathbf{x}_{\text{flr}}(t)} + \underbrace{\begin{pmatrix} \mathbf{0} \\ \mathbf{b}_{\text{slr},1} \\ \mathbf{0} \\ \mathbf{b}_{\text{slr},2} \\ \vdots \end{pmatrix}}_{\mathbf{B}_{\text{flr}}} \mathbf{i}_{\text{ext}}(t). \quad (4.51)$$

The state matrix \mathbf{A}_{flr} is skew symmetric and $\mathbf{0} \in \mathbb{R}^{1 \times N_{\text{ext}}}$. The subscripts “flr” denote that the quantities refer to a first-order representation of the linked system which is reduced. The output equation corresponding to (4.51) reads as

$$\mathbf{v}_{\text{ext}}(t) = \underbrace{\begin{pmatrix} \mathbf{0} & \mathbf{b}_{\text{slr},1}^T & \mathbf{0} & \mathbf{b}_{\text{slr},2}^T & \dots \end{pmatrix}}_{\mathbf{B}_{\text{flr}}^T} \underbrace{\begin{pmatrix} y_{\text{slr},1}(t) \\ x_{\text{slr},1}(t) \\ y_{\text{slr},2}(t) \\ x_{\text{slr},2}(t) \\ \vdots \end{pmatrix}}_{\mathbf{x}_{\text{flr}}(t)}, \quad (4.52)$$

where $\mathbf{0} \in \mathbb{R}^{N_{\text{ext}} \times 1}$.

4.5.2 Transfer into First-Order Scattering Formulation

The first-order impedance representation (4.51) - (4.52) is transferable to a scattering formulation by substituting the external voltages and currents of the concatenated structure by the amplitudes of incident and scattered waves. The derivations presented hereinafter are basically following [41, Subsection 3.3.3] and [2, Section II].

In order to obtain a time-domain relationship between modal voltages, modal currents, amplitudes of incident waves, and amplitudes of scattered waves, the identities (3.62) and (3.63) must be inversely transformed. The inverse transformation results in inconvenient convolutions (refer to [71, (7) - (8)]), if the frequency-dependent wave impedances of TE (2.57) and TM (2.59) modes are listed on the diagonal of $\underline{\mathbf{D}}_Z(j\omega)$. In order to avoid these convolutions, the frequency-dependent wave impedances are evaluated for an angular frequency ω_0 above the cutoff frequencies so that $\underline{\mathbf{D}}_Z(j\omega_0) = \mathbf{D}_Z$ becomes a real-valued frequency-independent diagonal matrix². Based on the specified assumptions, the convolutions are avoided and the inverse transformation of (3.62) and (3.63) reads as

$$\mathbf{a}_{\text{ext}}(t) = \frac{1}{2} \left(\mathbf{D}_Z^{-\frac{1}{2}} \mathbf{v}_{\text{ext}}(t) + \mathbf{D}_Z^{\frac{1}{2}} \mathbf{i}_{\text{ext}}(t) \right), \quad (4.53)$$

$$\mathbf{b}_{\text{ext}}(t) = \frac{1}{2} \left(\mathbf{D}_Z^{-\frac{1}{2}} \mathbf{v}_{\text{ext}}(t) - \mathbf{D}_Z^{\frac{1}{2}} \mathbf{i}_{\text{ext}}(t) \right). \quad (4.54)$$

Combining (4.53) - (4.54) and (4.51) - (4.52) delivers a first-order state-space model for the concatenated structure in a scattering formulation:

$$\begin{aligned} \frac{d}{dt} \mathbf{x}_{\text{flr}}(t) = & (\mathbf{A}_{\text{flr}} - \mathbf{B}_{\text{flr}} \mathbf{D}_Z^{-1} \mathbf{B}_{\text{flr}}^T) \mathbf{x}_{\text{flr}}(t) \\ & + 2 \mathbf{B}_{\text{flr}} \mathbf{D}_Z^{-\frac{1}{2}} \mathbf{a}_{\text{ext}}(t) \end{aligned} \quad (4.55)$$

and

$$\mathbf{b}_{\text{ext}}(t) = \mathbf{D}_Z^{-1/2} \mathbf{B}_{\text{flr}}^T \mathbf{x}_{\text{flr}}(t) - \mathbf{I} \mathbf{a}_{\text{ext}}(t). \quad (4.56)$$

It can be seen that the state matrix in the scattering representation is not skew symmetric on account of the term $\mathbf{B}_{\text{flr}} \mathbf{D}_Z^{-1} \mathbf{B}_{\text{flr}}^T$. This term covers the loss of energy via the waveguide ports, i.e. it accounts for external losses.

4.6 Computation of Relevant RF Quantities

This section refers to Step V in the top-level chart in Figure 1.1. The section describes how the generated reduced-order models are employed to deduce relevant RF properties of large and complex structures. The subsequent discussions are focused on state-space models which arise from the proposed concatenation approach such as (4.44) - (4.45) or (4.51) - (4.52). Nonetheless, the following approaches are usable as well for reduced-order models which do not result from the concatenation technique.

²Note that the line impedances of TEM port modes, which could be contained on the diagonal of $\underline{\mathbf{D}}_Z(j\omega)$ as well, are real and frequency-independent anyhow.

4.6.1 Field Distributions in 3D by Means of State Vectors

The state vectors $\mathbf{x}_{\text{slr}}(t)$ (in time domain) and $\underline{\mathbf{x}}_{\text{slr}}$ (in frequency domain) of the concatenated and reduced state-space model comprise data to reconstruct the 3D field distributions in large and complex structures. These state-vectors can be obtained for excitations at the waveguide ports as discussed in Subsection 4.6.2 or from eigenmode computations as depicted in Subsection 4.6.4. By way of example, the subsequent equations are focused on state vectors in time domain. Nonetheless, the entire approach is valid in frequency domain as well. For the sake of clarity, the construction of the 3D field distributions in the complete structure is visualized in the top-level chart in Figure 4.4. Note that this chart is a modification of the chart in Figure 1.1. In order to determine the field distribution in the complete structure, it is assumed that the state vector $\mathbf{x}_{\text{slr}}(t)$ of the linked and reduced state-space model is already determined. This vector is mapped to the state vector of the concatenated system (4.42) - (4.43) by means of

$$\mathbf{x}_{\text{sb}}(t) = \mathbf{M} \mathbf{x}_{\text{sl}}(t) = \mathbf{M} \mathbf{V}_{\text{slr}} \mathbf{x}_{\text{slr}}(t) \quad (4.57)$$

as indicated in Step V in Figure 4.4. The mapping results from (4.41) with (4.46) and gives the state vector $\mathbf{x}_{\text{sb}}(t)$ of the block system (4.18). Subsequently, this state vector is segmented in accordance with its definition given in (4.18) so that the reduced state vectors $\mathbf{x}_{\text{sr},r}(t)$ of the individual segments arise. These are mapped into the full space by means of the projection matrices of the state-space systems for the segments:

$$\mathbf{x}_{\text{s},r}(t) = \mathbf{V}_{\text{sr},r} \mathbf{x}_{\text{sr},r}(t). \quad (4.58)$$

If the r th segment is described by a state-space equation resulting from a FIT discretization (e.g. segment $r = 1$ and segment $r = 2$ in Figure 4.4), the vector $\widehat{\mathbf{e}}_r(t)$ comprising the electric grid voltages for this segment is determined by

$$\widehat{\mathbf{e}}_r(t) = \mathcal{M}_{\varepsilon,r}^{-1/2} \mathbf{x}_{\text{sd},r}(t), \quad (4.59)$$

where $\mathcal{M}_{\varepsilon,r}$ is the FIT matrix (2.39) for the r th segment and $\widehat{\mathbf{e}}'_r(t) = \mathbf{x}_{\text{sd},r}(t) = \mathbf{x}_{\text{s},r}(t)$. In the case where the r th segment is described by a second-order state-space equation which arises from the analytical techniques (for instance segment $r = 3$ in Figure 4.4), the vector $\mathbf{x}_{\text{sc},r}(t) = \mathbf{x}_{\text{s},r}(t)$ contains the weighting coefficients for the 3D eigenmodes of the r th segment. Thus, the continuous electric field in the segment is reconstructed by (3.18) based on the coefficients of $\mathbf{x}_{\text{sc},r}(t) = [x_{r,1}(t), x_{r,2}(t), \dots, x_{r,N_{\text{e},r}}(t)]^T$:

$$\mathbf{E}_r(\mathbf{r}, t) = \sum_{n=1}^{N_{\text{e},r}} \frac{\tilde{\mathbf{E}}_{r,n}(\mathbf{r})}{\sqrt{2W_{r,n}}} x_{r,n}(t). \quad (4.60)$$

Here, $\mathbf{E}_r(\mathbf{r}, t)$ is the electric field distribution in the r th segment, $N_{\text{e},r}$ the number of eigenmodes considered for the segment, $\tilde{\mathbf{E}}_{r,n}(\mathbf{r})$ the n th eigenmode in the r th segment, and $W_{r,n}$ the energy stored in the n th eigenmode of the r th segment.

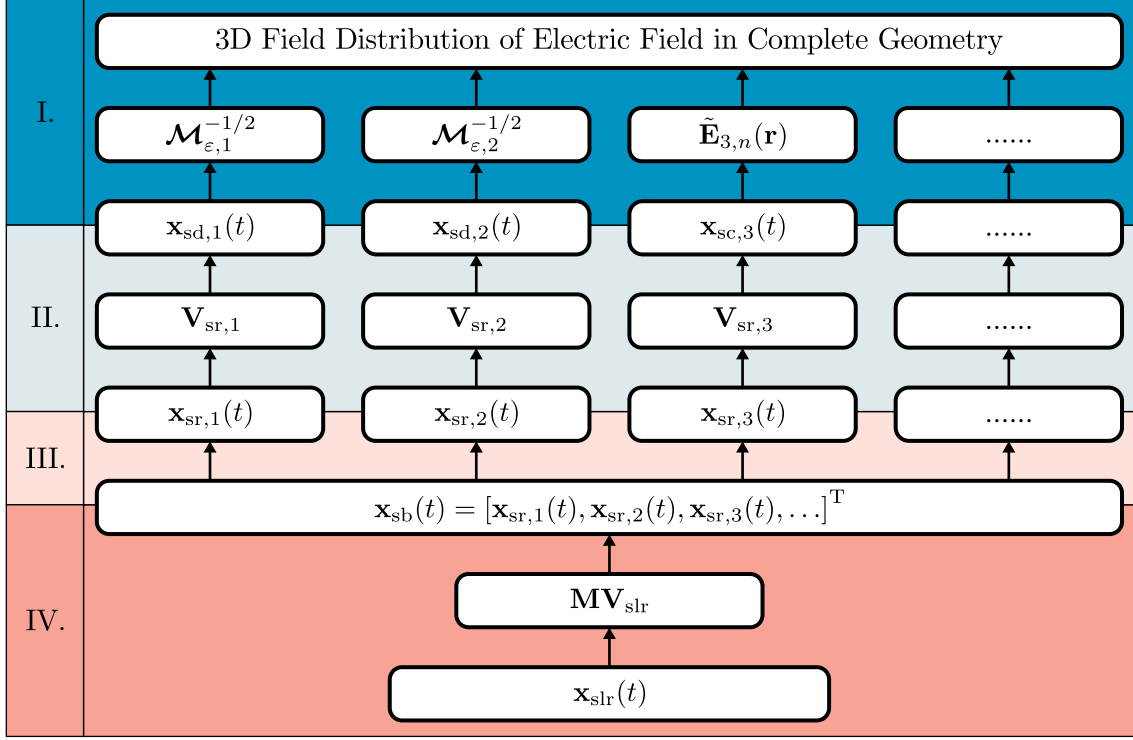


Figure 4.4: Determination of the 3D field distribution in the complete structure by the state-vector $\mathbf{x}_{\text{slr}}(t)$ of the linked and reduced-order state-space model. The chart is a modification of Figure 1.1. Based on $\mathbf{x}_{\text{slr}}(t)$, the vector $\mathbf{x}_{\text{sb}}(t)$ of the block system is calculated in Step IV. This vector is split into the states of the reduced-order models of the segments in Step III. These vectors are mapped into the full state space $\mathbf{x}_{\text{s},r}(t)$ of the individual segments in Step II. The emerging vectors finally deliver the field distributions in the segments in Step I. In the case where the segment is discretized with FIT (segment $r = 1$ and segment $r = 2$ in the chart), the electric grid voltages $\tilde{\mathbf{e}}_r(t)$ in the r th segment are determined by $\mathbf{x}_{\text{s},r}(t) = \mathbf{x}_{\text{sd},r}(t)$ and the matrix $\mathcal{M}_{\epsilon,r}^{-1/2}$. In the case where the RF properties of the segment are described by analytical techniques (segment $r = 3$ in the chart), the field distribution is reconstructed in accordance with (4.60) based on the eigenmodes $\tilde{\mathbf{E}}_{r,n}(\mathbf{r})$ in the r th segment and the weighting coefficients stored in $\mathbf{x}_{\text{s},r}(t) = \mathbf{x}_{\text{sc},r}(t)$.

The considerations mentioned above are focused on the electric field. This is sufficient since the magnetic field distributions in the structure may be determined straightforward from the electric field distributions by Maxwell's equations.

4.6.2 Frequency-Domain and Time-Domain Excitations

The computation of frequency-domain field distributions in the complete structure due to current stimuli at the waveguide ports is straightforward. The frequency-

domain transformation of (4.44) is determined in accordance with Subsection 3.3.4. The transformation is resorted to

$$\underline{\mathbf{x}}_{\text{slr}} = ((j\omega)^2 \mathbf{I} - \mathbf{A}_{\text{slr}})^{-1} \mathbf{B}_{\text{slr}} j\omega \underline{\mathbf{i}}_{\text{ext}}. \quad (4.61)$$

The matrix inversion is conveniently computable, because \mathbf{A}_{slr} is diagonal. Once $\underline{\mathbf{x}}_{\text{slr}}$ is determined for the current stimulus of interest, the field distribution in the concatenated arrangement is evaluated based on the approach described in Subsection 4.6.1.

In the case of computing transient field distributions due to transient current excitations, the first-order system (4.51) - (4.52) is used, since most ordinary differential equation solvers (e.g. routines implemented in [69]) require first-order systems. The second-order state-space vector is related to the first-order vector by

$$\underbrace{\begin{pmatrix} x_{\text{slr},1}(t) \\ x_{\text{slr},2}(t) \\ \vdots \end{pmatrix}}_{\mathbf{x}_{\text{slr}}(t)} \begin{pmatrix} 0 & 1 & 0 & 0 & \dots \\ 0 & 0 & 0 & 1 & \dots \\ \vdots & \vdots & \vdots & \vdots & \ddots \end{pmatrix} = \underbrace{\begin{pmatrix} y_{\text{slr},1}(t) \\ x_{\text{slr},1}(t) \\ y_{\text{slr},2}(t) \\ x_{\text{slr},2}(t) \\ \vdots \end{pmatrix}}_{\mathbf{x}_{\text{flr}}(t)}. \quad (4.62)$$

The field distribution at time t is constructed based on $\mathbf{x}_{\text{slr}}(t)$ and the technique presented in Subsection 4.6.1.

4.6.3 Impedance and Scattering Parameters

The impedance parameters of the full structure are readily available from the frequency-domain transfer function of (4.44) - (4.45) (refer to Subsection 3.3.4 for the derivation of transfer functions):

$$\underline{\mathbf{Z}}(j\omega) = \mathbf{B}_{\text{slr}}^T ((j\omega)^2 \mathbf{I} - \mathbf{A}_{\text{slr}})^{-1} \mathbf{B}_{\text{slr}} j\omega. \quad (4.63)$$

As already noted above, the required matrix inversion is easily computable, because the comparatively small state matrix \mathbf{A}_{slr} , obtained from the model order reduction, is a diagonal matrix. Thus, fast broadband frequency sweeps are feasible to receive the impedance parameters of the full structure. If scattering parameters are of interest, (4.63) is substituted in (3.67). Alternatively, the frequency-domain transfer function of (4.55) - (4.56) can be determined.

4.6.4 Eigenmodes

The proposed scheme provides field distributions and resonant frequencies of eigenmodes of the full structure in the frequency interval of interest. The approach

delivers eigenfrequencies and eigenmodes for perfect magnetic conducting and perfect electric conducting boundary conditions at the waveguide ports, whereas the remaining boundaries of the RF structure are assumed to be perfect electric conducting.

Eigenmodes with PMC Boundary Conditions at Waveguide Ports

Choosing perfect magnetic conducting boundary conditions on the facets of the waveguide ports is natural for the introduced approach as it is based on an impedance formulation. To compute the eigenmodes for the PMC case, the frequency-domain transformation of (4.44) is regarded following Subsection 3.3.4:

$$\underbrace{(j\omega)^2}_{-\omega^2} \mathbf{x}_{\text{slr}} = \mathbf{A}_{\text{slr}} \mathbf{x}_{\text{slr}} + \mathbf{B}_{\text{slr}} j\omega \underbrace{\mathbf{i}_{\text{ext}}}_{\mathbf{0}}. \quad (4.64)$$

In order to ensure that the transverse magnetic fields vanish on the waveguide port surfaces, the excitation currents have to be equal to zero. The arising equation is fulfilled if $-\omega^2$ is equal to an eigenvalue $\lambda_{\text{slr},n}^{\text{PMC}}$ and \mathbf{x}_{slr} is equal to an eigenvector $\mathbf{u}_{\text{slr},n}^{\text{PMC}}$ of \mathbf{A}_{slr} . As a consequence of the symmetry and the negative semidefiniteness of \mathbf{A}_{slr} , the eigenvalues are real-valued and are equal to or smaller than zero (refer to Appendix C.3.2). On account of the diagonality of the state matrix, the eigenvalues are listed directly on the main diagonal, i.e. $\mathbf{A}_{\text{slr}} = \text{diag}(\lambda_{\text{slr},1}^{\text{PMC}}, \lambda_{\text{slr},2}^{\text{PMC}}, \dots)$. Therefore, angular resonant frequencies of the eigenmodes with PMC conditions at the waveguide ports are given by

$$\tilde{\omega}_{\text{slr},n}^{\text{PMC}} = \sqrt{-\lambda_{\text{slr},n}^{\text{PMC}}} = \tilde{\omega}_{\text{slr},n}. \quad (4.65)$$

The corresponding 3D field distributions in the full structure are calculated by

$$\mathbf{x}_{\text{slr}} = \mathbf{u}_{\text{slr},n}^{\text{PMC}} \quad (4.66)$$

according to Subsection 4.6.1. It should be recalled that the n th coefficient of the normalized n th eigenvector of a diagonal matrix is equal to one whereas the remaining coefficients are equal to zero. For e.g. $n = 2$ this reads as $\mathbf{u}_{\text{slr},2}^{\text{PMC}} = (0 \ 1 \ 0 \ \dots)^T$.

Eigenmodes with PEC Boundary Conditions at Waveguide Ports

To account for perfect electric conducting boundary conditions at the waveguide ports, (4.44) - (4.45) have to be modified. To ensure that the tangential electric fields on the waveguide ports are equal to zero, the modal voltages have to vanish. Therefore, an orthogonal basis of the null space of $\mathbf{B}_{\text{slr}}^T$ is determined:

$$\Theta = \text{Null}\left(\mathbf{B}_{\text{slr}}^T\right), \quad (4.67)$$

where $\Theta^T \Theta = \mathbf{I}$. In a next step, the state of the combined system is expressed in terms of

$$\mathbf{x}_{\text{slr}}(t) = \Theta \mathbf{x}_{\text{slr}}^{\text{PEC}}(t). \quad (4.68)$$

Using this ansatz in (4.45) shows that all modal voltages are enforced to vanish:

$$\mathbf{0} = \mathbf{v}_{\text{ext}}(t) = \underbrace{\mathbf{B}_{\text{slr}}^T \Theta}_{\mathbf{0}} \mathbf{x}_{\text{slr}}^{\text{PEC}}(t). \quad (4.69)$$

Substituting the ansatz in the frequency-domain transformation of the state equation (4.44) yields

$$\underbrace{(j\omega)^2}_{-\omega^2} \mathbf{x}_{\text{slr}}^{\text{PEC}} = \Theta^T \mathbf{A}_{\text{slr}} \Theta \mathbf{x}_{\text{slr}}^{\text{PEC}} + \underbrace{\Theta^T \mathbf{B}_{\text{slr}}}_{\mathbf{0}} j\omega \mathbf{i}_{\text{ext}}. \quad (4.70)$$

It should be remarked that the state matrix is symmetric negative semidefinite, so that its eigenvalues $\lambda_{\text{slr},n}^{\text{PEC}}$ are smaller than or equal to zero (again refer to Appendix C.3.2). The identity (4.70) is fulfilled if $-\omega^2$ is equal to an eigenvalue $\lambda_{\text{slr},n}^{\text{PEC}}$ and $\mathbf{x}_{\text{slr}}^{\text{PEC}}$ is equal to an eigenvector $\mathbf{u}_{\text{slr},n}^{\text{PEC}}$ of $\Theta^T \mathbf{A}_{\text{slr}} \Theta$. Therefore, the angular resonant frequencies of eigenmodes with PEC conditions at the waveguide ports are given by

$$\tilde{\omega}_{\text{slr},n}^{\text{PEC}} = \sqrt{-\lambda_{\text{slr},n}^{\text{PEC}}}. \quad (4.71)$$

The corresponding 3D field distributions in the full structure are reconstructed by

$$\mathbf{x}_{\text{slr}} = \Theta \mathbf{u}_{\text{slr},n}^{\text{PEC}} \quad (4.72)$$

based on the description presented in Subsection 4.6.1. It is remarked that the computation of the eigenvalues of $\Theta^T \mathbf{A}_{\text{slr}} \Theta$ is straightforward due to the comparatively small size of the matrix.

4.6.5 Accounting for Losses and Computation of Quality Factors

Subsection 2.4.1 introduces several loss mechanisms related to electromagnetic fields. In the context of the considered RF structures losses due to finite surface resistivities and due to coupling to the waveguide ports are most important. As a matter of fact, the presented non-excited state-space models in the impedance formulation do not account for losses in general. Nonetheless, these state-space models can be modified to cover losses if additional constraints between electric and magnetic fields are taken into account. These constraints are briefly sketched hereinafter before the approach to compute (external) quality factors of resonances is presented in detail.

Remarks on Accounting for Surface Losses

Following [3, p. 466] or [54, pp. 534 - 536] the electromagnetic fields in the presence of large but finite surface conductivities can be estimated from the fields in the lossless case, i.e. from the case of infinite surface conductivities. Therefore, the flow of energy into the walls (surface losses) can be approximated by means of the lossless state-space models in the impedance representation. The approach is based on the assumption that the tangential magnetic field on the wall of the RF structure does not change significantly if large but finite surface conductivities are introduced. Moreover, the tangential electric field on the wall, which is basically proportional to the tangential magnetic field on the wall, is assumed to be so small that it can be considered as a perturbation of the field in the lossless structure. The relationship between tangential electric fields and tangential magnetic fields on lossy walls is expressed in frequency domain by the surface impedance boundary condition (SIBC) [54, 55]

$$\underline{\mathbf{E}}_t(\mathbf{r}) = \underline{Z}_s(j\omega_{\text{lsy}}) \underline{\mathbf{J}}_s(\mathbf{r}) \quad (4.73)$$

with the surface impedance

$$\underline{Z}_s(j\omega_{\text{lsy}}) = \sqrt{\frac{j\omega_{\text{lsy}}\mu}{\sigma}} \quad (4.74)$$

and the surface electric current density

$$\underline{\mathbf{J}}_s(\mathbf{r}) = \mathbf{n} \times \underline{\mathbf{H}}(\mathbf{r}). \quad (4.75)$$

Here, $\underline{\mathbf{E}}_t(\mathbf{r})$ is the tangential surface electric field due to finite surface conductivities, \mathbf{n} is the unit outward normal vector to the conducting surface, and $\underline{\mathbf{H}}(\mathbf{r})$ the magnetic field on the surface for the lossless case. In order to modify the state-space systems for the lossless case to account for surface losses, the SIBC has to be incorporated as it is done for instance in [72]. Generally, this incorporation requires the transfer of the SIBC to time domain which is an onerous task due to the $\sqrt{j\omega_{\text{lsy}}}$ dependence of (4.74). Nonetheless, a set of auxiliary differential equations can be constructed to approximate the non-rational dependence in time domain as proposed in [73].

Remarks on Accounting for Losses through Waveguide Ports

Similar to the treatment of surface losses, losses due to the propagation of energy through the waveguide ports are deducible from the lossless case as well. Rather than enforcing constraints between tangential electric and magnetic fields on the surfaces of the conducting walls, constraints between the tangential electric and magnetic fields on the facets of waveguide ports are required. As previously discussed in Section 3.1, the tangential fields on the facets of the waveguide ports are available

in terms of a decomposition of transverse field patterns weighted with the respective modal voltages and currents. To model the waveguide ports of the structure to be infinitely long such that no energy is reflected into the structure, the exact infinite guide [74, p. 476] modal termination conditions

$$\underline{V}_{p,m} = -\underline{Z}_{p,m}(j\omega_{\text{lsy}}) \underline{I}_{p,m} \quad (4.76)$$

are required at the terminals of the concatenated structure. Here, $\underline{V}_{p,m}$ and $\underline{I}_{p,m}$ refer to the modal voltages and currents of the m th mode at the p th port whereas $\underline{Z}_{p,m}(j\omega_{\text{lsy}})$ is selected to be the wave impedance (2.57) or (2.59) in the case of TE or TM port modes or the line impedance (2.63) in the case of TEM port modes. The application of the modal termination conditions can be interpreted in terms of connecting the matching impedances to the respective terminals as depicted in Figure 4.5. Note that the minus sign in (4.76) results from the definition of voltages and currents in Figure 4.5. In order to adapt the state-space systems for the lossless case to cover losses through waveguide ports, the modal termination conditions (4.76) have to be regarded in the impedance formulation of the lossless state-space models. This demands the transfer of the modal termination conditions to time domain. While this is straightforward for the TEM case due to the frequency-independent and real-valued line impedance, the inverse transformations of the wave impedances (2.57) and (2.59) of TE and TM port modes are not straightforward due to their non-rational characteristics: Below the cutoff frequency, the real part of the wave impedances is zero whereas the imaginary part is equal to zero above the cutoff frequency. For frequencies much larger than the cutoff frequency the wave impedance tends to Z_{fs} . In order to avoid the convolutions [71, (7) - (8)] resulting from the inverse transformations of (4.76) for TE and TM port modes, auxiliary differential equations can be constructed as proposed in [71]. Alternatively, the wave impedances for TE and TM modes can be calculated for a single evaluation angular frequency above the cutoff frequencies so that real-valued and constant wave impedances arise (cf. Subsection 4.5.2).

Computation of Quality Factors

As discussed in Subsection 2.4.1, quality factors are a substantial measure to quantify losses of resonances. The total quality factor of the n th resonance can be estimated³ from the external quality factor and the intrinsic quality factor by

$$\frac{1}{Q_{\text{tot},n}} \approx \frac{1}{Q_{\text{ext},n}} + \frac{1}{Q_{\text{int},n}}. \quad (4.77)$$

³The resonant frequencies in the case where only external losses are considered slightly differs from the case where exclusively intrinsic losses are regarded. Therefore, (4.77) is only an approximation.

As mentioned in the introduction, the small intrinsic losses (surface losses) of superconducting cavities result in intrinsic quality factors in the order of $10^9 \dots 10^{11}$. Compared to that, the external quality factors $Q_{\text{ext},n}$ are expected to be orders of magnitude smaller, so that $Q_{\text{ext},n}/Q_{\text{int},n} \ll 1$ holds. In that case (4.77) can be rearranged to

$$Q_{\text{tot},n} \approx \frac{Q_{\text{ext},n} Q_{\text{int},n}}{Q_{\text{ext},n} + Q_{\text{int},n}} = \frac{Q_{\text{ext},n}}{\underbrace{\left(\frac{Q_{\text{ext},n}}{Q_{\text{int},n}}\right)}_{\ll 1} + 1} \approx Q_{\text{ext},n}. \quad (4.78)$$

The equation conveys that the external quality factors mainly determine the total quality factors of superconducting RF structures. An experimental validation for this assumption is available in [1, Section IV] on the basis of a comparison between measured and simulated quality factors of superconducting third-harmonic cavities in the FLASH linac at DESY. It is shown that the order of magnitude of measured total quality factors $Q_{\text{tot},n}$ agrees with the order of magnitude of external quality factors $Q_{\text{ext},n}$ obtained from a simulation (the simulation does not cover surface losses). On account of these considerations, it is sufficient that the following derivations are focused on the computation of external quality factors.

In order to regard losses via the waveguide ports, the method described in [41, Subsection 3.3.3.] is applied. This approach can be considered as a generalization of the modal approach described in [3] and in [75] so that structures with more than one terminal can be treated. In a first step, the modal termination conditions (4.76) are collected by

$$\mathbf{i}_{\text{ext}} = -\underline{\mathbf{D}}_Z^{-1}(j\omega_{\text{lsy}}) \mathbf{v}_{\text{ext}}. \quad (4.79)$$

The matrix $\underline{\mathbf{D}}_Z(j\omega_{\text{lsy}})$ (also refer to Subsection 3.3.4) is a diagonal matrix which contains complex-valued and frequency-dependent wave impedances for external terminals accounting for TE and TM port modes and real-valued constant line impedances for external terminals accounting for TEM port modes. The modal termination conditions are used to replace the external voltages and currents in the frequency-domain transformation of the first-order state-space system (4.51) - (4.52). This delivers the nonlinear eigenproblem

$$j\omega_{\text{lsy}} \mathbf{x}_{\text{flr}} = (\mathbf{A}_{\text{flr}} - \mathbf{B}_{\text{flr}} \underline{\mathbf{D}}_Z^{-1}(j\omega_{\text{lsy}}) \mathbf{B}_{\text{flr}}^T) \mathbf{x}_{\text{flr}}. \quad (4.80)$$

In order to linearize this nonlinear problem [75, Section V. A.], the frequency-dependent diagonal matrix holding the matching impedances is evaluated for a real-valued evaluation angular frequency ω_0 in the frequency interval of interest so that $\underline{\mathbf{D}}_Z(j\omega_0) = \mathbf{D}_Z \in \mathbb{R}^{N_{\text{ext}} \times N_{\text{ext}}}$ is constant and real-valued. This results in the linear eigenvalue problem

$$j\omega_{\text{lsy}} \mathbf{x}_{\text{flr}} = (\mathbf{A}_{\text{flr}} - \mathbf{B}_{\text{flr}} \mathbf{D}_Z^{-1} \mathbf{B}_{\text{flr}}^T) \mathbf{x}_{\text{flr}}. \quad (4.81)$$

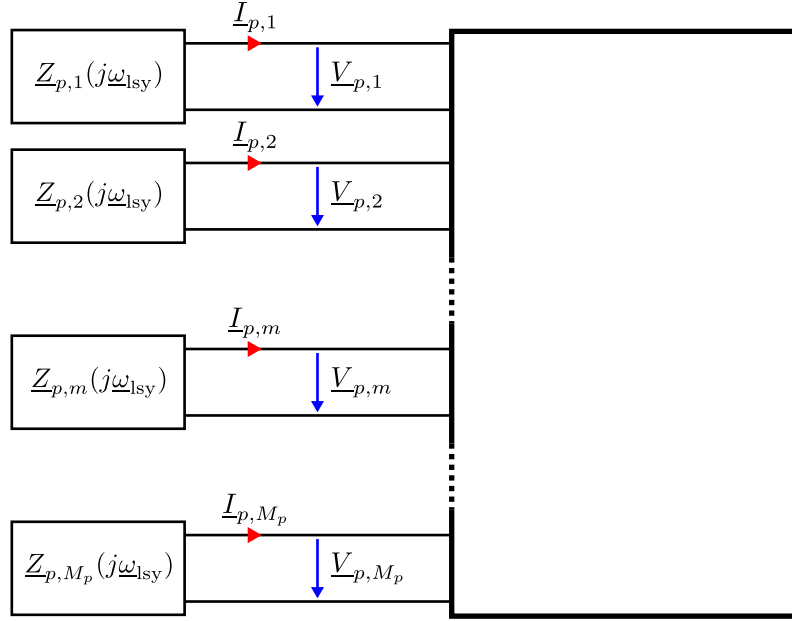


Figure 4.5: Accounting for external losses by matching of M_p terminals (corresponding to M_p 2D port modes at the p th port) with the matching impedances $Z_{p,m}(j\omega_{\text{lsy}})$. These impedances refer to the wave impedances (2.57) and (2.59) if the terminal corresponds to TE and TM port modes and to the line impedance (2.63) if the terminal corresponds to TEM port modes. At each terminal the modal terminal voltages $V_{p,m}$ and currents $I_{p,m}$ are indicated. For the sake of brevity solely the p th port of the concatenated structure is considered in the sketch.

Note that the state matrix is equal to the state matrix of the first-order state equation (4.55) in the scattering representation. This is natural because the scattering parameter representation also covers losses via waveguide ports. Moreover, the approximation $\underline{\mathbf{D}}_Z(j\omega_0) = \mathbf{D}_Z \in \mathbb{R}^{N_{\text{ext}} \times N_{\text{ext}}}$ is used in Subsection 4.5.2 as well. In order to compute the external quality factors of the concatenated structure, all complex-valued eigenvalues λ_n^{sct} of the nonsymmetric matrix $(\mathbf{A}_{\text{flr}} - \mathbf{B}_{\text{flr}} \mathbf{D}_Z^{-1} \mathbf{B}_{\text{flr}}^T)$ are computed. Note that the computation of the eigenvalues is feasible due to the comparatively small size of the matrix (several hundred rows and columns). Following Subsection 2.4.1, the external quality factors of the concatenated structure are related to the computed eigenvalues by

$$\lambda_n^{\text{sct}} = j\omega_{\text{lsy},n} = j\omega_{\text{lsy},n} - \frac{\omega_{\text{lsy},n}}{2Q_{\text{ext},n}}. \quad (4.82)$$

It should be stressed that $\Re(\omega_{\text{lsy},n}) = \omega_{\text{lsy},n}$ and $\Im(\omega_{\text{lsy},n}) = \omega_{\text{lsy},n}/2Q_{\text{ext},n}$. Finally, the identity (4.82) is rearranged to

$$Q_{\text{ext},n} = \frac{\Im(\lambda_n^{\text{sct}})}{2\Re(\lambda_n^{\text{sct}})}. \quad (4.83)$$

Note that the described approach does not suffer from difficulties of other techniques to compute quality factors of structures with small losses. Analyses in time domain require long settling times and their costs scale linearly with the quality factors as discussed in [75]. Direct analyses in frequency domain include the hard work of computing eigenvalues and eigenvectors of large, sparse, complex-valued, and nonsymmetric matrices [76]. Other frequency domain techniques are based on the computation of the scattering parameters followed by the application of a system identification algorithm (see e.g. [1] or [77] and references therein). As already mentioned in Section 1.4, the adequate computation of scattering parameters of resonant structures is a challenge in itself. Moreover, the system identification algorithm includes a multivariate nonlinear optimization.

5 Application Examples

This chapter presents a set of application examples for the proposed approach. The examples are sorted based on their complexity in an ascending order. The first example (refer to Section 5.1) is considered to be the proof of principle¹ since the geometry under concern is so simple that Maxwell's equations can be solved analytically. In contrast to the first, the last application example (see Section 5.5) demonstrates the ability of the introduced scheme to deal with very large and complex structures. All following sections are organized in a similar fashion. First, some general remarks on the structure under concern are given. Subsequently, details on the generation of state-space systems for the individual segments are discussed. Finally, the results from the concatenation scheme are presented and, if possible, are compared to direct computations. Note that the following application examples do not represent full and rigorous RF analyses of the investigated structures. Instead, the examples aim at showing the capabilities of the SSC scheme. In particular, the results presented in Section 5.4 and Section 5.5 are considered as predecessors for future detailed studies. All discrete formulations of Maxwell's equations are based on FIT and a hexahedral mesh despite the fact that tetrahedral meshes are expected to be more suitable for discretizing the fine features of the HOM couplers, for example. Nevertheless, tetrahedral meshes are not used since the respective system matrices generated with CST MWS [18] are difficult to export. The computations presented hereinafter are performed on a computer equipped with four Intel(R) Core(TM) i5-2400 CPUs @ 3.1 GHz and 8 GB RAM. The installed operating system is Windows 7 Professional. All concatenations are performed using a MATLAB [69] implementation of the SSC technique which has been created by Johann Heller. The specified computation times are wall-clock times.

5.1 Rectangular Waveguide

Initially, the presented scheme is validated by decomposing a lossless rectangular waveguide filled with air into four segments with different lengths L_r (see Figure 5.1). The lengths are deliberately chosen to be different: $L_1 = 100$ mm, $L_2 = \exp(5)$ mm = 148.41 mm, $L_3 = 25\pi$ mm = 78.54 mm, and $L_4 = 66$ mm. This ensures that the length of one segment is not a multiple of the length of another

¹Another proof of principle, which also works without numerical computations, can be found in [2].

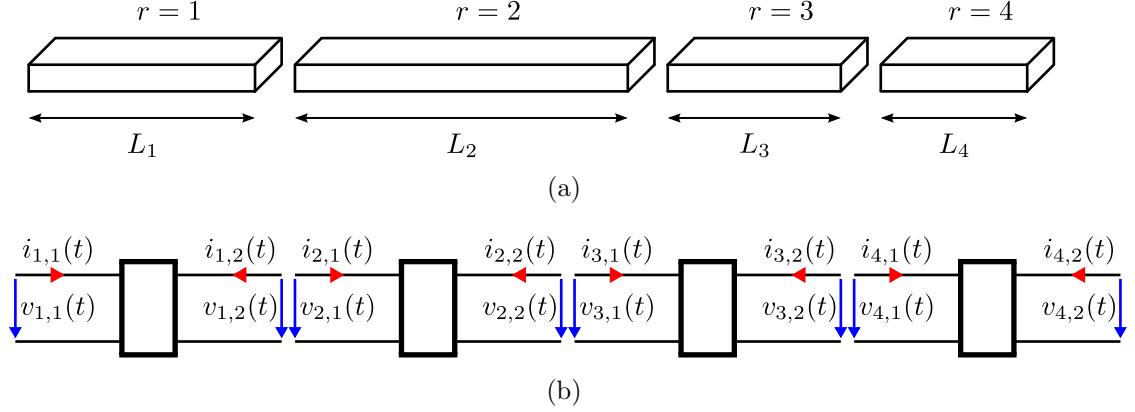


Figure 5.1: (a) Sketch of the decomposition of an R-100 waveguide with constant cross section into four segments with lengths $L_1 = 100$ mm, $L_2 = \exp(5)$ mm, $L_3 = 25\pi$ mm, and $L_4 = 66$ mm. (b) Abstract counterpart of the decomposition of the waveguide. The indicated modal voltages $v_{r,p}(t)$ and currents $i_{r,p}(t)$ refer to the TE₁₀ port mode.

segment or a multiple of the length of the entire waveguide. The cross section of the waveguide is chosen in accordance with the R-100 specification (width $a = 22.86$ mm and height $b = 10.16$ mm) [55]. For simplicity, the entire consideration is restricted to the TE₁₀ waveguide mode (refer to first row in Table A.1). Since Maxwell's equations can be analytically solved for the segments of the decomposed structure as well as for the entire structure, the complete consideration is free of discretization errors. This qualifies the example for an initial benchmark of the introduced concatenation scheme, because the results delivered by the method are directly comparable with analytical results. The validation example provides principal evidence for the extent to which broadband structures, such as open waveguides, can be accurately modeled based on state-space models with real-valued eigenfrequencies. In particular, the example allows for an estimation of the errors accumulated by the concatenation of reduced-order models. Moreover, the decomposition of the rectangular waveguide is considered as a toy example to become acquainted with the entire workflow of the scheme, in particular with the choice of the matrices \mathbf{P} and \mathbf{F} .

5.1.1 Generation of State-Space Systems for Segments

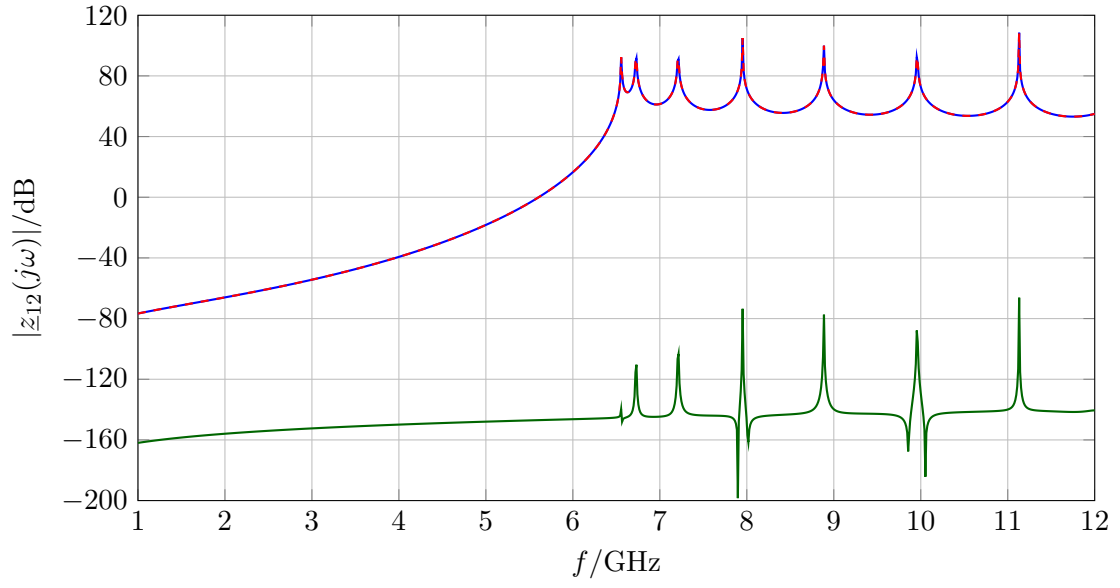
To generate the state-space models for the waveguide segments, their 3D eigenmodes with magnetic boundary conditions on the port planes, the respective eigenfrequencies, and the considered 2D port modes are required. The derivation of the eigenmodes and eigenfrequencies of a rectangular waveguide with width a , height b , and length L can be found in Appendix B.3: The electric field distribution (B.15) of the n th 3D eigenmode is described by the transverse field pattern $\mathbf{L}_t^{\text{TE}_{10}}(\mathbf{r}_t)$ and the voltage $\tilde{V}_n(z)$ of the eigenmode along the waveguide. This voltage accounts for

Table 5.1: Details on the state-space models of the individual segments of the waveguide: N_s is the number of states of the unreduced system, N_{sr} the number of states of the reduced system, and T_{rd} the computation time for reduction. The reduction interval is 1 GHz to 12 GHz and the stopping criterion for the reduction is $\epsilon_{rd} = 10^{-12}$.

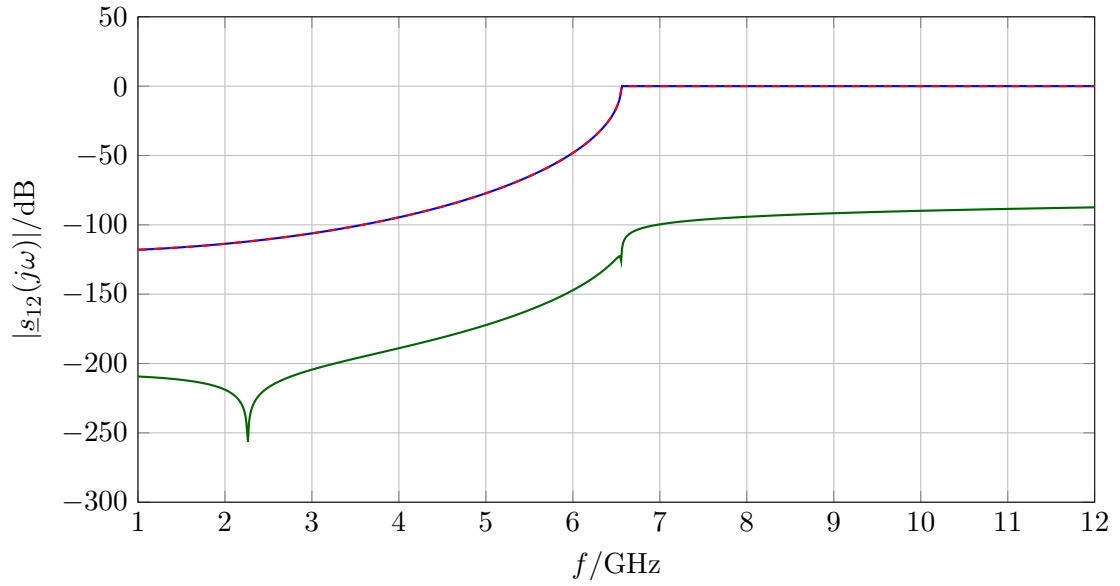
	$r = 1$	$r = 2$	$r = 3$	$r = 4$
N_s	100,000	100,000	100,000	100,000
N_{sr}	19	24	18	17
T_{rd}	1.3 sec	1.5 sec	1.3 sec	1.3 sec

the longitudinal dependence of the field distribution. For the current example, it is sufficient to exclusively regard the TE_{10n} 3D eigenmodes, because other 3D eigenmodes will not interact with the TE_{10} port modes used for the excitation. The field pattern $\mathbf{L}_t^{TE_{10}}(\mathbf{r}_t)$ of the 2D port modes arises from (A.1) for $m_x = 1$ and $m_y = 0$. The state-space systems for the lossless waveguide segments are determined in accordance with Appendix B.4. Every individual segment is described by second-order state-space equations accounting for 10^5 3D eigenmodes (or degrees of freedom) per segment. The model order reduction approach, presented in Section 4.2, delivers the compact models for each of the four segments. Table 5.1 collects details of the state-space systems for the individual segments of the waveguide. For the sake of brevity, properties of the reduced second-order state-space model of the first ($r = 1$) waveguide segment are discussed in detail exclusively. Figure 5.2(a) depicts the reference impedance spectrum $\underline{z}_{12}(j\omega) = \underline{z}_{21}(j\omega)$, obtained by analytical techniques (see Appendix B.2), as a solid blue line. For direct comparison, the impedance spectrum arising from the reduced-order model (19 degrees of freedom) is shown as a dashed red line. Both curves show an excellent agreement. The absolute difference between both spectra is indicated as a solid green line. The mean absolute error is in the order of -140 dB. Figure 5.2(b) is in close analogy to Figure 5.2(a) but shows the transmission parameter $\underline{s}_{12}(j\omega) = \underline{s}_{21}(j\omega)$ of the first segment. The transmission parameter is determined based on the impedance parameters and relation (3.67). The maximal values of the absolute difference between the blue and the red curve are in the order of -88 dB. The maximal artificial reflection $|\underline{s}_{11}(j\omega)| = |\underline{s}_{22}(j\omega)|$ arising from the reduced-order model approximately amounts to -100 dB (not depicted in a diagram).

Apart from frequency-domain transfer functions, field distributions inside the segments are of interest as well. Note that the following considerations related to field distributions in rectangular waveguides are restricted to the imaginary part of the modal voltage $\underline{V}(z)$ along the waveguide. This is sufficient because the real part of $\underline{V}(z)$ is equal to zero for the examined excitations in accordance with (B.10). In Figure 5.3 the imaginary parts of the longitudinal dependences of the modal volt-



(a)



(b)

Figure 5.2: Impedance spectrum $\underline{z}_{12}(j\omega) = \underline{z}_{21}(j\omega)$ and scattering spectrum $\underline{s}_{12}(j\omega) = \underline{s}_{21}(j\omega)$ of the first waveguide section ($r = 1$). Solid blue depicts the spectra directly obtained by analytical calculations (reference curves) whereas the dashed red curves represent the spectra arising from the reduced-order model with 19 degrees of freedom. The absolute differences between the spectra are plotted as solid green curves.

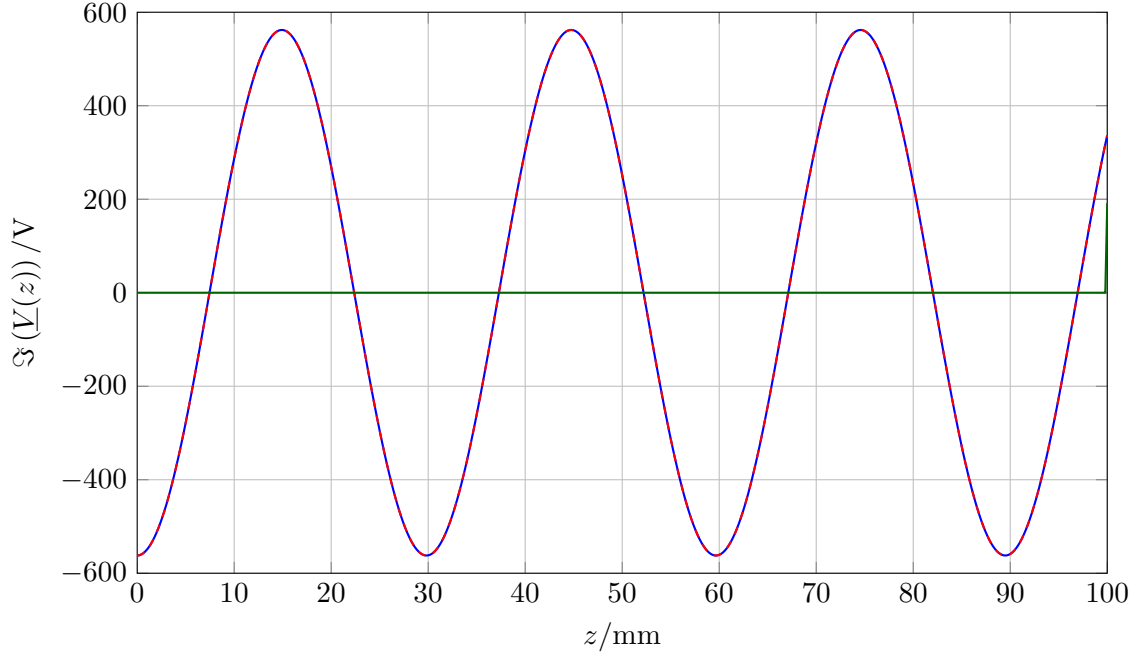


Figure 5.3: Longitudinal dependence of the voltages in the waveguide segment $r = 1$ emerging from the excitation $\underline{I}_1 = 0$ A and $\underline{I}_2 = 1$ A at $f = 12$ GHz. The distribution obtained by direct analytical calculations (solid blue line) shows an excellent agreement with the distribution generated by the reduced-order state-space model (dashed red line). The imaginary part of the difference between both curves is multiplied with the factor 10^4 and plotted as a solid green line. The maximal error is located at $z = 100$ mm and amounts to 20 mV.

ages $\underline{V}(z)$ in the waveguide segment $r = 1$ for the excitation $\underline{I}_1 = 0$ A and $\underline{I}_2 = 1$ A at $f = 12$ GHz are plotted. The blue curve shows the distribution obtained by direct analytical calculations (refer to Appendix B.1) whereas the dashed red line is generated by the reduced-order state-space model. The imaginary part of the difference between both curves is multiplied with the factor 10^4 and plotted as a green solid line. The multiplication with 10^4 ensures that at least the largest deviation at $z = 100$ mm (location of the excitation current density) becomes visible. The maximal imaginary part of the difference amounts to approximately 20 mV at $z = 100$ mm and to $10 \mu\text{V}$ in the rest of the domain.

5.1.2 Concatenation of Waveguide Segments

The concatenation of the four segments is accomplished by means of the SSC approach. As mentioned, the permutation matrix relates the canonical order to the

sorted order. For the four waveguide segments, this results in

$$\underbrace{\begin{pmatrix} i_{1,1}(t) \\ i_{1,2}(t) \\ i_{2,1}(t) \\ i_{2,2}(t) \\ i_{3,1}(t) \\ i_{3,2}(t) \\ i_{4,1}(t) \\ i_{4,2}(t) \end{pmatrix}}_{\mathbf{i}_{\text{can}}(t)} = \underbrace{\begin{pmatrix} 0 & 0 & 0 & 0 & 0 & 0 & 1 & 0 \\ 1 & 0 & 0 & 0 & 0 & 0 & 0 & 0 \\ 0 & 1 & 0 & 0 & 0 & 0 & 0 & 0 \\ 0 & 0 & 1 & 0 & 0 & 0 & 0 & 0 \\ 0 & 0 & 0 & 1 & 0 & 0 & 0 & 0 \\ 0 & 0 & 0 & 0 & 1 & 0 & 0 & 0 \\ 0 & 0 & 0 & 0 & 0 & 1 & 0 & 0 \\ 0 & 0 & 0 & 0 & 0 & 0 & 0 & 1 \end{pmatrix}}_{\mathbf{P}} \underbrace{\begin{pmatrix} i_{1,2}(t) \\ i_{2,1}(t) \\ i_{2,2}(t) \\ i_{3,1}(t) \\ i_{3,2}(t) \\ i_{4,1}(t) \\ i_{1,1}(t) \\ i_{4,2}(t) \end{pmatrix}}_{\mathbf{i}_{\text{sort}}(t)}. \quad (5.1)$$

Recall that the currents $i_{r,p}(t)$ correspond to the TE_{01} mode at the p th port of the r th segment. It should be stressed that the first six entries of the vector $\mathbf{i}_{\text{sort}}(t)$ refer to internal port quantities and the last two entries to external port quantities. In addition to the permutation matrix, the matrix \mathbf{F} expressing the linearly dependent currents in terms of linearly independent currents is needed as well:

$$\underbrace{\begin{pmatrix} i_{1,2}(t) \\ i_{2,1}(t) \\ i_{2,2}(t) \\ i_{3,1}(t) \\ i_{3,2}(t) \\ i_{4,1}(t) \end{pmatrix}}_{\mathbf{i}_{\text{int}}(t)} = \underbrace{\begin{pmatrix} 1 & 0 & 0 \\ -1 & 0 & 0 \\ 0 & 1 & 0 \\ 0 & -1 & 0 \\ 0 & 0 & 1 \\ 0 & 0 & -1 \end{pmatrix}}_{\mathbf{F}} \underbrace{\begin{pmatrix} i_{1,2}(t) \\ i_{2,2}(t) \\ i_{3,2}(t) \end{pmatrix}}_{\hat{\mathbf{i}}_{\text{int}}}. \quad (5.2)$$

The statement enforces $i_{1,2}(t) = -i_{2,1}(t)$, $i_{2,2}(t) = -i_{3,1}(t)$, and $i_{3,2}(t) = -i_{4,1}(t)$. The relations follow from Kirchhoff's current law and Figure 5.1. The employment of the matrices \mathbf{P} and \mathbf{F} in the framework of the concatenation algorithm leads to the second state-space model (4.42) - (4.43) of the coupled structure with 75 degrees of freedom (sum of degrees of freedom of the reduced individual segments minus number of internal terminals divided by two). This state-space model is reduced to the state-space model (4.44) - (4.45) with 41 degrees of freedom using the model order reduction approach described in Section 4.2. The error of the reduction is specified by $\epsilon_{\text{rd}} = 10^{-12}$. The concatenation of state-space models without the application of MOR would lead to a state-space model with 399,997 states (sum of degrees of freedom of the unreduced individual segments minus number of internal terminals divided by two). Thus, SSC allows for an overall reduction of states by a factor of approximately 10^{-4} .

5.1.3 Validation

This subsection compares RF properties delivered by the SSC scheme with directly calculated RF properties of a waveguide with length $L_{\text{tot}} = L_1 + L_2 + L_3 + L_4$.

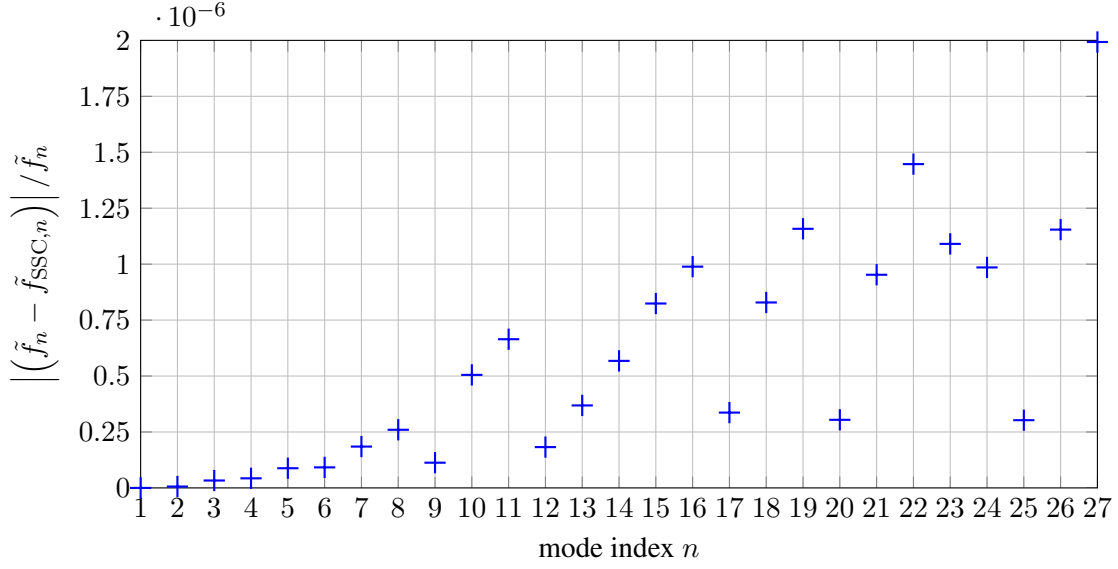
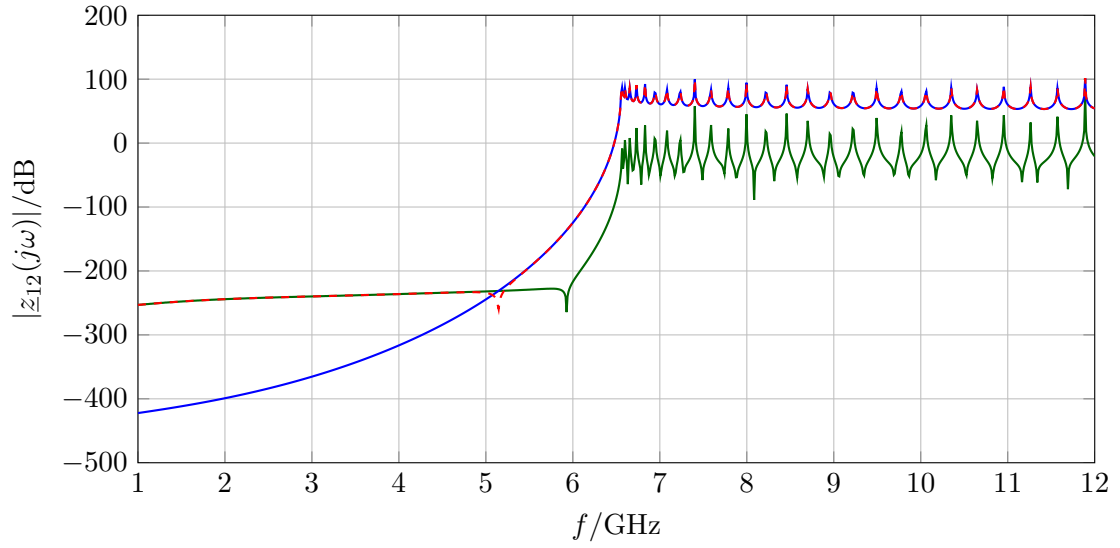


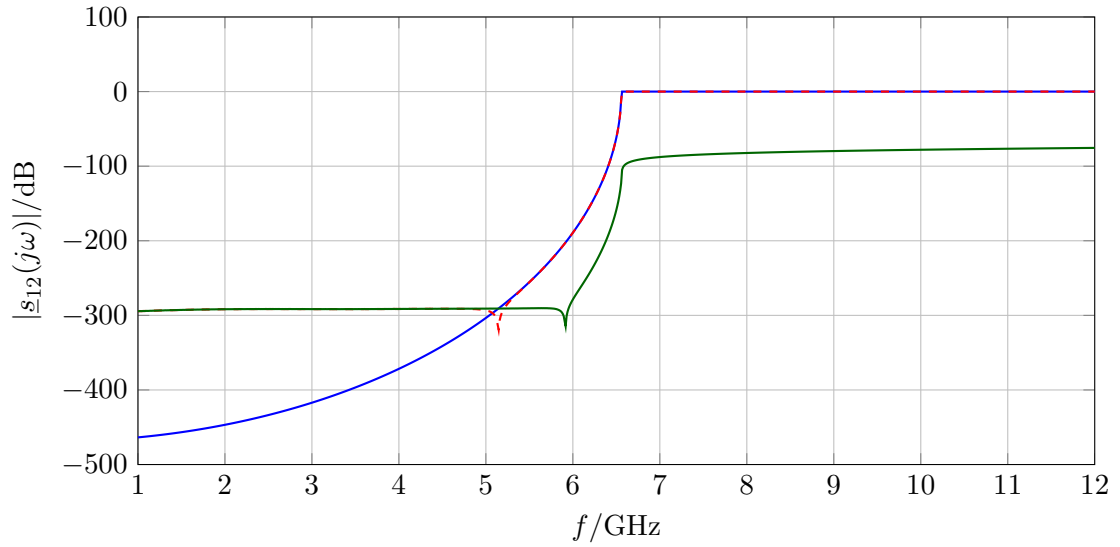
Figure 5.4: Absolute value of the relative errors of the resonant frequencies in the waveguide with length L_{tot} . The frequencies refer to an eigenvalue problem with PMC boundary conditions on the waveguide ports. Only eigenmodes with resonant frequencies in the interval 1 GHz to 12 GHz are shown. The resonant frequencies calculated by means of the analytical formula are denoted by \tilde{f}_n , whereas the resonant frequencies computed with the SSC scheme are given by $\tilde{f}_{\text{SSC},n}$.

Figure 5.4 presents the absolute value of the relative errors in the resonant frequencies of the waveguide whose ports are closed with perfect magnetic conducting walls. Solely eigenmodes with resonant frequencies in the interval 1 GHz to 12 GHz are considered. The resonant frequencies calculated by the analytical formula (B.23) are denoted by \tilde{f}_n , whereas the resonant frequencies computed with the SSC scheme according to Subsection 4.6.4 are given by $\tilde{f}_{\text{SSC},n}$. According to Figure 5.4, the relative error in the resonant frequencies computed with the SSC scheme amounts to 10^{-6} .

Figure 5.5 presents the comparison of network parameters. Again, the solid blue curves are obtained from direct analytical formulas and the dashed red curves are generated by the reduced-order state-space model of the full structure. The absolute difference between both curves is depicted in green. Figure 5.5(a) shows the impedance parameter $|\underline{z}_{12}(j\omega)| = |\underline{z}_{21}(j\omega)|$. The spectrum obtained from the concatenation does not agree with the reference curve for frequencies smaller than 5.5 GHz. However, $|\underline{z}_{12}(j\omega)|$ is small in this regime anyhow. Figure 5.5(b) presents the scattering spectrum $|\underline{s}_{12}(j\omega)| = |\underline{s}_{21}(j\omega)|$ which is computed based on the impedance spectra. The transmission curves show a very good agreement above 5.5 GHz. Below 5.5 GHz the transmission obtained from the state-space model is almost constant at approximately -278 dB. The reflection coefficient $|\underline{s}_{11}(j\omega)| =$



(a)



(b)

Figure 5.5: Impedance and scattering spectrum of the waveguide with length L_{tot} . The solid blue curves directly arise from analytical calculations whereas the dashed red curves are generated by the state-space model (41 states) based on the concatenation approach. The absolute differences between the spectra are plotted as solid green curves. Diagram (a) shows the frequency dependence of the absolute values of the impedance parameter $\underline{z}_{12}(j\omega) = \underline{z}_{21}(j\omega)$, whereas (b) plots the frequency dependence of $\underline{s}_{12}(j\omega) = \underline{s}_{21}(j\omega)$.

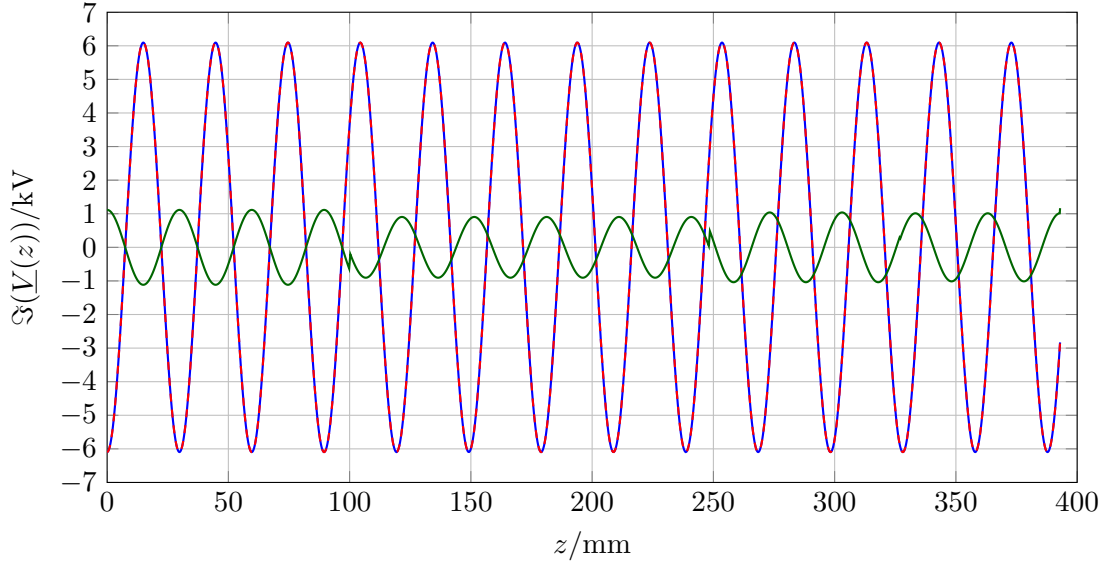


Figure 5.6: Voltage distribution of the waveguide with length L_{tot} due to the excitation $\underline{I}_1 = 0$ A and $\underline{I}_2 = 1$ A at $f = 12$ GHz. The blue curve is directly generated by analytical formulas, whereas the dashed red curve arises from the reduced-order state-space model of the full structure. The imaginary part of the difference between both curves is multiplied with the factor 10^3 and plotted as a solid green line.

$|\underline{s}_{22}(j\omega)|$ (not shown in the diagram) determined by the reduced-order state-space model from the concatenation is equal to approximately -100 dB.

Figure 5.6 depicts the imaginary part of the longitudinal dependence of the voltage $\underline{V}(z)$ in the complete waveguide due to the excitation $\underline{I}_1 = 0$ A and $\underline{I}_2 = 1$ A at $f = 12$ GHz. Blue is the reference curve obtained by direct analytical formulas, whereas the dashed red curve arises from the concatenation approach. Both curves agree very well. The imaginary part of the differences between both curves is multiplied with a factor of 10^3 so that the distribution become visible as a solid green line. The differences show discontinuities located at the decomposition planes. The relative error (C.8) in the SSC field distribution is equal to $1.6 \cdot 10^{-4}$.

5.2 Excitation of the Waveguide by Means of Coupling Probes

The previously considered rectangular waveguide with constant cross section is now extended with two coupling probes at both ends so that the obtained structure can be excited by coaxial waveguide ports (see Figure 5.7(a)). Both ports account exclusively for the TEM port mode (see Appendix A.3). Despite the fact that theoretical

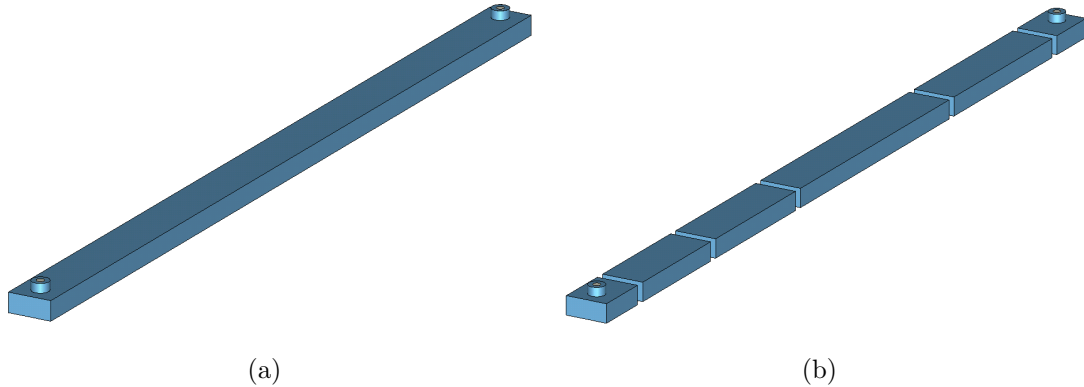


Figure 5.7: (a) Rectangular waveguide equipped with two coupling probes at both ends and (b) its segmentation based on the decomposition introduced in Section 5.1. The state-space model for the segments containing the probe couplers is generated with FIT using CST MWS. At the decomposition planes solely the TE_{10} port mode is considered for the concatenation, whereas at the two external waveguide ports only the TEM port mode is regarded.

considerations related to coupling probes exist in [54, pp. 276 - 281], closed formulas for the electromagnetic fields in the depicted structure, in particular in the vicinity of the coupling probes, are not available. Thus, the subsequent considerations involve discrete formulations. This example shows that the SSC scheme delivers reasonable results if segments are described by numerical and analytical techniques. Moreover, evidence is provided that time-domain computations are feasible with compact models obtained from SSC.

5.2.1 Generation of Compact State-Space Model by Means of SSC

To generate a compact state-space model of the complete structure by means of SSC, the decomposition depicted in Figure 5.7(b) is used. To model the four waveguides with constant cross section, the state-space systems which have been created for the calculations in Section 5.1, are reutilized. The state-space model for the segments with coupling probes is generated by means of FIT due to the absence of closed analytical formulas. A hexahedral discretization, which accounts for the symmetry of the segment, is created with CST MWS using 15 lines per wavelength and yields a second-order state-space system (3.43) - (3.44) with 100,548 states (refer to Figure D.1 for a mesh refinement study and a picture of the discretized coupling probe). The full FIT system of the coupling probe is reduced to a system with 13 states (computation time 1 min 8 sec). Subsequently, the models of all segments are combined using the TE_{10} port modes at the decomposition planes. The arising

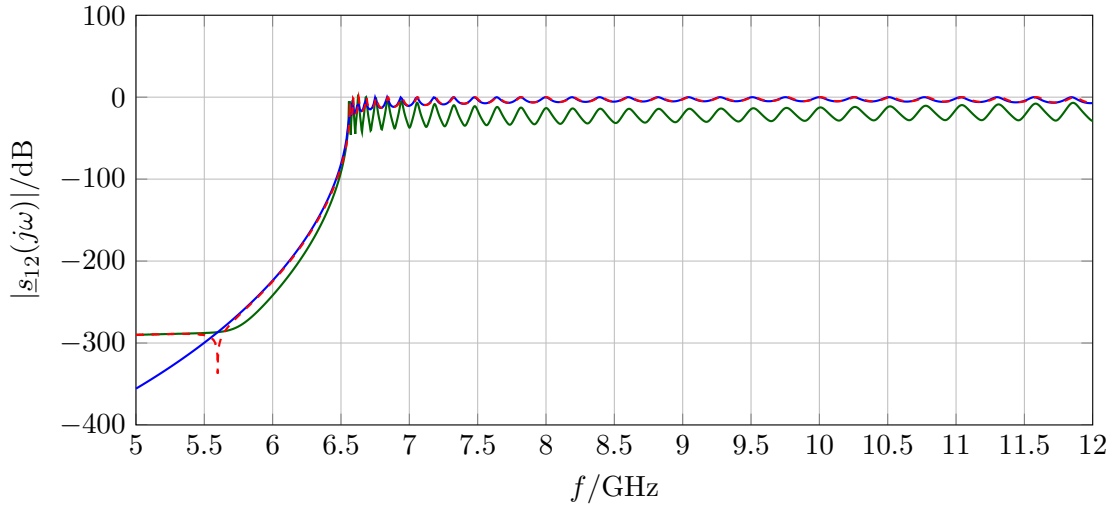
state-space model for the full structure has 99 states and is reduced to a compact state-space model with 46 states (computation time 0.03 sec). The computation time to compute the compact model of the full structure by means of the SSC approach is smaller than 1 min 10 sec. The stopping criteria for the described model order reductions are set to $\epsilon_{\text{rd}} = 10^{-11}$. Linking the state-space models without the application of MOR would result in a state-space model with 500,543 states, i.e. SSC enables an overall reduction of the number of states by a factor of approximately $8.2 \cdot 10^{-5}$.

5.2.2 Validation

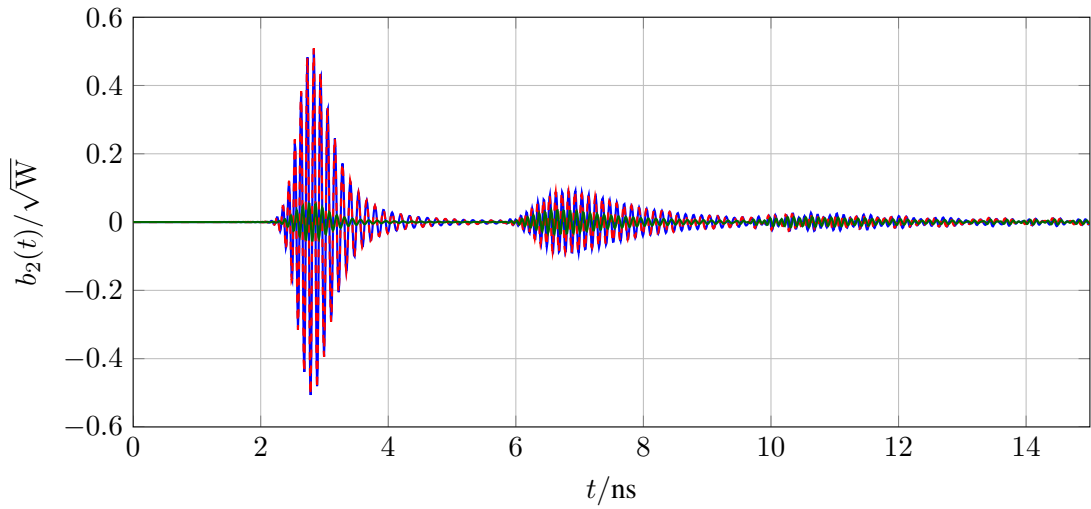
For validation purposes, the RF structure shown in Figure 5.7(a) is completely discretized with a hexahedral mesh using CST MWS. The discretization with 15 lines per wavelength accounts for one available symmetry plane² and results in a second-order state-space system (3.43) - (3.44) with 514,836 states. Based on this system, the scattering parameters of the structure are determined in the frequency range 1 GHz to 12 GHz on 10,001 equidistant frequency samples by means of the Fast Resonant solver of CST MWS (computation time 1 min 15 sec). Complementarily, the impedance and scattering parameters of the complete structure are determined based on the compact state-space model from SSC in accordance with Subsection 4.6.3 (computation time 2.7 sec). The direct computation of the network matrices and the computation using the SSC scheme approximately take the same amount of time. Figure 5.8(a) presents the comparison between the transmissions from one probe to the other via the rectangular waveguide. The blue curve is obtained from the aforementioned direct computation using the Fast Resonant solver. The dashed red curve is generated by means of the compact state-space model, which is delivered by the SSC approach. The absolute difference between both curves is depicted as a solid green line. Both curves show a reasonable agreement. Nonetheless, larger deviations are observable at frequencies below 6 GHz. Here, the transmission resulting from the direct computation exponentially drops to -356 dB, whereas the transmission from the SSC scheme stays at -284 dB. Furthermore, larger deviations of the transmission curves are noticeable in the vicinity of the TE_{10} cutoff frequency at 6.6 GHz. The absolute differences (green curve) are in the interval -15 dB to -32 dB for frequencies larger than 8 GHz.

In addition to the frequency-domain validation, the generated compact model of the full structure is validated by means of a time-domain computation. For this sake, one waveguide port of the structure is excited by a Gaussian pulse with the center frequency $f_0 = 9.5$ GHz and the bandwidth $\Delta f = 5$ GHz. The resulting system response is computed by the state-space system arising from the FIT discretization

²Both symmetry planes of the structure are not usable in a straightforward manner in CST MWS, because waveguides ports have to be completely inside the computational domain.



(a)



(b)

Figure 5.8: (a) Comparison of the transmission between the left probe coupler and the right probe coupler of the structure shown in Figure 5.7. The solid blue line is the reference curve which arises from the direct computation, whereas the dashed red line results from the compact model generated with SSC. The absolute value of the difference between both curves is shown as a solid green line. (b) Comparison between the scattered transient signals at the right probe of the structure due to an excitation with a Gaussian pulse at the left probe. The solid blue curve is the reference curve which is directly obtained from the full model. The dashed red curve is delivered by the compact SSC model. The difference between both curves is depicted as a solid green line.

of the complete structure and the transient solver of CST MWS (computation time 22 sec). To determine the system response with SSC, the second-order state-space equation in the impedance formulation is transferred to a first-order state-space equation in a scattering formulation (refer to Subsection 4.5.2 for a detailed description). Based on this first-order scattering representation, an ordinary differential equation solver, which is integrated in [69], is used to determine the scattered signals due to the probe excitation with the Gaussian pulse (computation time 0.05 sec). The system response computation using the SSC scheme approximately takes three times longer than the direct transient system response computation. Figure 5.8(b) depicts the comparison between the transient system responses resulting from the excitation with the Gaussian pulse. The solid blue line is delivered by the transient solver of CST MWS, whereas the dashed red curve is obtained from the SSC state-space model and an ordinary differential equation solver. The difference between both curves is plotted as a solid green line. The maximal absolute value of the difference amounts to $0.052 \sqrt{W}$.

5.3 Waveguide Power Splitter

This section presents a validation example for the proposed scheme using the waveguide power splitter depicted in Figure 3.3. This example shows that SSC is capable of dealing with topologies different from chains. The waveguide splitter is considered in the interval 1 GHz to 10 GHz. The TE_{10} 2D port modes are regarded at the three external waveguide ports exclusively.

5.3.1 Generation of State-Space Model by Means of SSC

To generate a compact model, the structure is split into segments as it is presented in Figure 4.1: tee piece (segment $r = 1$), waveguide bending (segment $r = 2$ and $r = 3$), and waveguide with constant cross section (segment $r = 4$ and $r = 5$). On the decomposition planes the TE_{10} 2D port modes are solely considered. The tee piece and the waveguide bending are discretized with CST MWS using 15 lines per wavelength and one symmetry plane. The symmetry conditions are selected in such a way that TE_{10} modes are regarded. Figure D.2 and Figure D.3 present mesh refinement studies for both segments as well as pictures of the discretization of the segments. The unreduced state-space model for the waveguide with constant cross section (segment $r = 4$ and $r = 5$) is generated by analytical techniques in accordance with Appendix B.4. Table 5.2 collects details of the state-space models for the individual segments. All state-space equations are combined to (4.42) - (4.43) according to the topology depicted in Figure 4.2. The combined system has 92 states and is reduced in a final step to the system (4.44) - (4.45) with 46 states (computation time 0.1 sec). For all model order reductions, the reduction

Table 5.2: Details on the state-space models of the power splitter segments: N_s is the number of states of the unreduced system, N_{sr} the number of states of the reduced system, and T_{rd} the computation time for reduction. The reduction interval is 1 GHz to 10 GHz and the stopping criterion for the reduction is $\epsilon_{rd} = 10^{-12}$.

	Tee Piece	Bending	Waveguide
N_s	12,672	47,628	100,000
N_{sr}	20	17	21
T_{rd}	2.7 sec	4.8 sec	1.3 sec

error is specified by $\epsilon_{rd} = 10^{-12}$. Concatenating the state-space models without reduction techniques would deliver a state-space model of the full structure with 160,296 states, i.e. SSC allows for an overall reduction of the number of states by a factor of approximately $2.9 \cdot 10^{-4}$.

5.3.2 Validation

The entire structure is discretized with a hexahedral mesh with 15 lines per wavelength by means of CST MWS. The discretization using one available symmetry plane delivers a second-order state-space system of the form (3.43) - (3.44) with 280,908 states. This second-order state-space system is employed to determine the impedance and scattering parameters in the frequency range 1 GHz to 10 GHz on 10,001 equidistant samples by means of the Fast Resonant solver of CST MWS (computation time 21 sec). For the sake of comparison, the frequency-domain transfer function of the state-space model arising from SSC is evaluated on 10,001 equidistant frequency samples and then transferred to scattering parameters in accordance with Subsection 4.6.3 (computation time 3 sec). The amount of time required for the direct computation of the network matrices is in the order of the amount of time needed to compute the transmission by means of the SSC scheme. Figure 5.9 presents the transmission $s_{13}(j\omega)$ of the waveguide power splitter (the indices refer to Figure 3.3). The solid blue curve represents the spectrum directly obtained from the full structure by means of CST MWS. This curve is used as reference, whereas the dashed red curve is generated by the compact SSC state-space model. The absolute difference between the spectra is indicated as a solid green line. The blue and the dashed red curve show a reasonable agreement above 5.5 GHz. Below 5.5 GHz, the reference curve (blue) exponentially drops to -391 dB at 1 GHz whereas the red curve is between -320 dB and -300 dB. Above the cutoff frequency $f_{co} = 7.494$ GHz, the blue and the dashed red curve are almost constant at -3 dB and the absolute difference is equal to approximately -23 dB.

In addition to the computation of network matrices, the eigenmodes of the wave-

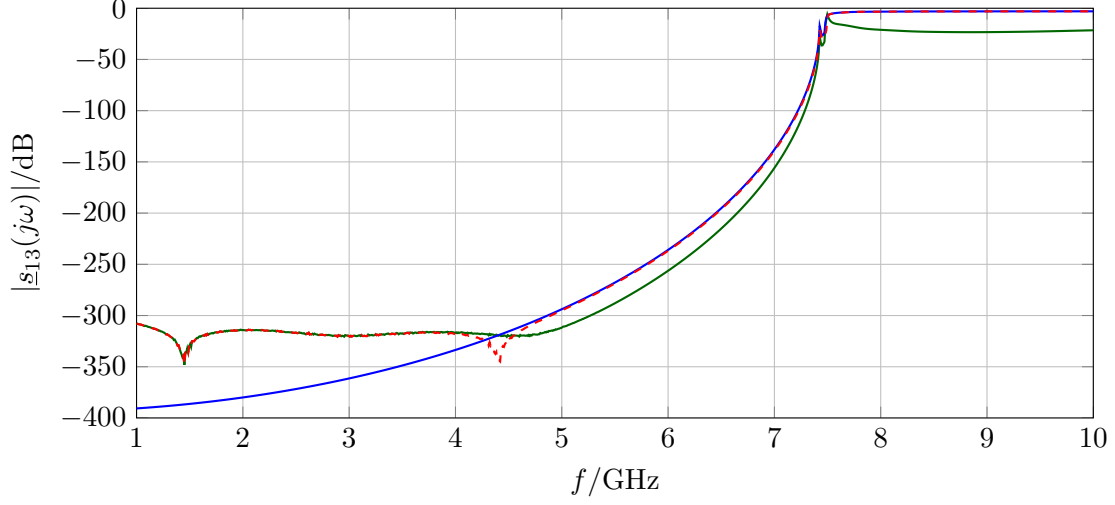


Figure 5.9: Transmission spectrum $s_{13}(j\omega) = s_{31}(j\omega)$ of the waveguide power splitter depicted in Figure 3.3. The solid blue line (reference curve) represents the transmission from waveguide port 1 to port 3 (refer to labeling in Figure 3.3) directly computed with CST MWS. The dashed red curve is delivered by the proposed concatenation approach. The absolute difference between the spectra is plotted as a solid green curve.

guide splitter are determined by the eigenmode solver of CST MWS based on the discretization of the complete structure. Here, one run is performed with PMC boundary conditions specified on the waveguide port planes and another run with PEC boundary conditions on the port planes. Both considerations are restricted to eigenmodes with resonant frequencies in the interval 1 GHz to 10 GHz. The eigenmode computations are performed with the Jacobi-Davidson solver of CST MWS (computation time 11 min 52 sec). Complementarily to the direct approach, the eigenmodes are computed for PEC and PMC conditions at the waveguide port planes based on the compact SSC model (computation time 0.03 sec). The application of the SSC result in shorter computation times when comparing with the direct eigenmode computation of the complete structure, i.e. less than 1 min using SSC versus approximately 12 min using the Jacobi-Davidson solver of CST MWS directly. The relative errors in the resonant frequencies in the waveguide power splitter are depicted in Figure 5.10. The resonant frequencies obtained from CST MWS are denoted by $\tilde{f}_{\text{CST},n}$, whereas the resonant frequencies delivered by the SSC scheme according to Section 2.4 are specified by $\tilde{f}_{\text{SSC},n}$. The blue plusses in Figure 5.10 indicate the relative errors of resonant frequencies of the waveguide splitter eigenmodes with PMC boundary conditions enforced on the waveguide port planes. The red crosses correspond to errors in the resonant frequencies of the waveguide splitter eigenmodes with PEC boundary conditions on the waveguide port planes. The relative errors in the resonant frequencies are in the order of 10^{-3} .

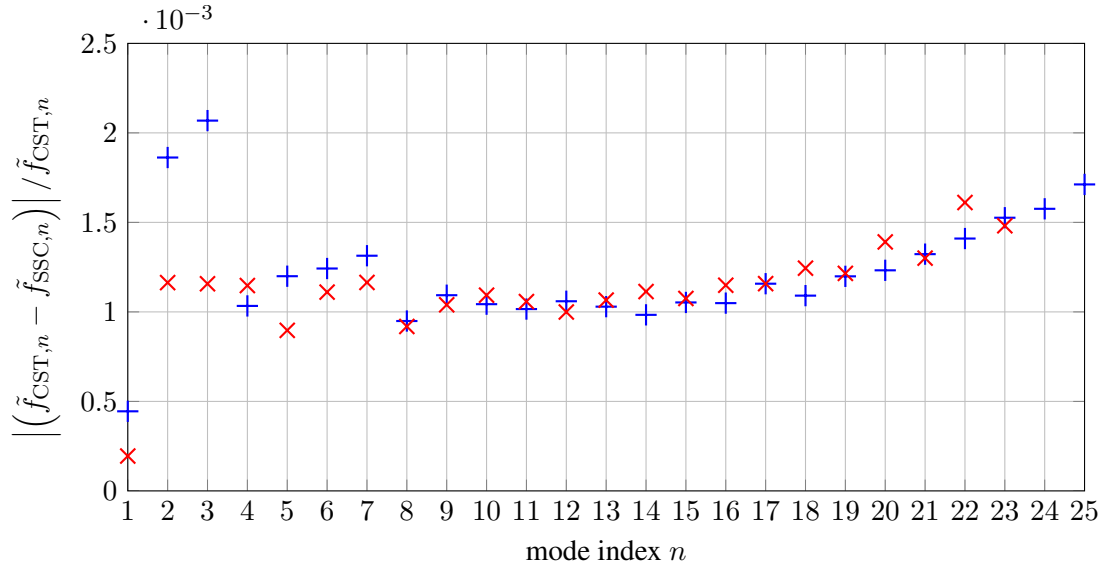


Figure 5.10: Absolute values of the relative errors of the resonant frequencies in the waveguide power splitter. The resonant frequencies delivered by SSC are denoted by $\tilde{f}_{\text{SSC},n}$. The resonant frequencies $\tilde{f}_{\text{CST},n}$ determined by the eigenmode solver of CST MWS, based on the full structure, are employed as reference values. The blue plusses emerge from an eigenvalue problem with PMC boundary conditions on the waveguide port planes, whereas the red crosses arise from an eigenvalue problem with PEC boundary conditions on the port planes.

5.4 Rotationally Symmetric Chains of Third-Harmonic Cavities

This section is focused on the application of SSC on rotationally symmetric chains of third-harmonic cavities of elliptical shape [13, 14, 15, 16]. The example shows that SSC is able to cope with long RF structures. Figure 5.11 depicts three structures which comprise third-harmonic resonators, beam pipes³, and bellows. The chain shown in Figure 5.11(a) is made of two resonators, one bellow, and four waveguides. This structure solely serves as validation example and does not have a practical correspondence. The chain depicted in Figure 5.11(b) comprises four resonators, eight beam pipes, and three bellows. This structure is a simplification of the cavity chain which is accommodated in the FLASH [9] module ACC39. The structure in Figure 5.11(c) is built up from eight resonators, sixteen beam pipes, and seven bellows. This structure models the cavity chain which will be part of the European XFEL [10] beamline. The RF properties are investigated in the interval 1 GHz to 8.5 GHz. It should be noted that due to the rotational symmetry of the three chains, their RF

³The beam pipes are in fact circular waveguides with constant cross section.

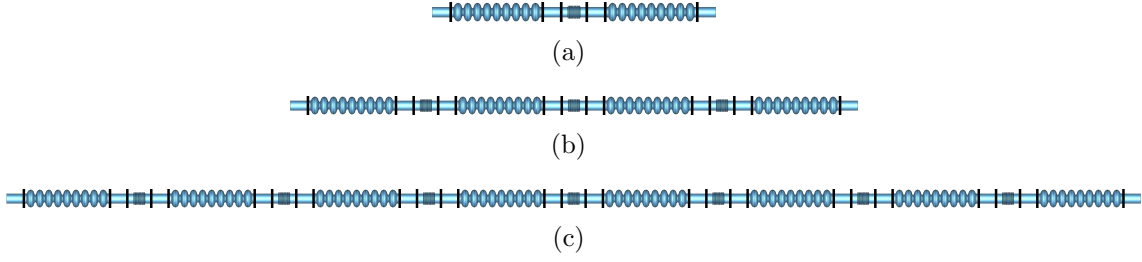


Figure 5.11: Rotationally symmetric chains of third-harmonic TESLA cavities with bellows in between. The chain (a) with two cavities is exclusively employed for validation purposes. The chain (b) with four cavities is a model of the cavity chain in the FLASH module ACC39 [9]. The chain (c) with eight cavities models the chain for the European XFEL [10]. The black lines indicate the decomposition planes which are used to generate the segments from the full structure.

properties could be determined by 2D solvers so that the computational costs are significantly reduced. However, CST MWS does not support 2D formulations of Maxwell's equations for 3D rotational symmetric structures. Instead, symmetry planes are chosen so that TM_{01} and TE_{21} field distributions are regarded. At both ends of the structures, waveguide ports are assigned. Each waveguide port accounts for two 2D port modes, namely TM_{01} and TE_{21} (see Figure A.2 for a drawing of the field distributions). It is worth highlighting that there is no coupling between modes with different azimuthal dependences or polarizations on account of the rotational symmetry of the structure.

5.4.1 Generation of State-Space Models for Chains

The structures depicted in Figure 5.11 are decomposed into third-harmonic resonators, bellows, and beam pipes. The black lines in Figure 5.11 denote the decomposition planes. At these planes, two 2D port modes (TM_{01} and TE_{21}) are considered. In a first step, all three segments are discretized using CST MWS with 15 lines per wavelength. Mesh refinement studies for the bellow, the beam pipe, and the third harmonic cavity as well as images of the discretizations of the segments are available in Figure D.4, Figure D.5, and Figure D.6, respectively. Per segment, two symmetry planes are chosen such that TM_{01} and TE_{21} field distributions and port modes are considered. In addition, the symmetry plane, whose normal vector is parallel to the rotational symmetry axis, is utilized as well to reduce computational costs. The approach requires two individual model order reductions per segment: One for the PEC boundary condition and one for the PMC boundary condition on this third symmetry plane. Based on these two arising reduced-order models, the reduced-order models of the entire segments are assembled. Details on the determination of reduced-order models for the segments are given in Table 5.3. Despite the fact

Table 5.3: Details on the state-space models of the individual segments of the rotationally symmetric chains of third-harmonic cavities: N_s is the number of states of the unreduced system, N_{sr} the number of states of the reduced system, and T_{rd} the computation time for reduction. The reduction interval is 1 GHz to 8.5 GHz and the stopping criterion for the reduction is $\epsilon_{rd} = 10^{-11}$. The reduced-order models for the rotationally symmetric segments are created based on two unreduced models accounting for different symmetry conditions.

	Nine-Cell Cavity	Bellow	Beam Pipe
N_s	(2 ·) 172,380	(2 ·) 61,893	(2 ·) 12,150
N_{sr}	73	35	24
T_{rd}	2 min 49 sec	46 sec	10 sec

Table 5.4: Number of states N_{sr} of the compact state-space models for the complete structures. The reduction interval is 1 GHz to 8.5 GHz and the stopping criterion for the reduction is $\epsilon_{rd} = 10^{-11}$. In total, less than 4 min computation time is required to create the compact models for the cavity chains using SSC.

	Figure 5.11(a)	Figure 5.11(b)	Figure 5.11(c)
N_{sr}	153	287	555

that Maxwell's equations can be analytically solved for circular beam pipes, the state-space model for the pipes is generated by FIT for the sake of convenience.

The generated compact state-space models of the segments are concatenated according to the topologies in Figure 5.11. The arising model for the chain with two cavities has 265 states and is reduced to a model with 153 states (computation time 0.42 sec). The concatenation of the segments to the arrangement with four elliptical cavities results in a second-order state-space model with 561 degrees of freedom which is reduced to a model with 287 states (computation time 1.3 sec). The concatenation to the arrangement with eight elliptical cavities results in a second-order state-space model with 1,153 degrees of freedom which is reduced to a model with 555 states (computation time 4.5 sec). Linking the state-space models without reduction techniques would deliver a state-space model for the two-cavity string with 910,494 states, a state-space model for the four-cavity string with 1,944,770 states, and a state-space model for the eight-cavity string with 4,013,322 states. SSC enables an overall reduction of the number of states by a factor of $1.7 \cdot 10^{-4}$, of $1.5 \cdot 10^{-4}$, and of $1.4 \cdot 10^{-4}$, respectively. The computation time to compute the compact models for the three cavity chains by means of the SSC approach is smaller than 4 min.

5.4.2 Validation Using Chain with Two Nine-Cell Resonators

The generated segments and the number of 2D port modes used for the concatenation are validated using the compact model of the chain with two cavities, because its RF properties can be determined with direct computations as well. To generate reference values for the RF properties, the chain with two cavities is completely discretized by means of a hexahedral mesh using CST MWS with 15 lines per wavelength. The discretization accounts for two symmetry planes, so that TM_{01} and TE_{21} are regarded. This discretization delivers a second-order FIT state-space system with 1,310,064 states which is employed to compute the scattering parameters of the chain with two cavities on 10,001 equidistant frequency samples by means of the Fast Resonant solver of CST MWS (computation time 22 min 22 sec). Subsequently, the impedance parameters of the compact SSC model of the string with two cavities are computed on 10,001 equidistant frequency samples and are transferred to scattering parameters by (3.67) (computation time 3 sec). The application of SSC results in shorter computation times when comparing with the direct scattering parameter computation of the complete structure, i.e. approximately 4 min using SSC versus approximately 22 min using the Fast Resonant solver of CST MWS directly.

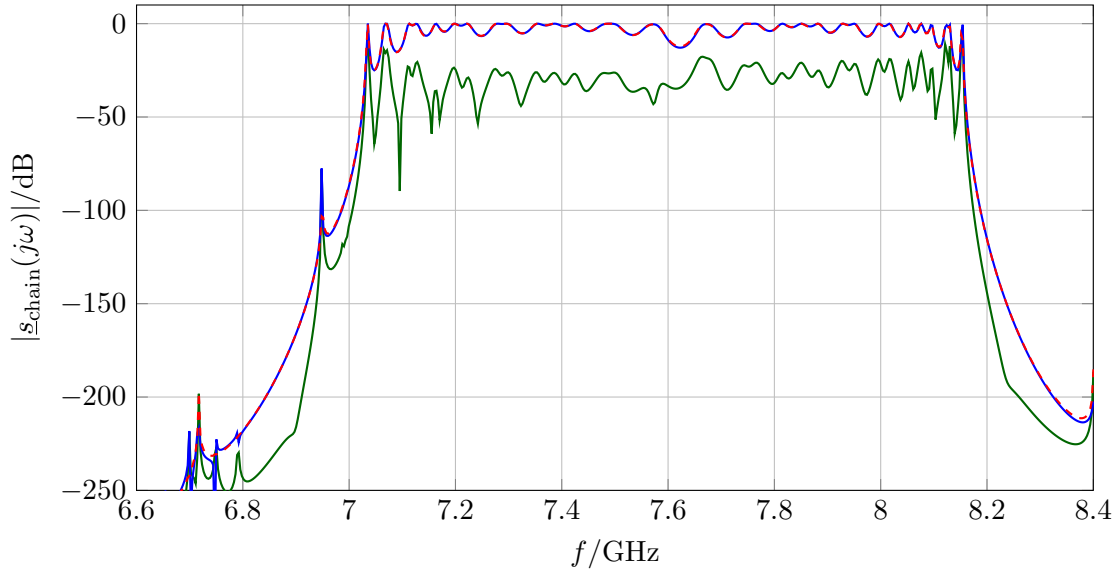


Figure 5.12: Absolute value of the transmission from the left end of the structure depicted in Figure 5.11(a) to the right end. The spectra refer to the TM_{01} port modes allocated at both ends and show the second monopole band. The solid blue curve (reference) is determined by a straightforward computation with CST MWS. The dashed red curve arises from the proposed concatenation approach. The absolute value of the difference between both curves is shown as a solid green line.

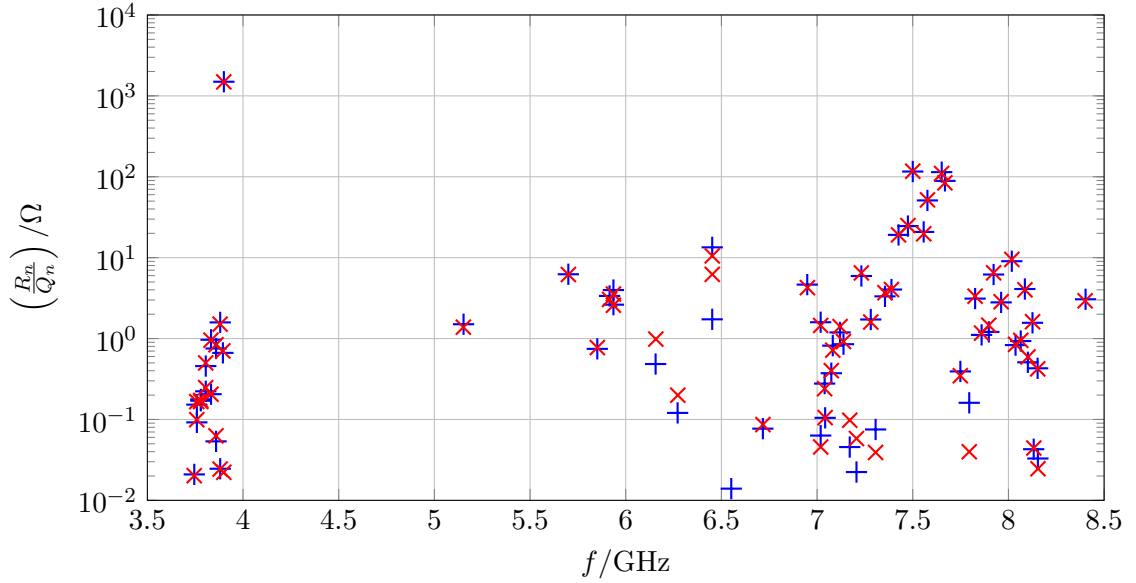


Figure 5.13: Normalized longitudinal voltages on the symmetry axis in the arrangement of two third-harmonic cavities as depicted in Figure 5.11(a). The blue plusses (references) are determined by straightforward eigenmode computations with CST MWS and its post-processing toolbox. The red crosses are generated by the eigenmode computation using the proposed concatenation approach. The relative error in the resonant frequencies of the eigenmodes is in the order of 10^{-4} .

Figure 5.12 presents the transmission curve from the TM_{01} port mode on the left end of the chain to the TM_{01} port mode on the right end of the chain. The axes are chosen such that the second TM_{01} band of the structure is visible in a detailed manner. The first TM_{01} band is barely visible in the transmission spectra because its resonant frequencies are below the cutoff frequencies of the circular waveguide-like beam pipes (see Figure 1.4). The reference transmission in Figure 5.12 is shown as a solid blue line, whereas the transmission arising from the concatenation approach is depicted again as a dashed red line. Both plots show a good agreement and the absolute value of the difference between both is shown as a solid green line.

In addition to the computation of network matrices, the eigenmodes of the chain with two cavities are determined. For these considerations, PMC conditions are specified on the symmetry planes which are tangential to the symmetry axis. To save numerical costs, the third symmetry plane⁴ is used as well and two eigenmode computations are performed to determine all eigenmodes whose resonant frequencies are in the interval of interest. Both eigenmode computations are performed by the Jacobi-Davidson solver of CST MWS (computation time 11 h 16 min). The application of SSC leads to significantly shorter computation times when comparing

⁴plane whose normal component is parallel to the symmetry axis

with the direct eigenmode computation of the complete structure, i.e. approximately 4 min using SSC versus approximately 11 h using the Jacobi-Davidson solver of CST MWS directly. Based on the direct eigenmode computation, the normalized longitudinal voltages (see Subsection 2.4.2) of the modes are determined by CST MWS in a post-processing step. Complementarily, the normalized longitudinal voltages are determined from the concatenation approach based on the field distributions and the resonant frequencies of the eigenmodes (refer to Subsection 4.6.4). Figure 5.13 presents the comparison between both results. Each plus (or cross) corresponds to an eigenmode in the cavity chain with PMC boundary conditions at the ends of the beam pipes. The horizontal position of the plusses (or crosses) is determined by the resonant frequency of the eigenmode. The relative error in the resonant frequencies of the eigenmodes is in the order of 10^{-4} (not depicted in the diagram). The vertical position of the plusses (or crosses) is fixed by the normalized longitudinal voltages of the eigenmode. The diagram conveys a good agreement between normalized longitudinal voltages directly delivered by CST MWS and SSC. Predominantly, the first monopole band in the interval 3.72 GHz to 3.9 GHz and the second monopole band in the interval 6.95 GHz to 8.4 GHz have considerable normalized longitudinal voltages (refer to resonant frequencies of monopole eigenmodes in a single cavity presented in Figure 1.4). While the monopole eigenmodes of the first band are trapped in the individual resonator, the eigenmodes of the second monopole band may be distributed along the entire cavity chain. In addition to monopole modes belonging to the first and the second band, monopole modes in between these bands arise. They cannot be observed in single cavity eigenmode computations and their field energy is mainly allocated in between the cavities at the bellows. Therefore, they are further referred to as bellow modes. Eigenmodes corresponding to quadrupole bands (TE₂₁-like) are not visible in the diagram due to their vanishing normalized longitudinal voltages.

5.4.3 Longitudinal Voltages Depending on Number of Cavities

After validating the reduced-order models of the individual segments and the number of 2D port modes used for the concatenation, the dependence of the longitudinal voltages of the eigenmode on the number of cavities is examined. For this purpose, the resonant frequencies and field distributions of the eigenmodes in the respective structures are determined in accordance with Subsection 4.6.4. In the chain with two cavities 125 eigenmodes exist in the frequency interval of interest, in the chain with four cavities 259 eigenmodes, and in the chain with eight cavities 527 eigenmodes. Figure 5.14 presents the longitudinal voltages of eigenmodes in the three different structures in direct comparison. The red crosses refer to the structure shown in Figure 5.11(a), the black plusses to the geometry depicted in Figure 5.11(b), and the

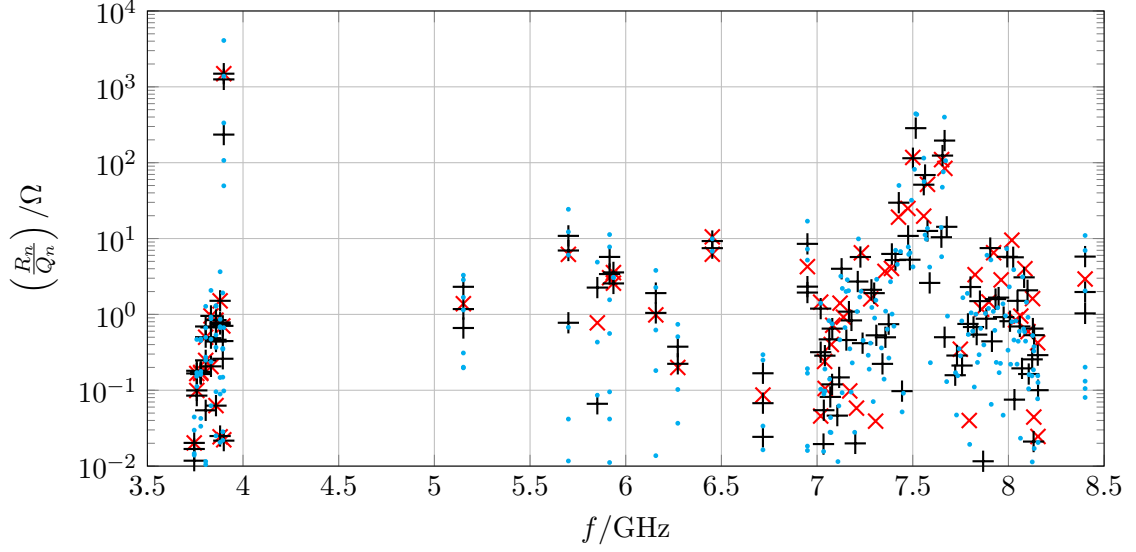


Figure 5.14: Normalized longitudinal voltages on the symmetry axis in the arrangement of two (red crosses), four (black pluses), and eight (cyan dots) third-harmonic cavities (refer to the geometries depicted in Figure 5.11). All presented normalized longitudinal voltages of the eigenmodes in the respective arrangements are computed by the SSC approach.

cyan dots to the chain presented in Figure 5.11(b). In close analogy to Figure 5.13, eigenmodes belonging to the first monopole band (3.72 GHz to 3.9 GHz) and to the second monopole band (6.95 GHz to 8.4 GHz) have non-negligible longitudinal voltages. In addition to these bands, eigenmodes with resonant frequencies in between 3.9 GHz and 6.95 GHz arise, which are attributed to bellow modes. The diagram in Figure 5.14 shows that the longer the chain becomes, the more the bands are populated with eigenmodes. Moreover, the eigenmodes of longer structures tend to have higher longitudinal voltages.

5.5 Third-Harmonic TESLA Cavities with HOM and Power Couplers

This section discusses a more sophisticated model of the previously considered cavity chains (refer to Section 5.4). The beam pipes, which are in fact circular waveguides with constant cross section, are extended by HOM couplers and power couplers as shown in Figure 5.15. The geometry of the HOM couplers (one-leg-design as depicted in [1, Figure 3(a)]) is taken from technical drawings and is modeled with CST MWS. The inclusion of HOM couplers in the resonator chains breaks the rotational symmetry of the structures. Thus, it is impossible to strictly distinguish

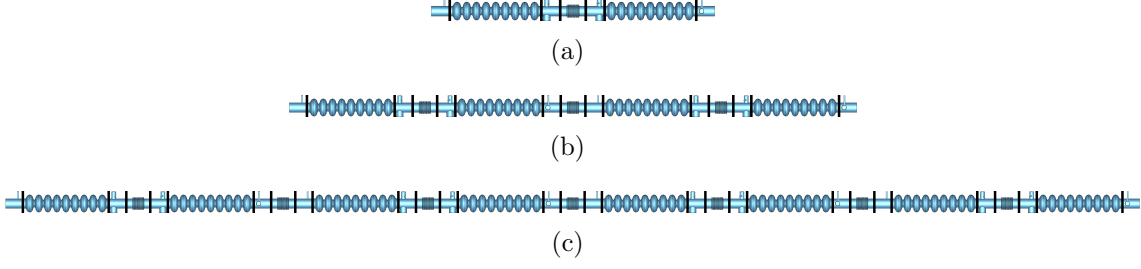


Figure 5.15: Chains of third-harmonic TESLA cavities with HOM and power couplers which break the rotational symmetry. Bellows are placed in between the cavity coupler combinations. The chain (a) does not have practical relevance. The chain (b) with four cavities is a model of the third-harmonic module in FLASH [9]. The chain (c) with eight cavities reflects the third-harmonic module of the European X-FEL [10]. The black lines indicate the decomposition planes.

between field patterns such as monopole, dipole or quadrupole modes. Moreover, the absence of symmetry results in drastically increased computational demands because a reduction of the complexity of the problem by means of symmetry planes is not possible for the complete discretization. An additional challenge of modeling the HOM couplers is the reasonable discretization of the tiny HOM coupler parts which are responsible for the notch effect. In close analogy to Section 5.4, the structures depicted in Figure 5.15(b) and in Figure 5.15(c) are models for the third-harmonic cavity chain in FLASH and in the European XFEL, respectively. Note that the models considered here do not take into account the fact that there are two different HOM coupler designs attached to the third-harmonic cavities in FLASH as shown in [1, Figure 3]. Furthermore, the HOM couplers at both ends of the cavities are rotated around the beam axis by 90° rather than by 115° and the power couplers are on the opposite sides of the HOM couplers (see Figure D.8(b) for a close-up). Note that rotations of individual segments of the chain around the beam axis can basically be taken into account in the SSC approach by means of rotational objects as discussed in [1, Appendix A] and in [39] for concatenations with CSC. In addition to the aforementioned deviations from the original design (cf. [78, Figure 4]), the position of the power couplers in the eight cavity string is chosen such that the power couplers are next to each other.

Hereinafter, the RF properties of the three chains depicted in Figure 5.15 and of the validation structure in Figure 5.16 are considered in the frequency interval 1 GHz to 6 GHz. Waveguide ports are allocated at both ends of the structures. They account for three 2D port modes each: Two TE_{11} dipole modes and the TM_{01} monopole mode (refer to Figure A.2 for a sketch of the field patterns). According to Table A.2, these three port modes correspond to all waveguide modes which are able to propagate in the frequency interval of interest. In addition to these hollow waveguide port modes, the TEM mode (see Figure A.3(a) for a sketch of the field

pattern) is considered at the ends of the HOM and power couplers. Note that further 2D port modes are not considered at the coaxial waveguide ports which correspond to the couplers.

5.5.1 Generation of Compact State-Space Models

To create compact state-space models of the structures shown in Figure 5.15, the three chains are decomposed into HOM couplers (HOMC), HOM couplers with power couplers (HOMPC), cavities, and bellows. The black lines in Figure 5.15 indicate decomposition planes. Three port modes, namely the two TE_{11} modes and the TM_{01} mode, are considered at the arising decomposition planes. In addition to these segments, a state-space model for a single-cell cavity is generated for the validation structure in Figure 5.16. All segments are discretized using a hexahedral mesh with 15 lines per wavelength. Table 5.5 collects details of the state-space models of the individual segments. While the treatment of the nonsymmetric segments is straightforward, the treatment of the rotational symmetric segments (nine-cell and one-cell cavities and bellows) is more elaborate, because all three symmetry planes are used. In total, four state-space models for each symmetric segment are required. The symmetry conditions are chosen such that TE_{11} modes in two polarizations and the TM_{01} are considered.

In a next step, the compact state-space models of the individual segments are concatenated to the structures depicted in Figure 5.15 and in Figure 5.16. Firstly, the couplers are connected to both ends of the nine-cell cavity. This yields a concatenated system with 213 states which is reduced to a system with 132 states (computation time 0.6 sec). The system is combined with the state-space model for the bellows in accordance with the topology of the structure depicted in Figure 5.15(a). This delivers a state-space system with 312 states which is reduced to a system with 236 states (computation time 1 sec). The obtained state-space system is used to investigate properties of the two-cavity chain with couplers as depicted in Figure 5.15(a). Moreover, the obtained state-space model is used in combination with the state-space model for the bellow to generate a state-space model for the four-cavity chain with couplers shown in Figure 5.15(b). The arising system has 520 states and is reduced to a model with 442 states (computation time 3 sec) which is used to determine the properties of the four-cavity chain with couplers. Apart from that, the arising system is exploited in combination with the state-space model for the bellow to generate a model for the eight-cavity chain with couplers as shown in Figure 5.15(c). This model has 932 states and is reduced to a model with 854 states (computation time 11 sec). In addition to state-space models of the chains, a state-space model for the validation structure shown in Figure 5.16 is generated. The concatenation of the state-space models for the couplers and the single cell delivers a system with 145 states which is reduced to a system with 98 states (computation time 0.2 sec). Table 5.6 collects the number of states of the final com-

Table 5.5: Details on the state-space models of the individual segments: N_s is the number of states of the unreduced system, N_{sr} the number of states of the reduced system, and T_{rd} the computation time for reduction. The reduction interval is 1 GHz to 6 GHz and the stopping criterion for the reduction is $\epsilon_{rd} = 10^{-11}$. The reduced-order models for the rotationally symmetric segments are created based on four unreduced models accounting for different symmetry conditions.

	HOMC	HOMPC	Nine-Cell Cav.	Bellow	Single-Cell Cav.
N_s	242,880	323,532	(4 ·) 71,478	(4 ·) 44,400	(4 ·) 2,916
N_{sr}	61	53	105	54	37
T_{rd}	9 min 1 sec	11 min 4 sec	1 min 3 sec	31 sec	6 sec

Table 5.6: Number of states N_{sr} of the compact state-space models for the complete structures. The reduction interval is 1 GHz to 6 GHz and the stopping criterion for the reduction is $\epsilon_{rd} = 10^{-11}$. In total, less than 22 min computation time is required to create the compact models for the cavity chains and the validation structure using SSC.

	Figure 5.15(a)	Figure 5.15(b)	Figure 5.15(c)	Figure 5.16
N_{sr}	236	442	854	89

compact models. Straightforwardly connecting the state-space models without MOR would result a state-space model for the two-cavity string with 1,882,230 states, a state-space model for the four-cavity string⁵ with 3,942,057 states, and a state-space model for the eight-cavity string with 8,061,702 states. Therefore, SSC allows for an overall reduction of the number of states by a factor of $1.3 \cdot 10^{-4}$, of $1.1 \cdot 10^{-4}$, and of $1.1 \cdot 10^{-4}$, respectively. The compact state-space models for the three chains and the validation structure are determined in less than 22 min computation time.

5.5.2 Validation

To validate the generated state-space models of the segments and the number of 2D port modes used at the decomposition planes, the structure illustrated in Figure 5.16 is discretized in its entirety by means of a hexahedral mesh with 15 lines per

⁵In Section 1.3, the presented number of states is one order of magnitude larger, because the direct discretization of the four-cavity chain with couplers by a hexahedral mesh leads to a significant amount of mesh overhead.

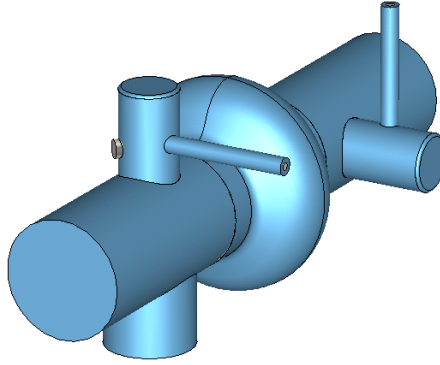


Figure 5.16: Single-cell cavity with HOM couplers and power coupler. The structure serves as validation example for the subsequent consideration. The geometry is chosen such that direct computations of its RF properties are feasible.

wavelength. The discretization results in a FIT state-space model with 1,616,877 degrees of freedom. At both ends of the beam pipes waveguide ports, which regard the three port modes, are defined. In addition, waveguide ports are allocated at the coaxial waveguide ports of the HOM and power couplers. These waveguide ports exclusively account for the TEM port mode. Based on these specifications, the Fast Resonant solver of CST MWS is employed to compute the scattering matrices on 10,001 equidistant frequency samples in the interval 1 GHz to 6 GHz (computation time 20 min). Apart from that, the scattering parameters are determined by means of the generated reduced-order model with 89 states in accordance with Section 4.6.3 (computation time 10 sec). The SSC scheme delivers the scattering parameters in approximately 22 min, whereas the direct scattering parameter computation with the Fast Resonant solver of CST MWS requires 20 min. Related to scattering parameters of this validation example, the concatenation scheme does not save computation time, i.e. the break even point for SSC is not reached. Figure 5.17 presents the comparison of the transmission from one HOM coupler to the other HOM coupler of the structure via the single cell. The solid blue curve represents the transmission obtained from the direct computation using CST MWS, whereas the dashed red line shows the transmission obtained from the SSC approach. Both curves show a reasonable agreement. The absolute value of the difference between both transmissions is indicated as a solid green line.

In addition to the comparison of scattering parameters, 28 resonant frequencies and field distributions of the validation structure shown in Figure 5.17 are determined. The eigenmode computation is performed by the Jacobi-Davidson solver of CST MWS based on the created discretization of the full structure with PMC boundary conditions on the waveguide ports (computation time 16 h 27 min). Complementarily to the direct eigenmode computation, the eigenmodes are computed with PMC boundary conditions on the port planes based on the SSC reduced-order

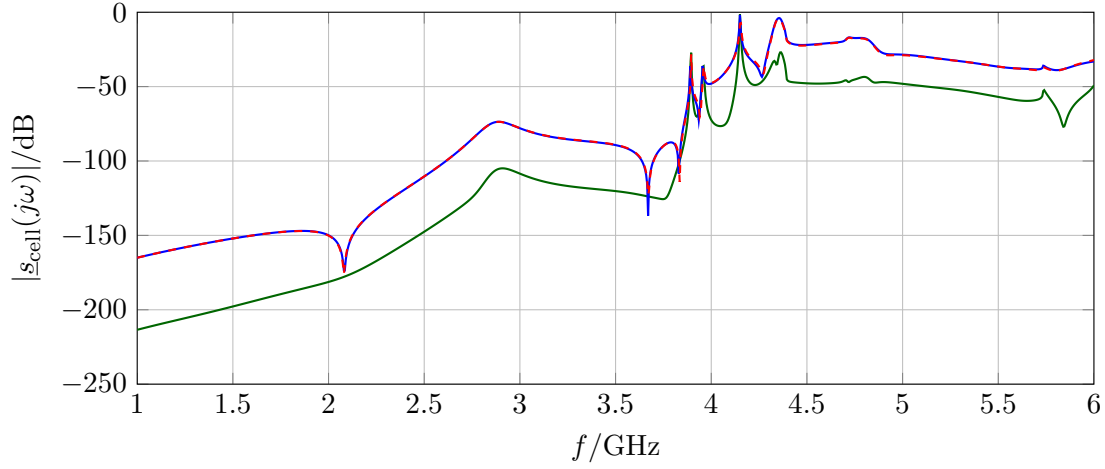


Figure 5.17: Transmission spectra from the left HOM coupler to the right HOM coupler of the validation structure shown in Figure 5.16. The solid blue curve arises from the direct computation of scattering parameters with CST MWS, whereas the dashed red curve is obtained by the SSC approach. The absolute value of the difference between the transmissions is plotted as a solid green line.

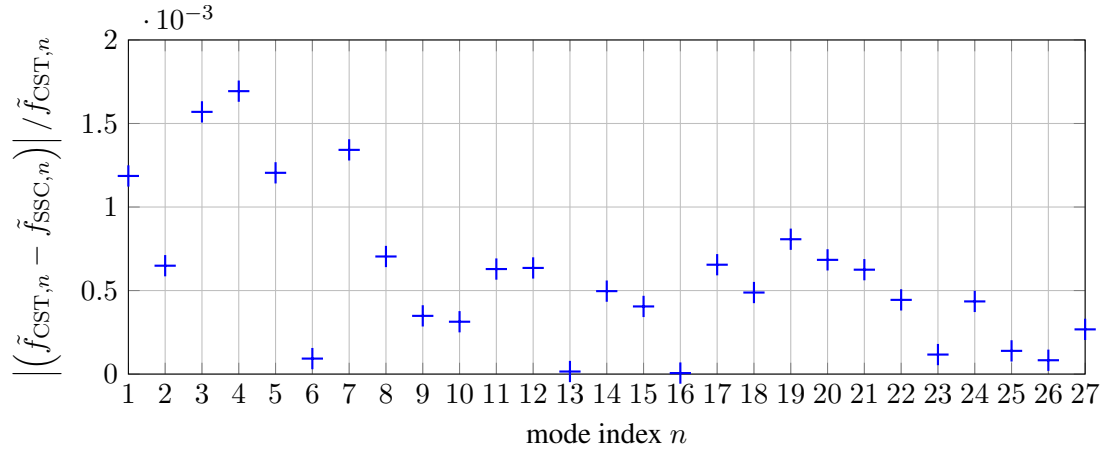


Figure 5.18: Absolute value of the relative errors of the resonant frequencies $\tilde{f}_{\text{SSC},n}$ of the eigenmodes computed with SSC. The reference resonant frequencies $\tilde{f}_{\text{CST},n}$ are determined by the eigenmode solver of CST MWS based on the full structure. The eigenmode computations refer to PMC boundary conditions on the waveguide port planes.

model following Subsection 4.6.4 (eigenmodes with PMC boundary conditions on the waveguide ports are directly available from the reduced-order model as discussed in Subsection 4.6.4). The SSC scheme determines the eigenmodes of the validation structure in approximately 22 min, whereas the direct computation with CST MWS requires 16 h 27 min.

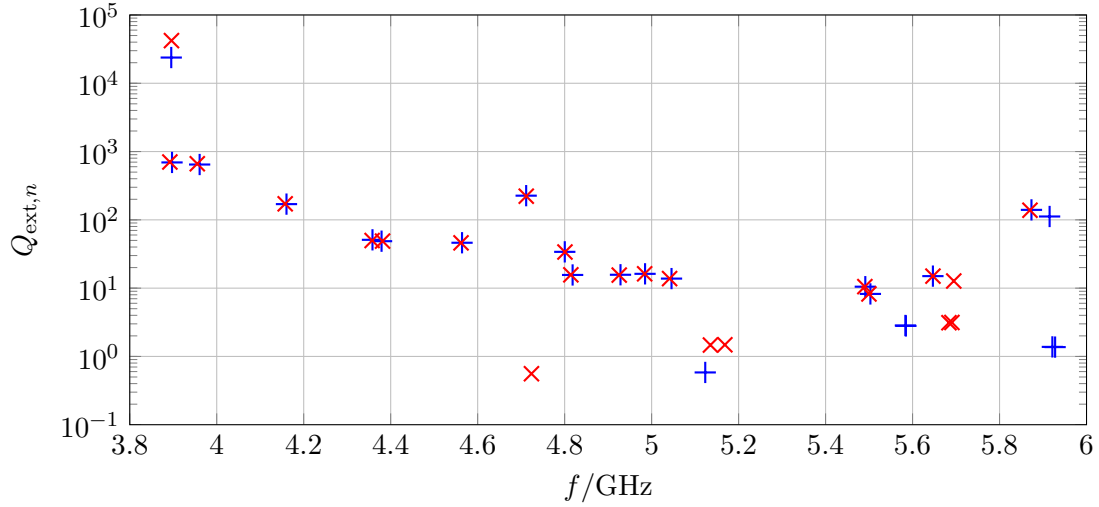


Figure 5.19: External quality factors of resonances in the validation structure shown in Figure 5.16. The blue plusses represent results obtained from the direct computation with CST MWS, whereas the red crosses represent quality factors delivered by the concatenation approach.

Figure 5.18 presents the absolute value of the relative error in the resonant frequencies of the eigenmodes. The frequencies directly determined with CST MWS are denoted by $\tilde{f}_{\text{CST},n}$, whereas the frequencies arising from the SSC approach are denoted by $\tilde{f}_{\text{SSC},n}$. The depicted relative errors are in the order of 10^{-3} . In addition to resonant frequencies of eigenmodes, the external quality factors of resonances in the validation structure are considered. The post-processing of CST MWS yields the external quality factors based on the full discretization of the structure. Complementarily, the quality factors are determined on the basis of the SSC approach as described in Subsection 4.6.5. Figure 5.19 presents the comparison between the methods. Both results agree reasonably well. However, larger deviations are observed for the TM_{01} monopole resonance of the single cell at 3.9 GHz. Moreover, some modes are observed in the direct computation which do not have a clear correspondence in the SSC computation and vice versa.

5.5.3 RF Properties of the Cavity Strings with Couplers

The scattering matrices for the different cavity chains in Figure 5.15 are determined on 10,001 equidistant frequency samples by means of the respective reduced-order state-space models following Subsection 4.6.3 (computation time 1 min 2 sec). The resulting transmission from the left HOM coupler to the right HOM coupler via the entire string is depicted in Figure 5.20. The red curve corresponds to the transmission via the two-cavity string, the black to the four-cavity string, and the cyan

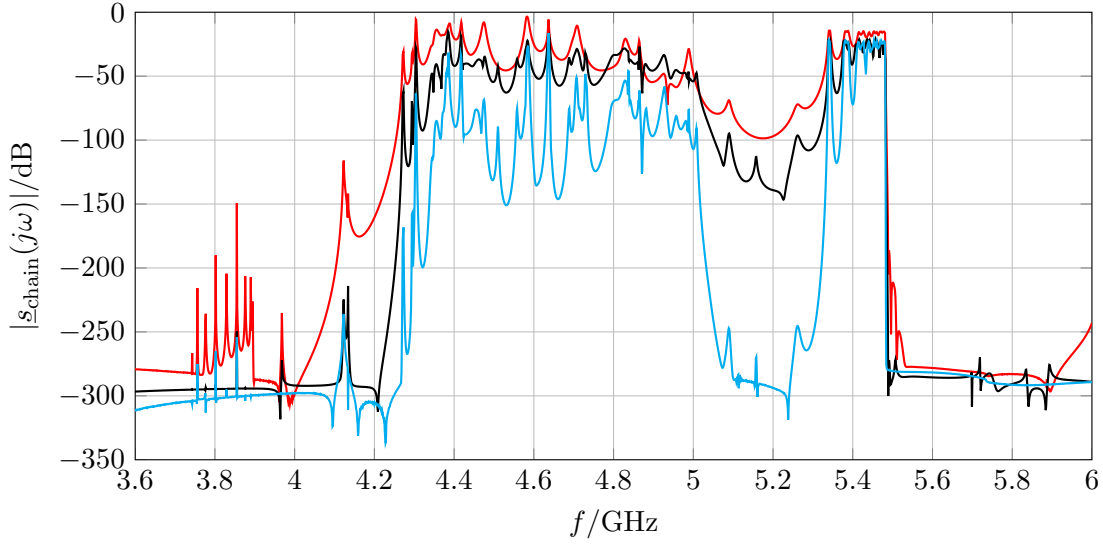


Figure 5.20: Transmissions from left HOM to right HOM coupler via the cavity chains illustrated in Figure 5.15. The red curve depicts the transmission of the chain with two, the black curve the transmission of the chain with four, and the cyan curve the transmission of the chain with eight resonators. All transmissions are determined by means of the SSC approach.

to the eight-cavity string. The transmission basically gets smaller, the longer the chain becomes. This is attributed to the fact that more couplers are present in longer chains, i.e. in Figure 5.15(a) four couplers are in between the left and the right HOM coupler, whereas in Figure 5.15(c) twentytwo intermediate couplers exist. Qualitatively speaking: The longer the chain, the more energy can be extracted (or is lost) by the intermediate couplers, so that the absolute value of the transmission coefficients becomes smaller as a consequence of the conservation of energy. Another observation follows from the transmission curves: The bands in the eight chain arrangements are much more distinct than the bands in the four chain or the two chain arrangement.

In addition to the scattering parameters, the eigenmodes of the three chains with PMC boundary conditions on the waveguide port planes are determined based on the compact models. The two-cavity chain has 140 resonances, the four-cavity chain has 288 resonances, and the eight-cavity chain has 584 resonances in the frequency interval 1 GHz to 6 GHz. Figure 5.21 presents seven typical examples of resonant field distributions inside the four-cavity chain. The eigenmodes in the chain with eight cavities are not shown, because the required scaling of the plots would prevent the visibility of HOM and power couplers. The field plots indicate the absolute value of the electric field. The plots were generated in joint work with Johann Heller by means of ParaView [79]. ParaView is an open-source visualization appli-

cation for scientific purposes. Figure 5.21(a) depicts an eigenmode which belongs to the TM_{01} - π -modes in the chain. The resonant frequency of the eigenmode is 3.9016 GHz. The field energy is exclusively located in two cavities of the four-cavity chain. Note that in addition to this TM_{01} - π -mode, three further TM_{01} - π -mode modes with the resonant frequency 3.9016 GHz exist in the chain. For instance, they can be superposed such that energy is solely stored in the first, second, third, or fourth cavity. Figure 5.21(b) presents an eigenmode with a resonant frequency of 3.9721 GHz. The field energy is predominantly allocated in the vicinity of the power couplers. The eigenmode in Figure 5.21(c) has the resonant frequency 4.6937 GHz and is distributed along the entire chain. Energy is predominantly stored close to the power couplers. Nonetheless, this mode is attributed to the first TE_{11} band. The resonant frequency of the eigenmode in Figure 5.21(d) is equal to 5.2794 GHz. Here, the field energy is mainly allocated in between the cavities in the bellow. The eigenmodes presented in Figure 5.21(e) - Figure 5.21(g) have the resonant frequencies 5.3840 GHz, 5.4073 GHz, and 5.4873 GHz, respectively. These modes belong to the second TE_{11} band and their field distribution is allocated along the entire cavity chain.

Figure 5.22 shows the external quality factors of the resonances computed in the three different arrangements, based on the reduced-order model according to Subsection 4.6.5 (computation time 11 sec). The quality factors of modes in the two-cavity chain are marked as red crosses, the quality factors of modes in the four-cavity chain as black plusses, and the quality factors of modes in the eight-cavity chain as cyan dots. According to Figure 5.22(a) there is a set of resonances with similar resonant frequencies and quality factors as the nine modes of the fundamental band in the vicinity of 3.8 GHz. These modes are localized in the individual cavities or couplers and do not couple with the adjacent segments. Apart from this set, some modes with large quality factors are observed in the four- and eight-cavity arrangements which do not occur in the two-cavity chain. These quality factors correspond to modes which predominantly have field energy in between the second and the third cavity in the four-cavity structure, i.e. sufficiently far away from the power couplers. In the string with eight cavities, these modes are particularly localized in between the second and the third, the third and the fourth, and the sixth and the seventh cavity. Figure 5.22(b) shows the magnification of modes belonging to the second TE dipole band. Two general tendencies can be observed: The longer the chain, the more dense the population with modes and the larger the quality factors become.

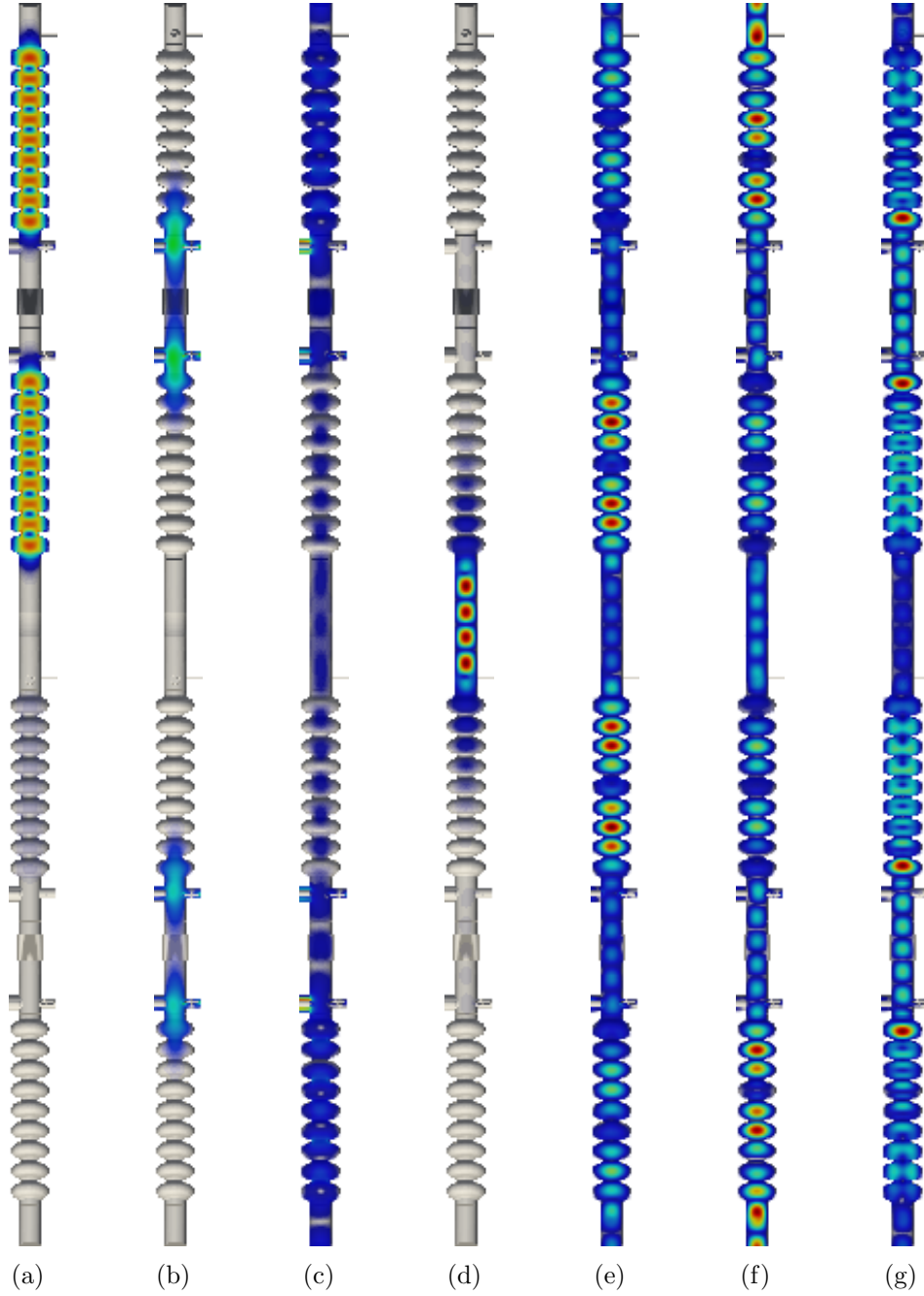


Figure 5.21: Seven arbitrarily selected examples for eigenmodes in the string with four-cavities which is shown in Figure 5.15(b). The plots qualitatively show the absolute value of the electric field. The resonant frequencies are listed as follows: (a) 3.9016 GHz, (b) 3.9721 GHz, (c) 4.6937 GHz, (d) 5.2794 GHz, (e) 5.3840 GHz, (f) 5.4073 GHz, (g) 5.4873 GHz. Note that the poor visibility of the bellow in the middle of the chain is a plot artifact.

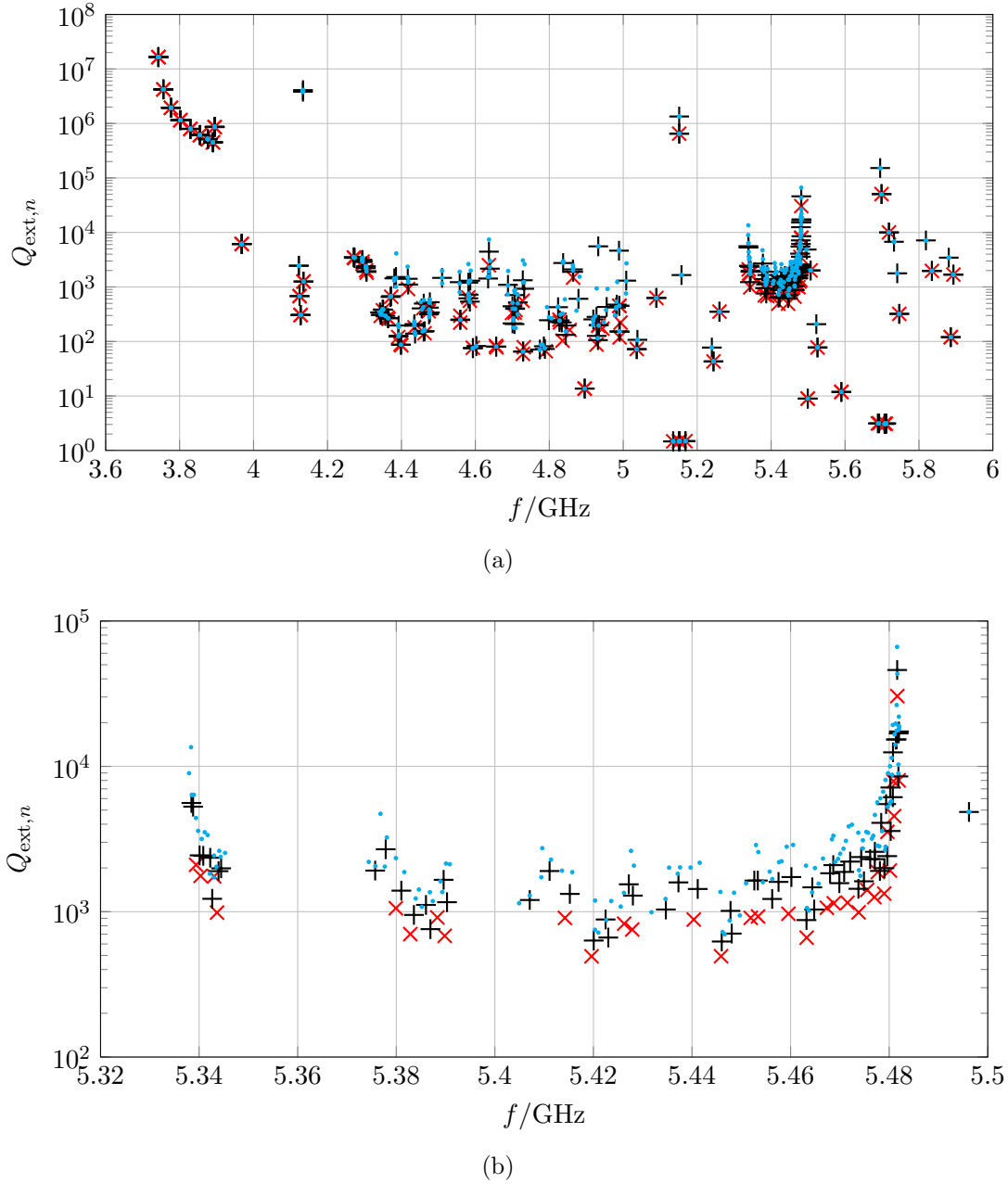


Figure 5.22: External quality factors of resonances in the cavity chains depicted in Figure 5.15. The red crosses refer to resonances in the chain with two, the black pluses to resonances in the chain with four, and the cyan dots to resonances in the chain with eight resonators. (a) External quality factors in the interval 1 GHz to 6 GHz and (b) zoom to external quality factors in the interval 5.32 GHz to 5.5 GHz. These modes are attributed to the second TE dipole band. All quality factors are computed in accordance with Subsection 4.6.5.

6 Discussion, Summary, and Outlook

The objectives of this thesis were the introduction of the State-Space Concatenation scheme and the presentation of suitable application examples. These examples aimed at showing that the scheme gives reasonable results on a wide band and that it allows for a significant reduction of computational costs which result from the determination of RF properties of complex structures. The novel contributions of this thesis are the SSC scheme itself and the generation of state-space models for (segments of) RF structures with multiple waveguide ports and waveguide modes using analytical techniques. The SSC approach is based on the decomposition of the complex structure into individual segments. Subsequently, reduced-order state-space models for the segments are generated. These are concatenated by means of algebraic constraints so that a reduced-order model of the complete structure emerges. In a final step, this model is reduced as well. The thesis starts with an introduction to particle accelerators and motivates the work in a detailed manner. Fundamentals of electromagnetic field theory and of system theory are revised before the SSC scheme is introduced and application examples are discussed. The examples show that SSC can handle topologies different from chains, see the waveguide power splitter in Section 5.3, for example. SSC can also handle different numbers of 2D port modes on the waveguide ports and decomposition planes: The segments of the examples in Section 5.4 and in Section 5.5 are concatenated using more than one 2D port mode on the cut planes. A further key feature of SSC is the considerable reduction (factors in the order of 10^{-4}) of degrees of freedom compared to state-space models generated by concatenations without model order reductions. Despite the fact that SSC describes the complete RF structures by a small number of states, the corresponding compact state-space systems accurately model the respective RF properties. The proof of principle in Section 5.1 works without the discretization of segments and shows that the relative errors in the resonant frequencies of the concatenated structure are in the order of 10^{-6} (cf. Figure 5.4). Similar comparisons of resonant frequencies are based on discrete formulations (see Figure 5.10 or Figure 5.18). In these cases, the relative errors in the resonant frequencies are in the order of approximately 10^{-4} to 10^{-3} . According to the mesh refinement studies in Appendix D, this is the order of error which is expected from the FIT discretization of the segments with a hexahedral mesh. It is therefore assumed that the errors of concatenations with reduced-order models from FIT are not governed

by an accumulation of errors resulting from the concatenation itself, but by errors resulting from the discretization of the segments. Apart from resonant frequencies, the thesis illustrates that SSC can determine field distributions. Figure 5.6 depicts the voltage of the TE_{10} mode along the concatenated waveguide. The discontinuities in the difference (green curve) between the reference field distribution and the SSC approximation are attributed to the fact that field errors are larger on the decomposition planes than field errors in the rest of the domain (cf. green curve in Figure 5.3). However, the relative error (C.8) in the approximated field distribution is small and amounts to $1.6 \cdot 10^{-4}$. Figure 5.13 and Figure 5.19 provide evidence that SSC can deliver longitudinal field profiles and external quality factors of modes in structures with sophisticated shape. Unfortunately, Figure 5.19 shows modes resulting from the direct computation which do not have a clear correspondence in the SSC computation and vice versa. The origin of this effect is unclear because it is not described how CST MWS exactly determines the external quality factors. In addition to eigenmodes and their properties, the application examples illustrate that SSC correctly determines impedance and scattering parameters on a wide band without the redundant handling of multi-frequency data. However, Figure 5.5(b), Figure 5.8(a), and Figure 5.9 depict that the SSC model fails if the transmission spectra fall below approximately -300 dB. This does not limit the proper dynamic description of the full structure, because the transmissions are small in this regime. Network analyzers typically have dynamic ranges¹ in the order of $100 \text{ dB} \dots 140 \text{ dB}$ so that transmissions of -300 dB do not play a role in practical applications. In addition to frequency-domain considerations, the SSC state-space models also allow for time-domain computations: Section 5.2 describes how state-space models arising from analytical considerations can be combined with such emerging from discretization approaches. The resulting compact model of the complete structure is stable and can be used for transient investigations.

In addition to the reduction of degrees of freedoms, the SSC scheme enables a significant reduction of computational costs, particularly for eigenmode computations: The direct computation of 125 eigenmodes in the rotationally symmetric chain of two cavities in Figure 5.11(a) requires approximately 11 h, whereas the SSC computation needs less than 4 min. The eigenmodes of the validation structure in Figure 5.16 are straightforwardly computed in 16 h 27 min, whereas the SSC delivers the eigenmodes in less than 22 min. Studies with CST MWS have shown that the computation times of the iterative eigensolvers scale with N_s per eigenmode, where N_s is the number of rows and columns of the corresponding sparse system matrix. Thus, it is estimated that the straightforward determination of one eigenmode in the chain with four cavities in Figure 5.11(b) requires approximately $2 \cdot 11 \text{ h}/125$. Compared to the two-cavity chain in Figure 5.11(a), the number of degrees of free-

¹For instance, the dynamic range of the scattering parameter measurement presented in Figure 1.5 is approximately -100 dB.

dom² is approximately doubled for the four-cavity chain, so that the computation times per eigenmode are expected to be two times larger. However, 259 eigenmodes exist in the four-cavity chain in the frequency range of interest for the specified symmetry conditions. Consequently, it is estimated that an eigenmode computation for the four-cavity chain requires $2 \cdot 11 \text{ h} \cdot 259/125$, i.e. four times longer than the computation for the two-cavity chain. The eight-cavity chain has 4,013,322 states, i.e. approximately four times the number of degrees of freedom of the two cavity chain. According to Subsection 5.4.3, 527 eigenmodes exist in the eight-cavity chain in the frequency range of interest for the specified symmetry conditions. Therefore, it is estimated that an eigenmode computation for the string in Figure 5.11(c) would require $4 \cdot 11 \text{ h} \cdot 527/125$, i.e. sixteen times longer than the computation for the two-cavity chain. In contrast to CST MWS, general statements about the scaling behavior of SSC computations cannot be made. The computation times to generate reduced-order models of complex structures by means SSC are heavily dependent on the structure itself: For instance, computation times can be drastically reduced if the complex structure contains repetitive segments or if the decomposition allows for exploiting the symmetry of segments. Basically, the reduction of the state-space models of the individual segments is the most expensive step in the scheme.

Section 5.5 presents the key strength of SSC. The described application example closely corresponds to the problem statement given in the introduction: As discussed in Section 1.3, brute-force approaches to determine the RF properties of the four-cavity string require hours of computing time on cluster computers due to the complexity of the problem. In contrast, the SSC computation of all eigenmodes in the interval from 1 GHz to 6 GHz in the two-, four-, and eight-cavity chains are determined on a standard workstation in 22 min. The significant reduction of computing infrastructure demands and computation times results from the combination of segmentation techniques with model order reduction approaches. Section 5.5 depicts the complexity of computed field patterns such as the $\text{TM}_{01}\text{-}\pi$ -mode excited in two cavities in Figure 5.21(a), a bellow mode in Figure 5.21(d), or a multi-cavity mode in Figure 5.21(e). Moreover, Figure 5.14 in Section 5.4 and Figure 5.22 in Section 5.5 show that RF bands of longer chains are more densely populated with modes. These results once more justify the need for multi-cavity analysis. In summary, the main contribution of SSC is that it enhances the application domain of cheap workstation computers, i.e. the technique empowers these machine to cope with problems which previously required supercomputers. In this sense, the SSC approach can also be classified as environmentally sustainable, because the usage of energy-intensive supercomputers can be avoided.

SSC is currently used for design studies to upgrade the BESSY facility such that bunches of charged particles with different lengths can be stored in the ring (refer to [80] for a concept of the upgrade). The planned upgrade of the machine requires

²The discussion refers to the numbers of degrees of freedom given in Subsection 5.4.1.

the insertion of four additional superconducting cavities in the beamline. Two cavities will be operated at 1.5 GHz whereas the other two cavities will be operated at 1.75 GHz. Both cavities will be accommodated in one cryomodule. Numerical studies with SSC revealed that multi-cavity HOMs with non-negligible longitudinal voltages exist in the two-cavity chain. It is planned to use SSC to optimize the design of cavities taking their mutual coupling into consideration. For instance, SSC conveniently allows for determining the influence of the location and the number of HOM couplers on RF properties of the cavity string. Thus, the novel method can contribute to find an adequate final design for the BESSY VSR cryomodule. Moreover, the SSC scheme could be applied in order to generate modal books of reference for the third harmonic cavity chains in FLASH [9] and in the European XFEL [10]. These modal books of reference could be structured similarly to [22] but could cover properties of eigenmodes of the entire chains. Consequently, the modal books could contribute to a more profound understanding of the beam-excited fields in the superconducting cavity chains. Complementary to the computation of RF properties for concrete geometries, issues directly related to the method itself are of interest from a scientific point of view: A direct comparison of the SSC scheme with other approaches using a benchmark structure with a well-defined geometry is preferable. It is also planned to use the SSC scheme to concatenate reduced-order models which emerge from FEM discretizations based on tetrahedral meshes. In this context, open-source FEM packages like FEniCS [81] are promising platforms, because the system matrices of the discrete formulation of Maxwell's equations are available. Moreover, this platform supports basis functions with different order.

A Commonly Used Waveguides

Modes or Port Modes

In the following, properties of 2D port or waveguide modes in waveguides with the three most common cross sections are shown. The presentation mainly follows [55, 63].

A.1 Modal Field Patterns in Rectangular Waveguides

The 2D Helmholtz equation (2.46) with the boundary condition (2.48) can be analytically solved for rectangular cross section such as shown in Figure 2.3. A separation technique [63] in a Cartesian coordinate system delivers the transverse patterns of TE waveguide modes

$$\mathbf{L}_t^{\text{TE}}(x, y) = A^{\text{TE}} \begin{pmatrix} -\frac{m_y \pi}{b} \cos\left(\frac{m_x \pi}{a} x\right) \sin\left(\frac{m_y \pi}{b} y\right) \\ \frac{m_x \pi}{a} \sin\left(\frac{m_x \pi}{a} x\right) \cos\left(\frac{m_y \pi}{b} y\right) \end{pmatrix} \quad (\text{A.1})$$

and the transverse patterns of TM waveguide modes

$$\mathbf{L}_t^{\text{TM}}(x, y) = A^{\text{TM}} \begin{pmatrix} \frac{m_x \pi}{a} \cos\left(\frac{m_x \pi}{a} x\right) \sin\left(\frac{m_y \pi}{b} y\right) \\ \frac{m_y \pi}{b} \sin\left(\frac{m_x \pi}{a} x\right) \cos\left(\frac{m_y \pi}{b} y\right) \end{pmatrix} \quad (\text{A.2})$$

in rectangular waveguides. The constants a and b specify the width and the height of the rectangular waveguide. The scaling constants A^{TE} and A^{TM} are chosen such that the orthonormality relation (2.49) is fulfilled. The variables m_x and m_y are integer numbers running from zero to infinity for (A.1) and from one to infinity for (A.2). The separation constants and the respective cutoff angular frequencies are given for the TE and the TM cases by

$$k_t = \omega_{\text{co}} \sqrt{\varepsilon \mu} = \pi \sqrt{\frac{m_x^2}{a^2} + \frac{m_y^2}{b^2}}. \quad (\text{A.3})$$

Table A.1 lists the properties of the first eight waveguide modes of a rectangular R-100 waveguide ($a = 22.86 \text{ mm}$ and $b = 10.16 \text{ mm}$) whereas Figure A.1 shows the corresponding field patterns $\mathbf{L}_{t,m}(\mathbf{r}_t)$ of TE and TM modes which are ordered according to their separation constants k_t (or cutoff frequencies ω_{co}).

Table A.1: Properties of waveguide modes in a rectangular R-100 waveguide ($a = 22.86$ mm and $b = 10.16$ mm) ordered in an ascending manner according to the separation constants. Degenerated couples are highlighted in grey. The corresponding field patterns are depicted in Figure A.1.

Figure A.1	Mode m	Type	m_x	m_y	$k_{t,m}/m$	$\omega_{co}/2/\pi/\text{sec}$
(a)	1	TE	1	0	137.428	$6.55869 \cdot 10^9$
(b)	2	TE	2	0	274.855	$13.1174 \cdot 10^9$
(c)	3	TE	0	1	309.212	$14.7571 \cdot 10^9$
(d)	4	TE	1	1	338.376	$16.1489 \cdot 10^9$
(e)	5	TM	1	1	338.376	$16.1489 \cdot 10^9$
(f)	6	TE	3	0	412.283	$19.6761 \cdot 10^9$
(g)	7	TE	2	1	413.712	$19.7443 \cdot 10^9$
(h)	8	TM	2	1	413.712	$19.7443 \cdot 10^9$

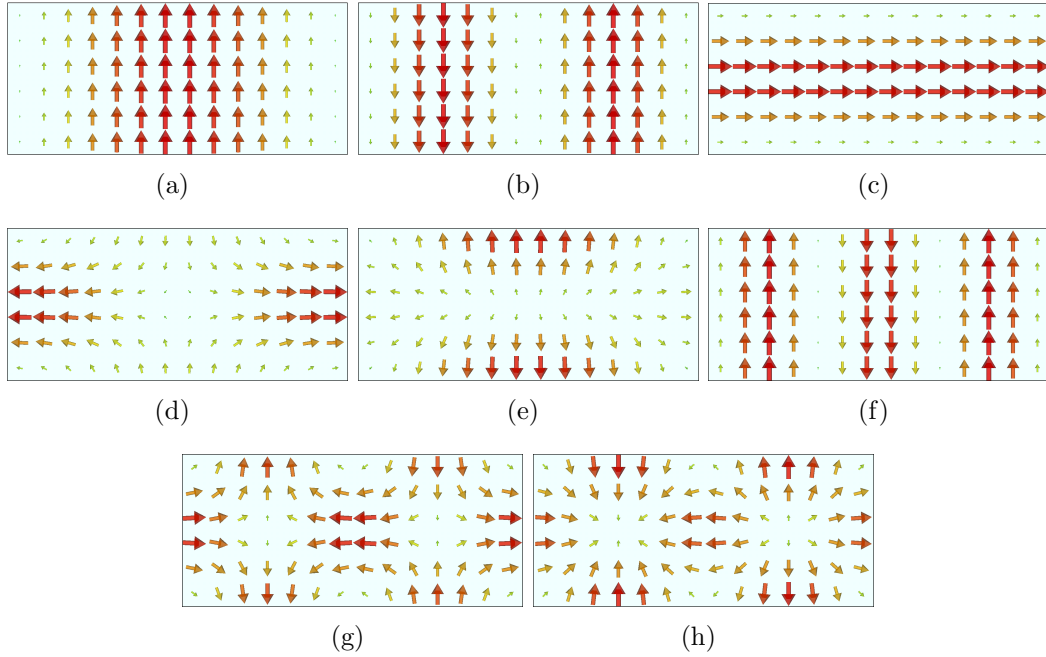


Figure A.1: First eight transverse modal patterns $\mathbf{L}_{t,m}(\mathbf{r})$ in a rectangular R-100 waveguide ($a = 22.86$ mm and $b = 10.16$ mm) ordered according to their separation constants. The respective properties are listed in Table A.1. The plots are created with CST MWS.

A.2 Modal Field Patterns in Circular Waveguides

Apart from the rectangular waveguide, the circular waveguide in Figure 2.3 is a structure of practical relevance whose transverse field patterns can be determined

analytically. Employing a separation technique [63] for the 2D Helmholtz equation (2.46) with the boundary condition (2.48) in a cylindrical coordinate system gives the transverse field patterns of TE waveguide modes

$$\mathbf{L}_t^{\text{TE}}(r, \varphi) = A^{\text{TE}} \begin{pmatrix} \frac{m_\varphi}{r} J_{m_\varphi} \left(\chi'_{m_\varphi, m_r} \frac{r}{R_o} \right) \cos(m_\varphi \varphi + \varphi_0) \\ \frac{\chi'_{m_\varphi, m_r}}{R_o} J'_{m_\varphi} \left(\chi'_{m_\varphi, m_r} \frac{r}{R_o} \right) \sin(m_\varphi \varphi + \varphi_0) \end{pmatrix} \quad (\text{A.4})$$

and of TM waveguide modes

$$\mathbf{L}_t^{\text{TM}}(r, \varphi) = A^{\text{TM}} \begin{pmatrix} \frac{\chi_{m_\varphi, m_r}}{R_o} J'_{m_\varphi} \left(\chi_{m_\varphi, m_r} \frac{r}{R_o} \right) \cos(m_\varphi \varphi + \varphi_0) \\ -\frac{m_\varphi}{r} J_{m_\varphi} \left(\chi_{m_\varphi, m_r} \frac{r}{R_o} \right) \sin(m_\varphi \varphi + \varphi_0) \end{pmatrix} \quad (\text{A.5})$$

in circular waveguides. Here, m_φ and m_r are integer numbers, J_{m_φ} is the m_φ th order Bessel function of the first kind, J'_{m_φ} is the derivative of the m_φ th order Bessel function of the first kind, and R_o the radius of the circular waveguide [63]. The m_r th root of the m_φ th order Bessel function of the first kind is given by χ_{m_φ, m_r} whereas χ'_{m_φ, m_r} is the m_r th root of the derivative of the m_φ th order Bessel function of first kind. The scaling factors A^{TE} and A^{TM} are selected in accordance with (2.49) and φ_0 is a constant phase angle. The separation constants for the TE case are given by

$$k_t^{\text{TE}} = \omega_{\text{co}} \sqrt{\varepsilon \mu} = \frac{\chi'_{m_\varphi, m_r}}{R_o} \quad (\text{A.6})$$

and for the TM case by

$$k_t^{\text{TM}} = \omega_{\text{co}} \sqrt{\varepsilon \mu} = \frac{\chi_{m_\varphi, m_r}}{R_o}. \quad (\text{A.7})$$

Table A.2: Properties of waveguide modes in a circular waveguide ($R_o = 20$ mm) ordered in an ascending manner according to the separation constants. Degenerated couples are highlighted in grey. The corresponding field patterns are depicted in Figure A.2.

Figure A.2	Mode m	Type	m_φ	m_r	$k_{t,m}/\text{m}$	$\omega_{\text{co}}/2/\pi/\text{sec}$
(a)	1	TE	1	1	92.0592	$4.39246 \cdot 10^9$
(b)	2	TE	1	1	92.0592	$4.39246 \cdot 10^9$
(c)	3	TM	0	1	120.241	$5.73713 \cdot 10^9$
(d)	4	TE	2	1	152.712	$7.28641 \cdot 10^9$
(e)	5	TE	2	1	152.712	$7.28641 \cdot 10^9$
(f)	6	TE	0	1	191.585	$9.1412 \cdot 10^9$
(g)	7	TM	1	1	191.585	$9.1412 \cdot 10^9$
(h)	8	TM	1	1	191.585	$9.1412 \cdot 10^9$

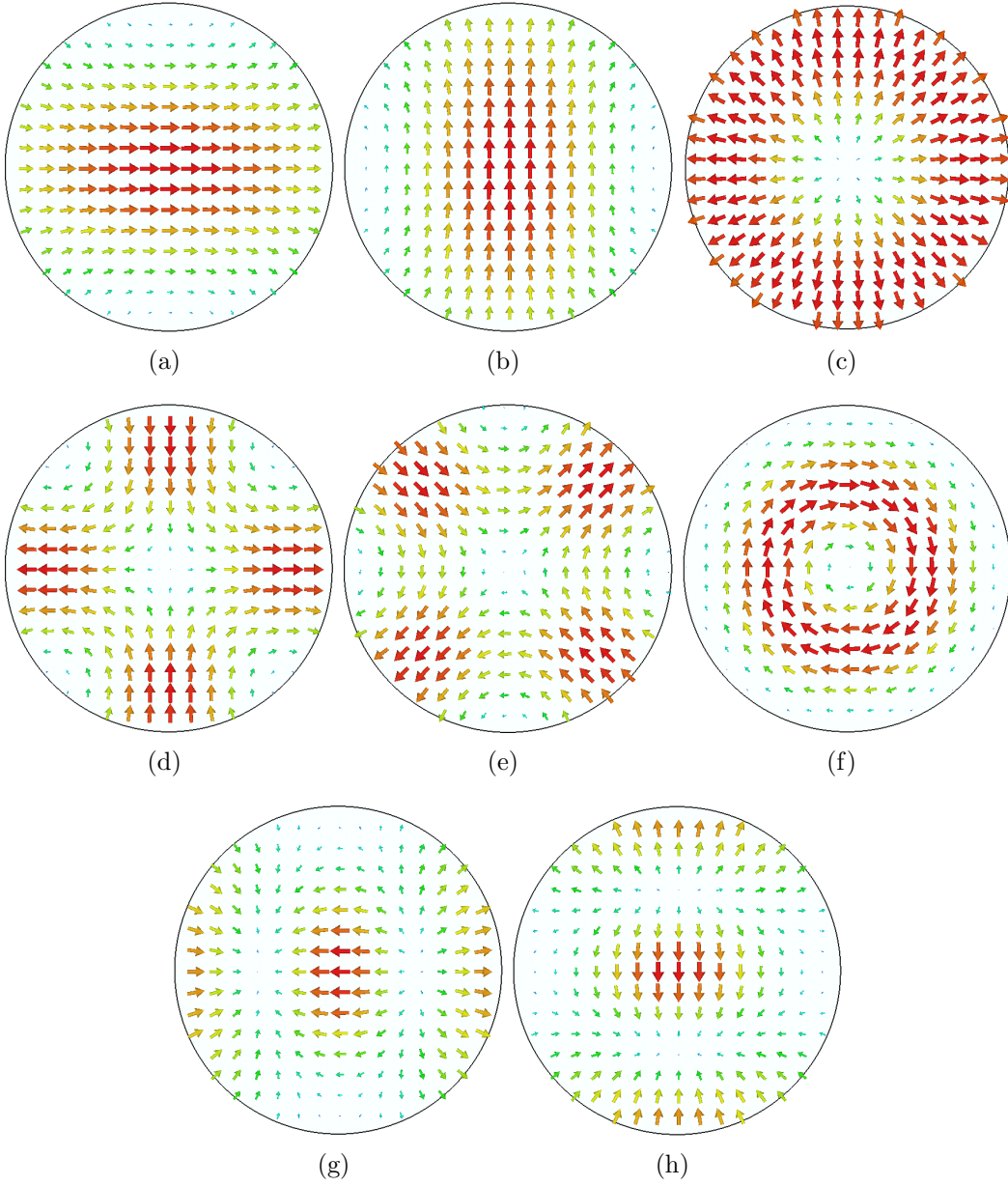


Figure A.2: First eight transverse modal patterns $\mathbf{L}_{t,m}(\mathbf{r})$ in a circular waveguide ($R_o = 20$ mm) ordered according to their separation constants. The respective properties are listed in Table A.2. The plots are created with CST MWS.

Table A.2 lists the properties of the first eight waveguide modes in a circular waveguide ($R_o = 20$ mm) and Figure A.2 depicts the respective field patterns $\mathbf{L}_{t,m}(\mathbf{r}_t)$ which are ordered based on their separation constants.

A.3 Modal Field Pattern in Coaxial Waveguides

A fundamental property of the coaxial waveguide is the existence of a TEM mode due to the inner conductor in the waveguide. The TEM mode can propagate for $\omega \geq 0$ and is typically used in most technical applications when operating coaxial cables. Nonetheless, TE and TM modes can also propagate in the coaxial cable if an excitation with frequencies larger than their respective cutoff frequencies takes place. TE and TM modes are often unwanted in the cable, because they limit the bandwidth due to modal dispersion effects. In the current thesis, TE and TM modes in coaxial cables are not discussed, because they are not able to propagate for

$$\omega < \frac{1}{\sqrt{\varepsilon\mu}} \frac{2}{R_i + R_o}, \quad (\text{A.8})$$

whereas R_i is the radius of the inner conductor and R_o is the radius of the outer conductor [55, p. 83, (3.89)]. The approximation (A.8) only holds for $R_i/R_o > 0.2$. A rigorous analysis of TE and TM modes in coaxial cables is available in [55, 63].

The field pattern for TEM modes in coaxial cables is given by

$$\mathbf{L}_t^{\text{TEM}}(r, \varphi) = A^{\text{TEM}} \begin{pmatrix} \frac{1}{r} \\ 0 \end{pmatrix} \quad (\text{A.9})$$

with the scaling constant A^{TEM} , so that (2.49) is satisfied. As previously discussed, the separation constant for TEM modes as well as their cutoff frequency is zero:

$$k_t^{\text{TEM}} = \omega_{\text{co}} \sqrt{\varepsilon\mu} = 0. \quad (\text{A.10})$$

The line impedance of the coaxial cable is determined by

$$Z_{\text{line}}^{\text{TEM}} = \frac{V^{\text{TEM,li,+}}(z)}{\underline{I}^{\text{TEM,li,+}}(z)} = \frac{\beta_v V^{\text{TEM,+}}(z)}{\beta_i \underline{I}^{\text{TEM,+}}(z)} = \frac{\ln(R_o/R_i)}{2\pi} Z_{\text{fs}}. \quad (\text{A.11})$$

Figure A.3(a) depicts the field pattern of a TEM mode in a coaxial cable.

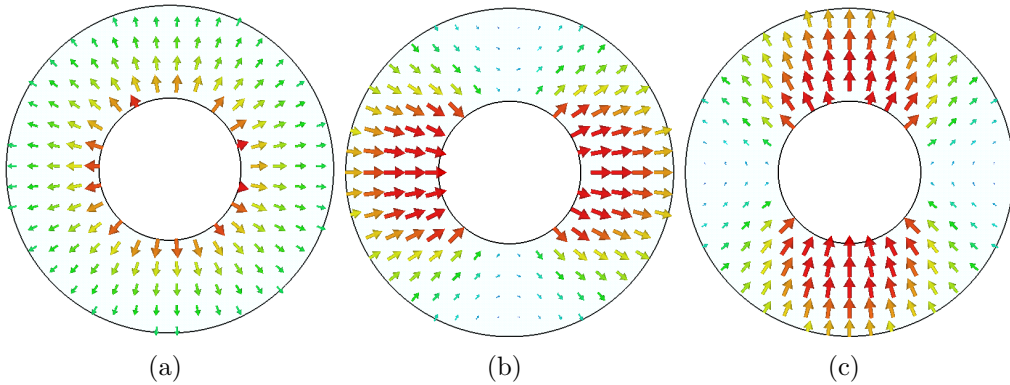


Figure A.3: Transverse field pattern $\mathbf{L}_t^{\text{TEM}}(r, \varphi)$ of a TEM mode (a), and of the first two TE modes (b) and (c) in a coaxial cable. The plots are created with CST MWS.

B Analytical Derivations Related to Rectangular Waveguides

This part of the appendix presents analytical considerations related to a rectangular waveguide as shown in Figure B.1. The boundary of the waveguide is assumed to be perfect electric conducting while the inner domain is assumed to be a perfect insulator. The length of the waveguide is given by L , its width by a , and its height by b . The grey facets in the sketch indicate waveguide ports which are used to excite the structure. The presented analytical considerations are restricted to TE_{10} waveguide modes. The following derivations are predominantly required for the proof of principle in Section 5.1. This part of the appendix covers the calculation of the following RF properties of the rectangular waveguide: 3D field distributions due to frequency-domain modal waveguide port stimuli, impedance parameters, 3D eigenmodes, and a state-space model.

B.1 Frequency-Domain Field Distributions

To derive electromagnetic field distributions due to modal current excitations at the waveguide ports in the rectangular waveguide, the ansatz (2.43) for electric fields in waveguides is transformed into frequency domain and the modal voltage along the

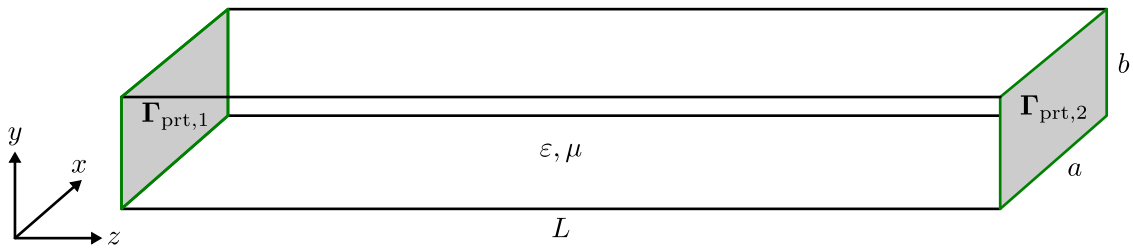


Figure B.1: Sketch of a rectangular waveguide with constant cross section. The length of the waveguide is denoted by L , the width by a , and the height by b . The grey facets $\Gamma_{\text{prt},1}$ and $\Gamma_{\text{prt},2}$ indicate waveguide ports which exclusively account for TE_{10} port modes. The wall of the waveguide is assumed to be a perfect electric conductor whereas the inner domain is assumed to be a perfect insulator with the permittivity ε and the permeability μ .

waveguide is expressed by (2.52):

$$\underline{\mathbf{E}}(\mathbf{r}) = \begin{pmatrix} \mathbf{L}_t^{\text{TE}_{10}}(\mathbf{r}_t) \\ 0 \end{pmatrix} \underbrace{(V^+ e^{-\gamma(j\omega)z} + V^- e^{\gamma(j\omega)z})}_{\underline{V}(z)}, \quad (\text{B.1})$$

with the transverse modal field pattern of the TE_{10} port mode

$$\mathbf{L}_t^{\text{TE}_{10}}(\mathbf{r}_t) = \sqrt{\frac{2}{ab}} \begin{pmatrix} 0 \\ \sin\left(\frac{\pi}{a}x\right) \end{pmatrix}. \quad (\text{B.2})$$

The voltage of the TE_{10} mode along the waveguide is denoted by $\underline{V}(z)$ whereas the voltages of the waves propagating in positive and negative z -direction are represented by \underline{V}^+ and \underline{V}^- . The propagation constant of the TE_{10} port mode is given by

$$\underline{\gamma}(j\omega) = \sqrt{\varepsilon\mu} \sqrt{(j\omega)^2 + \omega_{\text{co}}^2}, \text{ where } \omega_{\text{co}} = \frac{1}{\sqrt{\varepsilon\mu}} \frac{\pi}{a}. \quad (\text{B.3})$$

The magnetic field corresponding to (B.1) is determined by means of Faraday's law of induction (2.3):

$$\begin{aligned} \underline{\mathbf{H}}(\mathbf{r}) = & -\frac{1}{j\omega\mu} \nabla \times \underline{\mathbf{E}}(\mathbf{r}) = \\ & -\frac{1}{j\omega\mu} \begin{pmatrix} \sqrt{\frac{2}{ab}} \sin\left(\frac{\pi}{a}x\right) \underline{\gamma}(j\omega) [\underline{V}^+ e^{-\gamma(j\omega)z} - \underline{V}^- e^{\gamma(j\omega)z}] \\ 0 \\ \frac{\pi}{a} \sqrt{\frac{2}{ab}} \cos\left(\frac{\pi}{a}x\right) [\underline{V}^+ e^{-\gamma(j\omega)z} + \underline{V}^- e^{\gamma(j\omega)z}] \end{pmatrix}. \end{aligned} \quad (\text{B.4})$$

Following (2.44), this magnetic field can be reformulated in terms of

$$\underline{\mathbf{H}}(\mathbf{r}) = \mathbf{n}_z \times \mathbf{L}_t^{\text{TE}_{10}}(\mathbf{r}_t) \underbrace{\frac{1}{\underline{Z}_w^{\text{TE}_{10}}(j\omega)} [\underline{V}^+ e^{-\gamma(j\omega)z} - \underline{V}^- e^{\gamma(j\omega)z}]}_{\underline{I}(z)} + \mathbf{n}_z \underline{H}_z^{\text{TE}_{10}}(\mathbf{r}), \quad (\text{B.5})$$

where \mathbf{n}_z is the unit vector in longitudinal direction, $\underline{Z}_w^{\text{TE}_{10}}(j\omega)$ the wave impedance (2.57) of the TE_{10} waveguide mode, $\underline{I}(z)$ the current of the TE_{10} mode along the waveguide, and $\underline{H}_z^{\text{TE}_{10}}(\mathbf{r})$ the longitudinal component of the magnetic field of the waveguide mode.

In a next step, the amplitudes \underline{V}^+ and \underline{V}^- of the traveling waves are replaced by the modal currents at the ends of the waveguide. These currents are in fact the modal waveguide port currents:

$$\underline{I}_1 = \underline{I}(z=0) = \frac{1}{\underline{Z}_w^{\text{TE}_{10}}(j\omega)} [\underline{V}^+ - \underline{V}^-], \quad (\text{B.6})$$

$$\underline{I}_2 = -\underline{I}(z=L) = \frac{1}{\underline{Z}_w^{\text{TE}_{10}}(j\omega)} [-\underline{V}^+ e^{-\gamma(j\omega)L} + \underline{V}^- e^{\gamma(j\omega)L}]. \quad (\text{B.7})$$

These equations are combined and used to determine the voltages of the waves traveling in positive and negative z -direction in dependence on the port currents:

$$\underline{V}^+ = \frac{1}{2} \underline{Z}_w^{\text{TE}_{10}}(j\omega) \left([\coth(\underline{\gamma}(j\omega)L) + 1] \underline{I}_1 + \text{csch}(\underline{\gamma}(j\omega)L) \underline{I}_2 \right), \quad (\text{B.8})$$

$$\underline{V}^- = \frac{1}{2} \underline{Z}_w^{\text{TE}_{10}}(j\omega) \left([\coth(\underline{\gamma}(j\omega)L) - 1] \underline{I}_1 + \text{csch}(\underline{\gamma}(j\omega)L) \underline{I}_2 \right), \quad (\text{B.9})$$

where $\coth(x) = 1/\tanh(x)$ and $\text{csch}(x) = 1/\sinh(x)$. The identities (B.8) and (B.9) are used to substitute \underline{V}^+ and \underline{V}^- in the definition of $\underline{V}(z)$ in (B.1). Simplifying the arising equation finally delivers

$$\underline{V}(z) = \underline{Z}_w^{\text{TE}_{10}}(j\omega) \text{csch}(\underline{\gamma}(j\omega)L) \left[\cosh(\underline{\gamma}(j\omega)(L-z)) \underline{I}_1 + \cosh(\underline{\gamma}(j\omega)z) \underline{I}_2 \right]. \quad (\text{B.10})$$

In combination with (B.1) this statement allows for determining the electric field distribution inside the waveguide due to port current stimuli in frequency domain.

B.2 Impedance Parameters of Rectangular Waveguide

To derive the impedance parameters of the TE_{10} mode in the rectangular waveguide, the modal voltages at the waveguide ports are required:

$$\underline{V}_1 = \underline{V}(z=0) = \underline{Z}_w^{\text{TE}_{10}}(j\omega) \text{csch}(\underline{\gamma}(j\omega)L) \left[\cosh(\underline{\gamma}(j\omega)L) \underline{I}_1 + \underline{I}_2 \right], \quad (\text{B.11})$$

$$\underline{V}_2 = \underline{V}(z=L) = \underline{Z}_w^{\text{TE}_{10}}(j\omega) \text{csch}(\underline{\gamma}(j\omega)L) \left[\underline{I}_1 + \cosh(\underline{\gamma}(j\omega)L) \underline{I}_2 \right]. \quad (\text{B.12})$$

Based on definition (3.59) the impedance parameters are given as follows

$$\underline{z}_{1,1}(j\omega) = \underline{z}_{2,2}(j\omega) = \left. \frac{\underline{V}_1}{\underline{I}_1} \right|_{\underline{I}_2=0} = \left. \frac{\underline{V}_2}{\underline{I}_2} \right|_{\underline{I}_1=0} = \frac{\underline{Z}_w^{\text{TE}_{10}}(j\omega)}{\tanh(\underline{\gamma}(j\omega)L)}, \quad (\text{B.13})$$

$$\underline{z}_{1,2}(j\omega) = \underline{z}_{2,1}(j\omega) = \left. \frac{\underline{V}_1}{\underline{I}_2} \right|_{\underline{I}_1=0} = \left. \frac{\underline{V}_2}{\underline{I}_1} \right|_{\underline{I}_2=0} = \frac{\underline{Z}_w^{\text{TE}_{10}}(j\omega)}{\sinh(\underline{\gamma}(j\omega)L)}. \quad (\text{B.14})$$

B.3 Eigenmodes in a Rectangular Waveguide

To derive TE_{10n} eigenmodes of the rectangular waveguide, the product ansatz

$$\tilde{\mathbf{E}}_n(x, y, z) = \begin{pmatrix} \mathbf{L}_t^{\text{TE}_{10}}(\mathbf{r}_t) \\ 0 \end{pmatrix} \tilde{V}_n(z) = \begin{pmatrix} 0 \\ \sqrt{\frac{2}{ab}} \sin\left(\frac{\pi}{a}x\right) \\ 0 \end{pmatrix} \tilde{V}_n(z) \quad (\text{B.15})$$

is chosen. Here, $\tilde{V}_n(z)$ is a function accounting for the longitudinal dependence of the n th eigenmode. This function is referred to as voltage of the n th eigenmode along the waveguide. The expression in parenthesis denotes the transverse dependence of the electric field of the eigenmode. The substitution of the ansatz into (2.68) delivers

$$\tilde{k}_n^2 = \underbrace{\left(\frac{\pi}{a}\right)^2}_{k_t^2} - \underbrace{\frac{\tilde{V}_n''(z)}{\tilde{V}_n(z)}}_{-k_{n,z}^2}. \quad (\text{B.16})$$

The voltage $\tilde{V}_n(z)$ of the eigenmode along the waveguide has to satisfy

$$\tilde{V}_n''(z) + k_{n,z}^2 \tilde{V}_n(z) = 0. \quad (\text{B.17})$$

The real-valued solution of this differential equation is given by

$$\tilde{V}_n(z) = \Pi_n^{\text{TE}} \sin(k_{n,z} z) + \Psi_n^{\text{TE}} \cos(k_{n,z} z), \quad (\text{B.18})$$

where Π_n^{TE} and Ψ_n^{TE} are scaling constants. To ensure PMC boundary conditions at the ends of the waveguide as requested in Subsection 3.2.1, the magnetic field corresponding to (B.15) is determined by means of Faraday's law:

$$\tilde{\mathbf{H}}_n(x, y, z) = -\frac{1}{j\tilde{\omega}_n\mu} \nabla \times \tilde{\mathbf{E}}_n(x, y, z) \quad (\text{B.19})$$

$$= \frac{A_n}{j\tilde{\omega}_n\mu} \begin{pmatrix} \frac{\pi}{a} k_{n,z} \sin\left(\frac{\pi}{a}x\right) [\Pi_n^{\text{TE}} \cos(k_{n,z} z) - \Psi_n^{\text{TE}} \sin(k_{n,z} z)] \\ 0 \\ -\frac{\pi^2}{a^2} \cos\left(\frac{\pi}{a}x\right) [\Pi_n^{\text{TE}} \sin(k_{n,z} z) + \Psi_n^{\text{TE}} \cos(k_{n,z} z)] \end{pmatrix}. \quad (\text{B.20})$$

To ensure that the transverse magnetic fields at both ends of the waveguide (located at $z = 0$ and $z = L$) are equal to zero, the identity

$$\Pi_n^{\text{TE}} \cos(k_{n,z} z) - \Psi_n^{\text{TE}} \sin(k_{n,z} z) = 0 \quad (\text{B.21})$$

has to hold for $z = 0$ and $z = L$. Thus, $\Pi_n^{\text{TE}} = 0$ and $k_{n,z} = (n-1)\pi/L$. The constant Ψ_n^{TE} determines the energy stored in the n th eigenmode. In summary, the electric field distributions of TE_{10n} eigenmodes in a rectangular waveguide with PMC conditions at both ends is given by

$$\tilde{V}_n(z) = \Psi_n^{\text{TE}} \cos\left(\frac{(n-1)\pi}{L} z\right), \text{ where } n = 1, 2, \dots \quad (\text{B.22})$$

in combination with (B.15). The resonant angular frequencies which correspond to these 3D eigenmodes are determined by

$$\tilde{\omega}_n = 2\pi\tilde{f}_n = \frac{1}{\sqrt{\varepsilon\mu}} \tilde{k}_n = \frac{1}{\sqrt{\varepsilon\mu}} \sqrt{\left(\frac{\pi}{a}\right)^2 + \left(\frac{(n-1)\pi}{L}\right)^2}. \quad (\text{B.23})$$

B.4 State-Space System for Rectangular Waveguide

To generate a state-space system for a rectangular waveguide, the electric field distributions (B.15) of the eigenmodes in the structure, its resonant angular frequencies (B.23), and the 2D port modes (B.2) are required. The state matrix in the first-order representation is given by the block matrix

$$\mathbf{A}_{\text{fc}} = \text{diag} \left(\begin{pmatrix} 0 & \tilde{\omega}_1 \\ -\tilde{\omega}_1 & 0 \end{pmatrix}, \begin{pmatrix} 0 & \tilde{\omega}_2 \\ -\tilde{\omega}_2 & 0 \end{pmatrix}, \dots, \begin{pmatrix} 0 & \tilde{\omega}_n \\ -\tilde{\omega}_n & 0 \end{pmatrix}, \dots, \begin{pmatrix} 0 & \tilde{\omega}_{N_e} \\ -\tilde{\omega}_{N_e} & 0 \end{pmatrix} \right), \quad (\text{B.24})$$

whereas the state matrix in the second-order representation is determined by

$$\mathbf{A}_{\text{sc}} = \text{diag} \left(-\tilde{\omega}_1^2, -\tilde{\omega}_2^2, \dots, -\tilde{\omega}_n^2, \dots, -\tilde{\omega}_{N_e}^2 \right). \quad (\text{B.25})$$

As mentioned, the angular resonant frequencies $\tilde{\omega}_n$ are chosen in accordance with (B.23). Recall that N_e is the number of eigenmodes used for the electric field expansion (3.18). To establish the input and output matrices of the state-space system, the interaction coefficients (3.26) are required. Based on the field distributions of the 3D eigenmodes (B.15) and the field patterns of the 2D port modes the interaction coefficients¹ are given by

$$h_{n,1} = \frac{1}{\sqrt{2W_n}} \iint_{\Gamma_{\text{prt},1}} \tilde{\mathbf{E}}_n(\mathbf{r}_t) \cdot \mathbf{L}_t^{\text{TE}_{10}}(\mathbf{r}_t) dA = \frac{1}{\sqrt{\varepsilon L}} \begin{cases} 1 & \text{if } n = 1, \\ \sqrt{2} & \text{if } n > 1 \end{cases} \quad (\text{B.26})$$

and

$$h_{n,2} = \frac{1}{\sqrt{2W_n}} \iint_{\Gamma_{\text{prt},2}} \tilde{\mathbf{E}}_n(\mathbf{r}_t) \cdot \mathbf{L}_t^{\text{TE}_{10}}(\mathbf{r}_t) dA = \frac{1}{\sqrt{\varepsilon L}} \begin{cases} 1 & \text{if } n = 1, \\ \sqrt{2}(-1)^{n-1} & \text{if } n > 1. \end{cases} \quad (\text{B.27})$$

The coefficient $h_{n,1}$ quantifies the interaction between the n th 3D eigenmode and the TE_{10} port mode at port 1 whereas the coefficient $h_{n,2}$ describes the interaction between the n th 3D eigenmode and the TE_{10} port mode at port 2. Based on these coefficients the input matrix in the first-order representation reads as

$$\mathbf{B}_{\text{fc}} = \frac{1}{\sqrt{\varepsilon L}} \begin{pmatrix} 0 & 1 & 0 & \sqrt{2} & 0 & \sqrt{2} & 0 & \sqrt{2} & \sqrt{2} & \dots \\ 0 & 1 & 0 & -\sqrt{2} & 0 & \sqrt{2} & 0 & -\sqrt{2} & \sqrt{2} & \dots \end{pmatrix}^T. \quad (\text{B.28})$$

Following Subsection 3.2.1, the output matrix is equal to $\mathbf{C}_{\text{fc}} = \mathbf{B}_{\text{fc}}^T$. The input matrix in the second-order representation is given by

$$\mathbf{B}_{\text{sc}} = \frac{1}{\sqrt{\varepsilon L}} \begin{pmatrix} 1 & \sqrt{2} & \sqrt{2} & \sqrt{2} & \sqrt{2} & \dots \\ 1 & -\sqrt{2} & \sqrt{2} & -\sqrt{2} & \sqrt{2} & \dots \end{pmatrix}^T. \quad (\text{B.29})$$

The corresponding output matrix is obtained by $\mathbf{C}_{\text{sc}} = \mathbf{B}_{\text{sc}}^T$.

¹The third index of the interaction coefficients is neglected because only one 2D port mode is considered per waveguide port.

C Miscellaneous

This chapter examines the accuracy and the convergence of 3D eigenmode expansions. Furthermore, Kirchhoff's circuit laws are derived from field continuity constraints and properties of negative-semidefinite matrices, which are relevant to this thesis, are discussed.

C.1 Accuracy and Convergence of Eigenmode Expansions

This section discusses accuracy and convergence properties of 3D eigenmode expansions. Firstly, the order of approximation of 3D eigenmode expansions is examined by means of a theoretical consideration. Subsequently, the convergence properties of a 3D eigenmode expansion is examined by a concrete application example. In other words, the error in the electric field arising from a truncated series expansion is investigated in dependence on the number of 3D eigenmodes used.

C.1.1 Order of Approximation of Electric Fields

To investigate the order of approximation of an electric field arising from a truncated eigenmode expansion, the ansatz (3.18) is transformed into frequency domain:

$$\underline{\mathbf{E}}(\mathbf{r}) = \sum_{n=1}^{\infty} \frac{\tilde{\mathbf{E}}_n(\mathbf{r})}{\sqrt{2W_n}} \underline{x}_n. \quad (\text{C.1})$$

The complex-valued weighting coefficients \underline{x}_n (not to be confused with the x coordinate) are dependent on the excitation conditions at the waveguide ports. Expressing (3.33) for the n th weighting coefficient delivers

$$(j\omega)^2 \underline{x}_n = -\tilde{\omega}_n^2 \underline{x}_n + j\omega \mathbf{b}_{\text{sc},n} \underline{\mathbf{i}}, \quad (\text{C.2})$$

where $\mathbf{b}_{\text{sc},n}$ is the n th row of the matrix \mathbf{B}_{sc} . Recall that the matrix contains the constant terms $h_{n,p,m}$ which are determined by the interaction integrals between the n th 3D eigenmode and all considered 2D waveguide port modes. The identity (C.2) can be resorted to

$$\underline{x}_n = \frac{j\omega}{(j\omega)^2 + \tilde{\omega}_n^2} \mathbf{b}_{\text{sc},n} \underline{\mathbf{i}}. \quad (\text{C.3})$$

This statement is used to replace the complex weighting factors in (C.1):

$$\begin{aligned} \underline{\mathbf{E}}(\mathbf{r}) = & \sum_{n=1}^N \frac{\tilde{\mathbf{E}}_n(\mathbf{r})}{\sqrt{2W_n}} \frac{j\omega}{\tilde{\omega}_n^2 - \omega^2} \mathbf{b}_{\text{sc},n} \mathbf{i} \\ & + \underbrace{\sum_{n=N+1}^{\infty} \frac{\tilde{\mathbf{E}}_n(\mathbf{r})}{\sqrt{2W_n}} \frac{j\omega}{\tilde{\omega}_n^2 - \omega^2} \mathbf{b}_{\text{sc},n} \mathbf{i}}_{\underline{\mathbf{E}}_{\text{res}}(\mathbf{r})}, \end{aligned} \quad (\text{C.4})$$

where $\underline{\mathbf{E}}_{\text{res}}(\mathbf{r})$ is referred to as residual term of the summation. The integer number N (i.e. the splitting of the summation) is chosen such that $\omega \ll \tilde{\omega}_n$ holds. In other words, the frequencies of the poles of $\underline{\mathbf{E}}_{\text{res}}(\mathbf{r})$ are much larger than the evaluation frequency ω , so that $\underline{\mathbf{E}}_{\text{res}}(\mathbf{r})$ is a continuous function in ω . In that case, the frequency dependence of the residual of the electric field is expressible in terms of the Taylor series expansion:

$$\frac{j\omega}{\tilde{\omega}_n^2 - \omega^2} = \sum_{k=1}^{\infty} \frac{j}{\tilde{\omega}_n} (\bar{\omega}_n)^{2k-1} = \frac{j}{\tilde{\omega}_n} \left(\bar{\omega}_n + \underbrace{\bar{\omega}_n^3 + \bar{\omega}_n^5 + \dots}_{\mathcal{O}(\bar{\omega}_n^3)} \right), \quad (\text{C.5})$$

where $\bar{\omega}_n = \omega/\tilde{\omega}_n \ll 1$ is the angular frequency normalized with respect to the angular resonant frequency of the n th eigenmode. As $\bar{\omega}_n$ is much smaller than one, the inequalities $\bar{\omega}_n \gg \bar{\omega}_n^3 \gg \bar{\omega}_n^5$ hold. The symbol $\mathcal{O}(\bar{\omega}_n^3)$ indicates that the term with the smallest exponent of the underbraced sum is equal to three. This term governs the underbraced sum since $\bar{\omega}_n^3$ is much larger than the remaining terms. In other words, terms with exponents larger than three are negligible and the underbraced sum is approximately proportional to $\bar{\omega}_n^3$. Using the Taylor series expansion (C.5) to replace the frequency dependence of the residual electric field gives

$$\underline{\mathbf{E}}_{\text{res}}(\mathbf{r}) = \sum_{n=N+1}^{\infty} \frac{\tilde{\mathbf{E}}_n(\mathbf{r})}{\sqrt{2W_n}} \frac{j\bar{\omega}_n}{\tilde{\omega}_n} \mathbf{b}_{\text{sc},n} \mathbf{i} + \mathcal{O}(\bar{\omega}_n^3). \quad (\text{C.6})$$

If only a finite number of terms is used for the upper series expansion, terms which are linear in $\bar{\omega}_n$ are omitted. These terms are indicated by $\mathcal{O}(\bar{\omega}_n)$. The linear terms are governing the truncation error and therefore the terms contained in $\mathcal{O}(\bar{\omega}_n^3)$ can be neglected:

$$\underline{\mathbf{E}}_{\text{res}}(\mathbf{r}) = \sum_{n=N+1}^{N_e} \frac{\tilde{\mathbf{E}}_n(\mathbf{r})}{\sqrt{2W_n}} \frac{j\bar{\omega}_n}{\tilde{\omega}_n} \mathbf{b}_{\text{sc},n} \mathbf{i} + \mathcal{O}(\bar{\omega}_n). \quad (\text{C.7})$$

This equation shows that the approximation of the residual of the electric field by means of a truncated 3D eigenmode expansion is a first-order approximation in ω . Thus, the approximation of the electric field $\underline{\mathbf{E}}(\mathbf{r})$ is a first-order approximation in ω as well.

C.1.2 A Practical Convergence Consideration of Electric Fields

To check the convergence of a 3D eigenmode expansion, the electric field in the rectangular waveguide shown in Figure B.1 is expanded by means of 3D eigenmodes of the structure. The 3D eigenmode expansion is based on the results of Appendix B.4. The electromagnetic fields in the waveguide are determined for the excitation conditions $\underline{I}_1 = 1 \text{ A exp}(j2\pi ft)$ and $\underline{I}_2 = 1 \text{ A exp}(j2\pi ft)$ with $f = 7.5 \text{ GHz}$. The modal currents \underline{I}_1 and \underline{I}_2 refer to the TE_{10} port modes at both ends of the structure. The quantity

$$\epsilon_{\text{err}}(N_e) = \frac{\|\underline{V}(z) - \sum_{n=1}^{N_e} \frac{1}{\sqrt{2W_n}} \tilde{V}_n(z) \underline{x}_n\|}{\|\underline{V}(z)\|} \quad (\text{C.8})$$

is used as an error measure for the 3D eigenmode expansion which is truncated after N_e terms. The involved norm is defined in terms of

$$\|\dots\| = \int_0^L |\dots| dz. \quad (\text{C.9})$$

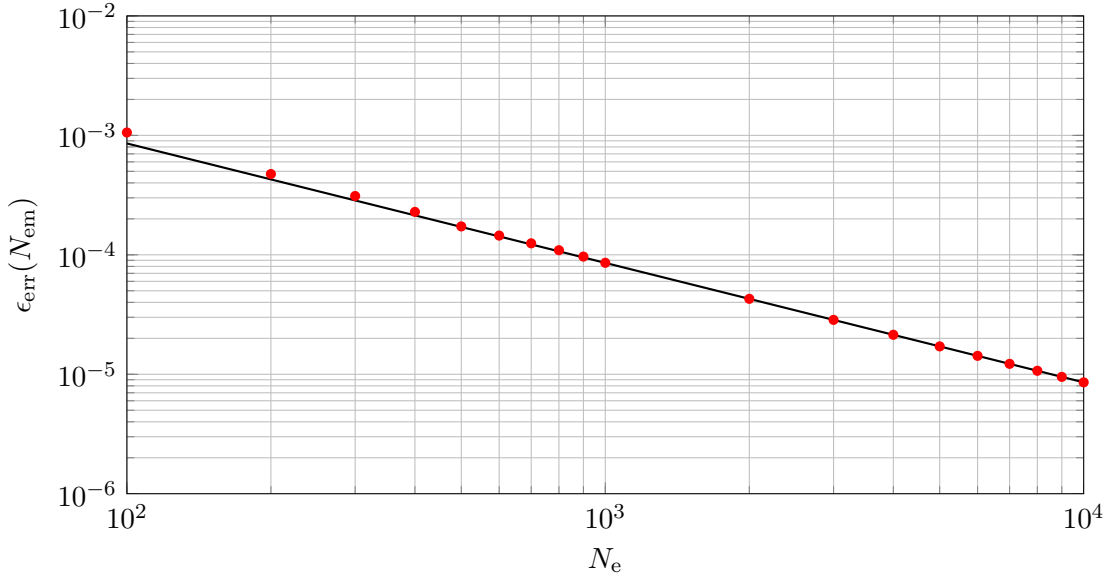


Figure C.1: Log-log plot of the relative error (red dots) of the 3D eigenmode expansion in the rectangular waveguide in dependence on the number N_e of used eigenmodes (red dots). The solid black line is determined by the function $c_s N_e^{-1}$ and is plotted for purposes of comparison. The scaling constant c_s is chosen such that the black line coincides with $\epsilon_{\text{err}}(N_e)$ for $N_e = 10^4$. The diagram shows that in the limit the error of the 3D eigenmode expansion shows a N_e^{-1} dependence.

For the sake of completeness, it is remarked that the practical convergence consideration is performed for a rectangular waveguide with the width $a = 22.86$ mm, the height $b = 10.16$ mm, and the length $L = 100$ mm. However, the convergence properties do not depend on these concrete dimensions.

Figure C.1 shows a log-log plot of the relative error $\epsilon_{\text{err}}(N_e)$ of the 3D eigenmode expansion depending on the number N_e of eigenmodes (red dots). The solid black line is computed by $c_s N_e^{-1}$. The scaling constant c_s is selected such that the black solid line agrees with $\epsilon_{\text{err}}(N_e)$ for $N_e = 10^4$. The purpose of this line is to illustrate the slope of a function with the exponent minus one. Figure C.1 shows that in the limit the error of the 3D eigenmode expansion is inversely proportional to the number of eigenmodes used, i.e. $\epsilon_{\text{err}}(N_e) = c_s N_e^{-1}$ if N_e is sufficiently large. Doubling the number of 3D eigenmodes leads to a reduction of the error by a factor of two.

C.1.3 Impedance Parameters based on Eigenmode Expansions

This subsection discusses the error in the impedance parameters which are obtained from truncated eigenmodes expansion (3.18), i.e. from an incomplete set of eigenmodes. For this purpose, the impedance parameters of the waveguide with constant cross section in Figure B.1 are regarded. Similarly to the previous derivations, this part of the appendix focuses on TE₁₀ port modes. To compute the impedance matrix based on the incomplete eigenmode expansion with N_e 3D eigenmodes, the frequency-domain transfer function of the second-order state-space system for the waveguide (see Appendix B.4) is determined:

$$\underline{\mathbf{Z}}(j\omega) = \mathbf{B}_s^T ((j\omega)^2 \mathbf{I} - \mathbf{A}_s)^{-1} \mathbf{B}_s j\omega. \quad (\text{C.10})$$

The expression in the outer parenthesis gives the diagonal matrix

$$((j\omega)^2 \mathbf{I} - \mathbf{A}_s) = \text{diag}(\tilde{\omega}_1^2 - \omega^2, \tilde{\omega}_2^2 - \omega^2, \tilde{\omega}_3^2 - \omega^2, \dots), \quad (\text{C.11})$$

where $\tilde{\omega}_n$ is defined by (B.23). The inversion of the matrix and its multiplication from the right-hand side with $j\omega$ and \mathbf{B}_s given by (B.29) results in the matrix

$$((j\omega)^2 \mathbf{I} - \mathbf{A}_s)^{-1} \mathbf{B}_s j\omega = \frac{1}{\sqrt{\epsilon L}} \begin{pmatrix} \frac{j\omega}{\tilde{\omega}_1^2 - \omega^2} & \frac{j\omega}{\tilde{\omega}_1^2 - \omega^2} \\ \frac{j\omega}{\tilde{\omega}_2^2 - \omega^2} \sqrt{2} & -\frac{j\omega}{\tilde{\omega}_2^2 - \omega^2} \sqrt{2} \\ \frac{j\omega}{\tilde{\omega}_3^2 - \omega^2} \sqrt{2} & \frac{j\omega}{\tilde{\omega}_3^2 - \omega^2} \sqrt{2} \\ \vdots & \vdots \end{pmatrix}. \quad (\text{C.12})$$

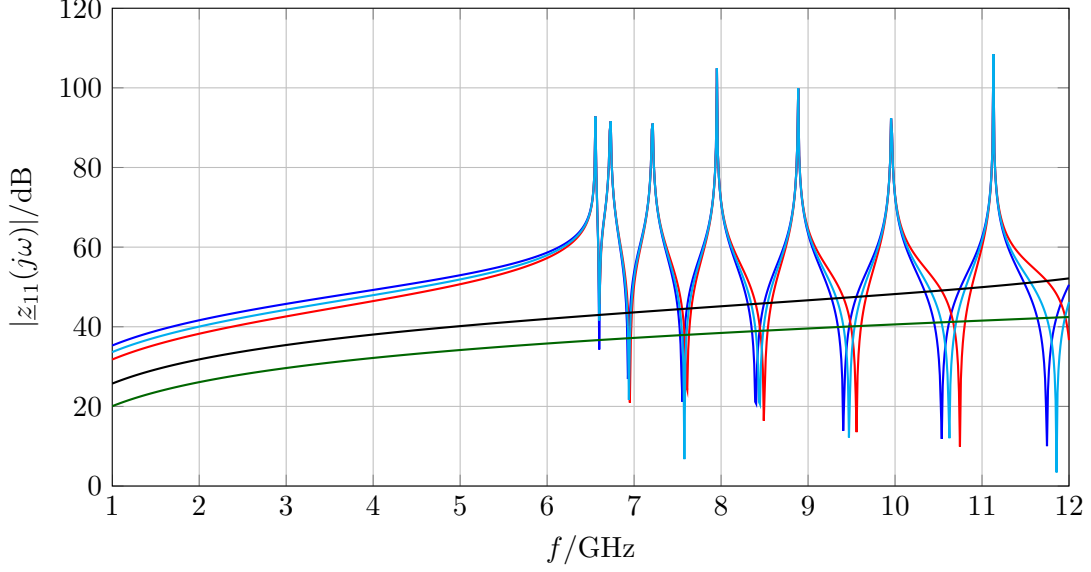


Figure C.2: Impedance parameter $\underline{z}_{11}(j\omega)$ of the waveguide with constant cross section depicted in Figure B.1. The dimensions of the waveguide are given by $L = 100$ mm, $a = 22.86$ mm, and $b = 10.16$ mm. The blue curve (reference) is obtained by (B.13), the solid red curve by (C.13) accounting for eight eigenmodes and the cyan curve by (C.13) accounting for sixteen eigenmodes. The black curve shows the absolute value of the difference between the blue and the red curve whereas the green curve depicts the difference between the blue and the cyan curve. A direct correspondence to the plot is available in [42, p. 94, Figure 6.4].

The multiplication of this equation with \mathbf{B}_s^T from the left-hand side yields the impedance matrix

$$\begin{aligned} \underline{\mathbf{Z}}(j\omega) = & \frac{1}{\varepsilon L} \left(\frac{j\omega}{\tilde{\omega}_1^2 - \omega^2} \begin{pmatrix} 1 & 1 \\ 1 & 1 \end{pmatrix} + \frac{j\omega}{\tilde{\omega}_2^2 - \omega^2} \begin{pmatrix} 2 & -2 \\ -2 & 2 \end{pmatrix} \right. \\ & + \frac{j\omega}{\tilde{\omega}_3^2 - \omega^2} \begin{pmatrix} 2 & -2 \\ -2 & 2 \end{pmatrix} + \dots + \frac{j\omega}{\tilde{\omega}_n^2 - \omega^2} \begin{pmatrix} 2 & -2 \\ -2 & 2 \end{pmatrix} \\ & \left. + \dots + \frac{j\omega}{\tilde{\omega}_{N_e}^2 - \omega^2} \begin{pmatrix} 2 & -2 \\ -2 & 2 \end{pmatrix} \right) \end{aligned} \quad (\text{C.13})$$

for the waveguide with constant cross section. The impedance matrix is determined based on N_e 3D eigenmodes. Height a and length b of the waveguide do not explicitly occur in the equation but are hidden in the resonant angular frequencies $\tilde{\omega}_n$ of the n th 3D eigenmode. Note that (C.13) is a special case of (3.60).

Figure C.2 presents impedance parameter emerging from an incomplete eigenmode expansion with $N_e = 8$ 3D eigenmodes (red curve) and $N_e = 16$ 3D eigenmodes

(cyan curve) in direct comparison with the impedance parameter obtained from (B.13) (blue curve). Following (3.60), the resonant frequencies of the 3D eigenmodes correspond to poles in the impedance spectra. Since at least $N_e = 8$ 3D eigenmodes are considered in the series expansion, all seven poles are observable in the approximations of $\underline{z}_{11}(j\omega)$ in Figure C.2. In contrast to the poles, the roots differ from the reference values. However, the locations of the approximated roots move to the locations of the reference roots as the number of 3D eigenmodes increases. The incorrect location of the roots and the deviations in the interval 1 GHz to 6 GHz are a result of the truncated series expansions. The absolute value of the difference between the blue and the red curve is shown as black line whereas the absolute value of the difference between the blue and the cyan line is shown in terms of the green line. These differences (or the truncation errors) correspond to the residual terms $\underline{\mathbf{E}}_{\text{res}}(\mathbf{r})$ in (C.4). Thus, the differences are smooth and bounded functions in $j\omega$ since they do not have poles in the considered frequency range (cf. Appendix C.1.1).

Despite the fact that the overall agreement between the reference impedance parameter and its approximation is remarkable for $N_e = 16$, it does not describe the properties of the waveguide structure in an appropriate manner: The location of the poles poorly agrees with the reference solution. Thus, it is not sufficient to restrict the model order reduction to eigenmodes whose eigenvalues correspond to resonant frequencies in the interval of interest (cf. Section 4.2). As a matter of fact, the snapshot matrix (4.9) aims to approximate the residual terms using a small number of poles with frequencies larger than ω_{max} .

C.2 Kirchhoff's Circuit Laws Emerging from Continuity Constraints

The applied circuit laws do not hold generally: Kirchhoff's voltage law demands the change in time of the magnetic flux linking through closed loops to be zero. Kirchhoff's current law assumes that currents which flow into one end of a conductor directly flow out the other end, i.e. the total charge in the conductor does not change in time. These assumptions typically hold if the wavelength is orders of magnitude larger than the size of the structure under concern. This assumption is not valid for RF structures, because they are operated at frequencies at which the resulting wavelengths are often smaller than the structure itself. Nonetheless, Kirchhoff's circuit laws are applicable to concatenate the segments of RF structures as it is proposed in Section 4.3. The circuit laws are used such that they express the continuity of tangential electric and magnetic fields on the decomposition planes. This statement is subsequently clarified with the aid of an example. Figure C.3(a) shows a close-up of two internal waveguide ports which are connected to each other. The plane Γ_{prt} of the two waveguide ports is indicated by the dashed black line.

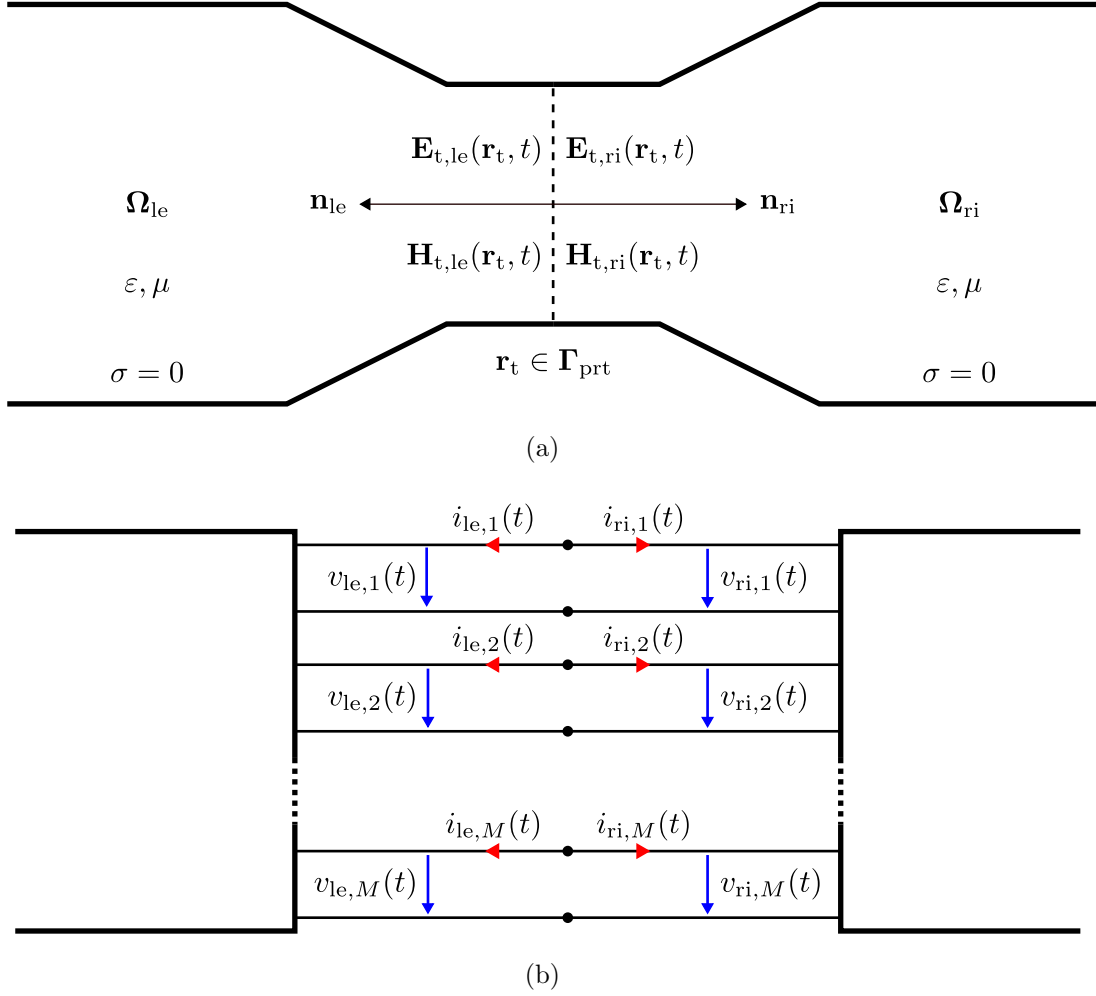


Figure C.3: (a) Cutplane of two internal waveguide ports which are connected to each other. The domains Ω_{le} and Ω_{ri} of the left and the right segment are filled with an insulator (conductivity $\sigma = 0$) with the permittivity ε and the permeability μ . The normal vectors on the common waveguide port plane Γ_{prt} (dashed line) are denoted by \mathbf{n}_{le} and \mathbf{n}_{ri} . The electric and magnetic field on the port plane of the left segment are denoted by $\mathbf{E}_{\text{t,le}}(\mathbf{r}_t, t)$ and $\mathbf{H}_{\text{t,le}}(\mathbf{r}_t, t)$ whereas the port quantities of the right segment are labeled as $\mathbf{E}_{\text{t,ri}}(\mathbf{r}_t, t)$ and $\mathbf{H}_{\text{t,ri}}(\mathbf{r}_t, t)$. (b) Abstract counterpart of the decomposition plane shown in (a). Voltages and currents of the left segment are denoted by $v_{\text{le},m}(t)$ and $i_{\text{le},m}(t)$ whereas voltages and currents of the right segment are marked by $v_{\text{ri},m}(t)$ and $i_{\text{ri},m}(t)$. Terminals which correspond to the same field patterns $\mathbf{L}_{\text{t},m}(\mathbf{r}_t)$ are connected to each other. The diagram solely accounts for M port modes.

The tangential electric field on the internal waveguide port of the left segment is denoted by $\mathbf{E}_{\text{t,le}}(\mathbf{r}_t, t)$ and the tangential electric field on the internal waveguide port of the right segment by $\mathbf{E}_{\text{t,ri}}(\mathbf{r}_t, t)$. The tangential magnetic fields on the waveguide

ports are given by $\mathbf{H}_{t,le}(\mathbf{r}_t, t)$ and $\mathbf{H}_{t,ri}(\mathbf{r}_t, t)$, respectively. The vectors \mathbf{n}_{le} and \mathbf{n}_{ri} are normal with respect to the internal port plane and point inside the left and the right segment. On account of the continuity of tangential electric and magnetic fields [33, 54, 55], the constraints

$$\mathbf{E}_{t,le}(\mathbf{r}_t, t) = \mathbf{E}_{t,ri}(\mathbf{r}_t, t), \quad (\text{C.14})$$

$$\mathbf{H}_{t,le}(\mathbf{r}_t, t) = \mathbf{H}_{t,ri}(\mathbf{r}_t, t) \quad (\text{C.15})$$

have to hold for concatenated internal waveguide ports (see Figure C.3(a)). Following Section 3.1, tangential electric and magnetic field can be expressed in terms of eigenfunctions $\mathbf{L}_{t,m}(\mathbf{r}_t)$ of the 2D Helmholtz equation (2.46) on the cross section of the waveguide ports. Using the expansion (3.3) for the tangential electric fields on the waveguide port planes in (C.14) gives

$$\sum_{m=1}^{\infty} \mathbf{L}_{t,m}(\mathbf{r}_t) v_{le,m}(t) = \sum_{m=1}^{\infty} \mathbf{L}_{t,m}(\mathbf{r}_t) v_{ri,m}(t), \quad (\text{C.16})$$

where $v_{le,m}(t)$ and $v_{ri,m}(t)$ are the modal voltages which correspond to the left and the right waveguide port, respectively. Note that the 2D eigenfunctions $\mathbf{L}_{t,m}(\mathbf{r}_t)$ can be used for both field expansions, because waveguide ports which arise from the decomposition have the same cross section (see Section 4.1). Therefore, the eigenfunctions of the 2D Helmholtz equation are the same for both waveguide ports. Multiplying (C.16) with the ξ th eigenfunction $\mathbf{L}_{t,\xi}(\mathbf{r}_t)$ and integrating over the port plane yields

$$\sum_{m=1}^{\infty} \iint_{\Gamma_{prt}} \mathbf{L}_{t,\xi}(\mathbf{r}_t) \cdot \mathbf{L}_{t,m}(\mathbf{r}_t) dA v_{le,m}(t) = \sum_{m=1}^{\infty} \iint_{\Gamma_{prt}} \mathbf{L}_{t,\xi}(\mathbf{r}_t) \cdot \mathbf{L}_{t,m}(\mathbf{r}_t) dA v_{ri,m}(t). \quad (\text{C.17})$$

On account of the orthonormality condition (2.49), the integrals are equal to one for $m = \xi$ and are equal to zero otherwise. Therefore, (C.17) can be simplified to

$$v_{le,m}(t) = v_{ri,m}(t). \quad (\text{C.18})$$

This statement directly corresponds to the application of Kirchoff's voltage law to the network in Figure C.3(b).

Substituting the tangential magnetic fields on the waveguide port planes in (C.15) with the expansion (3.4) yields

$$\sum_{m=1}^{\infty} \mathbf{n}_{le} \times \mathbf{L}_{t,m}(\mathbf{r}_t) i_{le,m}(t) = \sum_{m=1}^{\infty} \mathbf{n}_{ri} \times \mathbf{L}_{t,m}(\mathbf{r}_t) i_{ri,m}(t). \quad (\text{C.19})$$

Multiplying (C.19) from the left-hand side with $\mathbf{n}_{le} \times$ delivers

$$\sum_{m=1}^{\infty} \underbrace{\mathbf{n}_{le} \times \mathbf{n}_{le} \times \mathbf{L}_{t,m}(\mathbf{r}_t)}_{-\mathbf{L}_{t,m}(\mathbf{r}_t)} i_{le,m}(t) = \sum_{m=1}^{\infty} \underbrace{\mathbf{n}_{le} \times \mathbf{n}_{ri} \times \mathbf{L}_{t,m}(\mathbf{r}_t)}_{\mathbf{L}_{t,m}(\mathbf{r}_t)} i_{ri,m}(t). \quad (\text{C.20})$$

The operation $\mathbf{n}_{le} \times \mathbf{L}_{t,m}(\mathbf{r}_t)$ rotates the field pattern $\mathbf{L}_{t,m}(\mathbf{r}_t)$ around the normal vector \mathbf{n}_{le} with angle of $\pi/2$. Thus, $\mathbf{n}_{le} \times \mathbf{n}_{le} \times \mathbf{L}_{t,m}(\mathbf{r}_t)$ corresponds to two rotations with angle of $\pi/2$, i.e. a rotation with angle of π . To accomplish these two rotations, the field pattern of $\mathbf{L}_{t,m}(\mathbf{r}_t)$ is simply multiplied with minus one. The operation $\mathbf{n}_{ri} \times \mathbf{L}_{t,m}(\mathbf{r}_t)$ rotates the field pattern $\mathbf{L}_{t,m}(\mathbf{r}_t)$ around the normal vector \mathbf{n}_{ri} with angle of $\pi/2$. Due to the different directions of the parallel normal vectors \mathbf{n}_{le} and \mathbf{n}_{ri} , the operation $\mathbf{n}_{le} \times \mathbf{n}_{ri} \times \mathbf{L}_{t,m}(\mathbf{r}_t)$ corresponds to a rotation with angle of $\pi/2$ followed by a rotation with angle of $-\pi/2$ so that the original field pattern $\mathbf{L}_{t,m}(\mathbf{r}_t)$ results. Multiplying (C.20) from the left-hand side with the ξ th eigenfunction $\mathbf{L}_{t,\xi}(\mathbf{r}_t)$ and integrating over the waveguide port plane gives

$$-\sum_{m=1}^{\infty} \iint_{\mathbf{r}_{prt}} \mathbf{L}_{t,\xi}(\mathbf{r}_t) \cdot \mathbf{L}_{t,m}(\mathbf{r}_t) dA i_{le,m}(t) = \sum_{m=1}^{\infty} \iint_{\mathbf{r}_{prt}} \mathbf{L}_{t,\xi}(\mathbf{r}_t) \cdot \mathbf{L}_{t,m}(\mathbf{r}_t) dA i_{ri,m}(t). \quad (\text{C.21})$$

Again, on account of the orthonormality condition (2.49), the integrals are equal to one for $m = \xi$ and are equal to zero otherwise. Consequently, (C.21) can be simplified to

$$-i_{le,m}(t) = i_{ri,m}(t). \quad (\text{C.22})$$

This equation directly corresponds to the application of Kirchoff's current law to the network in Figure C.3(b).

C.3 Symmetric Negative-Semidefinite Matrices

This section discusses properties of symmetric negative-semidefinite matrices with real-valued coefficients. These properties are predominantly required in Chapter 3 for stability considerations of state-space models.

A matrix $\mathbf{A} \in \mathbb{R}^{N \times N}$ is called symmetric negative semidefinite if the symmetry condition

$$\mathbf{A} = \mathbf{A}^T \quad (\text{C.23})$$

and the negative-semidefiniteness condition

$$\mathbf{x}^T \mathbf{A} \mathbf{x} \leq 0 \quad \forall \quad \mathbf{x} \in \mathbb{R}^N \quad (\text{C.24})$$

are satisfied. Here, N denotes the number of rows and columns of \mathbf{A} and the number of rows of \mathbf{x} .

C.3.1 Generation of Negative-Semidefinite Matrices

If a quadratic matrix $\mathbf{A} \in \mathbb{R}^{N \times N}$ is generated by a rectangular matrix $\mathbf{R} \in \mathbb{R}^{M \times N}$ with M rows and N columns as follows

$$\mathbf{A} := -\mathbf{R}^T \mathbf{R}, \quad (\text{C.25})$$

the resulting quadratic matrix \mathbf{A} is symmetric negative semidefinite. While the symmetry of \mathbf{A} is directly observable from the definition (C.25), the negative semidefiniteness is shown by substituting (C.25) in (C.24):

$$\mathbf{x}^T (-\mathbf{R}^T \mathbf{R}) \mathbf{x} = -(\mathbf{x}^T \mathbf{R}^T) (\mathbf{R} \mathbf{x}) = -\underbrace{(\mathbf{R} \mathbf{x})^T}_{\mathbf{y}^T} \underbrace{(\mathbf{R} \mathbf{x})}_{\mathbf{y}} \leq 0 \quad (\text{C.26})$$

The vector $\mathbf{y} \in \mathbb{R}^M$ is the zero vector $\mathbf{y} = \mathbf{0}$, if \mathbf{x} is in the null space of \mathbf{R} or $\mathbf{x} = \mathbf{0}$. Otherwise $\mathbf{y} \neq \mathbf{0}$ holds. Since \mathbf{y} is real-valued, the scalar $\mathbf{y}^T \mathbf{y}$ is larger than or equal to zero. Therefore, the expression on the left-hand side of (C.26) is smaller than or equal to zero.

It is worth to mention that the state matrices of the presented second-order systems are expressible in terms of (C.25). For the state matrix \mathbf{A}_{sc} arising from the continuous case, the matrix \mathbf{R} is given by

$$\mathbf{R}_{\text{sc}} = \text{diag}(\tilde{\omega}_1, \tilde{\omega}_2, \dots, \tilde{\omega}_n, \dots, \tilde{\omega}_{N_e}), \quad (\text{C.27})$$

for the state matrix obtained from FIT by

$$\mathbf{R}_{\text{sd}} = \mathcal{M}_{\mu}^{-1/2} \mathcal{C} \mathcal{M}_{\epsilon}^{-1/2}, \quad (\text{C.28})$$

for the state matrix \mathbf{A}_{sr} created by the model order reduction by

$$\mathbf{R}_{\text{sr}} = \mathbf{R}_{\text{s}} \mathbf{V}_{\text{sr}}, \quad (\text{C.29})$$

and for the state matrix \mathbf{A}_{sl} arising from the concatenation by

$$\mathbf{R}_{\text{sl}} = \mathbf{R}_{\text{sb}} \mathbf{K} \mathbf{M}, \quad (\text{C.30})$$

where

$$\mathbf{R}_{\text{sb}} = \text{diag}(\mathbf{R}_{\text{sr},1}, \mathbf{R}_{\text{sr},2}, \dots, \mathbf{R}_{\text{sr},r}, \dots, \mathbf{R}_{\text{sr},R}). \quad (\text{C.31})$$

If the state-space model for the r th segment is obtained by analytical considerations, \mathbf{R}_{s} is equal to the matrix \mathbf{R}_{sc} . If the state-space model for the r th segment arises from the discretization approach, \mathbf{R}_{s} is equal to the matrix \mathbf{R}_{sd} .

C.3.2 Eigenvalues of Symmetric Negative-Semidefinite Matrices

The eigenvalues λ_n of real-valued symmetric matrices are real-valued as well and the corresponding eigenvectors $\mathbf{v}_n \in \mathbb{R}^N$ can be selected such that they form a complete set of orthonormal basis vectors [57, 82]:

$$\mathbf{v}_n^T \mathbf{v}_i = \begin{cases} 1 & \text{for } n = i, \\ 0 & \text{else.} \end{cases} \quad (\text{C.32})$$

In that case, each vector $\mathbf{x} \in \mathbb{R}^N$ can be expressed in terms of the eigenvectors \mathbf{v}_n of \mathbf{A} as follows

$$\mathbf{x} = \sum_{n=1}^N w_n \mathbf{v}_n, \quad (\text{C.33})$$

where $w_n \in \mathbb{R}$ are scalar weighting coefficients. Substituting this expansion in (C.24) gives

$$\left(\sum_{n=1}^N w_n \mathbf{v}_n \right)^T \left(\sum_{i=1}^N w_i \underbrace{\mathbf{A} \mathbf{v}_i}_{\lambda_i \mathbf{v}_i} \right) \leq 0. \quad (\text{C.34})$$

This inequality is simplified by means of the orthonormality condition (C.32) to

$$w_n^2 \lambda_n \leq 0. \quad (\text{C.35})$$

For arbitrary \mathbf{x} the constant w_n^2 must be larger than zero. Therefore, all eigenvalues of symmetric negative-semidefinite matrices must be smaller than or equal to zero:

$$\lambda_n \leq 0. \quad (\text{C.36})$$

D Mesh Refinement Studies

This chapter presents mesh refinement studies for the discretization of the segments used in Chapter 5. The studies investigate the dependence of the resonant frequencies on the number N_p of primary grid nodes, i.e. $\tilde{f}_n(N_p)$. The resonant frequencies refer to an eigenmode problem with PMC boundaries on the waveguide port planes. The relative accuracy criterion

$$\epsilon_{\text{FIT}} = \max_n \left| \frac{\tilde{f}_{\text{ref},n} - \tilde{f}_n(N_p)}{\tilde{f}_{\text{ref},n}} \right| \quad (\text{D.1})$$

is used for the subsequent mesh refinement studies. It is a measure for the extent to which RF properties of the segments are influenced by the hexahedral discretization of the segments. The accuracy criterion is in fact the maximal absolute value of the relative error in the resonant frequencies. The criterion exclusively accounts for resonant frequencies $\tilde{f}_n(N_p)$ in the interval f_{min} to f_{max} . The reference resonant frequencies $\tilde{f}_{\text{ref},n}$ are obtained from the eigenmode computation with the largest number N_p of grid nodes, i.e. from the final run. In the final run, $\tilde{f}_{\text{ref},n} = \tilde{f}_n(N_p)$ holds and ϵ_{FIT} is always equal to zero. However, this does not mean that the error in the computation is equal to zero because the relative accuracy criterion (D.1) does not refer to the exact values of the resonant frequencies \tilde{f}_n of the segments. These frequencies are not available because closed analytical solutions of Maxwell's equations do not exist for the segments.

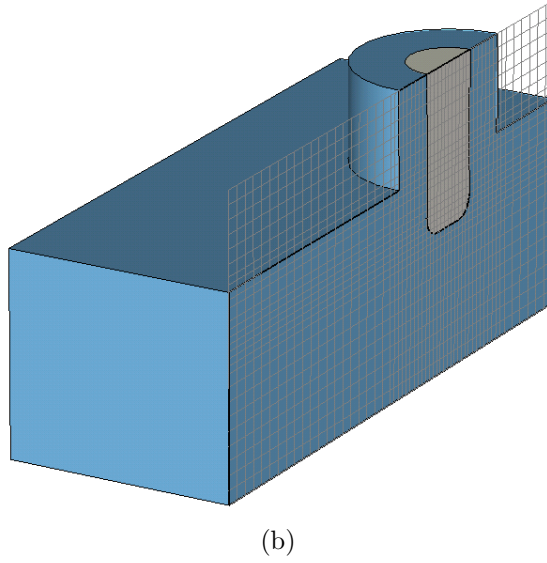
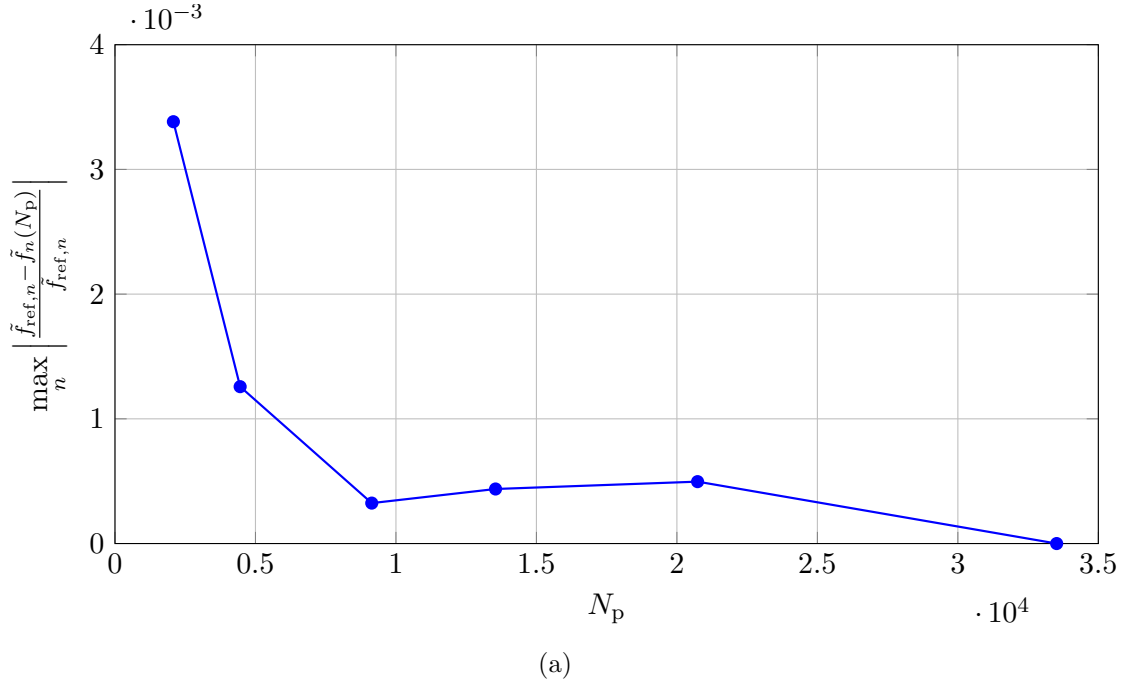
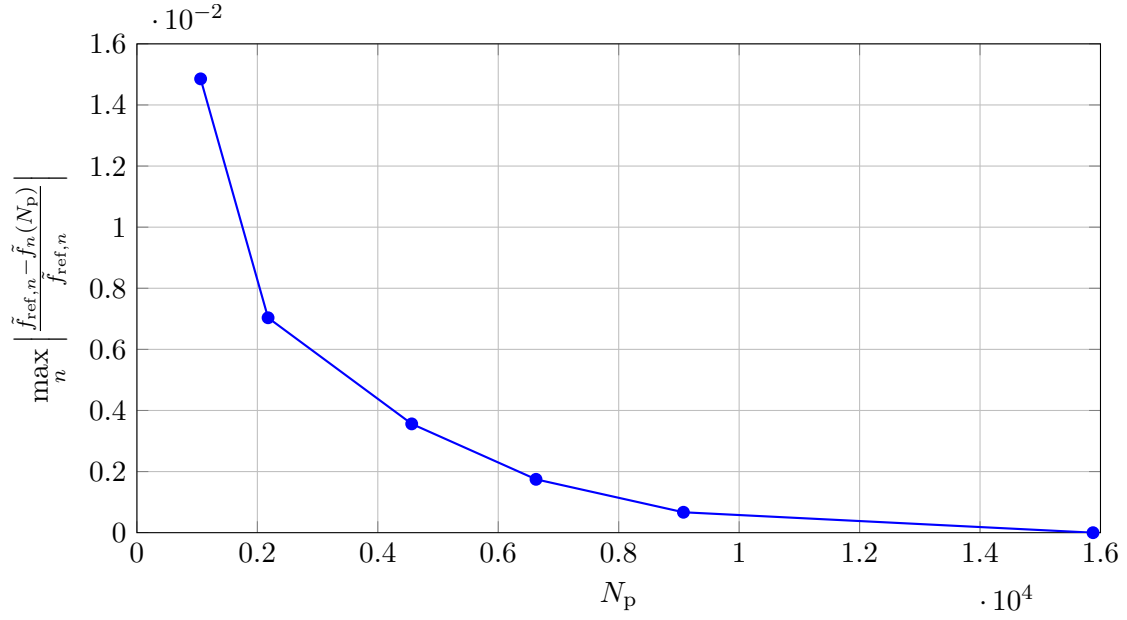
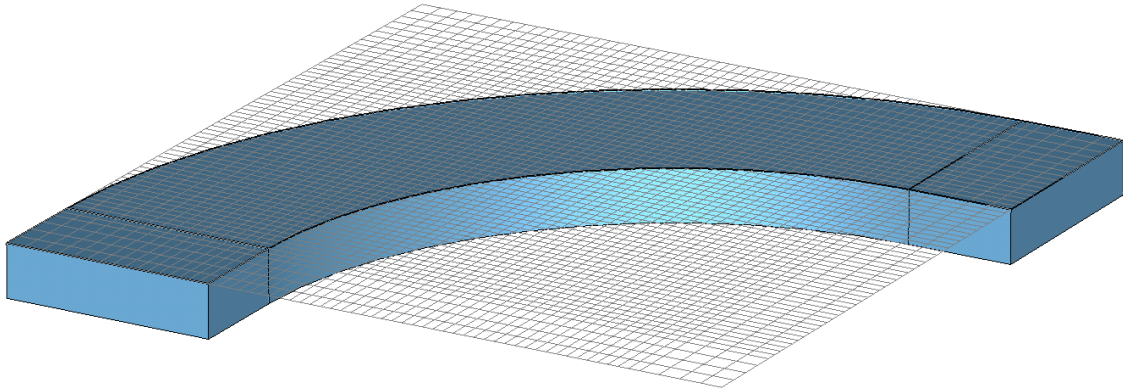


Figure D.1: (a) Mesh refinement study of the waveguide coupling probe which is used in Section 5.2. The dots refer to a mesh with 5, 7, 9, 11, 13, and 15 lines per wavelength. The considered frequency interval is 1 GHz to 12 GHz. The improvement for 15 lines per wavelength compared to 13 lines per wavelength approximately amounts to $5 \cdot 10^{-4}$. (b) Discretization of the waveguide coupling probe using 15 lines per wavelength ($N_p = 33,516$). The plane in which the mesh is depicted indicates the used symmetry plane.

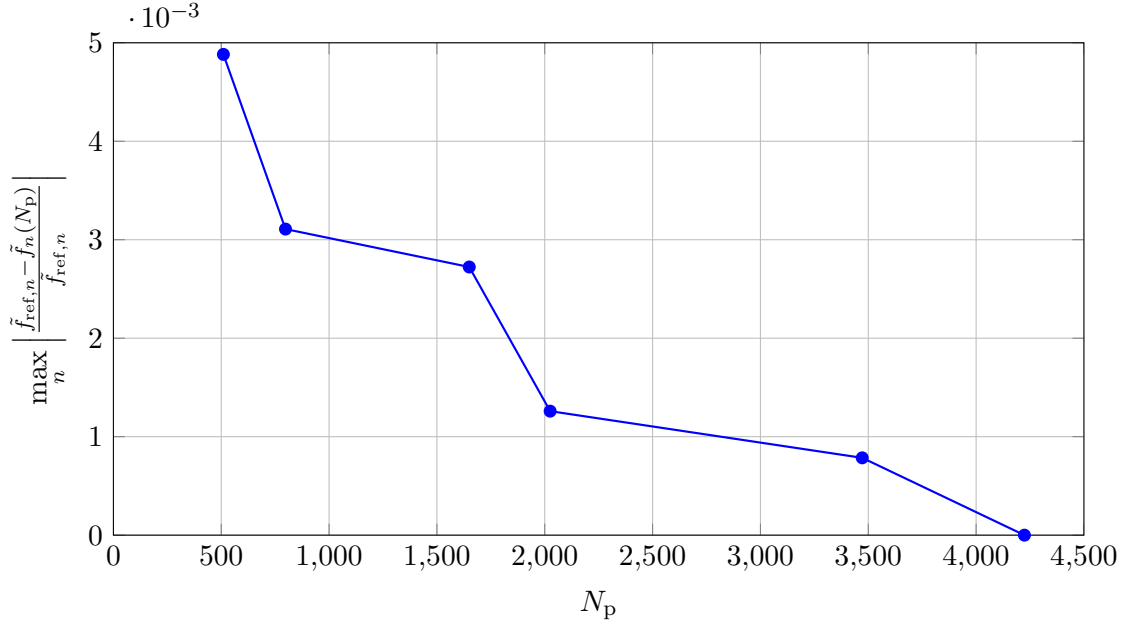


(a)

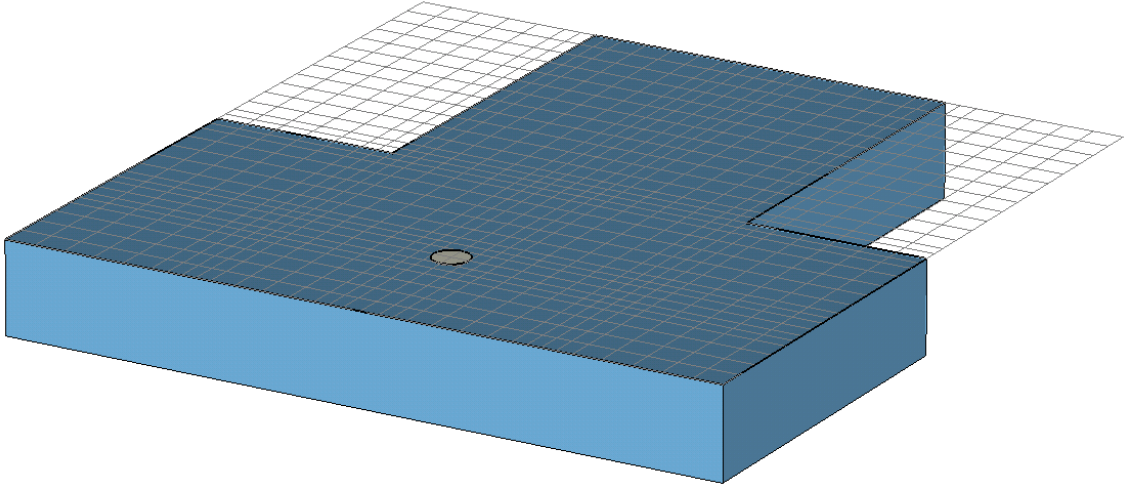


(b)

Figure D.2: (a) Mesh refinement study of the waveguide bending which is used in Section 5.3. The dots refer to a mesh with 5, 7, 9, 11, 13, and 15 lines per wavelength. The considered frequency interval is 1 GHz to 10 GHz. The improvement for 15 lines per wavelength compared to 13 lines per wavelength approximately amounts to $6.7 \cdot 10^{-4}$. (b) Discretization of the waveguide bending using 15 lines per wavelength ($N_p = 15,876$). The plane in which the mesh is depicted indicates the used symmetry plane.

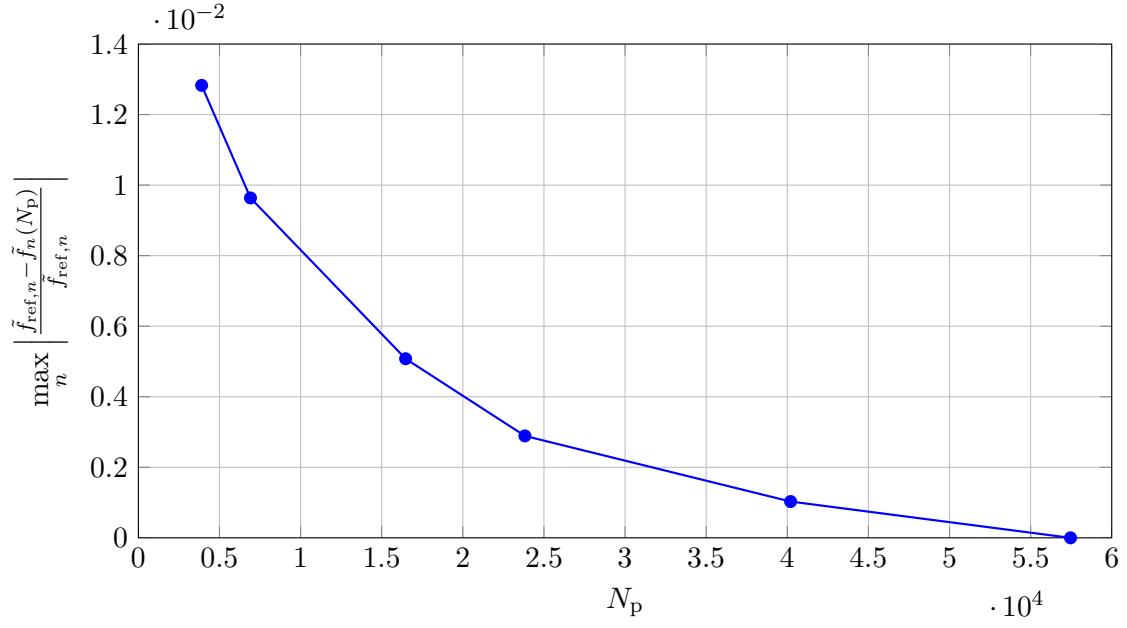


(a)

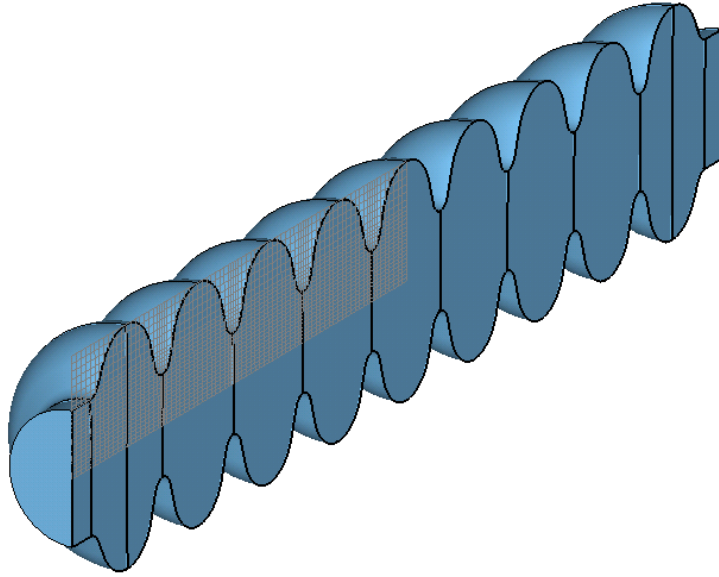


(b)

Figure D.3: (a) Mesh refinement study of the tee piece which is used in Section 5.3. The dots refer to a mesh with 5, 7, 9, 11, 13, and 15 lines per wavelength. The considered frequency interval is 1 GHz to 10 GHz. The improvement for 15 lines per wavelength compared to 13 lines per wavelength approximately amounts to $7.8 \cdot 10^{-4}$. (b) Discretization of the tee piece using 15 lines per wavelength ($N_p = 4,224$). The plane in which the mesh is depicted indicates the used symmetry plane.

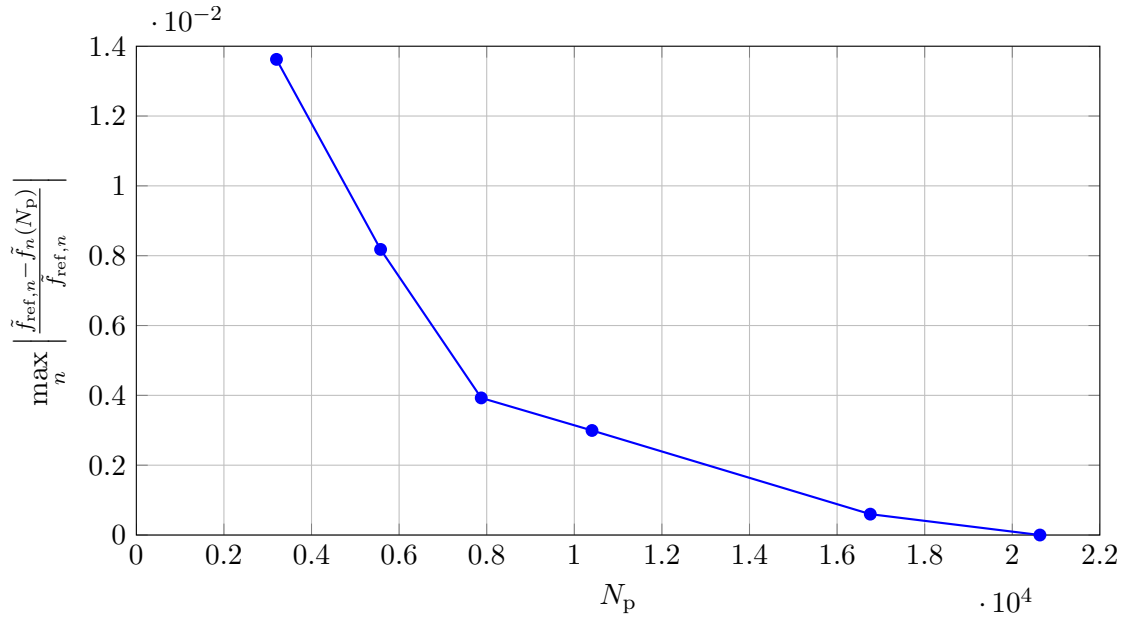


(a)

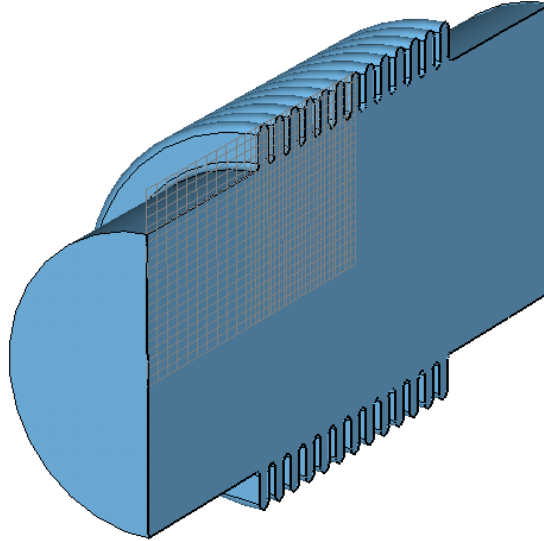


(b)

Figure D.4: (a) Mesh refinement study of the third harmonic cavity which is used in Section 5.4. The dots refer to a mesh with 5, 7, 9, 11, 13, and 15 lines per wavelength. The considered frequency interval is 1 GHz to 8.5 GHz. The improvement for 15 lines per wavelength compared to 13 lines per wavelength approximately amounts to $1 \cdot 10^{-3}$. (b) Discretization of the third harmonic cavity using 15 lines per wavelength ($N_p = 57,460$). The plane in which the mesh is shown indicates one of three used symmetry planes.

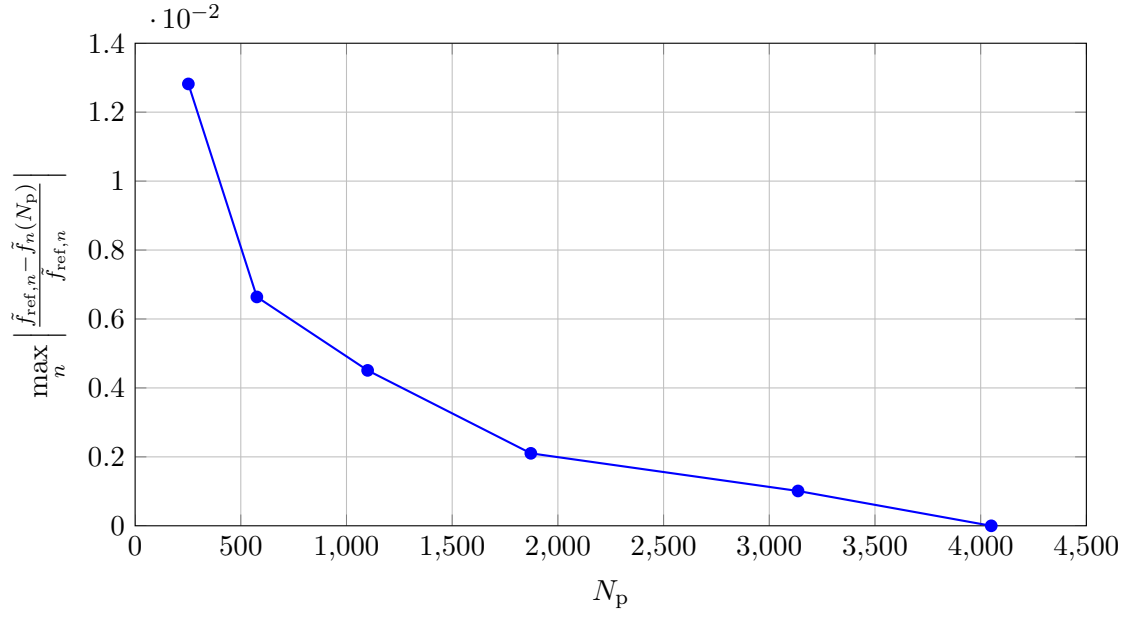


(a)

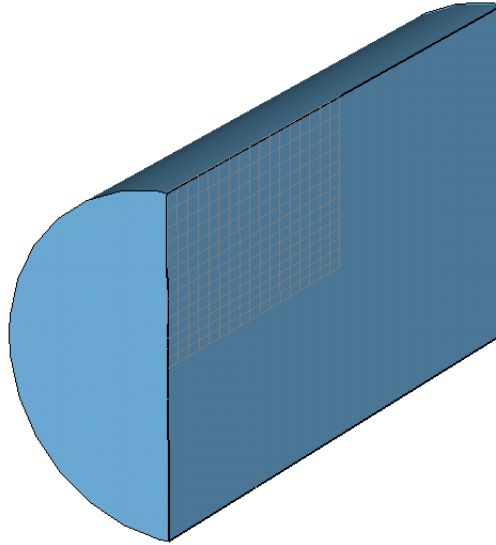


(b)

Figure D.5: (a) Mesh refinement study of the bellow which is used in Section 5.4. The dots refer to a mesh with 5, 7, 9, 11, 13, and 15 lines per wavelength. The considered frequency interval is 1 GHz to 8.5 GHz. The improvement for 15 lines per wavelength compared to 13 lines per wavelength approximately amounts to $6 \cdot 10^{-4}$. (b) Discretization of the bellow using 15 lines per wavelength ($N_p = 20,631$). The plane in which the mesh is depicted indicates one of three used symmetry planes.



(a)



(b)

Figure D.6: (a) Mesh refinement study of the circular waveguide (or beam pipe) which is used in Section 5.4. The dots refer to a mesh with 5, 7, 9, 11, 13, and 15 lines per wavelength. The considered frequency interval is 1 GHz to 8.5 GHz. The improvement for 15 lines per wavelength compared to 13 lines per wavelength approximately amounts to $1 \cdot 10^{-3}$. (b) Discretization of the circular waveguide using 15 lines per wavelength ($N_p = 4,050$). The plane in which the mesh is shown indicates one of three used symmetry planes.

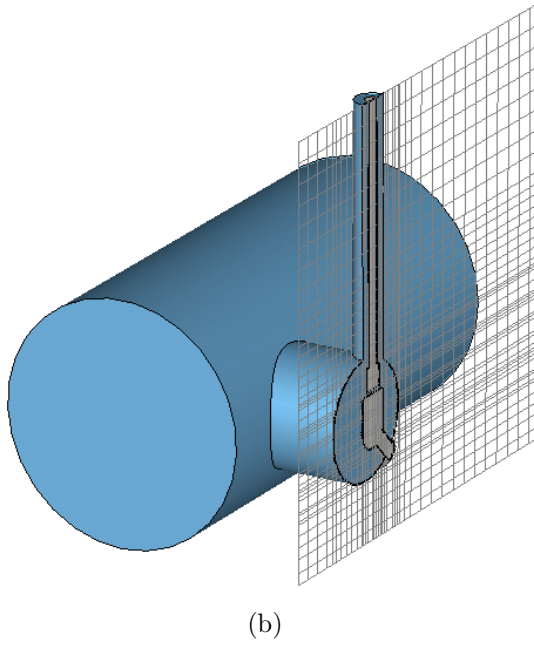
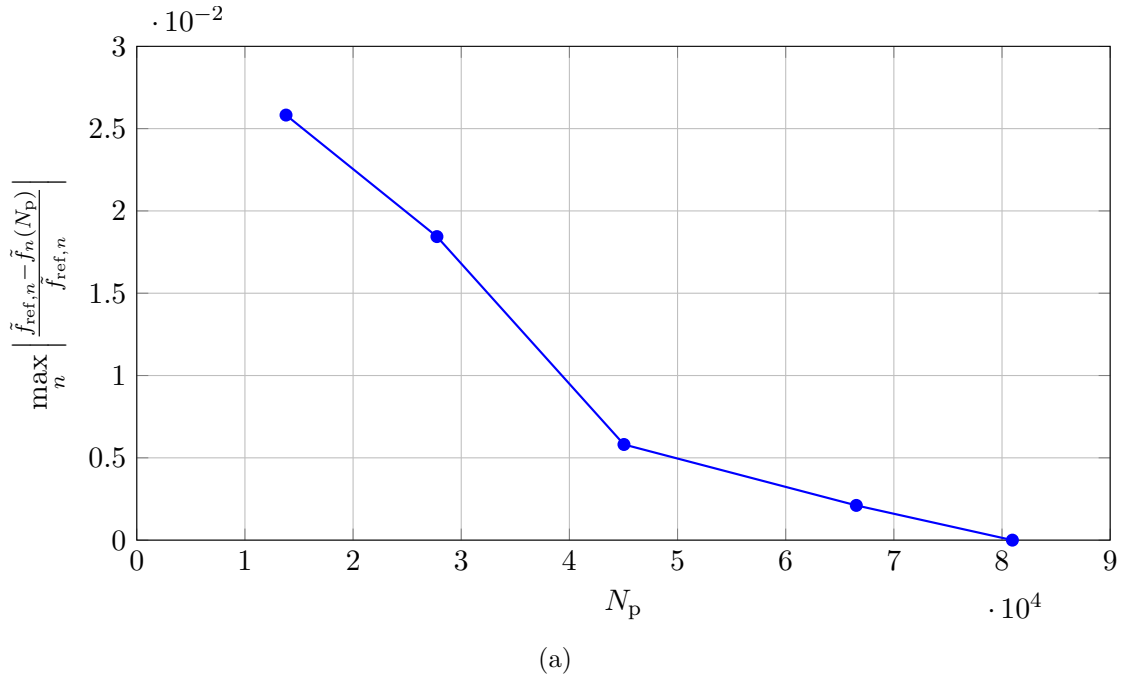
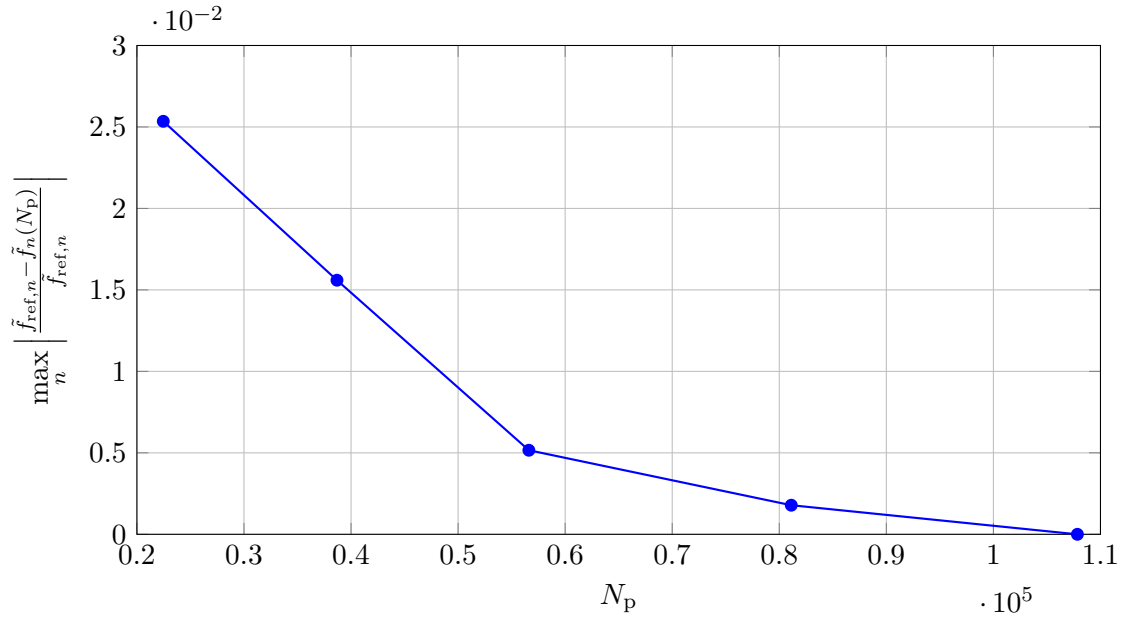
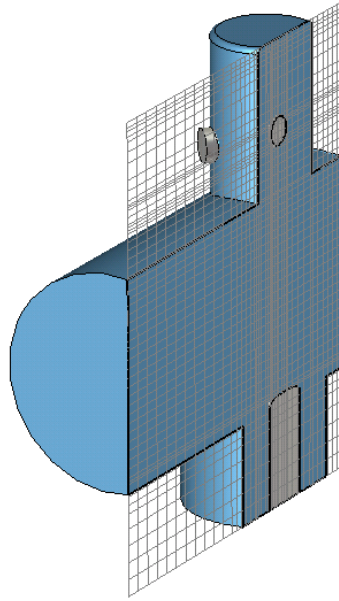


Figure D.7: (a) Mesh refinement study of the HOM coupler which is used in Section 5.5. The dots refer to a mesh with 7, 9, 11, 13, and 15 lines per wavelength. The considered frequency interval is 1 GHz to 6 GHz. The improvement for 15 lines per wavelength compared to 13 lines per wavelength approximately amounts to $2.1 \cdot 10^{-3}$. (b) Discretization of the HOM coupler using 15 lines per wavelength ($N_p = 80,960$). No symmetry planes can be used.



(a)



(b)

Figure D.8: (a) Mesh refinement study of the HOM coupler with power coupler which is used in Section 5.5. The dots refer to a mesh with 7, 9, 11, 13, and 15 lines per wavelength. The considered frequency interval is 1 GHz to 6 GHz. The improvement for 15 lines per wavelength compared to 13 lines per wavelength approximately amounts to $1.8 \cdot 10^{-3}$. (b) Discretization of the HOM coupler with input coupler using 15 lines per wavelength ($N_p = 107,844$). No symmetry planes can be used.

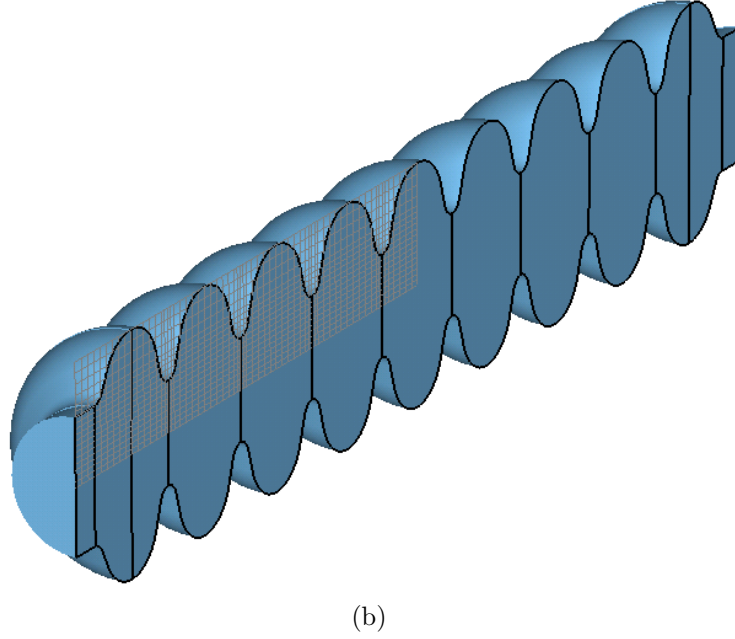
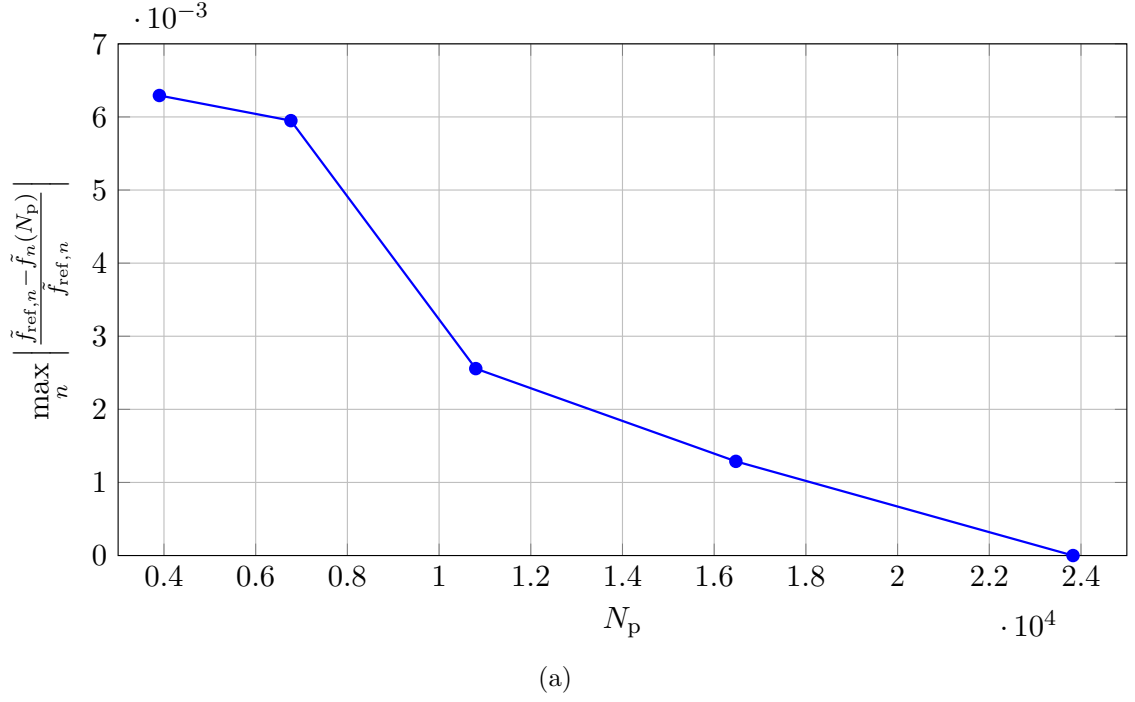
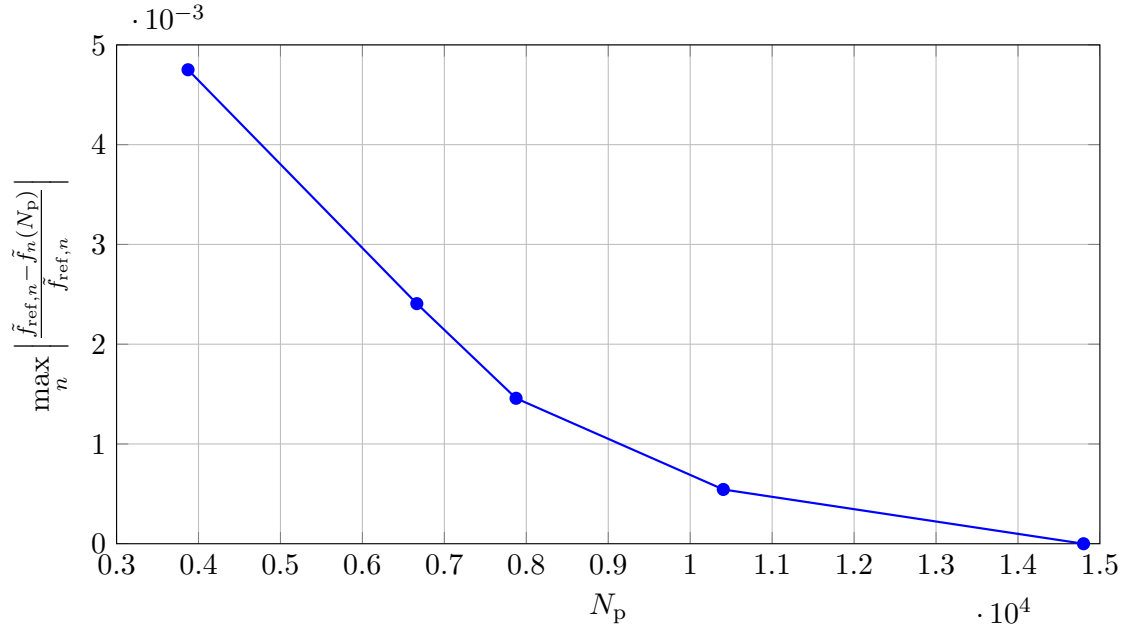
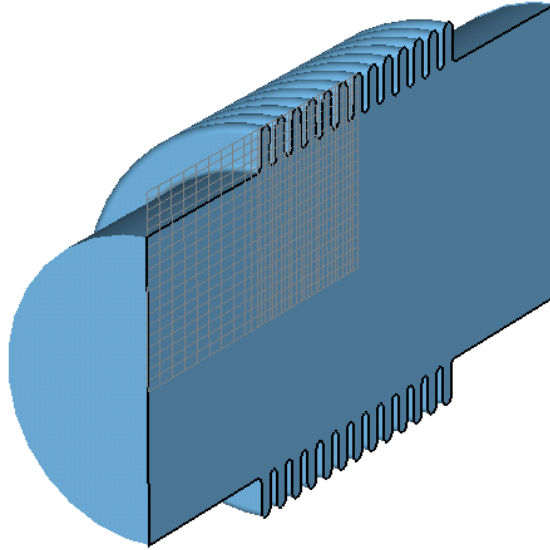


Figure D.9: (a) Mesh refinement study of the third harmonic cavity which is used in Section 5.5. The dots refer to a mesh with 7, 9, 11, 13, and 15 lines per wavelength. The considered frequency interval is 1 GHz to 6 GHz. The improvement for 15 lines per wavelength compared to 13 lines per wavelength approximately amounts to $1.3 \cdot 10^{-3}$. (b) Discretization of the single cell using 15 lines per wavelength ($N_p = 23,826$). The plane in which the mesh is depicted indicates one of three used symmetry planes.

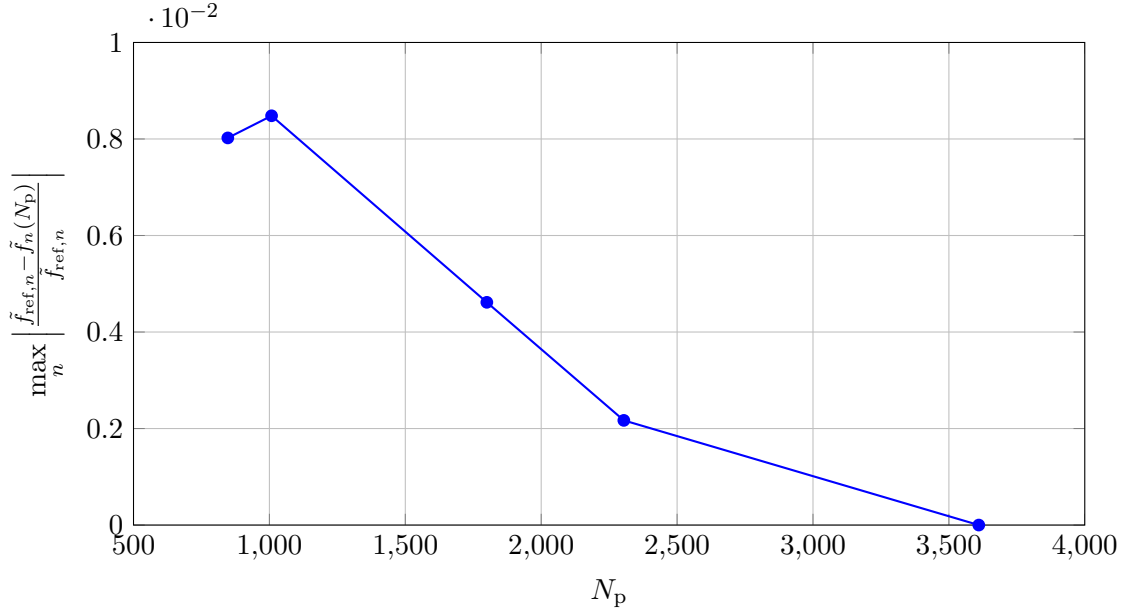


(a)

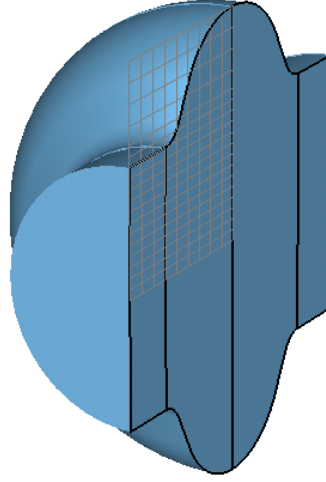


(b)

Figure D.10: (a) Mesh refinement study of the bellow which is used in Section 5.5. The dots refer to a mesh with 7, 9, 11, 13, and 15 lines per wavelength. The considered frequency interval is 1 GHz to 6 GHz. The improvement for 15 lines per wavelength compared to 13 lines per wavelength approximately amounts to $5.4 \cdot 10^{-4}$. (b) Discretization of the bellow using 15 lines per wavelength ($N_p = 14,800$). The plane in which the mesh is depicted indicates one of three used symmetry planes.



(a)



(b)

Figure D.11: (a) Mesh refinement study of the single cell which is used in Section 5.5 for validation purposes. The dots refer to a mesh with 7, 9, 11, 13, and 15 lines per wavelength. The considered frequency interval is 1 GHz to 6 GHz. The improvement for 15 lines per wavelength compared to 13 lines per wavelength approximately amounts to $2.2 \cdot 10^{-3}$. (b) Discretization of the single cell using 15 lines per wavelength ($N_p = 3,610$). The plane in which the mesh is depicted indicates one of three used symmetry planes.

Bibliography

- [1] T. Flisgen, H.-W. Glock, P. Zhang, I. R. R. Shinton, N. Baboi, R. M. Jones, and U. van Rienen. Scattering parameters of the 3.9 GHz accelerating module in a free-electron laser linac: A rigorous comparison between simulations and measurements. *Phys. Rev. ST Accel. Beams*, 17:022003, February 2014. doi: 10.1103/PhysRevSTAB.17.022003.
- [2] T. Flisgen, H.-W. Glock, and U. van Rienen. Compact Time-Domain Models of Complex RF Structures Based on the Real Eigenmodes of Segments. *IEEE Trans. Microw. Theory Tech.*, 61(6):2282 – 2294, June 2013. doi: 10.1109/TMTT.2013.2260765.
- [3] J. C. Slater. Microwave electronics. *Review of Modern Physics*, 18:441 – 512, October 1946. doi: 10.1103/RevModPhys.18.441.
- [4] M. Dohlus, H.-W. Glock, D. Hecht, and U. van Rienen. Filling and Beam Loading in TESLA Superstructures. TESLA-REPORT 98 - 14, DESY, Hamburg, Germany, 1998.
- [5] F. T. Cole (Ed.). Design Report Tevatron 1 Project. Technical Report FERMILAB-DESIGN-1984-01, Batavia, Illinois, USA, 1984.
- [6] S. Myers. *The LEP Collider, from design to approval and commissioning*. John Adams' Lecture. CERN, Geneva, 1991. Delivered at CERN, 26 November 1990.
- [7] T. S. Pettersson and P. Lefèvre. The Large Hadron Collider: conceptual design. Technical Report CERN-AC-95-05 LHC, CERN, Geneva, October 1995.
- [8] K. Balewski et al. PETRA III: A Low Emittance Synchrotron Radiation Source. Technical Design Report, DESY, Hamburg, Germany, February 2004.
- [9] Deutsches Elektronen-Synchrotron DESY. Free-Electron Laser FLASH. <http://flash.desy.de>, accessed 6th of October 2014.
- [10] European XFEL GmbH. X-Ray Free-Electron Laser XFEL. <http://www.xfel.eu>, accessed 6th of October 2014.
- [11] B. Aune et al. Superconducting TESLA cavities. *Phys. Rev. ST Accel. Beams*, 3:092001, September 2000. doi: 10.1103/PhysRevSTAB.3.092001.

- [12] H. Padamsee, T. Hays, and J. Knobloch. *RF Superconductivity for Accelerators*. Wiley series in beam physics and accelerator technology. John Wiley & Sons, Inc., New York, USA, 1998.
- [13] J. Sekutowicz, R. Wanzenberg, W. F. O. Müller, and T. Weiland. A Design of a 3rd Harmonic Cavity for the TTF 2 Photoinjector. TESLA-FEL Report: TESLA-FEL 2002-05, Hamburg, Germany, 2002.
- [14] N. Solyak, I. Gonin, H. Edwards, and M. Foley. Development of the Third Harmonic SC Cavity at FERMILAB. In *Proceedings of the Particle Accelerator Conference 2003*, pages 1213 – 1215, Portland, Oregon, USA, 2003.
- [15] T. Khabibouline, N. Solyak, and R. Wanzenberg. Higher Order Modes of a 3rd Harmonic Cavity with an Increased End-cup Iris. TESLA-FEL Report: TESLA-FEL 2003-01, Hamburg, Germany, 2003.
- [16] N. Solyak, H. Edwards, I. Gonin, M. Foley, T. Khabibouline, and D. Mitchell. Development of the 3.9 GHz 3rd harmonic cavity at FNAL. In *Proceedings of the International Conference on RF Superconductivity 2003*, pages 429 – 431, Hamburg, Germany, 2003.
- [17] K. Flöttmann, T. Limberg, and P. Piot. Generation of Ultrashort Electron Bunches by Cancellation of Nonlinear Distortions in the Longitudinal Phase Space. TESLA-FEL Report: TESLA-FEL-2001-06, Hamburg, Germany, 2001.
- [18] CST AG. *CST STUDIO SUITE 2014*. Bad Nauheimer Str. 19, 64289 Darmstadt, Germany.
- [19] S. Molloy et al. High precision superconducting cavity diagnostics with higher order mode measurements. *Phys. Rev. ST Accel. Beams*, 9:112802, November 2006. doi: 10.1103/PhysRevSTAB.9.112802.
- [20] P. Zhang, N. Baboi, R. M. Jones, I. R. R. Shinton, T. Flisgen, and H.-W. Glock. A study of beam position diagnostics using beam-excited dipole modes in third harmonic superconducting accelerating cavities at a free-electron laser. *Rev. Sci. Instrum.*, 83(8), 2012. doi: 10.1063/1.4748517.
- [21] P. Zhang. *Beam Position Diagnostics with Higher Order Modes in Third Harmonic Superconducting Accelerating Cavities*. PhD thesis, University of Manchester, 2013.
- [22] I. R. R. Shinton, N. Juntong, and R. M. Jones. Compendium of Eigenmodes in Third Harmonic Cavities for FLASH and the XFEL. DESY-REPORT 2012-53, DESY, Hamburg, Germany, 2012.

- [23] K. Rothemund, H.-W. Glock, M. Borecky, and U. van Rienen. Eigenmode Calculation in Long and Complex RF Structures Using the Coupled S-Parameter Calculation Technique. TESLA-REPORT 2000-33, DESY, Hamburg, Germany, 2000.
- [24] E. Vogel et al. Test and Commissioning of the Third Harmonic RF System for FLASH. In *Proceedings of International Particle Accelerator Conference 2010*, pages 4281 – 4283, Kyoto, Japan, 2010.
- [25] I. R. R. Shinton, R. M Jones, Z. Li, and P. Zhang. Simulations of Higher Order Modes in the ACC39 Module of FLASH. In *Proceedings of International Particle Accelerator Conference 2012*, pages 1900 – 1902, New Orleans, Louisiana, USA, May 2012.
- [26] K. Ko et al. Advances in Parallel Electromagnetic Codes for Accelerator Science and Development. In *Proceedings of the Linear Accelerator Conference 2010*, pages 1028 – 1032, Tsukuba, Japan, 2010.
- [27] F. Yaman, W. Ackermann, and T. Weiland. Comparison of Eigenvalue Solvers for Large Sparse Matrix Pencils. In *Proceedings of the 11th International Computational Accelerator Physics Conference 2012*, pages 287 – 289, Rostock-Warnemünde, Germany, 2012.
- [28] T.-W. Huang, B. Houshmand, and T. Itoh. The Implementation of Time-Domain Diakoptics in the FDTD Method. *IEEE Trans. Microw. Theory Tech.*, 42(11):2149 – 2155, November 1994. doi: 10.1109/22.330131.
- [29] K. Rothemund, H.-W. Glock, and U. van Rienen. Eigenmode Calculation of Complex RF-Structures using S-Parameters. *IEEE Trans. Magn.*, 36(4):1501 – 1503, Juli 2000. doi: 10.1109/20.8877722.
- [30] H.-W. Glock, K. Rothemund, and U. van Rienen. CSC - A Procedure for Coupled S-Parameter Calculations. *IEEE Trans. Magn.*, 38(2):1173 – 1176, March 2002. doi: 10.1109/20.996300.
- [31] T. Weiland, I. Munteanu, and M. Timm. From Component to System Simulation. In *Proceedings of 19th Annual Review of Progress in Applied Computational Electromagnetics 2003*, pages 1 – 6, Monterey, California, USA, March 2003.
- [32] P. Arcioni and G. Conciauro. Combination of Generalized Admittance Matrices in the Form of Pole Expansions. *IEEE Trans. Microw. Theory Tech.*, 47(10): 1990 – 1996, October 1999. doi: 10.1109/22.795073.

- [33] K. Zhang and D. Li. *Electromagnetic Theory for Microwaves and Optoelectronics*. Springer Publishing, 2nd edition, 2008. ISBN 9783540742951.
- [34] U. van Rienen. Higher Order Mode Analysis of Tapered Disc-Loaded Waveguides Using the Mode Matching Technique. *Particle Accelerators*, 41:173 – 201, 1993.
- [35] T. Sieverding and F. Arndt. Field Theoretic CAD of Open or Aperture Matched T-Junction Coupled Rectangular Waveguide Structures. *IEEE Trans. Microw. Theory Tech.*, 40(2):353 – 362, February 1992. doi: 10.1109/22.120109.
- [36] U. Papziner and F. Arndt. Field Theoretical Computer-Aided Design of Rectangular and Circular Iris Coupled Rectangular or Circular Waveguide Cavity Filters. *IEEE Trans. Microw. Theory Tech.*, 41(3):462 – 471, March 1993. doi: 10.1109/22.223746.
- [37] F. Arndt, R. Beyer, J. M. Reiter, T. Sieverding, and T. Wolf. Automated Design of Waveguide Components Using Hybrid Mode-Matching/Numerical EM Building-Blocks in Optimization-Oriented CAD Frameworks - State of the Art and Recent Advances. *IEEE Trans. Microw. Theory Tech.*, 45(5):747 – 760, May 1997. doi: 10.1109/22.575597.
- [38] U. van Rienen. *Numerical Methods in Computational Electrodynamics: Linear Systems in Practical Applications*. Springer, Berlin, Germany, 2001. ISBN 3540676295.
- [39] K. Rothemund. *Ein Verfahren zur Berechnung von Eigenmoden in langen und komplexen Hochfrequenzstrukturen*. PhD thesis, Universität Rostock, Shaker Verlag, Aachen, 2004.
- [40] T. Wittig, R. Schuhmann, and T. Weiland. Model order reduction for large systems in computational electromagnetics. *Linear Algebra and its Appl.*, 415 (2 - 3):499 – 530, June 2006.
- [41] T. Wittig. *Zur Reduzierung der Modellordnung in elektromagnetischen Feldsimulationen*. PhD thesis, TU Darmstadt, Cuvillier Verlag, Göttingen, 2004.
- [42] B. Trapp. *Zur numerischen Berechnung hochfrequenter elektromagnetischer Felder auf der Basis von Eigenlösungen*. PhD thesis, TU Darmstadt, Shaker Verlag, Aachen, 2003.
- [43] M. Dohlus, R. Schuhmann, and T. Weiland. Calculation of frequency domain parameters using 3D eigensolutions. *Int. J. Numer. Model.*, 12:41 – 48, January 1999.

- [44] P. Stenius and B. York. On the Propagation of Transients in Waveguides. *IEEE Trans. Antennas and Propag.*, 37(2):39 – 44, April 1995. doi: 10.1109/74.382337.
- [45] G. Kristensson. Transient Electromagnetic Wave Propagation in Waveguides. *Journal of Electromagnetic Waves and Applications*, 9(5/6):645 – 671, August 1995. doi: 10.1163/156939395X00866.
- [46] W. Geyi. A Time-Domain Theory of Waveguide. *Progress In Electromagnetics Research*, 59:267 – 297, 2006. doi: 10.2528/PIER05102102.
- [47] W. Geyi. A Time-Domain Theory of Metal Cavity Resonator. *Progress in Electromagnetics Research*, 78:219 – 253, 2008. doi: 10.2528/PIER07090605.
- [48] O. A. Tretyakov and O. Akgun. Derivation of Klein-Gordon Equation from Maxwell’s Equations and Study of Relativistic Time-Domain Waveguide Modes. *Progress in Electromagnetics Research*, 105:171 – 191, 2010. doi: 10.2528/PIER10042702.
- [49] F. Erden and O. Tretyakov. Excitation by a transient signal of the real-valued electromagnetic fields in a cavity. *Phys. Rev. E*, 77:056605, May 2008. doi: 10.1103/PhysRevE.77.056605.
- [50] J. C. Maxwell. *A Treatise on Electricity and Magnetism*, volume 1. Cambridge University Press, 2010. ISBN 9780511709333. doi: 10.1017/CBO9780511709333. Cambridge Books Online.
- [51] K. Klopfer, U. Niedermayer, H. Klingbeil, W. Ackermann, H. G. König, and T. Weiland. Measurement of the magnetic material properties for ferrite-loaded cavities. *Phys. Rev. ST Accel. Beams*, 18:010101, January 2015. doi: 10.1103/PhysRevSTAB.18.010101.
- [52] G. R. Eichhorn, J. Conway, Y. He, Y. Li, T. O’Connell, P. Quigley, J. Sears, V. D. Shemelin, and N. R. A. Valles. Cornell’s beam line higher order mode absorbers. In *Proceedings of the International Conference on RF Superconductivity 2013*, pages 1027 – 1029, Paris, France, 2013.
- [53] G. Waldschmidt, B. Brajuskovic, D. Bromberek, J. Fuerst, J. Holzbauer, A. Nassiri, V. Shemelin, Y. Shiroyanagi, G. Wu, and V. Shemelin. HOM dampers and waveguides for the Short Pulse X-Ray (SPX) project. In *Proceedings of the International Conference on RF Superconductivity 2013*, pages 1098 – 1100, Paris, France, 2013.
- [54] R. E. Collin. *Foundations for Microwave Engineering*. McGraw-Hill Ryerson, Limited, 1992. ISBN 9780070118119.

- [55] M. Kummer. *Grundlagen der Mikrowellentechnik*. VEB Verlag Technik, Berlin, Germany, 1989. ISBN 3341006877.
- [56] R. E. Collin. *Field Theory of Guided Waves*. IEEE Press, New York, USA, 2nd edition, 1991. ISBN 0879422378.
- [57] W. Hackbusch, H. R. Schwarz, and E. Zeidler. *Taubner-Taschenbuch der Mathematik*. B. G. Teubner Stuttgart, Leipzig, Germany, 1996. ISBN 3815420016.
- [58] A. Bondeson, T. Rylander, and P. Ingelström. *Computational Electromagnetics*. Springer, Berlin, Germany, 2005. ISBN 0849380138.
- [59] T. Weiland. A Discretization Method for the Solution of Maxwell's Equations for Six-Component Fields. *Electronics and Communications AEUE*, 31(3):116 – 120, 1977.
- [60] R. Schuhmann. *Die nichtorthogonale Finite-Integrations-Methode zur Simulation elektromagnetischer Felder*. PhD thesis, TU Darmstadt, Der Andere Verlag, Bad Iburg, 1999.
- [61] U. van Rienen. *Zur numerischen Berechnung zeitharmonischer elektromagnetischer Felder in offenen zylindersymmetrischen Strukturen unter Verwendung von Mehrgitterverfahren*. PhD thesis, TH Darmstadt, 1989.
- [62] M. Dohlus. *Ein Beitrag zur numerischen Berechnung elektromagnetischer Felder im Zeitbereich*. PhD thesis, TU Darmstadt, 1992.
- [63] J. G. van Bladel. *Electromagnetic Fields*. IEEE Press Series on Electromagnetic Wave Theory. John Wiley & Sons, 2007. ISBN 9780470124574.
- [64] H. Wiedemann. *Particle Accelerator Physics*. Springer, Berlin, Germany, 3rd edition, 2007. ISBN 9783540490432.
- [65] B. d'Andréa-Novel and M. De Lara. *Control Theory for Engineers. A primer*. Springer, Berlin, Germany, 2013. ISBN 9783642343230.
- [66] F. Szidarovszky and A. T. Bahill. *Linear Systems Theory*. CRC Press, Boca Raton, USA, 1992. ISBN 0849380138.
- [67] C.-T. Chen. *Linear System Theory and Design*. Oxford University Press, New York, USA, 2009. ISBN 9780195392074.
- [68] A. C. Antoulas. *Approximation of Large-Scale Dynamical Systems*. Society for Industrial and Applied Mathematics, Philadelphia, PA, USA, 2005. ISBN 9780898718713.

- [69] MATLAB. *Version R2011b*. The MathWorks, Inc., Natick, Massachusetts, USA, 2011.
- [70] A. Steidle. On the Reduction of State-Space Models for Coupled RF Structures. Bachelor's thesis, Universität Rostock, September 2013.
- [71] T. Flisgen, J. Heller, and U. van Rienen. Time-Domain Absorbing Boundary Terminations for Waveguide Ports Based on State-Space Models. *IEEE Trans. Magn.*, 50(2), February 2014. doi: 10.1109/TMAG.2013.2283065.
- [72] H.-W. Glock, M. Kurz, P. Hülsmann, and H. Klein. Rise time of the amplitudes of time harmonic fields in multicell cavities. In *Proceedings of the Particle Accelerator Conference 1993*, volume 1, May 1993.
- [73] I. Woyna, E. Gjonaj, and T. Weiland. Broadband surface impedance boundary conditions for higher order time domain discontinuous Galerkin method. *The International Journal for Computation and Mathematics in Electrical and Electronic Engineering*, 33(4):1082 – 1096, 2014. doi: 10.1108/COMPEL-08-2013-0260.
- [74] F. Moglie, T. Rozzi, P. Marcozzi, and A. Schiavoni. A New Termination Condition for the Application of FDTD Techniques to Discontinuity Problems in Close Homogeneous Waveguide. *IEEE Microw. Guided Wave Lett.*, 2(12):475 – 477, December 1992. doi: 10.1109/75.173399.
- [75] R. Schuhmann and T. Weiland. Rigorous analysis of trapped modes in accelerating cavities. *Phys. Rev. ST Accel. Beams*, 3:122002, December 2000. doi: 10.1103/PhysRevSTAB.3.122002.
- [76] W. Ackermann and T. Weiland. High Precision Cavity Simulations. In *Proceedings of the 11th International Computational Accelerator Physics Conference 2012*, pages 43 – 47, Rostock-Warnemünde, Germany, 2012.
- [77] K. Rothmund D. Hecht, H.-W. Glock, and U. van Rienen. Computation of RF-properties of long and complex structures. In *Proceedings of the European Particle Accelerator Conference 2002*, pages 1685 – 1687, Paris, France, 2002.
- [78] E. Vogel et al. Considerations on the Third Harmonic RF of the European XFEL. In *Proceedings of International Conference on RF Superconductivity 2007*, pages 481 – 485, Beijing, China, 2007.
- [79] A. Henderson and J. Ahrens. *The Paraview guide: a parallel visualization application*. Kitware, Inc., New York, 2004. ISBN 1930934149.

- [80] G. Wüstefeld, A. Jankowiak, J. Knobloch, and M. Ries. Simultaneous Long and Short Electron Bunches in the BESSY II Storage Ring. In *Proceedings of International Particle Accelerator Conference 2011*, pages 2936 – 2938, San Sebastián, Spain, September 2011.
- [81] A. Logg, K.-A. Mardal, and G. N. Wells. *Automated Solution of Differential Equations by the Finite Element Method*. Springer, 2012. ISBN 9783642230981. doi: 10.1007/978-3-642-23099-8.
- [82] K. Meyberg and P. Vachenauer. *Höhere Mathematik 1: Differential- und Integralrechnung. Vektor- und Matrizenrechnung*. Springer, Berlin, Germany, 2003. ISBN 9783540418504.